

Electronic Thesis and Dissertation Repository

9-26-2023 2:30 PM

Structural Control of Metallothionein Metallation and Oxidation


Natalie C. Korkola, *Western University*

Supervisor: Stillman, Martin J., *The University of Western Ontario*

A thesis submitted in partial fulfillment of the requirements for the Doctor of Philosophy degree in Chemistry

© Natalie C. Korkola 2023

Follow this and additional works at: <https://ir.lib.uwo.ca/etd>

 Part of the [Analytical Chemistry Commons](#), [Biochemistry Commons](#), [Inorganic Chemistry Commons](#), and the [Other Chemistry Commons](#)

Recommended Citation

Korkola, Natalie C., "Structural Control of Metallothionein Metallation and Oxidation" (2023). *Electronic Thesis and Dissertation Repository*. 9738.

<https://ir.lib.uwo.ca/etd/9738>

This Dissertation/Thesis is brought to you for free and open access by Scholarship@Western. It has been accepted for inclusion in Electronic Thesis and Dissertation Repository by an authorized administrator of Scholarship@Western. For more information, please contact wlsadmin@uwo.ca.

Abstract

Metallothioneins (MT) are a family of cysteine-rich metal-binding intrinsically disordered proteins that are ubiquitous across life. The proposed functions of MTs are to maintain Zn(II) homeostasis, participate in heavy metal detoxification, and protect against oxidative stress by binding to a variety of metals in a range of stoichiometries. However, due to their disordered nature and ability to form multiple metallated species, these diverse structures are not well characterized. Electrospray ionization mass spectrometry (ESI-MS) is a technique that allows quantification of heterogeneous metallation states through analysis of the speciation distributions. In this thesis, ESI-MS in combination with other spectroscopic techniques is used to probe the structural features of apo-MT, the early Zn(II) and Cd(II) metallation steps, the binding of the xenobiotic metal Bi(III), and the pathway of oxidation and subsequent Zn(II) and Cd(II) displacement upon exposure to H₂O₂. These speciation details shown using ESI-MS have not yet been described using other techniques. It was concluded that both the apo-MT structure and the metal-loading status impact MT's metallation and oxidation properties, which provides insight into the structure-function relationship of MTs.

Keywords

Metallothionein, protein folding, metalloproteins, intrinsically disordered proteins, metal-induced folding, protein denaturation, cadmium, zinc, bismuth, electrospray ionization mass spectrometry, absorption spectroscopy, circular dichroism spectroscopy, stopped flow, molecular dynamics, density functional theory.

Summary for Lay Audience

Many proteins require metals such as zinc or copper for their physiological functions. However, the correct balance of these metals must be maintained as a concentration that is too low or too high may be toxic to cells. Additionally, environmental exposure to toxic heavy metals can lead to adverse health effects. Metallothioneins (MTs) are cysteine-rich, low molecular weight proteins that bind a variety of metals, balancing the availability of nutritionally essential metals and providing protection against toxic heavy metals. MTs may also act as an antioxidant. However, this process results in the release of bound metals from MT. The pathways of metal binding and metal release are relevant to our understanding of how MTs function, but these pathways are not currently well-described. MTs can bind multiple metals at once, making determination of the individual states difficult. Mass spectrometry (MS) is a technique that can identify these individual species and their relative concentrations based on mass changes caused by the binding of each metal. Using this technique, the metal binding pathways and metal release pathways to and from MTs can be described. The effect of the MT structure on these processes can also be considered, providing more insight into the relationship between protein structure and function.

Co-Authorship Statement

This thesis contains material from previously published manuscripts. Dr. Martin Stillman supervised Ms. Natalie Korkola and is a coauthor of all the published manuscripts. For each publication, Dr. Martin Stillman played a major role in manuscript revision.

For all Chapters apart from the exceptions noted below, Ms. Natalie Korkola was responsible for experimental design, data collection, data interpretation, figure preparation, and drafting of the Chapter. Dr. Martin Stillman provided guidance at each step.

Ms. Amelia Yuan was responsible for the MT3 expression and purification in Chapter 3. For the data presented in Chapter 3 involving MT3, the experimental design, data collection, and figure preparation was carried out by Ms. Amelia Yuan. For the associated manuscript, Ms. Amelia Yuan was responsible for writing the paper for publication. Ms. Amelia Yuan, Ms. Natalie Korkola, and Dr. Martin Stillman collaborated on experimental design, data collection, data interpretation, and editing of the manuscript. Ms. Natalie Korkola rewrote sections of the manuscript for Chapter 3 to fit with the other results presented in the Chapter.

Chapter 5 has two associated publications which were edited into one Chapter along with new results by Ms. Natalie Korkola. Ms. Patti Scarrow was a coauthor for one of the associated publications in Chapter 5 and carried out preliminary work and assisted with manuscript revision. Ms. Elyse Hudson was a coauthor for the other associated publication in Chapter 5 and carried out expression and purification of the β MT, carried out preliminary work, and assisted with manuscript revision. Ms. Adyn Melenbacher carried out expression and purification of the α MT used in the experiments described in Chapter 5. The work on Bi(III) binding to Zn₇MTs was a collaborative project with Ms. Anne-Lena Ostertag. She performed many preliminary experiments and described her work of a similar nature in her Master's Thesis. Ms. Emily Toswell also carried out preliminary experiments in Bi(III) binding to Zn₇MTs.

Acknowledgments

First, I would like to thank my supervisor, Dr. Martin Stillman for giving me this opportunity to experience research, for being an excellent mentor, allowing me to travel to present my work in Japan, France, and Australia, and for always enthusiastically celebrating group accomplishments. There are two past group members that I would like to acknowledge, as much of my project was built on their preliminary work: Dr. Kelly Rigby Duncan for her excellent stopped flow results and Dr. Gordon Irvine for his novel use of cysteine modification methods for metallothioneins. I would also like to acknowledge and thank the Stillman Group members, past and present. Special mentions go to Dr. Daisy Wong for passing along her knowledge to me and to Ms. Adyn Melenbacher and Ms. Amelia Yuan for being excellent lab mates and collaborators throughout the years. Thank you as well to Ms. Angel Zhang, Mr. Riley Hooper, Ms. Patti Scarrow, Ms. Anne-Lena Ostertag, Ms. Alice Jin, Mr. Jason Zhang, Ms. Elyse Hudson, Mr. Connor Durfy, Ms. Emily Toswell, Ms. Lina Heinlein, Ms. Yue Li, and Ms. Jessica Pereira. Each of you made the lab such a nice place to work.

Special thanks go to the support staff at the University of Western Ontario. Thank you to Mr. John Vanstone, Mr. Barakat Misk, and Ms. Melanie Glover at the Electronics Shop for excellent maintenance and repair of our equipment. Thank you to the past and present Mass Spectrometry Facility managers Mr. Doug Hairsine, Dr. Haidy Metwally, and Dr. Chathu Pulukkody for excellent maintenance and troubleshooting of our mass spectrometer.

Next, I would like to thank my Mom and Dad for all of their support and encouragement over the years. I would not be where I am today without you. A special thank you to my brother Matthew for being a great roommate and my dog Nina for always greeting me with such enthusiasm every time I come home to visit.

Finally, I would like to thank my wonderful fiancé Zach. I am so grateful to have you in my life and your support while completing my PhD has been so valuable to me. Thank you for always being up to discuss my project and for giving me great advice from a new perspective. I am so excited to enter this next stage of my life with you.

Table of Contents

Abstract.....	ii
Summary for Lay Audience.....	iii
Co-Authorship Statement.....	iv
Acknowledgments.....	v
Table of Contents.....	vi
List of Tables.....	xiv
List of Figures.....	xv
List of Appendices.....	xx
List of Abbreviations.....	xxi
Amino Acid Three and One Letters Codes.....	xxii
Chapter 1.....	1
1 Introduction.....	1
1.1 Structural Properties of Proteins.....	1
1.1.1 Protein folding: the relationship between sequence, structure, and function.....	1
1.1.2 Metalloprotein binding site structure.....	2
1.1.3 Intrinsically disordered proteins.....	3
1.1.4 Protein disfunction: misfolding, oxidative stress, and metal toxicity.....	4
1.1.5 Metallothionein: an intrinsically disordered metal binding protein.....	6
1.2 Metallothioneins: Discovery and Classification.....	7
1.2.1 Discovery of metallothioneins.....	7
1.2.2 Metallothionein classification systems.....	7
1.2.3 Isoforms of mammalian metallothioneins.....	8
1.3 Biological Functions of Metallothioneins.....	9

1.3.1	Metal content of metallothioneins	9
1.3.2	Upregulation of metallothioneins: sources and pathway	9
1.3.3	Protective effects of metallothioneins.....	10
1.3.4	Metallothioneins' role in Zn(II) homeostasis	11
1.4	Metallothionein Structural Characterization.....	13
1.4.1	Early characterization of metal-thiolate bonds and the two-domain structure.....	13
1.4.2	The elusive structure of apo-metallothionein	14
1.4.3	Beyond two-domains: partially metallated Zn(II) and Cd(II) metallothionein structures and binding pathways.....	15
1.4.4	Non-traditional metallothionein structures	17
1.4.5	The effect of metallothionein structure on oxidation.....	20
1.5	Scope of the Thesis	21
Chapter 2.....		23
2	Materials and Methods.....	23
2.1	Instrumental Methods: Theory and Applications	23
2.1.1	UV-visible absorption spectroscopy	23
2.1.2	Circular dichroism spectroscopy.....	26
2.1.3	Electrospray ionization mass spectrometry	27
2.1.4	Stopped flow kinetic methods.....	35
2.2	Computational Methods.....	37
2.3	Solution Preparation.....	38
2.4	Protein Expression and Purification.....	40
2.4.1	Transformation of bacteria with plasmid.....	40
2.4.2	Cell growth and protein expression	40
2.4.3	Protein purification	41

2.5 Preparation of Apo-MT for Experimental Analysis	44
Chapter 3.....	46
3 Human Apo-Metallothionein 1a is not a Random Coil: Evidence from Chemical, Temperature, and pH Unfolding	46
3.1 Introduction.....	46
3.2 Materials and Methods.....	51
3.2.1 Determination of mean hydrophobicity	51
3.2.2 Molecular dynamics simulations	52
3.2.3 MT1a and MT3 expression and purification	53
3.2.4 Apo-MT1a and apo-MT3 preparation	54
3.2.5 Proteolysis experiments	54
3.2.6 Titration of cysteine modifier at various pHs	54
3.2.7 pH denaturation experiments	55
3.2.8 Temperature denaturation experiments.....	55
3.2.9 GdmCl denaturation experiments	56
3.2.10 Fitting of the unfolding curves.....	57
3.3 Results and Discussion	59
3.3.1 Apo-MT1a and apo-MT3 sequences predict ordered structures.....	59
3.3.2 MD simulations of apo-MT1a reveal a compact structure	60
3.3.3 MD simulations indicate both buried and exposed cysteines in the apo- MT1a native structure	62
3.3.4 Cysteine modification and trypsin digestion experimentally monitor cysteine exposure in apo-MT1a	64
3.3.5 Apo-MT1a and apo-MT3 exhibit different pH-dependent structures.....	67
3.3.6 The cooperative pH-dependent unfolding transition of apo-MT1a monitored using ESI-MS	74

3.3.7	The cooperative temperature-dependent unfolding transition of apo-MT1a monitored using ESI-MS.....	77
3.3.8	The cooperative GdmCl-dependent unfolding transition of apo-MT1a monitored using ESI-MS	77
3.3.9	The cooperative GdmCl-dependent unfolding transition of apo-MT1a monitored using CD spectroscopy	82
3.3.10	Metallothionein as an intrinsically disordered protein.....	84
3.4	Conclusions.....	86
Chapter 4	87
4	Structural Motifs in the Early Metallation Steps of Zn(II) and Cd(II) binding to Apo-Metallothionein 1a	87
4.1	Introduction.....	87
4.2	Materials and Methods.....	91
4.2.1	Stopped flow methods.....	91
4.2.2	Analysis of kinetic Data.....	92
4.2.3	Circular dichroism methods.....	93
4.2.4	ESI-MS methods.....	94
4.3	Results and Discussion	95
4.3.1	The nature of the observed kinetic traces	95
4.3.2	The effect of multistep reactions on the kinetic fitting parameters	95
4.3.3	The rate of Zn(II) and Cd(II) metallation is pH-dependent	96
4.3.4	The difference in metallation rates of Zn(II) and Cd(II) to apo-MT is amplified under acidic conditions.....	98
4.3.5	The rates of Zn(II) and Cd(II) metallation slow under denaturing conditions.....	102
4.3.6	Denaturation of the apo-MT structure reduces the rate of the early Zn(II) and Cd(II) metallation steps.....	106
4.3.7	Stepwise Zn(II) and Cd(II) titrations monitored using CD spectroscopy suggest different pathways under native and denaturing conditions	107

4.3.8	Specific bridging thiolate structures form in metal-unsaturated Zn(II) and Cd(II) MTs	111
4.3.9	Denaturation of apo-MT disrupts formation of bridging metal-thiolate structures	115
4.4	Conclusions.....	117
Chapter 5	118
5	The pH and Structure-Dependent Binding of Bismuth to Metallothionein 1a	118
5.1	Introduction.....	118
5.2	Materials and Methods.....	121
5.2.1	Protein expression, purification, and preparation for experiments	121
5.2.2	Electrospray ionization mass spectrometry experiments	121
5.2.3	Titrations of [Bi(cit)] ⁻ into apo-MT at pH 2.6.....	121
5.2.4	Titrations of [Bi(EDTA)] ⁻ into apo-MT at pH 2.6.....	122
5.2.5	Titrations of [Bi(EDTA)] ⁻ into apo-MT at pH 7.4.....	122
5.2.6	Trypsin digestion experiments	122
5.2.7	Cysteine modification experiments.....	123
5.2.8	Metallation of denatured apo-βMT with [Bi(EDTA)] ⁻	123
5.2.9	pH dependence of Bi ₂ βMT	124
5.2.10	Metal exchange between Bi ₂ βMT, Cd ₃ βMT, and Zn ₃ βMT	124
5.2.11	Titration simulations and determination of conditional binding constants.....	124
5.2.12	UV-Visible absorption experiments	125
5.3	Results and Discussion	128
5.3.1	The pH and anion dependence of Bi(III) binding to apo-MT.....	128
5.3.2	Determination of free cysteines in Bi(III)-bound βαMT species.....	134
5.3.3	Studies of the [Bi(EDTA)] ⁻ binding pathways in apo-βMT and apo-αMT.	137

5.3.4	Investigating the location of Bi(III) in the Bi ₂ β _α MT structure.....	143
5.3.5	Bi(III) binding to apo-MT does not display domain specificity	146
5.3.6	The structure of apo-βMT inhibits the formation of Bi ₃ βMT.....	146
5.3.7	There is a pH dependence in the competition between the EDTA and the nine cysteines of βMT for the Bi(III).....	149
5.3.8	Bi ₂ βMT will not exchange metals with Cd ₃ βMT and Zn ₃ βMT.....	151
5.3.9	Studies of [Bi(EDTA)] ⁻ binding to Zn ₇ β _α MT.....	151
5.4	Conclusions.....	158
Chapter 6.....		160
6	The Structural Role of Cadmium And Zinc In Metallothionein Oxidation By Hydrogen Peroxide: The Resilience of Metal-Thiolate Clusters	160
6.1	Introduction.....	160
6.2	Materials and Methods.....	163
6.2.1	Expression, purification, and preparation of apo-MT.....	163
6.2.2	Preparation of Cd ₇ MT, Zn ₇ MT, Cd ₃ MT, and Zn ₃ MT	164
6.2.3	Creation of the oxidizing environment	164
6.2.4	Electrospray ionization mass spectral studies.....	165
6.2.5	Reversibility experiments	166
6.2.6	Proteolysis experiments	166
6.2.7	UV-visible absorption spectroscopy experiments	166
6.2.8	Quantification of Zn(II) release	167
6.2.9	Determination of the rate constants	167
6.2.10	Circular dichroism spectroscopy experiments.....	168
6.2.11	Theoretical calculations	168
6.3	Results and Discussion	169

6.3.1	H ₂ O ₂ selectively oxidizes the cysteine and methionine residues of apo-MT.....	170
6.3.2	Metal-thiolate bonds provide protection against MT oxidation	172
6.3.3	Individual metallated and oxidized species are identified using ESI-MS.....	174
6.3.4	The extent of disulfide bond formation predicts the metal-loading status	177
6.3.5	The metals in MT are remarkably resistant to displacement	178
6.3.6	Metal redistribution occurs upon exposure to H ₂ O ₂	178
6.3.7	The species distributions following oxidation depend on the metal-loading status of the MT	179
6.3.8	Circular dichroism spectroscopy reveals the presence of α -domain cluster structures in partially oxidized MTs.....	180
6.3.9	MT regains its metal-binding ability upon reduction of disulfide bonds	185
6.3.10	The demetallation pathways are dependent on the metal-loading status of the MT	185
6.3.11	Major species from the metal-release are identified from the kinetic traces	187
6.3.12	The rate constants quantify the demetallation steps of MT due to oxidation by H ₂ O ₂	189
6.3.13	The rate of demetallation of individual metals depends on the metal-thiolate cluster structures	192
6.3.14	Density function theory calculations suggest different reactivity of terminally bound and bridging cysteines	193
6.3.15	Metal displacement from MT depends on the extent of cluster formation.....	195
6.4	Conclusions.....	196
Chapter 7	198
7	Conclusions	198
7.1	The Bias in Metallothionein Research: Challenges of Studying Intrinsically Disordered Proteins.....	198

7.1.1	Characterization of the apo-MT structure.....	199
7.2	Metallothionein as a Zn(II)-Binding Intrinsically Disordered Protein	201
7.3	Partially Metallated Structures Formed in the Native Apo-MT and Their Impact on Oxidation	202
7.4	pH-Dependence of Metallation.....	204
7.5	Structural Control of Non-Traditional Metallation.....	208
7.6	The Many Structures of Metallothionein.....	211
	References.....	212
	Appendix A: ESI-MS Mass Values	242
	Appendix B: Additional MD Simulation Data	244
	Appendix C: Additional CD Spectroscopy Data	246
	Appendix D: ESI-MS Validation Experiments.....	247
	Curriculum Vitae	251

List of Tables

Table 1-1. Sequences of human MT isoforms.	8
Table 1-2. Various metal binding stoichiometries for mammalian MTs.	19
Table 2-1. Instruments and laboratory equipment used in this thesis.	24
Table 2-2 The ESI-MS parameters used during experimental analysis of MT on the Bruker MicroTOF II instrument.	32
Table 2-3. Reagents and solutions prepared for use in the research described in this thesis and their suppliers.	39
Table 3-1. Parameters used for MD simulations.	52
Table 4-1. Table of pH-dependent rate constants of Zn(II) and Cd(II) binding to apo-MT.	100
Table 4-2. Table of GdmCl-dependent rate constants of Zn(II) and Cd(II) binding to apo-MT.	105
Table 5-1. Relative Bi(III)-MT binding constants.	132
Table 5-2. Relative Bi(III)-MT binding constants of $\beta\alpha$ MT and fragments.	143
Table 6-1. Apo-MT tryptic peptides.	172
Table 6-2. Number of oxidized and reduced cysteines throughout oxidation reactions.	177
Table 6-3. Rate constants resulting from MT oxidation-induced metal release.	191

List of Figures

Figure 1-1. Sequence of human MT1a.	14
Figure 2-1. UV-visible absorption spectra of MTs.	25
Figure 2-2. CD spectra of MTs.	26
Figure 2-3. A schematic of the Bruker MicroTOF II mass spectrometer.	28
Figure 2-4. ESI mass spectrum of recombinant human apo-MT1a.	31
Figure 2-5. Speciation simulations showing different binding pathways.	34
Figure 2-6. Stopped flow schematic.	36
Figure 2-7. Sequences of rh β α MT1a, rh β MT1a, and rh α MT1a.	43
Figure 3-1. Sequences of apo-rhMT1a and apo-rhMT3.	49
Figure 3-2. MD simulations of apo-MT.	60
Figure 3-3. Radius of gyration for apo-MT MD simulations over time.	61
Figure 3-4. The median cysteine ASA based on MD simulations.	63
Figure 3-5. Apo-MT1a partially modified with NEM at pH 7.4 and digested by trypsin.	65
Figure 3-6. NEM titration into apo-MT1a at pH 7.4 monitored by ESI-MS.	68
Figure 3-7. NEM titration into apo-MT1a at pH 5.0 monitored by ESI-MS.	69
Figure 3-8. NEM titration into apo-MT3 at pH 7.4 monitored by ESI-MS.	71
Figure 3-9. NEM titration into apo-MT3 at pH 5.0 monitored by ESI-MS.	72
Figure 3-10. NEM titration into apo-MT3 at pH 2.9 monitored by ESI-MS.	73

Figure 3-11. Effect of pH on apo-MT1a cysteine modification pattern monitored by ESI-MS.....	75
Figure 3-12. Fraction unfolded apo-MT1a vs pH monitored by ESI-MS.	76
Figure 3-13. Effect of Temperature on apo-MT1a cysteine modification pattern monitored by ESI-MS.	78
Figure 3-14. Fraction unfolded apo-MT1a vs Temperature monitored by ESI-MS.	79
Figure 3-15. Effect of GdmCl on apo-MT1a cysteine modification pattern monitored by ESI-MS.	80
Figure 3-16. Fraction unfolded apo-MT1a vs GdmCl monitored by ESI-MS.	81
Figure 3-17. GdmCl-induced unfolding of apo-MT monitored by CD spectroscopy.	83
Figure 4-1. pH-dependent kinetic traces of Zn(II) binding to apo-MT.	97
Figure 4-2. pH-dependent kinetic traces of Cd(II) binding to apo-MT.	99
Figure 4-3. Plot of pH-dependent rate constants of Zn(II) and Cd(II) binding to apo-MT.	101
Figure 4-4. GdmCl-dependent kinetic traces of Zn(II) binding to apo-MT.	103
Figure 4-5. GdmCl-dependent kinetic traces of Cd(II) binding to apo-MT.	104
Figure 4-6. Plots of GdmCl-dependent rate constants of Zn(II) and Cd(II) binding to apo-MT with fraction unfolded curves.	106
Figure 4-7. Titrations of Zn(II) or Cd(II) into apo-MT under native and denaturing conditions monitored by CD spectroscopy at pH 7.4.	109
Figure 4-8. The early metallation steps of Zn(II) and Cd(II) to apo-MT at pH 7.4 under native and denaturing conditions monitored using ESI-MS.	112

Figure 4-9. Intermediate Zn_xS_y and Cd_xS_y structures formed.....	113
Figure 5-1. A titration of $[Bi(cit)]^-$ into apo- $\beta\alpha$ MT at pH 2.6 monitored using ESI-MS.	126
Figure 5-2. A titration of $[Bi(EDTA)]^-$ into apo- $\beta\alpha$ MT at pH 2.6 monitored using ESI-MS.....	127
Figure 5-3. A titration of $[Bi(EDTA)]^-$ into apo- $\beta\alpha$ MT at pH 7.4 monitored using ESI-MS.....	129
Figure 5-4. Speciation curves and calculated binding constants for the titration of Bi(III) into apo- $\beta\alpha$ MT.	131
Figure 5-5. UV-visible absorption spectra of Bi(III)-bound $\beta\alpha$ MT.	134
Figure 5-6. Cysteine modification of Bi(III)-bound apo $\beta\alpha$ -MT species monitored using ESI-MS.	136
Figure 5-7. A titration of $[Bi(EDTA)]^-$ into apo- β MT at pH 7.4 monitored using ESI-MS.	138
Figure 5-8. A titration of $[Bi(EDTA)]^-$ into apo- α MT at pH 7.4 monitored using ESI-MS.	140
Figure 5-9. Speciation curves and calculated binding constants for the titration of Bi(III) into apo- $\beta\alpha$ MT, apo- β MT, and apo- α MT.....	142
Figure 5-10. Trypsin digestion of apo- $\beta\alpha$ MT and $Bi_2\beta\alpha$ MT monitored by ESI-MS.	144
Figure 5-11. Analysis of the trypsin digestion of apo- $\beta\alpha$ MT and $Bi_2\beta\alpha$ MT.	145
Figure 5-12. Cysteine modification of $Bi_2\beta$ MT with Bq monitored using ESI-MS.....	147
Figure 5-13. Bi(III) binding to apo- β MT in the absence and presence of 4 M GdmCl monitored using ESI-MS.	148

Figure 5-14. The pH dependence of Bi ₂ βMT cooperativity monitored using ESI-MS..	150
Figure 5-15. Test of metal exchange between Bi ₂ MT, Cd ₃ MT, and Zn ₃ MT monitored using ESI-MS.....	152
Figure 5-16. A titration of [Bi(EDTA)] ⁻ into Zn ₇ βαMT at pH 7.4 monitored using ESI-MS.....	153
Figure 5-17. Speciation curves for the titration of [Bi(EDTA)] ⁻ into Zn ₇ βαMT.	155
Figure 5-18. UV-visible absorption spectra of [Bi(EDTA)] ⁻ binding to Zn ₇ βαMT.	157
Figure 6-1. Oxidation of apo-MT monitored using ESI-MS.	169
Figure 6-2. Oxidation, reduction, and trypsin digestion of apo-MT.....	171
Figure 6-3. Oxidation of apo-MT, Cd ₇ MT, and Zn ₇ MT monitored using absorption spectroscopy.....	173
Figure 6-4. Oxidation of Cd ₇ MT and Zn ₇ MT monitored using ESI-MS.....	174
Figure 6-5. Oxidation of Cd ₃ MT and Zn ₃ MT monitored using ESI-MS.....	176
Figure 6-6. Reduced and oxidized MTs monitored using circular dichroism spectroscopy.	181
Figure 6-7. Reduced and oxidized MTs monitored using ESI-MS.	182
Figure 6-8. Cd(II) and Zn(II) binding to MTs after reversal of oxidation.....	184
Figure 6-9. Oxidation-induced MT demetallation pathways.....	186
Figure 6-10. Fitted kinetic traces of MT oxidation monitored using ESI-MS.....	188
Figure 6-11. Rate constants resulting from MT oxidation-induced metal release.....	190
Figure 6-12. Molecular models and electron density surfaces of CH ₃ SH structures.....	194

Figure 7-1. Comparison between the GdmCl-dependent unfolding curves monitored using CD spectroscopy and ESI-MS.....	200
Figure 7-2. Comparison between the GdmCl-dependent unfolding curves monitored using CD spectroscopy, the Zn(II) metallation rate, and the Cd(II) metallation rate.	202
Figure 7-3. Major Zn(II) and Cd(II) structures formed during metallation and oxidation.	205
Figure 7-4. Comparison between the pH dependence of the rate constants of Zn(II) and Cd(II) binding to apo-MT, and the degree of cooperativity in the Zn(II) and Cd(II) binding pathways.	207
Figure 7-5. comparison between exposed cysteines in apo-MT and cysteines involved in Bi ₂ MT binding.	209
Figure 7-6. Speciation curves for the titration of Bi(III) into apo-β _α MT and Zn ₇ β _α MT.	210

List of Appendices

Appendix A: ESI-MS Mass Values	242
Appendix B: Additional MD Simulation Data	244
Appendix C: Additional CD Spectroscopy Data	246
Appendix D: ESI-MS Validation Experiments.....	247

List of Abbreviations

ASA	Accessible Surface Area
Bq	Benzoquinone
CD	Circular Dichroism
CEM	Channel Electron Multiplier
CI	Chemical Ionization
CRM	Charged Residue Model
DFT	Density Functional Theory
DI	Deionized
DNA	Deoxyribonucleic Acid
DTNB	5,5'-dithiobis-(2-nitrobenzoic acid)
EI	Electron Ionization
ESI-MS	Electrospray Ionization Mass Spectrometry
EXAFS	Extended X-ray Absorption Fine Structure
FRET	FRET Förster Resonance Energy Transfer
GdmCl	Guanidinium Chloride
GSH	Glutathione
GTP	Guanosine triphosphate
HDX	Hydrogen-Deuterium Exchange
HPLC	High Performance Liquid Chromatography
IAM	Iodoacetamide
ICP	Inductively Coupled Plasma
IDP	Intrinsically Disordered Protein
IDR	Intrinsically Disordered Region
IEM	Ion Ejection Model
IPTG	Isopropyl β -D-1-thiogalactopyranoside
LMCT	Ligand to Metal Charge Transfer
m/z	Mass to Charge Ratio
MALDI	Matrix Assisted Laser Desorption
MCD	Magnetic Circular Dichroism
MCP	Microchannel Plate
MD	Molecular Dynamics
MM3	Molecular Mechanics
MO	Molecular Orbital
MRE	Metal Response Element
MT	Metallothionein
MTF-1	MRE-binding transcription factor-1
NEM	N-Ethylmaleimide
NMR	Nuclear Magnetic Resonance
PTM	Post Translational Modification
rhMT	Recombinant Human Metallothionein
ROS	Reactive Oxygen Species
TCEP	Tris(2-carboxyethyl)phosphine
TOF	Time of Flight
UV	Ultraviolet

Amino Acid Three and One Letters Codes

Alanine	Ala	A
Arginine	Arg	R
Asparagine	Asn	N
Aspartic acid	Asp	D
Cysteine	Cys	C
Glutamic acid	Glu	E
Glutamine	Gln	Q
Glycine	Gly	G
Histidine	His	H
Isoleucine	Ile	I
Leucine	Leu	L
Lysine	Lys	K
Methionine	Met	M
Phenylalanine	Phe	F
Proline	Pro	P
Serine	Ser	S
Threonine	Thr	T
Tryptophan	Trp	W
Tyrosine	Tyr	Y
Valine	Val	V

Chapter 1

1 Introduction

This thesis concerns the small metal-binding protein metallothionein (MT). This protein is unique when it comes to its structural properties. The apo form of MT is fluxional with no defined metal-binding sites but can bind a variety of metals in a range of stoichiometries. Mammalian MTs have 20 cysteines, which can undergo redox reactions resulting in disulfide bond formation and metal displacement. In this introductory chapter, an overview of the general structural properties of both metal-binding proteins and intrinsically disordered proteins, and the discovery, classification, structure, and function of MTs is provided.

1.1 Structural Properties of Proteins

1.1.1 Protein folding: the relationship between sequence, structure, and function

Proteins play a variety of critical roles in the function of cells, from catalysis to transport to cell-signalling, with the specificity to their targets attributed to their overall structure and binding sites.¹ The question of what drives protein folding to its final structure has been challenging scientists for many decades. In 1961, Christian B. Anfinsen published his work on ribonuclease A where he found that protein unfolding via denaturation inhibited activity and that reversing the denaturation returned the protein to full activity.² The ability to refold a protein back into the native, biologically active conformation eventually led to the proposal of the Thermodynamic Hypothesis. This states that the native state of a protein is the single lowest free energy conformation and that this 3D fold is encoded in the amino acid sequence of the protein.³

Although today it is understood that cellular components such as molecular crowding and chaperones assist in the protein folding process, it is still accepted that the amino acid sequence, or primary structure, ultimately dictates the final native conformation.¹ The amino acids in the sequence possess various properties that are important in determining

the native structure; including hydrogen bonding, the hydrophobic effect, van der Waals forces, salt bridges, and disulfide bonds. All of these properties depend on amino acid identity. Typical globular proteins fold in such a way where hydrophobic residues form the inner “core” of the protein and charged residues sit near the surface.¹ The overall packing can leave crevices in the protein which can act as active sites, shielding catalytic residues from the environment where chemistry can take place.¹ For example, the active site of the enzyme lysozyme is located in a cleft between its two domains and utilizes a glutamic acid and an aspartic acid for its activity.⁴

1.1.2 Metalloprotein binding site structure

Many elements are essential for life. These include the bulk elements H, C, N, O, P, S, Ca, Na, Mg, S, Cl and K and the trace elements Mn, Fe, Co, Cu, Zn, and Mo.⁵ The majority of the trace metals in physiology perform their roles as cofactors for metalloproteins, which make up about 25–50 % of all proteins.⁶

In metalloproteins, N, O, and S donor atoms have an affinity for metals and will typically form the binding sites.¹ The amino acids involved in metal binding are commonly cysteine, methionine, histidine, tyrosine, aspartic acid, glutamic acid, asparagine, and glutamine.¹ Based on Hard Soft Acid Base Theory, hard acids such as Ca(II) will prefer to bind to harder bases such as RO^- , and soft acids such as Cu(I) will prefer softer bases such as RS^- .⁷ Intermediate acids such as Zn(II) will prefer intermediate bases such as R_2N^- but will often bind to hard and soft bases as well.⁷

Metalloproteins can bind to transient or permanent cofactors. Examples of proteins with transient cofactors include metal transporters and chaperones that bind metals and then donate them to enzymes. For example, free Cu(I) and Cu(II) are toxic to the cell and must be bound to proteins for protection.⁸ The copper chaperone for superoxide dismutase 1 (CCS) binds copper in the cytoplasm and delivers it to Cu, Zn superoxide dismutase (SOD) which uses the redox activity of Cu(I) to protect the cell from oxidative stress.⁹⁻¹⁰ Zn-regulated GTPase metalloprotein activator (ZNG1) is a family of zinc chaperones that has been identified as donating zinc to the Zn-metalloprotease methionine aminopeptidase 1 (METAP1) through GTP hydrolysis.¹¹

In some proteins permanent cofactors must remain bound for the protein to perform their functions. In hemoglobin, the iron is linked to protoporphyrin-IX as well as to a histidine residue on the protein. Iron can then bind oxygen, creating an octahedral complex. The heme group itself fits into a pocket created by the helical structure of the hemoglobin protein.¹²

Zn(II) in particular plays an important role in protein function. It has been stated that there are approximately 3000 known Zn(II) proteins in the human proteome.¹³ There are two specific roles that Zn(II) has in protein function: catalytic and structural. Zn(II) will catalyze reactions despite its lack of redox ability. For example, the Zn(II) in carbonic anhydrase uses its Lewis acidity to stabilize the hydroxide anion created in the first step of the reaction.¹⁴⁻¹⁷ Structural Zn(II) does not participate in reactions but rather stabilizes the protein backbone fold. The DNA-binding Zn-finger proteins require a Zn(II) to link the two antiparallel beta sheets and alpha helix of the protein and is required for correct protein folding.¹⁸

1.1.3 Intrinsically disordered proteins

The view held that proteins must have a specific or rigid structure to perform a function was challenged as more proteins were discovered that do not adopt a well-defined structure under native conditions.¹⁹⁻²¹ This newly discovered group of proteins were labelled intrinsically disordered proteins (IDPs). Some proteins are entirely disordered, while others have one or more intrinsically disordered regions (IDRs).²² Approximately 60% of the human proteome consists of either IDPs or proteins with IDRs.²³ Eukaryotes have more disorder in their proteomes than prokaryotes.²⁴

The fluxionality of IDPs gives them an advantage for certain functions. IDPs are commonly hubs in intracellular protein networks, their flexibility allowing for interaction with many different proteins.²⁰ IDPs are more often targets for post-translational modifications (PTMs) than regularly ordered proteins and are commonly implicated in signalling pathways. For example the transcription factor p53 interacts with 14 different binding partners.²⁵

IDPs and IDRs utilize disorder for function in many different ways. Some IDRs act as flexible linkers, allowing for movement of other domains such as the flexible linker region in SNAP25.²⁶ An IDP can remain permanently disordered. The milk protein α_s -casein, a Ca(II) chaperone, binds proteins to prevent aggregation.²⁷ Order to disorder transitions are possible, such as with the PEVK domain in the titin protein. Titin is an entropic spring, with the helical domain unfolding during passive stretching of muscle tissue.²⁸ Other IDPs can undergo a disorder to order transition upon binding to a partner, such as the disordered phosphorylated kinase-inducible domain (pKID) of CREB when binding to the KIX domain of CPB. The pKID adopts an alpha-helical structure upon the binding event.²⁹ This is referred to as coupled binding and folding. Sometimes IDPs can form multiple different structures with multiple partners.³⁰ Following a coupled binding and folding event, complexes can remain somewhat fluxional. This is called a fuzzy complex.³¹ An example of this is methylated DNA binding protein 2 (MeCP2), where fuzzy regions mediate the conformational selection of the protein during binding.³²⁻³³ This concept expands upon the traditional concepts of induced fit or conformational control by considering intrinsic disorder and suggests that protein rigidity may better be described on a spectrum.

IDPs were once considered a strange anomaly. However, they have become accepted as an important part of the proteome where their unique structures, or lack thereof, contribute to important functions.

1.1.4 Protein disfunction: misfolding, oxidative stress, and metal toxicity

Correct folding is not only important for function but misfolding is linked to many diseases. Chaperones assist in the correction of off pathway folding by binding to exposed hydrophobic areas, preventing aggregation. When this system fails, misfolded proteins are degraded. However, the degradation systems also become less effective with age. Proteins that are left misfolded are susceptible to aggregation, which can ultimately form beta-amyloid plaques which are associated with neurodegenerative diseases.³⁴⁻³⁵ Metals such as Cu and Zn are also involved in the formation of the beta-amyloid fibrils.³⁶ Additionally, toxic metals with no known biological role may also be involved in protein misfolding and aggregation.³⁷

Misfolding can occur due to a genetic mutation, producing the wrong amino acid sequence and thus the wrong protein structure. Sometimes the misfolded protein does not aggregate but results in a protein that has lost its function. This is the case in sickle cell anemia, where a change from a glutamic acid to a valine in hemoglobin prevents the correct structure from forming. This change in charge decreases the solubility and the red blood cells take on an abnormal shape.^{12, 38} Deletions, missense mutations, and truncation that lead to the CFTR protein degradation are a cause of cystic fibrosis.³⁹ Protein misfolding can also cause cancer due to misfolding of cell differentiation regulator proteins.³⁵

Another way proteins can become damaged is through oxidative stress. Reactive oxygen species (ROS) are constantly generated in healthy cells. ROS can be produced from either normal endogenous processes such as cellular respiration or from external factors such as UV irradiation or air pollution.⁴⁰⁻⁴² Under normal circumstances, the cell has multiple antioxidant defense systems that keep ROS levels under control. These can be proteins such as the enzyme superoxide dismutase or non-protein molecules such as ascorbate.^{40, 43} However, when there is an imbalance of these systems in favour of the ROS, a state of oxidative stress will occur.⁴³⁻⁴⁵ Oxidative stress is linked to diseases such as Alzheimer's, Parkinson's, cardiovascular disease, cancer, and diabetes. It is also associated with aging, particularly due to degradation of antioxidant defense mechanisms.⁴⁶⁻⁵¹

Proteins are common targets for ROS due to their abundance in cells and their reactivity. ROS can cause backbone fragmentation and side chain oxidation, particularly on sulfur containing side chains.^{43, 45, 52-53} Proteins can also undergo carbonylation, which is a common biomarker of oxidative stress.^{44, 54} When proteins become oxidized, they can sometimes be repaired by cellular mechanisms but are otherwise usually degraded.^{45, 55}

Cysteine and methionine containing proteins often can undergo oxidation and reduction cycles, as their most common oxidative modifications, sulfoxide and disulfide bond formations, are reversible. This property provides a controlled pathway linking oxidation and reduction without permanent damage to the protein.^{52-53, 56-57} An example is the small peptide glutathione, an antioxidant that can neutralize the threat from an ROS by reducing it, forming a disulfide bond as a result.⁵⁸

Proteins can also be damaged through deactivation, misfolding, or oxidative stress caused by toxic metals.³⁷ Although many metals are essential for protein function, complications can occur if homeostasis is not maintained.⁸ Additionally, many metals have no known biological function and only cause toxic effects, such as Hg, Pb, Cd, or As.⁵⁹ These metals adopt many different oxidation states depending on chemical composition.¹ Low level exposure to these metals is commonplace but industrial activity can result in chronic effects and in some cases, acute effects. Health issues can arise in cases of toxic metal poisoning due to the softer heavy metals with a higher affinity displacing the normal metal in metalloproteins. For example, Cd(II) can replace Zn(II) in enzymes.⁶⁰ Organic mercury can cross the blood-brain barrier and bind to sulfur ligands with high affinity.⁶¹ Additionally, the presence of toxic heavy metals can cause or exacerbate oxidative stress.⁶²

1.1.5 Metallothionein: an intrinsically disordered metal binding protein

Most metalloproteins, whether utilizing a transient or permanent metal, have one or more well-defined binding sites for a specific metal. IDPs use their flexibility to their advantage, often by binding to multiple targets. These targets are often other proteins in a cellular network.

The focus of the research described in this thesis is a family of intrinsically disordered proteins that undergo coupled binding and folding with a variety of metal targets without defined binding sites: metallothioneins (MTs). Apo-MTs fit the IDP model in that they contain no secondary structural elements, have a fluxional structure, and can undergo metal-induced folding to form metal-thiolate clusters. In many organisms, fully metallating MT with Zn(II) will form distinct domains with flexible linker regions.

MTs are cysteine-rich proteins. These cysteines allow for a diverse set of functions. MTs are generally thought to be involved in the homeostasis of Zn(II) and Cu(I), sequestration of toxic heavy metals, and protection against oxidative stress.

¹Unless the specific oxidation state of the metal is relevant to the discussion, it will not be specified in the text.

1.2 Metallothioneins: Discovery and Classification

1.2.1 Discovery of metallothioneins

In 1957, Margoshes and Vallee discovered a small cadmium-binding protein with low aromatic amino acid content isolated from equine kidney cortex.⁶³ After further characterization by Kagi and Vallee, the protein was named metallothionein (MT) for its high metal (cadmium and small amounts of zinc) and cysteine content.⁶⁴ In 1966, MT was first isolated from human liver bound to cadmium, zinc, mercury, and copper.⁶⁵

The characteristics of the isolated equine MT formed the initial definition of MTs. These characteristics were a molecular weight of around 6000 – 7000 Da, high cysteine content (~30% of the sequence), a lack of aromatic amino acids or histidine, the characteristic cysteine sequence motifs of CXC and CCXCC (where X = any other amino acid), and possessing the optical features of metal-thiolates.⁶⁶

1.2.2 Metallothionein classification systems

As additional MTs were isolated from various organisms, classification systems were developed. Fowler et al. proposed the first classification system at the Second International Meeting on Metallothionein and Other Low Molecular Weight Metal-binding Proteins in 1985, which sorted MTs into 3 different classes.⁶⁷ Class I MTs were those whose cysteine sequence motifs particularly resembled that of the equine MT. This class included all mammalian MTs, as well as some fish, crab, and mould MTs.⁶⁸⁻⁶⁹ Class II MTs included all other MTs whose sequences did not resemble that of the equine MTs, including that of yeast⁷⁰ and sea urchin.⁷¹ Class III MTs were non-ribosomally synthesized MT-like γ -glutamylcysteine (GGC) peptides found in plants, including phytochelatins and cadystins.⁷²

This classification eventually proved inadequate after the discovery of additional MTs, with a system being proposed by Binz and Kagi in 1999.⁷³ MTs were divided into 15 families based on sequence characteristics, taxonomic range, and phylogenetic relationships. These families, in numerical order are vertebrate, mollusc, crustacean, echinodermata, diptera, nematoda, ciliate, fungi-I, fungi-II, fungi-III, fungi-IV, fungi -V,

fungi-VI, prokaryota, and planta. Phytochelatins and non-proteinaceous MTs were classed as Family 99. Additionally, in 2002 Cobbett further divided Family 15 (planta) into 4 classes building off of Robinson in 1993.⁷⁴⁻⁷⁵ More recently in 2011, Capdevila proposed a new way to classify MTs based on whether they preferentially bind either Zn(II) or Cu(I).⁷⁶

1.2.3 Isoforms of mammalian metallothioneins

MTs are now considered to be ubiquitous across life, having been discovered in many different organisms. The research in this thesis focuses on mammalian MTs, which have their own unique properties. Mammalian MTs have 20 conserved cysteine residues. There are four subfamilies of MTs in mammals: MT1, MT2, MT3, and MT4. These originated from a common ancestor via gene duplication events before mammals radiated into separate species.⁷⁷ MT1 and MT2 were initially named based on the order they eluted off an ion exchange column during isolation and purification.⁷⁸ However, they are now differentiated due to differences in their genes, specifically the introns and 5'UTR regions.⁷³ Human MT1 can be further separated into sub-isoforms as the gene was amplified to 13 paralogs in humans with eight genes that code for MTs and five pseudogenes. Human MTs are coded at chromosome 6q13.⁷⁹

Table 1-1 shows the sequences of the human MT isoforms that are expressed with the cysteines highlighted in yellow.⁸⁰⁻⁸¹ The only phenotypic difference between MT1 and MT2 is a single negative charge in the N-terminal domain.⁷⁸ MT2 contains an aspartic acid while most MT1 sub isoforms have either a glycine or a valine residue. MT3, first isolated

Table 1-1. Sequences of human MT isoforms. Sequences of expressed human MT isoforms with the cysteine residues highlighted in yellow.

Isoform	Sequence
MT1A	MDPNCSCAT - GGSCCTCTGSCCKCKECKCTSCCKKSCCSCCPMSCAKCAQGCICKGAS - - - - - EKCSCCA
MT1B	MDPNCSCATT - GGSCACAGSCKCKECKCTSCCKKSCCSCCPVGC AKCAQGC VCKGSS - - - - - EKCRCCA
MT1E	MDPNCSCA - TGGSCCTCAGSCKCKECKCTSCCKKSCCSCCPVGC AKCAQGC VCKGAS - - - - - EKCSCCA
MT1F	MDPNCSCA - AGVSCTCAGSCKCKECKCTSCCKKSCCSCCPVGC SKCAQGC VCKGAS - - - - - EKCSCCD
MT1G	MDPNCSCAAAGVSCTCASSCKCKECKCTSCCKKSCCSCCPVGC AKCAQGC ICKGAS - - - - - EKCSCCA
MT1H	MDPNCSCA - GGSCACAGSCKCKKCKCTSCCKKSCCSCCPVGC AKCAQGC ICKGAS - - - - - EKCSCCA
MT1M	MDPNCSCATT - GVSCACTGSCCTCKECKCTSCCKKSCCSCCPVGC AKCAHGCVCKGTL - - - - - ENCSCCA
MT1X	MDPNCSCSPV - GSCACAGSCKCKECKCTSCCKKSCCSCCPVGC AKCAQGC ICKGTS - - - - - DKCSCCA
MT2	MDPNCSCA - AGDSCTCAGSCKCKECKCTSCCKKSCCSCCPVGC AKCAQGC ICKGAS - - - - - DKCSCCA
MT3	MDPETCPSPSGGSCTCADSCKCEGCKCTSCCKKSCCSCCPAEEKCAKDCVCKGGEEAEAEAEKSCCQ
MT4	MDPRECVCMSSGICMCGDNCKTTNCKTCRKS CCPCCPPGCAKARGCICKGGS - - - - - DKCSCCP

in the brain and named growth inhibitory factor (GIF) while searching for a cause of neurofibrillary tangles, contains a CPCP motif in the β -domain and an acidic loop rich in aspartic acid in the α -domain that are not present in any other isoform.⁸² MT1 and MT2 are expressed ubiquitously in tissues, but are more concentrated in the liver and kidneys.⁸³ MT3 is expressed in the brain and central nervous system.⁸⁴ MT4 is expressed in epithelial tissues.⁸⁵ MTs are involved in essential metal homeostasis, heavy metal detoxification, and protection against oxidative stress. The next sections will discuss these functions in detail.

1.3 Biological Functions of Metallothioneins

Mammalian MTs have 20 cysteines that can both bind metals and undergo reversible redox reactions to form disulfide bonds. Therefore, it is important to explore MT's functions in the context of metal binding and redox activity and how these features interplay with each other.

1.3.1 Metal content of metallothioneins

Metallothionein was discovered while Vallee was looking for a potential biological role for Cd(II): specifically, a Cd(II) protein much like the known Zn(II) proteins. He searched equine kidneys due to the organ's high Cd(II) content and discovered Cd(II)-bound MT.^{63, 66}

MT extracted from human renal tissues was bound mainly to Cd(II) and Zn(II) with some Cu(I) content,^{65, 81} while MT extracted from human liver was primarily Zn(II)-bound.⁸⁶ Cu(I)-bound MTs are more common in mammalian fetuses,⁸⁷⁻⁸⁸ in yeast and other fungal MTs,⁸⁹ and in the mammalian brain MT3.⁸² These findings suggest a possible role in metal storage, homeostasis, or protection.

1.3.2 Upregulation of metallothioneins: sources and pathway

MT is always expressed at a basal level. However, many agents can upregulate MTs including metals, oxidative stress, glucocorticoids, and cytokines. MT1 and MT2 are inducible by metals, while MT3 and MT4 are not.^{83, 90} As the research described in this thesis primarily focuses on MT1, only the proposed functions of MT1 and MT2 are described in this section.

MT1 and MT2 induction in mammals can be caused by a variety of metals, including Zn, Cd, Cu, Hg, Bi, Cr, Fe, Pb, Mn, Ni, As, Ag, and Au.⁹¹⁻⁹⁹ However, Zn and Cd are the most effective at MT induction and expression. Expression is ubiquitous for MT1 and MT2, however it is most concentrated in the liver and kidneys.⁸³

Many studies have also explored MT induction by oxidative stress. The source of this can include heavy metal exposure,¹⁰⁰⁻¹⁰³ stressors such as cold, food restriction, exercise, or radiation, chemicals such as acetaminophen or glyphosate,¹⁰⁴⁻¹⁰⁵ superoxide generators like paraquat,^{104, 106-107} and free radical generators such as H₂O₂.¹⁰⁸

The pathway through which MT is primarily upregulated specifically involves Zn(II). If the cellular environment has a high enough level of free Zn(II), this Zn(II) binds to the MRE-binding transcription factor-1 (MTF-1), a Zn-finger protein. The Zn(II)-bound MTF-1 then binds to metal response elements (MREs) in the promoter region of MT genes, inducing their transcription.¹⁰⁹ This allows the cell to maintain homeostasis by way of inducing MT to bind the excess Zn(II).

This induction pathway, while it requires Zn(II), can indirectly be stimulated by other metals and ROS. When a heavy metal enters the system, it can bind MT, displacing the Zn(II), which then binds to MTF-1.¹⁰⁸ A similar pathway occurs with ROS. These oxidize MT's cysteine thiols to disulfide bonds, causing release of the bound Zn(II). It has been shown that H₂O₂, Zn, Cd, and Cu can induce MT production when Zn-saturated MT is present by way of the MTF-1 pathway in a cell-free system.¹⁰⁸ Additionally, ROS can induce MTs directly, independent of Zn(II) through the antioxidant response element (ARE). The implications are that ROS can induce MT via either pathway: they can displace metals and upregulate MT through MREs or directly through AREs.⁸³ Other pathways through different response elements exist as well, however, discussions of these REs are beyond the scope of this thesis.¹¹⁰

1.3.3 Protective effects of metallothioneins

MTs were found to have a protective effect against heavy metals. Many studies using MT knockout mice have shown greater sensitivity to metals such as Cd, Zn, Cu, and As.¹¹¹⁻¹¹⁴

However, although MT mitigates Cd toxicity, it does not cause excretion of Cd. Rather, it accumulates in the kidneys.¹¹³ MT has also been associated with formation of Pb inclusion bodies, which protect against Pb toxicity. MT-null mice do not form these inclusion bodies, and thus suffer greater effects of Pb poisoning.¹¹⁵

MT has also been shown to protect against oxidative stress. MT has a redox potential of about -366 mV, which is lower than GSH¹¹⁶ and reacts with free radicals faster than GSH.¹¹⁷ In V79 Chinese hamster fibroblasts, MT was shown to prevent oxidative damage by H₂O₂ to DNA strands.¹¹⁸ MT also was able to protect NIH 3T3 cells from nitric oxide induced DNA strand breaks.¹¹⁹ Zn, Cu, Bi, Co, Cd, and Hg induction of MT prior to administration of paraquat to mice decreased mortality, with Zn being the most effective.¹²⁰ In another study, MT was induced in HL-60 cells using Zn. It was confirmed that no GSH was induced. A higher lethal dose of H₂O₂ was required after MT induction compared to a control, suggesting MT had a protective effect.¹²¹

It is important to note that these studies do not consider the effect of possible Zn deficiency on the protective effect of MT. Since Zn is required for upregulation, particularly in the case for heavy metals, its absence may decrease MT's protection in the wild type mice.

1.3.4 Metallothioneins' role in Zn(II) homeostasis

Zn(II) plays an important role in the functions of MT. It is similar to a transient metal cofactor as it is required to upregulate MT in cases of stress. The total concentration of Zn(II) in mammalian cells is between 100 and 500 μ M,¹²²⁻¹²⁴ while free Zn(II) is estimated to be in the nanomolar to picomolar range, meaning that the majority of cellular Zn(II) is bound to the Zn-proteome.^{122, 124-126} A cellular concentration of 13 μ M has been reported for MT.¹²⁷⁻¹²⁸

Metallothionein has been proposed to be involved in Zn(II) homeostasis. When a Zn(II)-enriched diet was fed to rats, Zn-MT accumulated in the liver and kidneys. Conversely, when the rats were starved of Zn(II), the Zn(II) was released from the MT and excreted from the rats, suggesting that MT will release Zn(II) in times of Zn(II)-deficiency.¹²⁹

MT-null mice given either deficient or excess Zn(II) showed higher sensitivity to the effects of Zn(II) deficiency or toxicity than controls with normal MT expression levels.¹¹¹ Additionally, MT-null mice were shown to have development problems even under conditions of only mild Zn(II) deficiency.¹³⁰⁻¹³¹ However, another study concluded that MT-null mice are viable and born phenotypically normal, although more susceptible to Cd(II) toxicity.¹³² As discussed by Petering, the lab mice in this study were under optimal conditions and obtaining an adequate amount of Zn(II) which may have mitigated the possible impact of a Zn(II) deficiency.¹²⁴ This suggests that MT plays the most important role under sub-optimal nutritional conditions.

Zn(II) is normally transported into the cytoplasm by ZRT-IRT-like proteins (ZIP) and out of the cytoplasm by Zn(II) transporters (ZnT).¹²⁴ There is evidence that MT may bind some of this cellular Zn(II) and can distribute it to other proteins. For example, Zn(II)-bound MT has been shown to donate Zn(II) to the DNA binding domain of Gal4,¹³³ carbonic anhydrase,¹³⁴⁻¹³⁵ alkaline phosphatase, and carboxypeptidase A¹³⁶ *in vitro*. Apo-MT can inactivate the zinc finger containing factor Spl,¹³⁷ as well as alkaline phosphatase when in the presence of Zn(II) chelators.¹³⁶ An *in vivo* experiment showed that Zn(II)-bound MT delivers Zn(II) to mitochondrial aconitase in mouse hearts.¹³⁸ It has also been shown that Zn₇MT can transport Zn(II) into liver and prostate mitochondria.¹³⁹ These experiments show that MT may participate in Zn(II) trafficking.

Based on the available research, MTs appear to play roles in metal homeostasis, heavy metal detoxification, and protection against oxidative stress. To this point, however, there has been no discussion of possible structure-function relationships for MTs. Based on the proposed functions, it is clear that the structure of MT is dynamic and is controlled by the binding and releasing of metals and the oxidation and reduction of the cysteines. In the next section, the structural characterization of MT is described.

1.4 Metallothionein Structural Characterization

1.4.1 Early characterization of metal-thiolate bonds and the two-domain structure

During the early years of MT research, MT's lack of aromatic amino acids or secondary structural elements meant that the metal content and metal-thiolate bonds were the most prominent feature that could be easily studied. Common techniques used were atomic absorption spectrometry (AAS) for analyzing the metal content, UV-visible absorption and circular dichroism (CD) spectra to characterize metal-thiolate structures, and X-ray absorption spectroscopy (XAS) for elucidation of the coordination and local structure of the metal-thiolate bonds.¹⁴⁰ Metallated MTs will have a ligand to metal charge transfer (LMCT) bands in the UV or near UV region depending on the metal identity. The CD spectrum of fully metallated Cd(II) and Zn(II) bound MTs contains a characteristic derivative shape. This is sometimes referred to as the "Cotton Effect" and is due to splitting of excited states.¹⁴¹

To date, only two X-ray crystal structures of MT have ever been reported. The first was for Cd₅Zn₂MT₂ from rat liver in 1986, which has the 20 cysteines typical of mammalian MTs.¹⁴²⁻¹⁴³ This structure was further refined in 1991.¹⁴³⁻¹⁴⁴ The connectivity of the metal-thiolate clusters was determined through ¹H and ¹¹³Cd nuclear magnetic resonance (NMR) spectroscopy studies from rabbit liver Cd₇MT₂,¹⁴⁵ human liver Cd₇MT₂,¹⁴⁶ and recombinant mouse Cd₇MT₁.¹⁴⁷ This connectivity is shown in Fig. 1-1 using the human MT1a sequence, the isoform which is the focus of this thesis. It has been confirmed using NMR spectroscopy that recombinant human MT1a exhibits the same metal thiolate clusters as the other isoforms studied.¹⁴⁸ Cd₇MT and Zn₇MT, have two metal thiolate clusters in distinct domains connected by a short linker region. The clusters have a mix of bridging and terminal thiolates. The N-terminal domain, which contains an M₃S₉ structure (where M = divalent metal and S = cysteinyl sulfur), is called the β-domain. The C-terminal domain, which contains an M₄S₁₁ structure, is called the α-domain. The metals are bound with a tetrahedral coordination geometry.

The second crystal structure was reported in 2005 for a yeast Cu₈MT, which has a dissimilar structure to mammalian MTs. A single cluster of six trigonally and two diagonally coordinated Cu(I) to 10 cysteines was reported.¹⁴⁹ MTs are notoriously difficult to crystallize due to their fluxional nature compared to more traditionally ordered proteins. Even fully metallated MTs are difficult to crystallize as evidenced by the existence of only two structures. This means that less well-defined apo and partially metallated MTs are next to impossible to crystallize. In fact, these other structures were so difficult to study, it was initially thought that only the fully metallated forms were relevant *in vivo*.^{144, 150-152}

1.4.2 The elusive structure of apo-metallothionein

It was previously not known whether any forms other than the fully metallated MT existed. Due to its rapid degradation by proteases compared to the fully metallated Zn₇MT counterpart,¹⁵⁰ it was assumed that apo-MTs did not exist *in vivo*.¹⁵¹ Therefore, there was little interest in the study of apo-MTs. However, metal unsaturated MTs were eventually discovered *in vivo* using fluorescent sensors¹⁵³ and Cd(II) saturation methods¹⁵⁴⁻¹⁵⁵ which challenged this view and piqued the interest of researchers to consider other forms of MT.¹⁵³

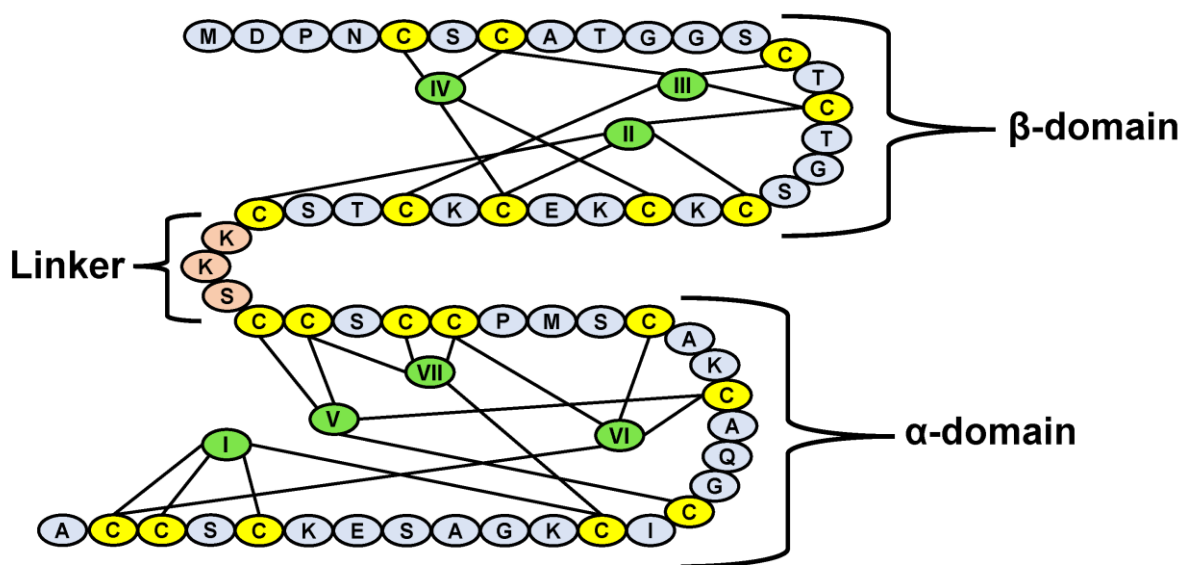


Figure 1-1. Sequence of human MT1a. The sequence of human MT1a showing the two-domain connectivity of the metals based on data from Messerle et al., 1990. The Cd(II) are shown in green and the cysteines are shown in yellow. The linker region is shown in peach.

The structure of apo-MT is very difficult to study by traditional methods. Apo-MTs lack significant secondary structural elements. This means minimal information is obtained from CD spectra, which reveal a largely disordered structure.¹⁵⁶ Their fluxionality and heterogeneity also means that NMR spectra show blurry, averaged signals.¹⁵⁷ The conclusion from these data is that apo-MT is intrinsically disordered. However, some researchers have attempted to further characterize the apo-MT structure.

Studies using ESI-MS charge state analysis¹⁵⁸ and a fluorescence resonance energy transfer (FRET) sensor¹⁵⁹ have shown that the difference in size between apo-MT and fully metallated MT is minimal, implying that the apo-MT is already in a compact conformation. Stopped flow kinetic studies have revealed that Cd(II) binds to apo-MT under native conditions more rapidly than apo-MT under denaturing conditions, which implies that structure of apo-MT is arranged in such a way to favourably bind metals.¹⁶⁰⁻¹⁶¹ IM-MS studies showed that apo-MT exists in an ensemble of both compact and extended structures under native conditions, which shifts to include only the compact conformations upon full metallation to Cd₇MT.¹⁶²⁻¹⁶³

Molecular dynamics (MD) simulations of MTs have shown that MT retains its backbone fold after sequential demetallation.¹⁶⁴ This contrasts with the results obtained from MD simulations of MTs beginning from a linear sequence, which revealed a collapsed but random coil. In both simulations, the cysteine residues were shown to be solvent-exposed in apo-MT.¹⁶⁴ Conversely, cysteine modification experiments monitored using ESI-MS have shown that apo-MT under physiological conditions has some cysteines buried in the interior of the protein. This experiment was also performed on apo-MT under denaturing conditions, where it was found that all the cysteines are equally solvent-exposed, suggesting an unfolded protein.¹⁶⁵

1.4.3 Beyond two-domains: partially metallated Zn(II) and Cd(II) metallothionein structures and binding pathways

Previously, it was thought that the two-domain Zn₇MT and Cd₇MT always formed cooperatively.^{144, 152} This thought persisted even after acknowledgement of metal-

unsaturated MTs.¹⁵³ Due to the limitation of many spectroscopic techniques only showing an average of species in solution, it was difficult to determine the metal binding pathway.

The use of ESI-MS techniques proved an ideal solution to this problem as the spectra show individual species while maintaining gentle conditions that often reflect the solution phase. When this technique was employed for metal binding titrations, it was found that the formation of Zn₇MT and Cd₇MT were non-cooperative.¹⁶⁶⁻¹⁶⁸ There were, however, conflicting reports on the exact metal-binding pathway, particularly on the first four metals. Results reported an initial cooperative formation of Zn₄MT or Cd₄MT,¹⁶⁹ a semi cooperative formation of Cd₄MT¹⁷⁰, or a non-cooperative formation where significant amounts of Zn₁₋₃MT¹⁶⁸ and Cd₁₋₃MT¹⁶⁶⁻¹⁶⁷ species exist in a distribution.

The pathway of metallation was also found to be highly dependent on pH environment, which provides a likely explanation for the varying results in these studies. Metal-binding releases the thiol proton, which reduces the pH level, particularly in ESI-MS compatible solvents which typically do not buffer at neutral pH. At pH > 7, Cd(II) will bind primarily non-cooperatively, reaching full non-cooperativity by pH 8.¹⁷¹ At pH < 7, a cooperative pathway where apo-MT forms Cd₄MT and then Cd₇MT will dominate.¹⁷¹ With Zn(II), at pH > 5, the non-cooperative pathway dominates. Below pH 5 some cooperativity to Zn₄MT is observed, however it is never fully cooperative before the point where metals become displaced due to protons competing for the thiols. Species between Zn₁₋₃MT are still observed.¹⁷¹ In the same study, these structures were also confirmed by CD spectroscopy by presence or absence of the derivative signal characteristic of the cluster structures.¹⁷¹ An additional Cd₈MT species has also been characterized by ESI-MS and CD spectroscopy.¹⁴⁸

Mass spectrometry also allows determination of individual relative binding constants by titrating in the metal against a competitor with a known binding constant such as carbonic anhydrase. Using this method, both the binding constants for the formation of Zn₁₋₇MT and Cd₁₋₈MT have been determined.^{135, 172} Other methods used, such as fluorescence spectroscopy and isothermal titration calorimetry (ITC) cannot distinguish all of the individual species.¹⁷³⁻¹⁷⁴

The specific binding sites of partially metallated Zn(II) and Cd(II) at physiological pH have also been investigated using a combination of cysteine modifiers and tandem mass spectrometry. In one study, the initial four Cd(II) were found to preferentially bind in the α -domain.¹⁷⁵ Another study found that the partially metallated Zn(II) and Cd(II) bound MT structures were different from each other. Cd₄MT had Cd(II) localized primarily in the α -domain, while Zn(II) was found in both domains of Zn₄MT.¹⁷⁶

1.4.4 Non-traditional metallothionein structures

It is generally agreed upon that Zn(II) is the most biologically relevant metal that MT binds in mammals. Due to Zn(II) being generally spectroscopically silent, Cd(II) is often used in place of Zn(II) for structural studies as it binds in a very similar manner. Based on the available X-ray crystallography data, it can also be inferred that mixed Cd(II) and Zn(II) bound MTs retain the two-domain structure. Therefore, the majority of MT metallation studies focus on Zn(II) and Cd(II). However, MT also binds a variety of metals including the group 11 and 12 elements and various transition metals with unique stoichiometries. Table 1-2 summarizes the currently known key stoichiometries and coordination geometries of metals binding to apo-MT along with the major technique(s) that contributed to the knowledge. For simplicity, only the maximum stoichiometry or well-defined key structures are included. The binding affinities for various metals have been reported as being in the order (Hg > Cu > Ag > Cd > Pb > Zn > Co > Ni > Fe) at physiological pH.¹¹⁰

The metals can bind through many different pathways, some which differ depending on pH conditions. These pathways can be entirely non-cooperative where no specific species are favoured, or no cluster structure is observed. This is the case with As(III) and Bi(III), which bind to apo-MT with a maximum stoichiometry of As₆MT or Bi₆MT, respectively¹⁷⁷⁻¹⁷⁸ under low pH conditions.

Some metals display cooperative and domain specific cluster formation regardless of pH environment. An example is Cu(I) which has recently been extensively studied using ESI-MS techniques. Studies using the full $\beta\alpha$ MT and the fragment β -domain and α -domain reveal that Cu₄MT and Cu₆MT clusters form initially in the β -domain, followed by a Cu₄MT cluster in the α -domain (Cu₁₀ $\beta\alpha$ MT). Additional Cu(I) can bind to the α -domain to

form a Cu₇MT cluster in the α -domain and Cu₁₃MT in the full protein.¹⁷⁹ This is followed by non-cooperative addition of Cu(I) up to Cu₂₀MT.¹⁷⁹⁻¹⁸⁰

Ag(I) also binds through a cooperative pathway that differs from that of Cu(I). Studies using CD spectroscopy have shown that cluster formation occurs at stoichiometries of Ag₆MT with three Ag(I) in each domain, then Ag₁₂MT, and Ag₁₈MT. Studies on the individual domains showed that Ag₃ β MT, Ag₃ α MT, and Ag₆ α MT could form.¹⁸¹ More recently, Ag₄MT and then Ag₆MT were shown by ESI-MS to form cooperatively in the β -domain. After formation of these species, up to Ag₁₇MT forms non-cooperatively.¹⁸²

Metal binding can also vary based on anions present. Hg(II) appears to bind Hg₇MT in a two-domain cluster similar to Cd₇MT or Zn₇MT based on sulfur L-edge XANES.¹⁸³⁻¹⁸⁴ However, Hg₁₈MT has also been reported, a structure which produces a distinct CD spectrum and is highly dependent on pH and Cl⁻ availability.¹⁸⁵ Hg₁₈MT is quite different from Hg₇MT in terms of the sulfur coordination.¹⁸⁴ XAFS shows that Hg₇MT is coordinated by four sulfurs with two long and two short bonds. Hg₁₈MT is more disordered with each Hg(II) having two bonds to sulfur and occasionally one to a Cl⁻ anion.¹⁸⁶

Metal centers of metallodrugs also bind to MTs, resulting in ligand dissociation. This may provide insight into MTs role in drug resistance. When MT interacts with the anticancer drug cisplatin, the removal of the Pt(II) takes place in a stepwise manner with the dissociation of the ligands being monitored using ESI-MS.¹⁸⁷ The Pt(II) in cisplatin can also cause Zn(II) displacement from MT in a non-cooperative, biphasic manner.¹⁸⁸⁻¹⁸⁹ Cisplatin has also been shown to prefer reaction with Zn₇MT over zinc finger proteins, which leads to Zn(II) displacement and thus the potential upregulation of MT by MTF-1.¹⁹⁰ A similar pathway occurs for dirhodium tetraacetate, a potential anticancer agent, where the ligands dissociate from the complex after MT binding to the metal center.¹⁹¹⁻¹⁹² This is also the case with the drug [Ru(η^6 -*p*-cymene)Cl₂(pta)] (RAPTA-C).¹⁹³ The destructive interactions of MT with metallodrugs highlights the importance of understanding the binding of xenobiotic metals to MT.

Table 1-2. Various metal binding stoichiometries for mammalian MTs. The stoichiometries and coordination geometries of various metals binding to mammalian MTs at neutral pH (unless otherwise noted) indicating the instrumental techniques used. Adapted from Scheller et al, 2018.¹⁹⁴

Metal	Stoichiometry	Coordination	Technique
Zn(II)	Zn ₇ βMT (Zn ₃ βMT + Zn ₄ αMT)	Tetrahedral	X-ray crystallography ¹⁴²⁻¹⁴³
Cd(II)	Cd ₇ βMT (Cd ₃ βMT + Cd ₄ αMT)	Tetrahedral	X-ray crystallography ¹⁴²⁻¹⁴³ NMR spectroscopy ¹⁴⁵⁻¹⁴⁷ ESI-MS ¹⁴⁸ CD spectroscopy ¹⁴⁸
	Cd ₈ βMT		
Hg(II)	Hg ₇ MT Hg ₁₈ MT (low pH)	Tetrahedral	Absorption spectroscopy ¹⁹⁵ XANES ¹⁸⁴ CD spectroscopy ^{185, 196} XAFS ¹⁸⁶
Cu(I)	Cu ₁₀ βMT (Cu ₆ βMT + Cu ₄ αMT) Cu ₁₃ βMT (Cu ₆ βMT + Cu ₇ αMT) Cu ₂₀ βMT		ESI-MS ¹⁷⁹ Emission spectroscopy ¹⁷⁹ ESI-MS ¹⁸⁰
Ag(I)	Ag ₆ βMT (Ag ₃ βMT + Ag ₃ αMT) Ag ₁₂ βMT Ag ₁₈ βMT Ag ₄ βMT Ag ₆ βMT Ag ₁₇ βMT	Linear	CD spectroscopy ¹⁸¹ EXAFS ¹⁹⁷⁻¹⁹⁸ ESI-MS ¹⁸²
Au(I)	Unknown	Mixed monodentate and bidentate	Absorption spectroscopy ¹⁹⁹⁻²⁰¹ EXAFS/XANES ¹⁹⁹ Emission spectroscopy ²⁰⁰
Bi(III)	Bi ₇ βMT Bi ₃ βMT (low pH) Bi ₄ αMT (low pH)	Mixed trigonal pyramidal and tetrahedral	ESI-MS ¹⁷⁸ NMR/EXAFS ²⁰²
As(III)	As ₆ βMT (low pH) As ₃ βMT As ₃ αMT	Trigonal pyramidal	ESI-MS ¹⁷⁷
Pt(II)	Pt ₇ MT Pt ₁₇ MT (low pH)	Square planar	AAS ²⁰³ Absorption spectroscopy ²⁰³
Ni(II)	Ni ₇ MT	Tetrahedral	MCD ²⁰⁴
Rh(II)	Rh ₂ βMT Rh ₆ βMT		ESI-MS ¹⁹¹ ESI-MS ¹⁹²
Co(II)	Co ₇ MT	Tetrahedral	MCD ²⁰⁴ ¹ H NMR spectroscopy ²⁰⁵
Pb(II)	Pb ₇ MT Pb ₉ MT	Tetrahedral	Absorption spectroscopy ¹⁸³ ESI-MS ²⁰⁶
Fe(II)	Fe ₇ MT	Tetrahedral	Absorption spectroscopy and MCD ²⁰⁷
Tc(V)	Tc ₇ MT	Square pyramidal	Absorption spectroscopy ²⁰⁸ Raman spectroscopy ²⁰⁸ Radiolabeling ²⁰⁸

1.4.5 The effect of metallothionein structure on oxidation

Although many MT studies focus on metal binding pathways, studying demetallation is equally important to understanding MTs functions. This is because, as discussed previously, the Zn(II) displacement from MTs by various agents is a major pathway for the upregulation of MTs. Likewise, as MTs act as a “sponge” for a variety of metals, the release of xenobiotic metals is also important to study.

The two domain cluster structures of Zn₇MT and Cd₇MT have an impact on the pathway of metal release. Most notably, each domain has a different reactivity towards agents inducing metal displacement. Reaction of Zn₇MT and Cd₇MT with 5,5'-dithiobis-(2-nitrobenzoic acid) (DTNB), which forms an intermolecular disulfide bond with individual cysteines, revealed biphasic kinetics.²⁰⁹ The same reaction using only the α -domain showed that Cd₄ α MT was displaced according to monophasic kinetics.²¹⁰ This difference was evidence that the biphasic kinetics were caused by different reactivity of the clusters. Reaction of Cd₇MT with the cysteine modifier NEM monitored by ESI-MS also shows the metals from the Cd₃ β MT are displaced first.¹⁷⁵ This also is the case when using other metals to displace Zn(II) or Cd(II), such as Bi(III).²⁰²

The interactions of reactive oxygen species (ROS) and reactive nitrogen species (RNS) with MTs are also important to study due to their biological roles and participation in the state of oxidative stress. Exposure of MTs to oxidative stress has been shown to both cause disulfide bond formation²¹¹⁻²¹⁴ and metal displacement.^{116-117, 128, 136, 211, 215-224}

The reactivity of the two domains have been studied using oxidizing agents. ¹¹³Cd NMR spectroscopy confirmed that, upon oxidation by nitric oxide (NO), the three metals from the β -domain are more labile and thus released first.²²⁴ On the contrary, a tandem MS study showed disulfide formation on both the β -domain and α -domain in mouse heart MT upon exposure to ROS *in vivo*.²²⁵ It should be noted however, that no investigations of the metallated structures were conducted. It is possible that the formation of disulfide bonds does not necessarily result in immediate metal release due to the stable network of metal-thiolate clusters, particularly in the α -domain.

Matrix-assisted laser desorption/ionization (MALDI) MS-MS has been used to investigate the disulfide bond structures formed in the γ -domain of the wheat Ec-1 MT upon oxidation with H_2O_2 .²²³ This protein domain is unlike mammalian MTs in that it only binds two Zn(II). Nevertheless, it can serve as a model for MTs in general. This study found that the disulfides formed were specific and were the same regardless of whether the protein was in the apo or fully metallated form, suggesting that a similar overall backbone fold of the MT in both states played a role.

The effect of whether a metal-bound thiolate was bridging or terminal on MT's resistance to oxidation was also studied using computational methods.²²⁶ When simulating the release of Zn(II) from the β -domain of MT, it was found that the terminally bound cysteines were more susceptible to oxidation than bridging cysteines within the cluster.²²⁶ This suggests that there may be a difference in susceptibility to oxidation between the fully metallated two-domain structure and a partially metallated structure that has not yet formed the complete network of bridging cysteines.

1.5 Scope of the Thesis

MTs can adopt many different structures that depend on factors such as pH conditions, metal-loading status, and redox conditions. These structures formed can involve free reduced or oxidized cysteines and mixed metal species. The more fluxional and heterogenous, the more difficult the structures are to analyze using traditional methods.

In this thesis, research using ESI-MS in combination with MD simulations, stopped-flow, CD spectroscopy, and absorption spectroscopy to characterize various dynamic MT structures is described. In Chapter 2, an overview of these techniques and their applications to MTs is provided.

The structural characterization of the apo-MT using MD simulations, ESI-MS, and CD spectroscopy is described in Chapter 3. The response of apo-MT to various denaturing conditions was studied which was found to be different than expected for a random coil. Rather, apo-MT adopts a bundled conformation under physiological conditions which can be cooperatively denatured.

In Chapter 4, the study of the partially metallated Zn(II) and Cd(II) species is described. Using stopped flow methods, CD spectroscopy, and ESI-MS, the dependence of the Zn(II) and Cd(II) metallation pathways on the pH and the apo-MT structure was investigated. Cysteine modification monitored by ESI-MS under native and denaturing conditions revealed the individual M_xS_y species formed in the early steps of the reaction, revealing that these early metal-thiolate species depend on the apo-MT structure.

The focus of Chapter 5 is on the stepwise binding of Bi(III) to apo- β MT, apo- β MT, apo- α MT, and Zn₇ β MT to study the formation of non-traditional structures in MTs. The results were found to differ depending on pH or Bi(III) salt used. Using EDTA as a competitor, the relative stepwise binding constants of Bi(III) binding to apo- β MT, apo- β MT, and apo- α MT at pH 7.4 were determined. The stoichiometries and domain specificities were studied using cysteine modifier and trypsin digestion experiments. A difference in species was observed whether the Bi(III) was titrated into apo- β MT or Zn₇ β MT, suggesting that the initial metal-loading status of the MT impacts the metal binding pathways.

The ROS-induced disulfide bond formation and metal displacement has not yet been studied in mammalian MTs using ESI-MS techniques. The impact of metal-loading status and metal-thiolate structures as a mechanism for protection have also not been considered. Chapter 6 details the oxidation of fully and partially metallated Cd(II) and Zn(II) bound MTs with H₂O₂. Kinetic studies monitored by ESI-MS revealed each of the $M_x(SH)_y$ MT species formed during the reaction and allowed for determination of the individual rate constants. The partially oxidized structures were characterized using CD spectroscopy. The partially metallated Cd(II) MTs were found to be more resilient against ROS than the partially metallated Zn(II) MTs.

Together, these studies show the different fluxional MT structures that can be observed using ESI-MS in combination with solution techniques. The results provide a more detailed picture of the dynamic structures of MT with some insight into the possible structure-function relationships for MTs.

Chapter 2

2 Materials and Methods

This section describes the instrumental theory and methods used in the work presented throughout this thesis in greater detail than what a typical journal article would contain. Absorption spectroscopy, circular dichroism spectroscopy, electrospray ionization mass spectrometry, stopped flow, and molecular modelling techniques were employed to characterize MT and are described in this Chapter. Combined, these techniques provide information on the dynamic folding, metallation, and redox state of this protein.

2.1 Instrumental Methods: Theory and Applications

This section outlines the theory behind the instrumental methods used and describes their applications to the research presented in this thesis. Some general procedures, example spectra, and instrument parameters are provided in this section. More specific procedures are described in the relevant chapters. All of the instruments and laboratory equipment used are listed in Table 2-1.

2.1.1 UV-visible absorption spectroscopy

Absorption spectroscopy relies on the phenomenon of electron excitation upon the absorption of light. An electron in a compound is promoted to the excited state when it absorbs light at a particular wavelength, which can be measured using absorption spectroscopy. During an absorption experiment, the spectrometer shines light on the sample at the desired wavelength(s) and measures the difference in the incident radiation (I_0) and the transmitted radiation (I). From this, Transmittance (T) and Absorbance (A) can be calculated using Equations 2-1 and 2-2, respectively.

$$T = \frac{I}{I_0} \quad (2-1)$$

$$A = -\log T \quad (2-2)$$

Table 2-1. Instruments and laboratory equipment used in this thesis. The supplier, country of origin if not Canada, model name, and the type of instrument are shown.

Supplier	Name and Instrument/Equipment Type
Agilent	Cary 60 UV-visible absorption spectrometer
Beckman-Coulter (USA)	Avanti J-26 XPI fixed rotor Centrifuge Rotors: JLA 8.1000 JA 25.50
Beckman-Coulter (USA)	Allegra X-30R Centrifuge
BioLogic (France)	MOS-250 UV-visible absorption spectrometer
BioLogic (France)	SFM 400 Stopped Flow
Blue M (USA)	Dry Type Bacteriological Incubator, Gravity Convection
Bruker	MicroTOF II Mass spectrometer (ESI Source and TOF Analyser)
Büchi (Switzerland)	F-105 Recirculating Chiller
Constant Systems (UK)	E1061 Cell disruptor
Eppendorf (Germany)	Centrifuge 5418 Microcentrifuge Rotor: FA-45-18-11
GE Healthcare (USA)	HiTrap SPHP Cation exchange column
GE Healthcare (USA)	HiTrap QHP Anion exchange column
Hach (USA)	H160 Portable pH Meter
Jasco (USA)	J-810 Spectropolarimeter
Millipore-Sigma (USA)	Amicon® Ultra 4 mL Centrifugal Filter (3 kDa)
Millipore-Sigma (USA)	Stirred ultrafiltration cell with a 5 kDa cellulose membrane
New Brunswick Scientific	Excella E24 Incubator Shaker
Sigma (USA)	Thrombin CleanCleave™ Kit
Thermo Fisher Scientific (USA)	Dionex™ UltiMate 3000 HPLC Pump
Thermo Fisher Scientific (USA)	Fisherbrand™ accumet™ AB15 Basic pH Meter
Thermo Fisher Scientific (USA)	Fisherbrand™ accumet™ Gel-Filled Pencil-Thin pH Combination Electrode - Mercury-Free
Thermo Fisher Scientific (USA)	Orion™ 9863BN Micro pH Electrode
Thermo Fisher Scientific (USA)	Sterilemax Table Top Steam Sterilizer (Autoclave)
Thermo Fisher Scientific (USA)	Thermix® Stirring Hot Plate Model 210T
Varian (USA)	Cary 50 UV-visible absorption spectrometer
Varian (USA)	DMS 80 UV-visible absorption spectrometer

The absorbance is directly proportional to the concentration of the sample. The Beer-Lambert Law (Equation 2-3) can be used to calculate the absorbance expected if the concentration of the sample (C) in M, the path length (l) in cm, and the molar extinction coefficient (ϵ) in $M^{-1}cm^{-1}$ are known.

$$A = \epsilon l C \quad (2-3)$$

Typical proteins absorb in the UV region of the electromagnetic spectrum. The amide of the peptide backbone absorbs at 190 nm due to a $\pi \rightarrow \pi^*$ transition and at 220 nm due to an $n \rightarrow \pi^*$ transition. The aromatic amino acids tryptophan, tyrosine, and phenylalanine absorb at 280 nm, 275 nm, and 257 nm, respectively. Cystine, a disulfide bond originating from the oxidized form of the amino acid cysteine, also absorbs at 280 nm. These signals are due to $\pi \rightarrow \pi^*$ transitions.²²⁷

The focus of this thesis is on metallothioneins (MTs), which lack aromatic amino acids. However, MTs produce a ligand to metal charge transfer (LMCT) band upon formation of

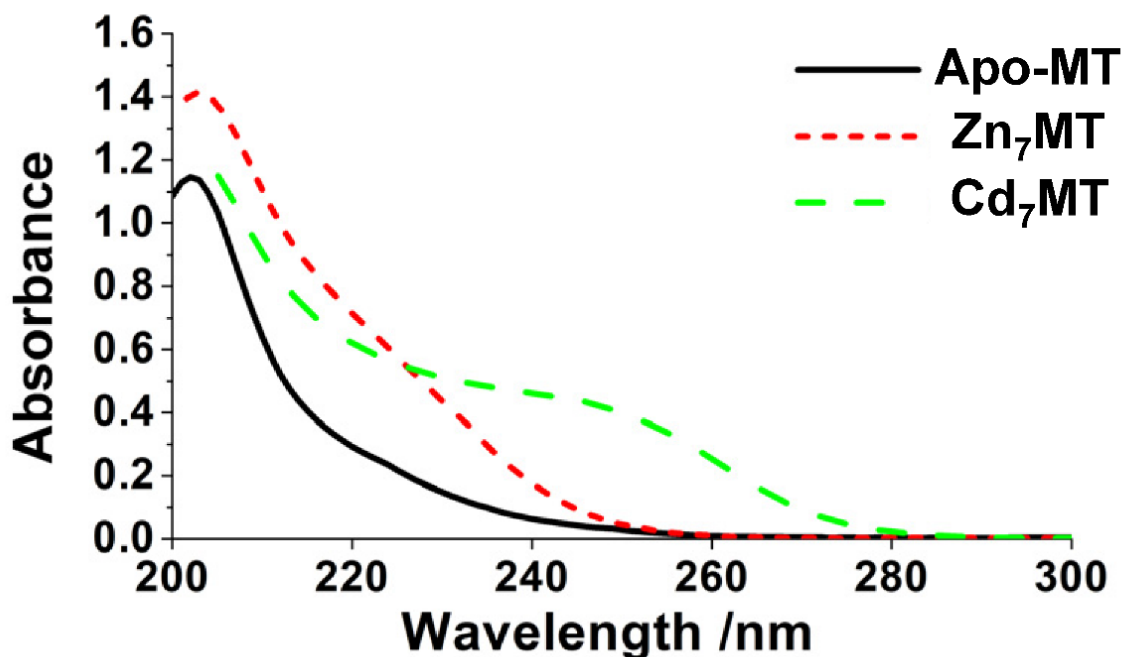


Figure 2-1. UV-visible absorption spectra of MTs. UV-visible absorption spectra of 25 μ M apo-MT, Zn₇MT, and Cd₇MT measured at pH 7.4 in 5 mM ammonium formate.

metal-thiolate bonds. This transition is caused by the transfer of the highest occupied p orbital π electron to the empty ns orbital of the metal ($\pi \rightarrow \sigma^*$ transition), where $n = 4$ for Zn(II) and $n = 5$ for Cd(II).¹⁴¹ Fig. 2-1 shows the absorption spectra of apo-MT, Cd₇MT, and Zn₇MT measured using a Cary 60 UV-visible absorption spectrometer. The S \rightarrow Zn and S \rightarrow Cd LMCT bands are seen at 230 nm and 250 nm, respectively. Due to the lack of characteristic signals in the apo-MT, UV-visible absorption spectroscopy is most useful for monitoring metal binding reactions. For the research described in this thesis, it was used in combination with stopped-flow, which will be discussed in a later section.

2.1.2 Circular dichroism spectroscopy

Circular dichroism (CD) spectroscopy measures the difference in the absorption of left and right circularly polarized light (Equation 2-4). This difference occurs when there is chirality in a molecule.

$$\Delta\varepsilon = \varepsilon_L - \varepsilon_R \quad (2-4)$$

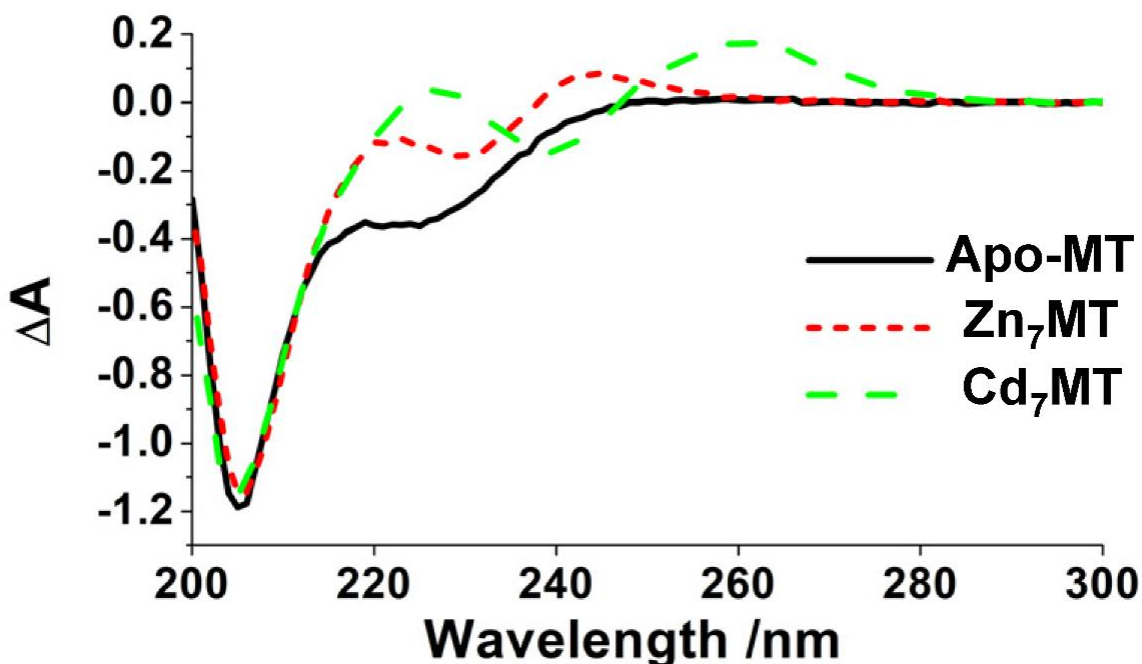


Figure 2-2. CD spectra of MTs. CD spectra of 25 μ M apo-MT, Zn₇MT, and Cd₇MT measured at pH 7.4 in 5 mM ammonium formate.

Proteins display unique CD signals when an α -helix or β -sheet is present, which makes CD spectroscopy ideal for studying protein folding. MT does not contain α -helices or β -sheets, rather the apo-MT CD spectrum in the near-UV region more so resembles that of a disordered protein with a characteristic negative signals in the near-UV region.²²⁸⁻²²⁹ However, the two-domain Zn₇MT and Cd₇MT cluster structures display derivative signals at 230 nm (–) and 245 nm (+) and 240 nm (–) and 260 nm (+), respectively. This biphasic signal arises from the excited state splitting of the metal-cluster chromophores, which are chiral in nature.¹⁴¹ Fig. 2-2 shows the CD spectra of apo-MT, Cd₇MT, and Zn₇MT measured using a J-810 Spectropolarimeter. These characteristics provide solution structural information about the nature of the metal-thiolate clusters. Additionally, the apo-MT signal at 222 nm can be used to probe the degree of disorder in the structure. An ellipticity closer to zero at this wavelength indicates a more disordered structure, more similar to a random coil.^{228, 230}

2.1.3 Electrospray ionization mass spectrometry

Mass spectrometry measures analytes based on their mass-to-charge ratio (m/z) in the gas phase. The main components of a mass spectrometer are the inlet system, ion source, mass analyzer, and detector. From the detector, the signal is processed and displayed as a graph of intensity vs mass-to-charge ratio (m/z).

The source generates the ions. There are hard and soft ionization methods. Hard ionization methods such as electron ionization (EI) and chemical ionization (CI) are commonly used for small molecules as they have predictable fragmentation patterns useful for identification. Soft ionization techniques produce minimal to no fragmentation and are typically used for large macromolecules such as proteins. The two most common ionization methods used for proteins are electrospray ionization (ESI) and matrix-assisted laser desorption/ionization (MALDI), both soft techniques. This thesis focuses on ESI-MS, which was developed for use on biological macromolecules in the 1980's.²³¹⁻²³³

Figure 2-3 shows a simple schematic of the Bruker MicroTOF II mass spectrometer, the instrument used for the research in this thesis, with a close-up view of the ESI source in positive ion mode. This figure was based on the schematic shown in the user manual. For

simplicity, the mechanism will be described for positive ion mode. First, the solution containing the analyte is introduced via the inlet system to a stainless-steel capillary under atmospheric pressure (Fig. 2-3A). The ESI source showing the formation of charged droplets is depicted in Fig. 2-3B. A voltage ($\sim 3000\text{-}5000\text{ V}$) is applied to the capillary. The mass spectrometer acts as an electrochemical cell with the capillary as the anode and the spray shield as the cathode. At the anode, an oxidation reactions occurs, typically the oxidation of water in the solution (Equation 2-5).²³⁴

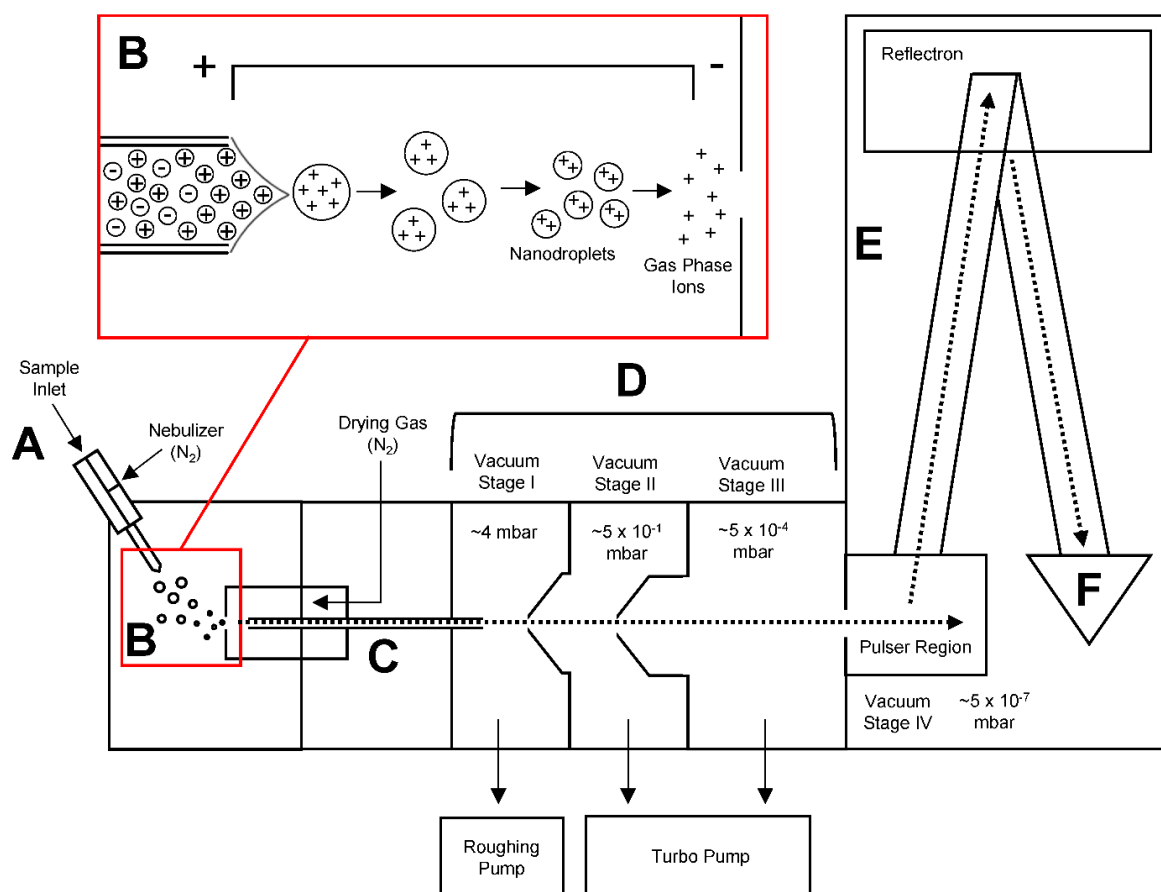


Figure 2-3. A schematic of the Bruker MicroTOF II mass spectrometer. Shown are (A) the inlet system, (B) the ESI source showing the mechanism of droplet formation, (C) the glass capillary, (D) the transfer optics, (E) the TOF analyser, and (F) the MCP detector. The dotted arrows show the pathway of ions through the instrument.

This oxidation generates the protons in solution responsible for creating the charge found in the solution and later the droplets. The electrons are removed via a wire and create the negative charge at the cathode.²³⁴ Due to the potential difference between the capillary and the spray shield, the positive charges become localized on the tip of the capillary. They become distorted and form a Taylor Cone until they break off and form charged droplets.²³⁵ A nebulizer gas (usually nitrogen) assists in the formation of droplets.

As the solvent evaporates, the droplets become smaller. Eventually, the Rayleigh limit will be reached, and the droplets will undergo fission, releasing charge. Equation 2-6 describes the number of charges that are allowed at the Rayleigh limit, where z_R is the number of charges, e is the charge of an electron in C, ϵ_0 is the vacuum permittivity, γ is the surface tension, and r is the droplet radius.²³⁶

$$z_R = \frac{8\pi}{e} \sqrt{\epsilon_0 \gamma r^3} \quad (2-6)$$

This process repeats in a cascade. There are two different models to describe the release of the ions final nanodroplets to the gas phase. These are the ion evaporation model (IEM) and the charged residue model (CRM). The IEM, which is likely for small molecules, describes the emission of single charges from the droplet. The CRM, which is more likely for macromolecules, involves a single analyte in the final nanodroplet, which evaporates.²³⁷ A chain ejection model (CEM) has also been proposed for unfolded peptides where the peptide is ejected from the droplet due to the exposed hydrophobic interior of the protein having unfavourable interactions with the droplet interior.²³⁷⁻²³⁸ Throughout these processes, which occur on the millisecond timescale, the positive droplets are pulled towards the negative spray shield.

In the next stage, the ions are pulled through a glass capillary (Fig. 2-3C) which focuses the ions into a straight pathway and brings them through a series of vacuum drops and voltage drops (Fig. 2-3D). The skimmers keep the ions on the correct pathway.

A mass analyzer is used to separate the generated ions based on their mass to charge ratio. In this thesis, a time-of-flight (TOF) mass analyzer is used (Fig. 2-3E). This is a pulsed method that measures the m/z of the ions based on the time they take to reach the detector.

A voltage pulse provides potential energy to ions. These ions undergo orthogonal acceleration and end up with different velocities as the potential energy is transformed into kinetic energy.²³⁹ Equation 2-7 shows how the different masses result in different times (t) to reach the detector, where l = length of the TOF analyzer, z = charge, ΔU = potential energy, m = mass, and t_0 = the time of the delay.²³⁷

$$t = \frac{l}{\sqrt{\frac{2ze\Delta U}{m}}} + t_0 \quad (2-7)$$

A reflectron can be used to improve the resolution, as is the case with the Bruker MicroTOF II instrument. Instead of a linear TOF analyzer, the reflectron reverses the flight direction partway through to correct for slight differences in applied potential energy. The more reflectrons used will further increase the resolution but will also decrease the sensitivity.²³⁹

The ions arrive at the detector (Fig. 2-3F). Microchannel plates (MCPs) are used as the detector for TOF analyzers. MCPs contain multiple channel electron multipliers (CEMs) and are ideal for TOF analyzers as they can handle multiple pulses close in time. They consist of a dynode, which causes emission of electrons when struck by an incoming ion.²⁴⁰

In mass spectrometry, ions are always measured by their mass-to-charge ratio (m/z). Since ESI produces multiply charged ions, the resulting protein ESI spectrum will have multiple peaks corresponding to one species, which complicates the analysis. Deconvolution converts the x-axis of the spectrum from m/z to mass (Da) using Equation 2-8, where M = mass in Da, R_z = observed mass to charge ratio, m = mass of adduct ion (typically H^+) in Da, and z = charge.²⁴¹ A typical mass spectrum of recombinant human apo-MT1a is shown in Fig. 2-4. This apo-MT displays charge states from 3+ to 8+ in positive ion mode (Fig. 2-4A). The deconvoluted spectrum displays a single peak corresponding to the mass of the apo-MT (Fig. 2-4B).

$$M = (R_z - m)z \quad (2-8)$$

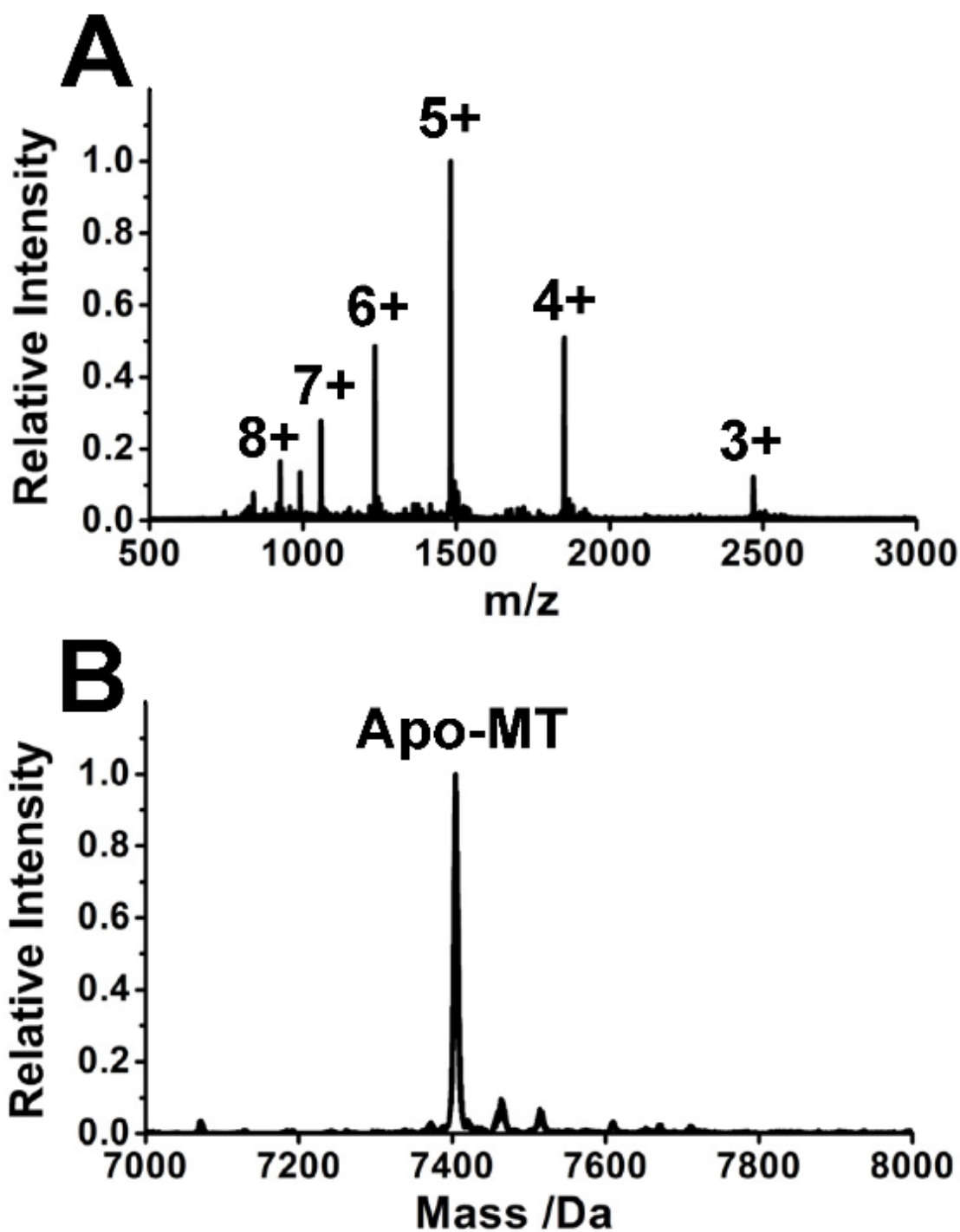


Figure 2-4. ESI mass spectrum of recombinant human apo-MT1a. A typical ESI mass spectrum of apo-MT at pH 7.4 obtained using the Bruker MicroTOF II instrument in positive ion mode. The spectrum in (A) shows the charge states and the spectrum in (B) has been deconvoluted. Both spectra's intensities have been normalized between 0 and 1.

The typical settings used for ESI-MS experiments, optimized to study MT are shown in Table 2-2. The mass spectrometer was calibrated externally using ESI low concentration tuning mix. The theoretical average masses expected in the deconvoluted ESI mass spectra for each experiment described in this thesis are shown in Tables A-1 through A-4 (Appendix A).

Mass spectrometry can be used to identify species in solution based on the exact mass but is only a semi-quantitative technique with respect to the concentration of these species. It does not measure the actual concentration of the sample, but it can measure the relative abundance of a species compared to others using peak intensity, provided they have the same ionization efficiency.

Table 2-2 The ESI-MS parameters used during experimental analysis of MT on the Bruker MicroTOF II instrument.

Parameter	Value
Ion mode	Positive
Capillary	3500–4500 V
End plate offset	500 V
Nebulizer	1.0–2.0 bar (0.2 bar for calibration)
Dry gas	4.0 Lmin ⁻¹
Dry temperature	100 °C
Capillary exit	180.0–220.0 V
Skimmer 1	22.0 V
Hexapole 1	22.5 V
Hexapole RF	600.0 V
Skimmer 2	22.0 V
Lens 1 transfer	88.0 μs
Lens 1 pre-pulse storage	28.0 μs
Mass range	500–3000 m/z

ESI-MS is a powerful technique for studying MTs due to the ability to resolve individual species. In the titration of a metal binding to MT, relative binding constants can be calculated from the ESI mass spectra for each individual metallation step. For example, each step of a Zn(II) titration into MT can be described by Equation 2-9, where K_n describes the binding constant for the n th Zn(II) binding to MT.

$$K_n = \frac{[Zn_n MT]}{[Zn_{n-1} MT][Zn(II)]} \quad (2-9)$$

Binding constants are often expressed in the form $\log K$. The cumulative addition of each individual $\log K_n$ is expressed as $\log \beta_n$. To obtain binding constants from ESI mass spectral data, the metal must be titrated in against a competitor with a known binding constant to the metal. Experimental speciation curves can then be plotted and fit using the Hyperquad Simulation and Speciation (HySS) program which generates simulated speciation curves based on user-input $\log \beta$ values.²⁴²

Calculated binding constants as well as characteristic speciation patterns can be analyzed to determine whether the sequential metal-binding is non-cooperative (all binding constants are the same), negatively cooperative (binding constants sequentially decrease), or cooperative (binding constants sequentially increase). Examples of these binding pathways for the binding of seven metals to MT are shown in Fig. 2-5, modelled using HySS. Simulated speciation curves (Fig. 2-5i) can be converted to simulated mass spectra at any point in the titration (Fig. 2-5ii). Taking “slices” of the 3D spectra, a simulation of the corresponding mass spectra can be generated (Fig. 2-5iii-v). In a titration experiment, multiple points are measured using ESI-MS and their relative intensities are used to generate a speciation graph. This graph is then fitted using HySS and the relative binding constants are determined. It should be noted that for a real non-cooperative condition (Fig. 2-5A) the sequential binding constants will not be the same but will decrease as binding sites become occupied and less are available for binding. The extreme condition shown in Fig. 2-5A is to provide a baseline in which to compare the strength of negative cooperativity between different conditions and to show how a more non-cooperative pathway would broaden the distribution seen in the mass spectra.

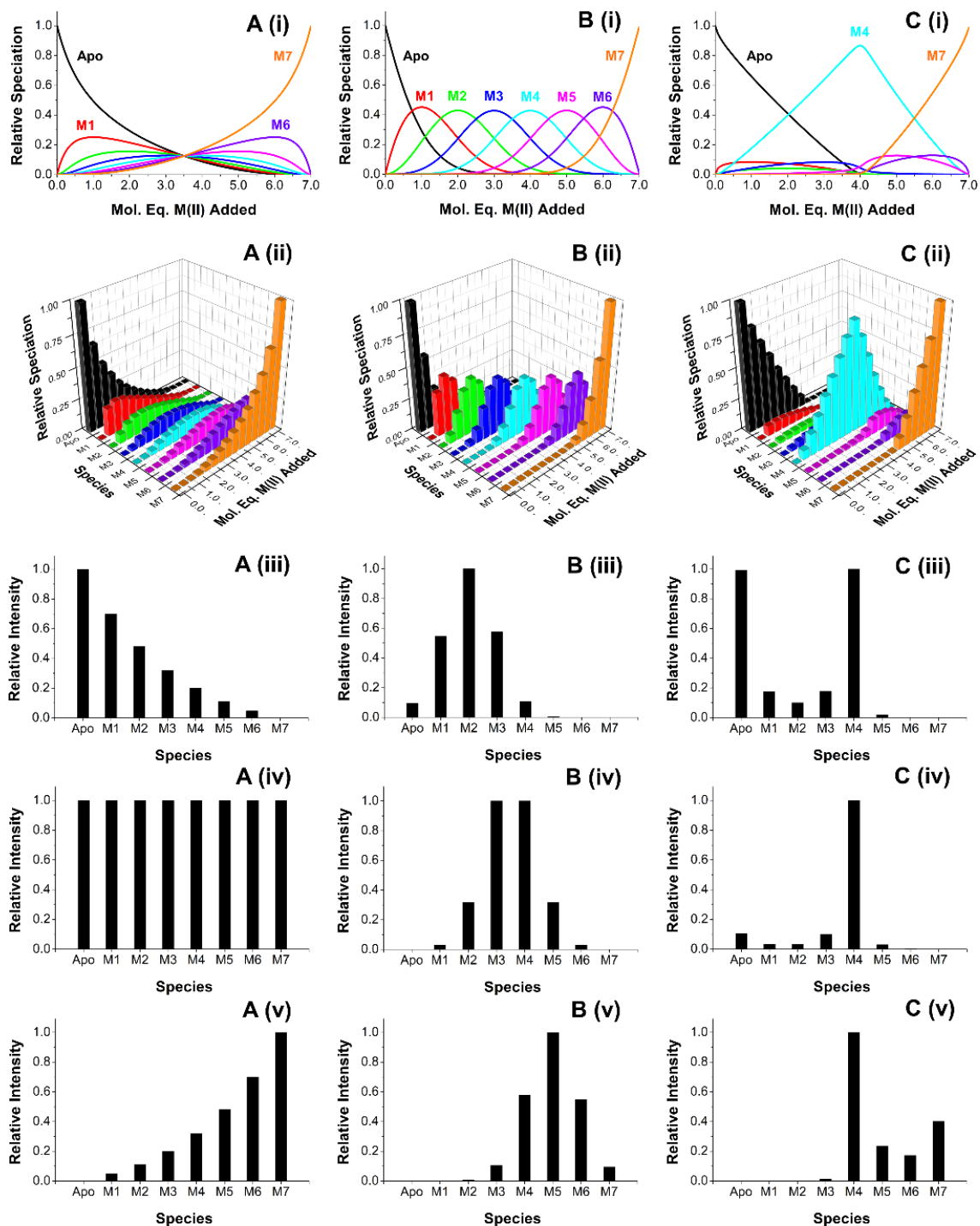


Figure 2-5. Speciation simulations showing different binding pathways. A simulation of MT with seven binding sites showing (A) a non-cooperative, (B) negatively cooperative, and (C) cooperative to M₄MT and M₇MT binding pathways. The speciation is shown as (i) a speciation vs metal added graph, (ii) a 3D graph of speciation, species identity, and metal added, and simulations of mass spectra at (iii) 2, (iv) 3.5, and (v) 5 mol. eq. metal added.

2.1.4 Stopped flow kinetic methods

Stopped flow is a method used to study kinetics on millisecond timescales. A schematic of the SFM-400, the instrument used for the research in this thesis, is shown in Fig 2-6, based on information in the user manual.

Syringes are used to deliver the samples in the desired ratios. These flow to the mixer, where they are rapidly mixed for a defined amount of time and then transferred to a cuvette. After the specified volume has been delivered, the hard stop closes, and the solution is trapped in the cuvette and allowed to age. A spectrometer (usually UV-visible or CD) collects a kinetic trace at a single specified wavelength. For the research in this thesis, a MOS-250 UV-visible absorption spectrometer was used in stopped-flow studies.

Stopped flow in combination with absorption spectroscopy can be used to study MT metallation reactions by monitoring formation of the LMCT band. From this technique, rate constants can be determined by fitting the kinetic traces.

The metallation of MTs can be described as a series of sequential bimolecular second order reactions. For example, for the formation of Zn_7MT from apo-MT, there would be a series of seven reactions. Equation 2-10 describes the binding of the n th $Zn(II)$ to MT. Equation 2-11 describes the dependence of the rate of Zn_nMT formation on the rate constant and the concentration of reactants.



$$d[Zn_nMT] = k_n[Zn_{n-1}MT][Zn(II)] \quad (2-11)$$

However, in an experiment where the LMCT band is monitored over time, only an average of all species in solution is observed. In reality, the the observed kinetic trace will consist of multiple overlapping bimolecular reactions, making the individual k_{1-7} impossible to resolve. The solution is to approximate by fitting the kinetic trace as a single bimolecular reaction to obtain a single rate constant describing the overall binding.

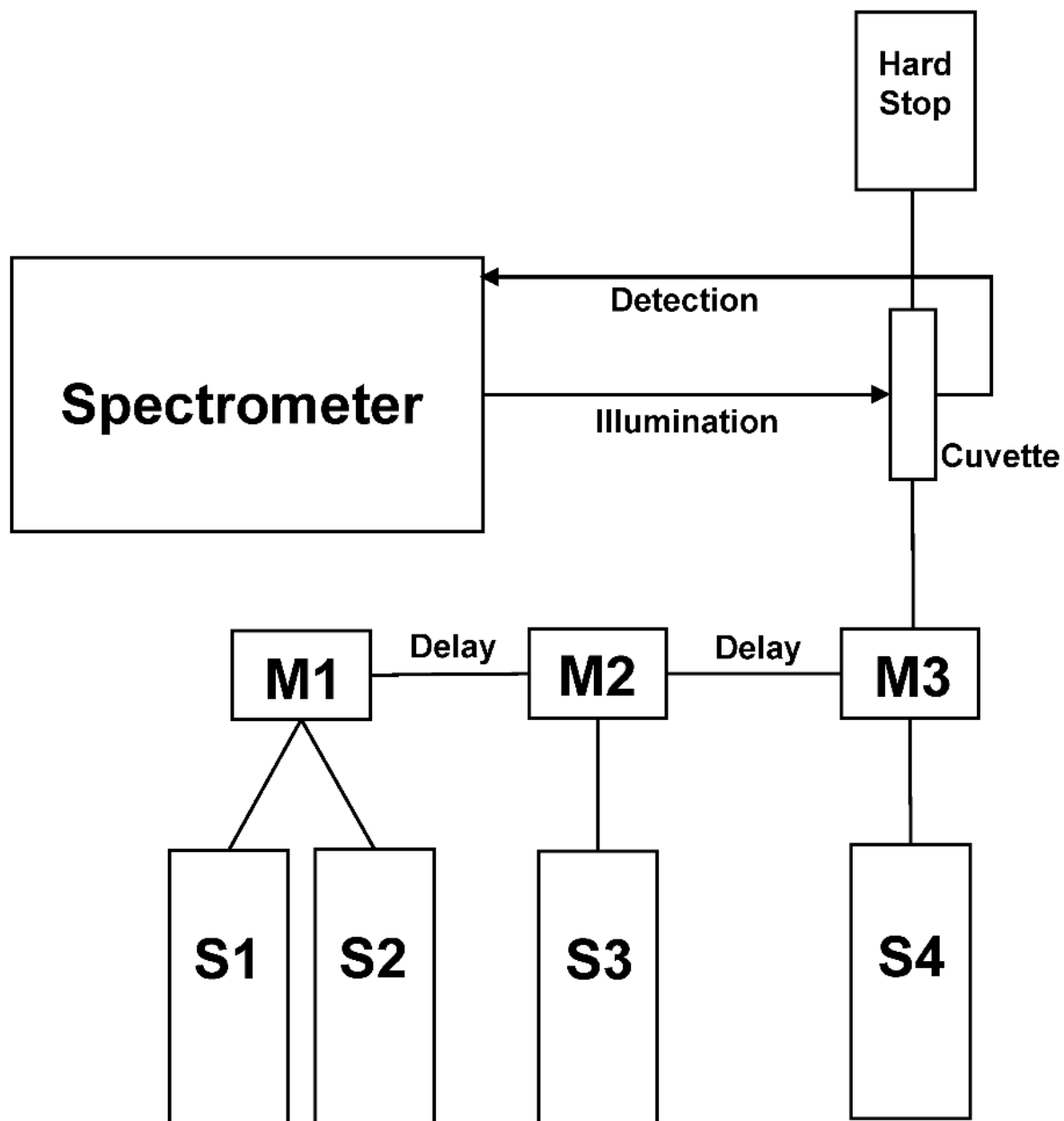


Figure 2-6. Stopped flow schematic. A schematic of the stopped flow apparatus showing the flow of the reagents from the syringes (S) to the mixers (M) and to the cuvette. The hard stop controls the flow of the sample out of the cuvette. The spectrometer monitors the reaction in the cuvette. Optional delay lines can be installed in between each mixer.

2.2 Computational Methods

Molecular mechanics (MM) can be used to calculate the lowest energy conformation of a molecule. This technique is computationally inexpensive and is typically used in systems with a large number of atoms, making it ideal for proteins. MM treats atoms and bonds as hard spheres with defined van der Waals radii and springs which follow Newtonian physics. Force field parameters are input, which define the equilibrium energies. The deviation from these equilibrium energies is calculated as a sum of independent energy terms for bond stretching, bond bending, torsional strain, van der Waals interactions, stretch-bend interactions, dipole-dipole, and hydrogen bonding (Equation 2-12).²⁴³ The molecule arranges itself to minimize these energy terms during an MM calculation. The work presented in this thesis uses Allinger's MM3 force fields.²⁴⁴⁻²⁴⁶

$$E_{Total} = E_{Stretch} + E_{Bend} + E_{S-B} + E_{Torsion} + E_{vdW} + E_{DP-DP} + E_{H-bonding} \quad (2-12)$$

For larger molecules, MM may not find the true energy minimum. Molecular dynamics (MD) simulations can overcome this by searching for minima at higher temperatures. This allows the system to overcome conformational barriers which may have the structure stuck in a local minimum. In MD, the motion of the system is calculated over time at a particular temperature which directly relates to kinetic energy. At each time point, the total energy is calculated as in Equation 2-12.²⁴³

MM/MD calculations are ideal for the study of MTs. MTs are difficult to crystallize, particularly apo or partially metallated forms. Computational simulations can provide a visualization of the dynamic MT structure and can provide a complement to experimental work. All MM/MD simulations described in this thesis were performed using the Scigress software package, version 6.0 (Fujitsu, Poland).

Density functions theory (DFT) calculations are used to compute the molecular orbitals of a system and their respective energies. Basis sets describe the atomic orbitals of the individual atoms found in the system. The basis sets used depend on the elements. For the research in this thesis, 6-31g(d,p) and lanl2dz were used, with the latter required for the heavier elements Zn(II) and Cd(II). The functional is a set of equations which describes the

how the atomic orbitals interact to form the MOs.²⁴³ For the work in this thesis, the functional B3LYP was used, which combines a functional developed by Becke²⁴⁷ with one developed by Lee, Yang, and Parr.²⁴⁸ For MTs, DFT calculations are ideal for calculating the ground state electronic structure of the metal-thiolate clusters. In this thesis, all DFT calculations were performed using Gaussian G09.²⁴⁹

2.3 Solution Preparation

Table 2-3 lists all of the reagents used throughout the research described in this thesis with their respective supplier. Unless otherwise mentioned below, all solutions were prepared by dissolving the reagent in the appropriate volume of Milli-Q water to produce the desired concentration.

Concentrated hydrochloric acid (HCl), formic acid, and ammonium hydroxide were individually diluted in water to use for pH adjustment. Solutions of Tris-HCl were adjusted to the desired pH using dilute HCl. Solutions of ammonium formate were adjusted to the desired pH using dilute formic acid or dilute ammonium hydroxide.

Solid benzoquinone (Bq) was dissolved first in a small volume of methanol, then diluted using water to the final desired concentration. The final solution was 10% methanol and 90% water. $[\text{Bi}(\text{cit})]^-$ was prepared by dissolving in the minimal amount of concentrated HCl. The solution was made up to the correct volume using ammonium formate at pH 2.6. $[\text{Bi}(\text{EDTA})]^-$ was prepared using the method detailed in Summers et al.²⁵⁰ Briefly, H_4EDTA was added to boiling water. $(\text{BiO})_2\text{CO}_3$ was slowly added. After 30 min, the mixture was filtered and left to allow the water to evaporate. 10 mM $[\text{Bi}(\text{EDTA})]^-$ solutions were prepared by dissolving the resulting crystals in water.

8 M GdmCl was prepared by mixing solid GdmCl with Tris-HCl and heating until completely dissolved. The solution was cooled to room temperature and the pH was adjusted using ammonium hydroxide. Trypsin solutions were prepared immediately before use by dissolving solid trypsin in 1 mM HCl.

Table 2-3. Reagents and solutions prepared for use in the research described in this thesis and their suppliers. The concentration of solutions and small molecule chemical formulae are included.

Solution	Supplier
Ammonium formate (NH ₄ HCO ₂) (20 mM)	J.T. Baker
Ammonium hydroxide (NH ₄ OH)	Honeywell-Fluka
Benzoquinone (Bq) (10 mM)	Alfa Aesar
Bismuth citrate [Bi(cit)] ⁻ (10 mM)	Sigma-Aldrich
Bismuth EDTA [Bi(EDTA)] ⁻ (10 mM)	
Bismuth subcarbonate ((BiO) ₂ CO ₃)	Sigma-Aldrich
Broth (Miller) (25 g/L LB)	Bioshop Canada
Cadmium acetate (CdOAc ₂) (100 mM and 10 mM)	Acros
Cadmium sulfate (CdSO ₄) (1 M)	Thermo Fisher
Competent BL21DE3 Cells	Thermo Fisher
ESI Tuning Mix	Agilent
Ethylenediamine tetraacetic acid (H ₄ EDTA)	Thermo Fisher
Formic Acid (CH ₂ O ₂)	Caledon
Glycerol (80 % v/v)	Thermo Fisher
Guanidinium chloride (GdmCl) (8 M)	Sigma-Aldrich
Hydrochloric acid (HCl)	Thermo Fisher
Hydrogen peroxide (H ₂ O ₂)	Sigma-Aldrich
Isopropyl β-D-1-thiogalactopyranoside (IPTG) (1 M)	Bioshop Canada
Kanamycin sulfate (50 mg/mL)	Teknova
N-ethylmaleimide (NEM) (10 mM)	Sigma-Aldrich
Plasmid	GENEWIZ
Thrombin CleanCleave™ Kit	Sigma-Aldrich
Tris(2-carboxyethyl)phosphine HCl (TCEP-HCl) (200 mM)	Soltec Ventures
Tris(hydroxymethyl)aminomethane HCl (Tris-HCl) (10 mM)	Sigma-Aldrich
Trypsin (1 mg/mL)	Sigma-Aldrich
Zinc acetate (ZnOAc ₂) (10 mM)	Fisher

2.4 Protein Expression and Purification

2.4.1 Transformation of bacteria with plasmid

The construct for the sequence MGKAAAAMDP NCSCATGGSC TCTGSKCKE CKCTSCKKSC CSCCPMSCAK CAQGCICKGA SEKCSCCAKK AAAA (β MT1a) with an N-terminal S-tag with the sequence MKETAAAKFE RQHMDSPDLG TLVPRGS in a pET29a plasmid was purchased from GENEWIZ. This plasmid codes for kanamycin resistance.

Competent *Escherichia coli* BL21(DE3) cells were thawed on ice for 30 min. The 2 μ g of DNA plasmid was resuspended in 100 μ L of H₂O. 2 μ L of this DNA was added to the cells and left on ice for 30 min. The mixture was heat-shocked at 42 °C for 45 s and then incubated on ice for 2 min. 250 μ L of either SOC media or LB media was added and the mixture was shaken at 37 °C for 1 h. 80 μ L of this mixture was spread on an agar plate containing 50 mg/mL kanamycin using a sterile inoculation loop and was allowed to grow for 16-18 h at 37 °C in an incubator.

A single colony was added to 10 mL of autoclaved LB Miller broth and shaken at 37 °C until the absorbance at 600 nm reached 0.6 (about 3 h). Individual glycerol stocks were prepared by thoroughly mixing 900 μ L of cell culture with 100 μ L of 80 % glycerol. The glycerol stocks were allowed to sit at room temperature for 30 min to ensure the absorption of glycerol into the cell membrane and were then frozen and stored at -80 °C.

Additionally, *E. coli* BL21(DE3) cells transformed with pET29a plasmids coding for the sequences MGKAAAAC SCATGGSCTC TGSKCKECK CNSCKKAAAA (β MT) and MGKAAAACCS CCPMSCAKCA QGCVCKGASE KCSCCKKAAA A (α MT) with an N-terminal S-tag were donated by Dr. Peter Kille (Cardiff University, Wales). From this point onwards, the same protein expression and purification procedures were applied to both these cells and the ones transformed in our lab.

2.4.2 Cell growth and protein expression

A starter culture was prepared using 100 mL autoclaved LB Miller broth, 10 μ L 1M CdSO₄, 100 μ L 50 mg/mL kanamycin. The CdSO₄ was added for the purpose of binding any MT

and protecting it from oxidation or degradation in the event of leaky expression. The purpose of the kanamycin, an antibiotic, was to eliminate any cells without the plasmid or any other unwanted bacteria growing in the flasks. An inoculation loop of glycerol stock was added to this mixture and allowed to grow overnight, shaking at 37 °C (about 16 h).

The next morning, the starter culture was split into 4 flasks each with 1 L of autoclaved LB Miller Broth, each containing 1 mL 50 mg/mL kanamycin and 100 μ L 1 M CdSO₄. The flasks were shaken at 37 °C until A₆₀₀ = 0.6. The temperature was reduced to 32 °C and 280 μ L of 1 M Isopropyl β -D-1-thiogalactopyranoside (IPTG) was added to each flask to a final concentration of 0.28 mM to begin expression of the MT. IPTG is a mimic of allolactose, a metabolite of lactose. As the gene coding for MT expression is under control of the lac operon, when IPTG binds the lac repressor it begins transcribing the MT genes. IPTG is not metabolized by the cell, meaning the amount of IPTG remains constant over the whole expression period.

After 30 min, 400 μ L of 1 M CdSO₄ was added to each flask. The purpose of this Cd was to bind to and stabilize the newly produced MT. This would prevent oxidation of the thiols and degradation in the cell. The cells were shaken for another 3.5 hours and then were harvested by centrifugation at 8983 g (6000 rpm) using a JLA 8.1 rotor for 15 min. The pellet was collected and resuspended in 35 mL of argon-saturated 10 mM Tris-HCl buffer at pH 7.4. The cell mixture was frozen at -80 °C until the next purification step.

2.4.3 Protein purification

The cell mixture was thawed in a water bath and put on ice immediately after thawing. The cells were lysed at 4 °C using a Constant Systems Cell Disruptor at pressures ranging from 18-24 kpsi. The lysate was centrifuged for 1 h at 20,442 g (13 000 rpm), using a JA 25.50 rotor at 4 °C and the supernatant was passed through a filter. The supernatant was loaded onto 2.5 mL HiTrap SPHP cation exchange columns connected in sequence at a rate of 2.5 mL/min. The theoretical pI of MT is around 8, therefore at pH 7.4 the protein will be positively charged and will stick to the column. The column was washed with 10 mM Tris-HCl buffer at pH 7.4 and the flow-through was monitored using UV-visible absorption spectroscopy on a Cary-50 spectrometer from 200-300 nm. Once the flow-through was

completely clean, an increasing salt gradient was applied to the column to elute the bound MT. The MT was monitored for using the characteristic 250 nm shoulder band caused by the S to Cd LMCT. The collected MT was concentrated.

The expressed protein contained an S-tag, which was added in the sequence due to its stabilizing effect on the MT during the expression stage. To avoid potential structural interference from the additional amino acids, the S-tag was removed in the purification process. The S-tag was cleaved using a Thrombin CleanCleave™ kit following the manufacturer's directions. The reaction was allowed to proceed for either 12–14 h at 4 °C or 1–2 h at room temperature. Both conditions resulted in complete cleavage of the S-tag without any non-specific cleavage.

The MT was separated from the thrombin beads via centrifugation at 2152 g (2500 rpm) and removal of the supernatant containing the MT. The thrombin beads in the pellet were cleaned according to the manufacturer's directions.

The MT was then desalted using a G25 column. The MT was collected in the flow through, monitored by UV-visible absorption spectroscopy. The purpose of this was to remove the salt accumulated in the previous ion exchange step and the thrombin reaction step so the protein would stick to the cation exchange column.

The desalted MT was diluted and loaded again onto a HiTrap SPHP cation exchange column. As before, the UV spectrum from 200-300 nm was monitored as the column was washed with 10 mM Tris-HCl buffer at pH 7.4. The S-tag was eluted at this step, indicated by an absorbance at 205 nm from the peptide backbone. Once this absorbance was no longer observed, The MT was eluted by applying an increasing salt gradient to the column, while monitoring the absorption spectrum for thr characteristic band at 250 nm.

The collected MT was concentrated to approximately 20 mL and stored at -20 °C in 1 mL aliquots until needed for experimental analysis. The total protein yield was typically between 5 and 10 mg for 4 L of cell culture.

Fig. 2-7 shows the sequences of $\text{rh}\beta\alpha\text{MT1a}$, $\text{rh}\beta\text{MT1a}$, and $\text{rh}\alpha\text{MT1a}$ with the metal connectivity produced through this process. The final sequence of the $\beta\alpha\text{MT}$ after the S-tag removal is GSMGKAAAAM DPNCSCATGG SCTCTGSCKC KECKCTSCCK SCCSCPMSC AKCAQGCICK GASEKSCCA KKAAAA. The final sequence of the βMT after S-tag removal is GSMGKAAAAC SCATGGSTC TGSCCKECK CNSCKKAAAA. The final sequence of the αMT after S-tag removal is GSMGKAAAAC CSCCPMSCAK CAQGCVCKGA SEKSCCKKA AAAA.

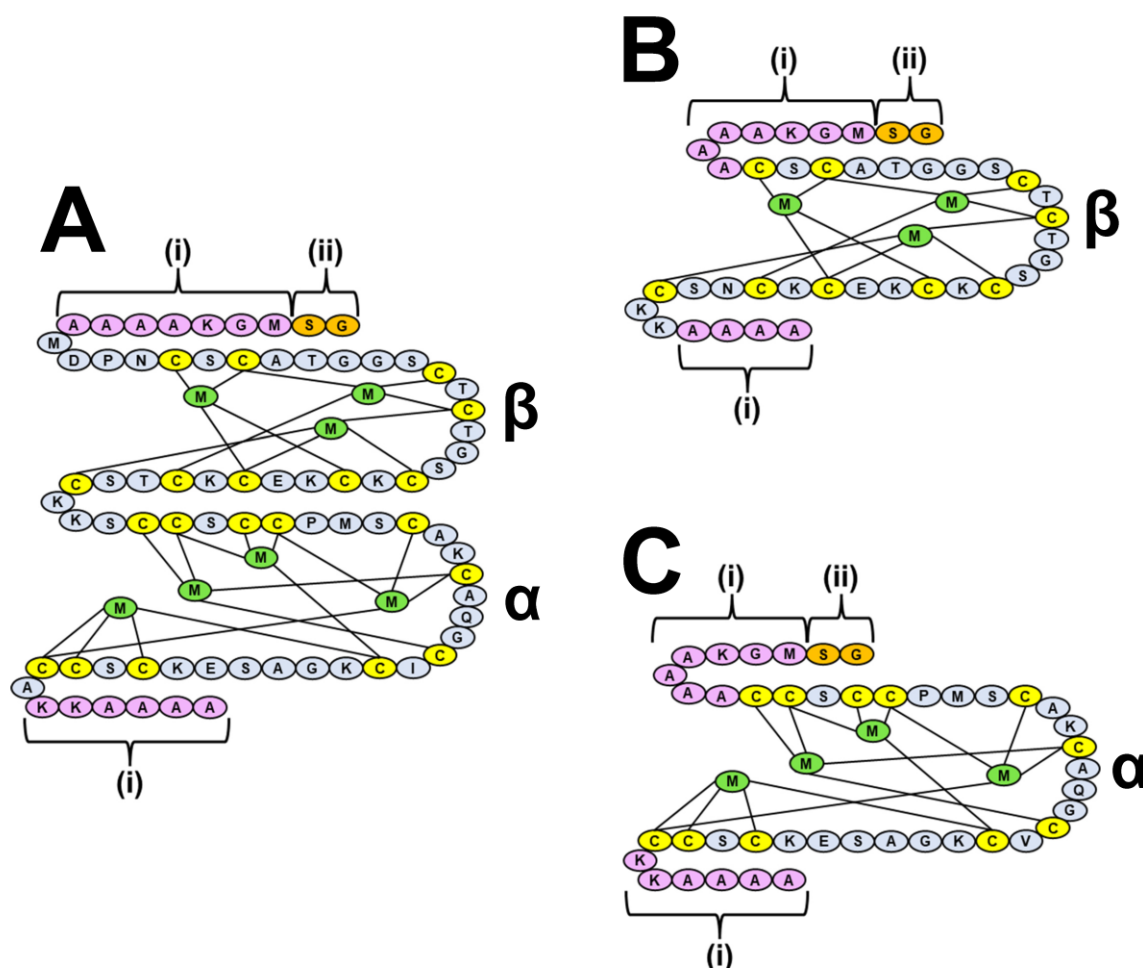


Figure 2-7. Sequences of $\text{rh}\beta\alpha\text{MT1a}$, $\text{rh}\beta\text{MT1a}$, and $\text{rh}\alpha\text{MT1a}$. Sequences of (A) $\text{rh}\beta\alpha\text{MT1a}$, (B) $\text{rh}\beta\text{MT1a}$, and (C) $\text{rh}\alpha\text{MT1a}$ showing the connectivity of the clusters formed in each domain when fully metalated with divalent metals. The cysteine residues are highlighted in yellow. (i) indicates nonendogenous amino acids added to the sequence for stability during purification, highlighted in purple and (ii) indicates amino acids originating from the S-tag left over after cleavage, highlighted in orange. M (green) = divalent metal.

Throughout the remainder of this thesis, the rhMT1a produced here will be referred to as MT, except for when comparisons are made between different isoforms, in which case it will be called MT1a. The fragments will be referred to as β MT and α MT.

2.5 Preparation of Apo-MT for Experimental Analysis

The process of preparing MT for experimental analysis involved removing the Cd(II) that was bound during expression in *E. coli*, adjusting the protein to the desired pH level, buffer exchanging to replace the Tris-HCl with ammonium formate, and removing the high salt content caused by the salt gradient applied in the purification step. The latter two processes were necessary for electrospray ionization mass spectrometry (ESI-MS) analysis. A volatile solution such as ammonium formate is needed for effective ionization and excess salt results in observation of multiple adduct peaks on the protein, reducing the intensity of the signal and clarity of the data.

Due to the 20 reduced cysteines, MT is very sensitive to oxygen, particularly in its metal-free form. When exposed to air or solutions where oxygen is present, the cysteines tend to oxidize, forming disulfide bridges. A custom airtight chamber with a valve was built for the purpose of creating an oxygen-free environment. One side of the valve was connected to a vacuum line and the other side was connected to an argon gas tank.

A 20 mM ammonium formate solution at pH 2.6 was gently bubbled with argon gas to displace dissolved oxygen. Another bottle of 20 mM ammonium formate at pH 7.4 was also gently bubbled with argon gas. If another pH was desired for the experiment, then a bottle of ammonium formate at the desired pH was bubbled with argon instead.

200 mM Tris(2-carboxyethyl)phosphine HCl (TCEP-HCl) solution at pH 7.4 (or other desired pH) was added to the pH 7.4 ammonium formate to a final concentration of 0.5 mM to prevent or reverse any oxidation of the cysteines that took place.

One vial of purified MT was placed in the airtight chamber and thawed under vacuum. Once fully thawed, the MT was placed in an Amicon® Ultra 4 mL Centrifugal Filter with a 3 kDa cut-off along with 20 mM ammonium formate at pH 2.6 and centrifuged for 30 min at 3901 g (4500 rpm). This process was repeated a total of three times, re-filling the

centrifugal filter with pH 2.6 ammonium formate before each spin. This centrifugation process was repeated again another three to four times using 20 mM pH 7.4 ammonium formate in place of the pH 2.6 ammonium formate. Starting on the second spin, one drop of dilute NH_4OH was added into the centrifugal filter to help gradually raise the pH. The pH of the MT solution was tested after each spin. Once it reached pH 7.4, the MT was removed from the centrifugal filter to a glass vial with a septum cap and its final volume was measured using a 100 μL micropipette. Typical final volumes ranged from 0.5 to 1 mL. The amount of buffer exchange by centrifugation described here was consistent in producing apo-MT with minimal to no salt and metal contamination.

The concentration of the MT was determined by taking a small aliquot of the prepared apo-MT (typically 25 μL), metallating it using a 100 mM CdOAc_2 solution, and measuring the absorbance spectrum between 200 and 300 nm using a Cary-60 UV-visible absorption spectrometer in a 1 cm path length cuvette. The molar extinction coefficient of the 250 nm S \rightarrow Cd LMCT band for $\beta\alpha\text{MT}$ is known ($\epsilon = 89\,000\ \text{M}^{-1}\text{cm}^{-1}$),²⁵¹ therefore Beer's Law can be used to determine the concentration of MT in the cuvette.

The relationship $C_1V_1 = C_2V_2$ can then be used to find the concentration of the initial apo-MT solution before dilution into the cuvette. The protein was then diluted to the desired concentration for the experiment. An ESI mass spectrum of the apo-MT was obtained before performing any experiment to ensure no metal or salt contamination or oxidation had taken place. A peak maximum that was a multiple of 2 Da below the expected mass in the deconvoluted spectrum indicated disulfide bond formation.

Chapter 3

3 Human Apo-Metallothionein 1a is not a Random Coil: Evidence from Chemical, Temperature, and pH Unfolding*

The structures of apo-metallothioneins have been relatively elusive due to their fluxional, disordered state which is difficult to characterize. However, the structures of intrinsically disordered proteins (IDPs) are rather diverse, which raises questions about where the structure of apo-MTs fit into the protein structural spectrum. Flexible apo-MTs are able to bind to multiple metals, paralleling IDPs that can bind to multiple partners. However, the idea that the apo-MT structure could be relevant to its function has not been largely explored. In this chapter, the folded status of apo-MT1a is discussed with respect to the chemical denaturant GdmCl, temperature conditions, and pH environment. Some of the data in this chapter has been previously published (Yuan et al. 2023)²⁵² which is indicated in the appropriate figure captions.

3.1 Introduction

Within the last few decades, intrinsically disordered proteins (IDPs) and intrinsically disordered regions (IDRs) within proteins have been increasingly recognized as an important part of the proteome,²¹ with approximately 60% of human proteins either having IDRs or being entirely disordered.²³⁻²⁴ IDPs and IDRs use disorder to their advantage and are often hubs in intracellular protein networks.^{25, 30}

IDPs tend to lack “order-promoting” residues such as Trp, Cys, Phe, Ile, Tyr, Val, Leu, and Asn.^{21, 253} Conversely, the presence of Ala, Arg, Gly, Gln, Ser, Pro, Glu, and Lys is common in IDPs.^{21, 253}

* A portion of this chapter has been published:

Yuan, A. T.; Korkola, N. C.; Stillman, M. J., Apo-metallothionein-3 cooperatively forms tightly compact structures under physiological conditions. *J. Biol. Chem.* **2023**, 299 (3), 102899.

Reproduced with permission from: A.T. Yuan, N.C. Korkola, and M.J. Stillman.

Uversky et al. have developed a method for predicting intrinsic disorder in proteins based on only the amino acid sequence.²⁵³ Analysis of natively folded and intrinsically disordered proteins revealed a relationship between the mean net charge $\langle R \rangle$, mean hydrophobicity $\langle H \rangle$, and the protein structure. Plotting the mean net charge vs. the mean hydrophobicity for different proteins revealed a boundary line described by Equation 3-1, above which a protein would be predicted to be intrinsically disordered.

$$\langle R \rangle = 2.785 \langle H \rangle - 1.151 \quad (3-1)$$

There is a large diversity of possible protein structures within the category of intrinsically disordered proteins. Rather than classifying proteins as natively folded or disordered, a “protein quartet” has been proposed that places proteins into categories of natively folded, native molten globule, native pre-molten globule, and native random coil.²²⁸

The folding of globular proteins from an unfolded random coil to the functional native state is generally a cooperative process which can involve one or more intermediates. Folding intermediates have been discovered in proteins such as myoglobin²⁵⁴, carbonic anhydrase B²⁵⁵, α -lactalbumin,²⁵⁶ cytochrome C,²⁵⁷ lysozyme,²⁵⁸ and β -lactamase.²⁵⁹ These intermediate structures formed the basis of the categories for the protein quartet model. The molten globule intermediate has most of the secondary structural elements formed along with a loosely compact topology but lacks the close side chain packing found in tertiary structure. The folding transitions between the molten globule and either the unfolded or native state are characterized as cooperative transitions.²⁶⁰⁻²⁶¹ The pre-molten globule intermediate has also been described as a state where even less characteristics have formed but is still distinct from the unfolded state, being much more compact.²²⁸ The random coil is based on the idea of a freely jointed chain, where the protein dihedral angles are essentially random and the protein adopts an ensemble of loosely compact and extended conformations with minimal residual structure.²⁶² Kohn et al. have shown that many real denatured proteins follow a type of random coil behavior with the relationship in Equation 3-2 where R_g is the radius of gyration of the denatured protein, $R_0 = 1.297 \text{ \AA}$, N is the length of the polypeptide, and $\nu = 0.598$.²⁶³

$$R_g = R_0 N^\nu \quad (3-2)$$

The protein quartet model acknowledges a structural continuum where IDPs may adopt native structures that are random coil-like to more ordered molten globular structures, even in the absence of their binding partners. Numerous IDPs have displayed this type of structural diversity,²² which may be identified based on whether or not the protein has a cooperative unfolding transition upon exposure to denaturant.²⁶⁴

Metallothioneins (MTs) are small, cysteine-rich, metal-binding proteins that are ubiquitous in life and are intrinsically disordered in their apo forms.^{143, 229, 265} Mammalian MTs in particular have 20 conserved cysteine residues that are used to bind a variety of metals.

The sequences of recombinant human MT1a and recombinant human MT3, the isoforms which are the focus of this chapter, are shown in Fig. 3-1. The CPCP motive in the MT3 β -domain (Fig. 3-1Biii) is associated with MT3's growth inhibitory function, as mutation causes loss of activity.²⁶⁶ The two-domain cluster structures of MT1 and MT3 have been shown to be nearly identical when fully metallated with 7 Cd(II) metals.^{147, 267} However, a loop with a glutamic acid rich hexapeptide located in the α -domain (residues 52-60) is only present in MT3 (Fig. 3-1Biv) and has been shown to be disordered compared to the rest of the metallated protein.²⁶⁷ It has been suggested that this motif impacts Cd(II)²⁶⁸ and Cu(I)²⁶⁹⁻²⁷⁰ binding. To date however, no studies have systematically compared the apo structures of different isoforms.

Apo-MTs and partially metallated MTs are rather difficult to characterize. Apo-MTs and partially metallated MTs have never been successfully crystallized, likely due to their fluxional structure. NMR spectra of apo-MTs indicate a disordered protein with some residual structure.¹⁵⁷ The CD spectra are also characteristic of an IDP with a negative signal in the near-UV region, showing that apo-MTs contain minimal to no traditional secondary structural elements such as α -helices or β -pleated sheets.²²⁹ Mammalian MT sequences also lack aromatic amino acids²⁷¹ meaning that fluorescence spectroscopy methods are not particularly useful for unfolding studies.

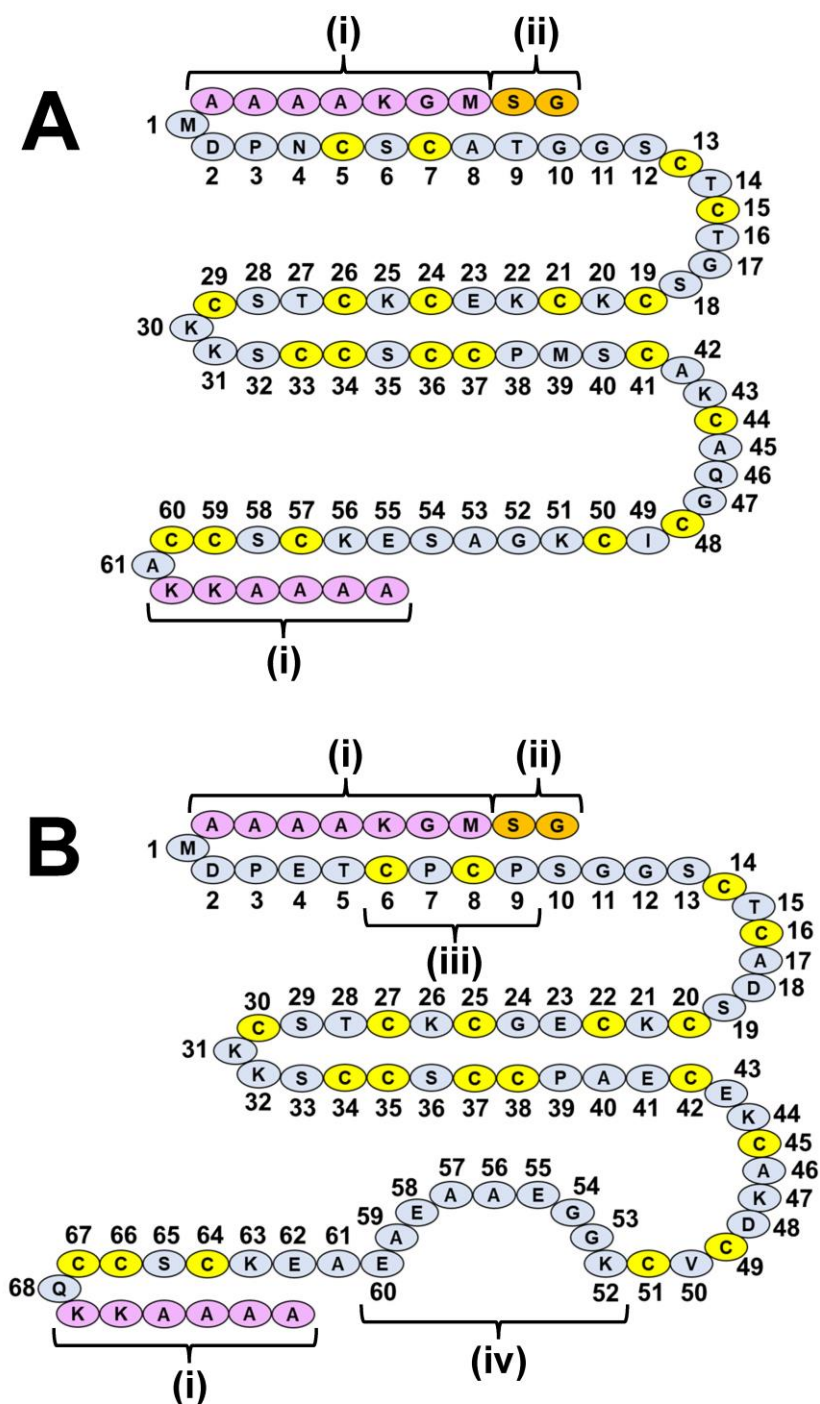


Figure 3-1. Sequences of apo-rhMT1a and apo-rhMT3. Sequences of (A) rh-apo- β MT1a and (B) rh β MT3 with the cysteine residues highlighted in yellow. (i) indicates nonendogenous amino acids added to the sequence for stability during purification, highlighted in purple and (ii) indicates amino acids originating from the S-tag left over after cleavage, highlighted in orange. The MT3 (iii) CPCP motif and (iv) the loop from Lys₅₂ to Glu₆₀ containing the glutamic acid-rich hexapeptide are also indicated. The endogenous amino acids are numbered.

Despite the difficulties, the interest in studying the structural properties of apo-MTs arose when metal-unsaturated MTs were discovered in tissues and thus deemed biologically relevant.¹⁵³⁻¹⁵⁵ To date, methods used for studying apo-MTs have included molecular dynamics (MD) simulations,^{162-164, 272} electrospray ionization mass spectrometry (ESI-MS),^{158, 165, 273} ion mobility mass spectrometry (IM-MS),¹⁶²⁻¹⁶³ fluorescence resonance energy transfer (FRET),¹⁵⁹ and stopped-flow kinetics.¹⁶⁰

Studies have shown that the dimensions of the apo-MT compared to the metallated MT are similar.^{158-159, 162-163, 162-163} ESI-MS used in combination with cysteine modification revealed that the cysteines were more equally exposed under denaturing conditions compared to native conditions, suggesting unfolding of a native structure.^{165, 272-273} Additionally, the binding of Cd(II) to the α -domain of apo-MT was slower under denaturing conditions compared to native conditions, showing a functional difference between the native apo-MT and the denatured apo-MT.¹⁶⁰

These studies indicate that apo-MT may take on a bundled structure with the cysteines arranged in such a way to efficiently bind metals, despite the absence of traditional ordered secondary or tertiary structure. The observation that apo-MT has altered structural and metal binding properties under denaturing conditions suggests that the apo-MT structure may not be a random coil. However, no studies to date have attempted to characterize apo-MTs with consideration to the diversity of IDP structures in the proteome.

In this chapter, the apo-MT1a structure and unfolding transitions were characterized in terms of backbone structure and cysteine exposure. MD simulations were performed under native and denaturing conditions to study both the protein dimensions and the cysteine accessible surface area (ASA). Under denaturing conditions, the apo-MT1a behaved as a random coil with solvent-exposed cysteines, while under native conditions it took on a more compact but still fluxional conformation with a mixture of buried and exposed cysteines.

The cysteine exposure was further investigated using cysteine modification in combination with ESI-MS methods. Titrations of NEM under different pH conditions into apo-MT1a and apo-MT3 revealed that the native structure of apo-MT1a had more exposed cysteines

than that of apo-MT3 at pH 7.4. Additionally, at pH 5.0 all of the apo-MT1a cysteines were equally exposed due to unfolding, while apo-MT3 at pH 5.0 had two distinct populations of folded and unfolded protein, indicating a cooperative transition.

Partial cysteine modification and trypsin digestion of apo-MT1a showed that while some segments of the protein were more solvent-exposed than others, a clear distinction was not made, suggesting a collapsed but not rigid structure. The experimentally determined exposed cysteines generally agreed with those determined in the simulations.

The seemingly cooperative unfolding transition seen for apo-MT3 prompted studies into the unfolding transition of apo-MT1a. The unfolding of apo-MT1a was monitored in terms of cysteine exposure using cysteine modification and ESI-MS using pH, temperature, and GdmCl as denaturants. In all cases, the unfolding transitions were found to be cooperative and could be fit to a sigmoidal two-state protein folding model. The inflection points in the unfolding curves which indicate the switch to fully exposed cysteines occurred at approximately pH 5.8, 96 °C (369 K), and 1.7 M GdmCl.

The unfolding transition of apo-MT1a using GdmCl was also characterized using CD spectroscopy, a more traditional method, and found to be cooperative. From these data, the m value and protein stability for GdmCl ΔG_0 were calculated and found to be low but in a similar range to typical proteins. The inflection point of unfolding occurred at 2.3 M GdmCl, which is a higher concentration than for the cysteine exposure measured using ESI-MS. This may indicate that apo-MT1a undergoes a multistep unfolding process where cysteine exposure occurs early on. The conclusion from these data is that apo-MT1a is best described as a molten globule type IDP rather than a random coil and that there is likely a difference in apo-MT structure for different isoforms which may indicate that the apo-MT structure plays a biological role.

3.2 Materials and Methods

3.2.1 Determination of mean hydrophobicity

The intrinsic disorder of apo-MT1a and apo-MT3 were predicted based on the protein mean net charge and mean hydrophobicity.²⁵³ The mean hydrophobicity and mean net charge

were determined using the Swiss Institute of Bioinformatics (SIB) server ExPASy²⁷⁴ using the method detailed in Uversky et al.²⁵³ Briefly, the mean net charge was calculated by dividing the net charge at pH 7.0 by the total number of amino acid residues. The hydrophobicity for each residue in apo-MT1a was calculated using the Kyte and Doolittle approximation with the hydrophobicity of each residue normalized between 0 and 1.²⁷⁵ The mean hydrophobicity was calculated using the sum of all amino acid hydrophobicities and dividing by the total number of residues. The boundary line for intrinsic disorder was calculated using Equation 3-1 and compared to the calculated mean hydrophobicity.

3.2.2 Molecular dynamics simulations

MD simulations were performed using Scigress version 6.0 (Fujitsu, Poland). The sequence of rh β MT1a used in the experimental work was input and the geometry was optimized from the linear sequence using the MM3 procedure. This was also carried out for an apo-MT1a sequence where all of the cysteine residues were mutated to lysines. Additionally, a Cd₇rh β MT1a structure with the connectivity determined by Messerle et al.¹⁴⁶ was modeled and also optimized using the MM3 procedure. The MD (MM3) procedure was then run on the optimized structures using the parameter sets in Table 3-1. MD procedures were performed on both structures using parameter set A (Table 3-1).

Table 3-1. Parameters used for MD simulations.

Parameter	A	B	C
Equilibration period	0.005 ps	0.1 ps	0.1 ps
Temperature	1000 K	1000 K or 300 K	300 K
Duration	5 ps	5000 ps	250 ps
time step: 0.002 ps	0.002 ps	0.002 ps	0.002 ps
Dielectric	78	78	78
output frequency	100 steps	100 steps	100 steps
refresh rate	10 steps	10 steps	10 steps
Van der waals cutoff distance	9 Å	9 Å	9 Å
Van der waals interaction update rate	50	50	50

MD simulations on apo-MT1a beginning from the linear sequence were then run using parameter set B at either 1000 K to mimic denaturing conditions or 300 K to mimic native conditions. An MD simulation on the Cd₇MT1a structure was performed using parameter set C at 300 K.

Following this, the one Cd(II) was removed from the structure and the MD simulation was run using parameter set C again. This procedure was repeated until apo-MT1a was obtained. The resulting structures at each step of the demetallation are shown in Fig. B-1 (Appendix B). An MD simulation was run on the resulting apo-MT1a using parameter set B. The sequence of Cd(II) demetallation was the same as used in Rigby et al.¹⁶⁴ and was determined based on which Cd(II) removed produced the lowest energy structure at each demetallation step. The order of Cd(II) removal was IV, III, II, VI, VII, V, I. The numbering used for the Cd(II) was the same as the original numbers assigned using NMR spectroscopy.²⁷⁶

For each MD simulation that had been run for 5000 ps, the resulting structures were saved every 250 ps. For each of these saved structures, the accessible surface area (ASA) of all atoms was calculated using the Scigress software with a probe radius of 1.4 Å. The ASA over time for each cysteinyl sulfur is shown in Fig. B-2 (Appendix B). PDB files of each structure were exported, and the radius of gyration was calculated using PyMOL. Additionally, the structure of ubiquitin was obtained from the protein data bank²⁷⁷ and its radius of gyration was also measured using PyMOL.

3.2.3 MT1a and MT3 expression and purification

Recombinant human MT1a (rhMT1a) was expressed and purified as described in Chapter 2. The rhMT3 with the sequence MGKAAAAMPD ETCPCPSGGS CTCADSCKCE GCKCTSCKKS CCSCCPAECE KCAKDCVCKG GEAAEAEAEK CSCCQKKAAA A with an N-terminal S-tag was expressed in the same manner as the rhMT1a.

The cells containing expressed MT3 were lysed in the same manner as for MT1a and passed through a filter. Concentrated HCl was used to lower the supernatant to pH 2. This caused precipitation of larger *Escherichia coli* proteins. This mixture was centrifuged for

15 min at 13,000 rpm and the supernatant was filtered and adjusted to pH 7.4 using ammonium hydroxide. The supernatant was passed through a DEAE anion exchange column at a flow rate of 2.5 mL/min. The flow through, which contained the MT3 was collected. The MT3 was concentrated to 20 mL and the S-tag was then cleaved in the same manner as for MT1a. The separation of the S-tag from MT3 was performed by raising the pH of the protein to 8.6 and loading it onto a HiTrap QHP anion exchange column. As the theoretical pI of MT3 is approximately 6.4, the protein will be negatively charged at this pH and will stick to the column. A salt gradient was used to elute the protein from the column, and it was concentrated and stored at -20 °C until ready for experimental analysis.

3.2.4 Apo-MT1a and apo-MT3 preparation

The apo-MT1a (at pH 7.4 and 5.0) and apo-MT3 (at pH 7.4, 5.0, and 2.9) were prepared and the concentrations were measured as described in Chapter 2. For the experiments involving denaturation with GdmCl, a 20 mM Tris-HCl buffer at pH 7.4 was used instead of the 20 mM ammonium formate at pH 7.4.

3.2.5 Proteolysis experiments

NEM was added in 6 molar equivalences to apo-MT1a in 20 mM ammonium formate at pH 7.4. This sample was measured using ESI-MS. Trypsin was added to the sample in a 1:50 w/w ratio. This sample was incubated in a 37 °C water bath for 30 min, then measured using the Bruker MicroTOF II ESI mass spectrometer. The settings used were the same as those described in Chapter 2, with the exception of the hexapole, which was set to 200 V, and the range, which was set between 50 and 3000 m/z. The sample was measured for 2 min and averaged. The resulting spectrum was not deconvoluted.

3.2.6 Titration of cysteine modifier at various pHs

Samples of apo-MT1a (pH 7.4 and 5.0) and apo-MT3 (pH 7.4, 5.0, and 2.9) were diluted to a concentration of 50 µM using 20 mM ammonium formate at the appropriate pH. N-ethylmaleimide (NEM) was titrated from a 10 mM solution into each sample in a stepwise manner. The samples were measured using ESI-MS after each addition using the settings

described in Chapter 2. The samples were each measured for 1 to 2 min, averaged, and deconvoluted between 7000 and 11 000 Da.

3.2.7 pH denaturation experiments

Samples of apo-MT1a in 20 mM ammonium formate at pH 7.4 were diluted into 20 mM ammonium formate at varying pH levels to a final concentration of 50 μ M. The pH was measured and adjusted to the desired level using dilute ammonium hydroxide and formic acid if necessary. NEM was added to 8 molar equivalences to each sample, which was then measured using the Bruker MicroTOF II ESI mass spectrometer using the settings described in Chapter 2. The samples were each measured for 1 to 2 min and averaged. All data were deconvoluted between 7000 and 11 000 Da.

3.2.8 Temperature denaturation experiments

Apo-MT1a in 20 mM ammonium formate at pH 8.3 was diluted to a concentration of 50 μ M using 20 mM ammonium formate at pH 8.3 and split into different samples. These samples were incubated in a water bath under varying temperature conditions for 10 min. Samples over 80 °C were incubated in a custom high temperature bath with the temperature verified by an external thermometer for 2 min. While submerged in the water, 10 molar equivalents of NEM were added to a sample. The sample was incubated for a further minute and then measured using the Bruker MicroTOF II ESI mass spectrometer using the settings described in Chapter 2. The samples were each measured for 1 to 2 min and averaged. All data were deconvoluted between 7000 and 11 000 Da.

The pH of a solution varies with temperature which can interfere with the experiment as the NEM modification profile is pH dependent. Therefore, all temperature experiments were conducted at pH 8.3 to ensure the changes in the modification profile were in fact due to temperature. The modification profile at pH 8.3 and pH 7.4 were verified to be very similar. It was also verified that the pH was no lower than 7.4 at 99 °C, the highest temperature used in the experiment, when the solution at 22 °C was pH 8.3.

3.2.9 GdmCl denaturation experiments

Samples of apo-MT1a in Tris-HCl at pH 7.4 were mixed in varying ratios of Tris-HCl at pH 7.4 (20 mM Tris-HCl for ESI-MS experiments and 5 mM Tris-HCl for CD experiments) and 8 M GdmCl at pH 7.4 to result in solutions with GdmCl concentrations ranging from 0-7 M. The final concentration of the MT ranged from 40-70 μ M for ESI-MS experiments and was 15 μ M for CD experiments. The samples were thoroughly mixed and equilibrated at room temperature for 20 min.

For ESI-MS experiments, NEM was added to each sample to equal 7 molar equivalences. The samples were mixed thoroughly and again equilibrated at room temperature for 20 min. The samples were then buffer exchanged with 20 mM ammonium formate at pH 7.4 using an Amicon centrifugal filter tube with a 3 kDa cut-off five times at 4000 rpm for 30 min each. The purpose of this step was to remove the GdmCl and Tris-HCl prior to ESI-MS analysis, as these compounds are incompatible with the ESI technique. The samples were then measured using the Bruker MicroTOF II ESI mass spectrometer using the settings described in Chapter 2. The samples were each measured for 1 to 2 min and averaged. All data were deconvoluted between 7000 and 11 000 Da.

For CD experiments, each sample of apo-MT1a with no addition of cysteine modifier was measured using a Jasco J-810 spectropolarimeter in a 0.2 cm cuvette. The samples were run between 200 and 310 nm with a data pitch of 1 nm, a response of 2 s, and a band width of 2 nm. Between 1 and 2 accumulations were made. A water baseline was collected and subtracted automatically from each sample by the instrument. A separate sample of only 5 mM Tris-HCl buffer at pH 7.4 was run and was manually subtracted from the samples during data workup. The ellipticity (θ) was measured by the spectropolarimeter in units of mdeg. The relationship $\theta = 32.98(\Delta A)$ was used to convert the units to absorbance.

An additional experiment was conducted to test whether observed changes in signal between samples were due to structural differences in the protein or a signal arising from the absorbance of the added GdmCl alone. 15 μ MT apo-MT in 5 mM Tris-HCl was measured in a 0.2 cm cuvette with a separate 1 cm cuvette behind it. The 1 cm cuvette was

filled with either 5 mM Tris-HCl or 1.4 M GdmCl. 1.4 M GdmCl in a 1 cm cuvette would result in the same absorbance of light as 7 M GdmCl in a 0.2 cm cuvette.

The CD spectra are shown in Fig. C-1 (Appendix C). No change in the apo-MT signal was observed between these two samples, which shows that any change in signal due to mixing apo-MT with GdmCl results from an interaction between the apo-MT and the GdmCl.

3.2.10 Fitting of the unfolding curves

For each denaturation experiment, structural changes in the apo-MT were observed by monitoring changes in ESI mass spectra or CD spectra. These spectral changes were used to quantify the degree of apo-MT unfolding and produce unfolding curves as a function of denaturant.

For the ESI-MS data, the folded status of the MT was determined by taking the peak intensity for each NEM-bound species, finding the fraction of the total for each, and determining the weighted average NEM bound. The deviation from the weighted average for each NEM species was found and this number was multiplied by the fractional contribution of the peak intensity. These numbers were added to find the average deviation from the weighted average NEM bound. For Equations 3-3, 3-4, and 3-5, n is the number of bound NEM, I is the peak intensity extracted from the deconvoluted mass spectrum, and WA is the calculated weighted average NEM bound.

$$I_t = \sum_{n=0}^{20} I_n \quad (3-3)$$

$$WA = n \times \sum_{n=0}^{20} \frac{I_n}{I_t} \quad (3-4)$$

$$\text{Average Deviation from } WA = \sum_{n=0}^{20} \frac{I_n}{I_t} |WA - n| \quad (3-5)$$

A high deviation indicated a more cooperative modification pattern, and thus a more folded MT. All of these data were converted to a fraction unfolded curve using Equation 3-6 where

f_u is the fraction of the protein that is unfolded and where x represents the observed signal, in this case the average deviation from the weighted average. In cases where there was a high deviation between baseline points, the average minimum and maximum values were used.

$$f_u = \frac{(x - x_{max})}{(x_{min} - x_{max})} \quad (3-6)$$

For the CD experiment, the ΔA values at 222 nm were extracted from the spectrum at each point in the titration as this wavelength has been previously used to measure structural changes in intrinsically disordered proteins.²³⁰ Equation 3-6 was used to convert the signal at 222 nm into a fraction unfolded curve.

The calculated fraction unfolded curves were fit using Origin Pro 8.5 to a two-state sigmoidal curve. The data from the pH experiments were fit using Equation 3-7, a Boltzmann fitting equation where A_1 is the maximum signal, A_2 is the minimum signal, x_0 is the point where $y = 0.5$, and dx is $x_{max} - x_{min}$.

$$y = \frac{(A_1 - A_2)}{(1 + e^{\frac{(x-x_0)}{dx}})} + A_2 \quad (3-7)$$

For the GdmCl denaturation experiments, Equations 3-8 through 3-11 were used in the fitting parameters to find the protein stability, ΔG_0 , and the m-value for GdmCl using the linear extrapolation method.²⁷⁸⁻²⁷⁹ The errors were the standard errors on the fit and, for the CD experiment, were used to find the boundary lines $\Delta G = \Delta G_{0max} - m_{min}[\text{GdmCl}]$ and $\Delta G = \Delta G_{0min} - m_{max}[\text{GdmCl}]$.

$$K = \frac{[U]}{[N]} \quad (3-8)$$

$$K = \frac{e^{\left(\frac{-\Delta G}{RT}\right)}}{1 + e^{\left(\frac{-\Delta G}{RT}\right)}} \quad (3-9)$$

$$\Delta G = -RT \ln K \quad (3-10)$$

$$\Delta G = \Delta G_0 - m[GdmCl] \quad (3-11)$$

For the temperature denaturation experiments, the thermodynamic parameters enthalpy (ΔH) and entropy (ΔS) can be found experimentally from the unfolding curve.²⁸⁰ However, these parameters are dependent on the heat capacity of the protein. As the heat capacity of apo-MT has not been measured only Equations 3-8 and 3-9 were used for the fitting, and ΔH and ΔS were not calculated. Additionally for these experiments, as the protein unfolding took place near 99 °C, no post-transition baseline was observed. To aid in visualization of the unfolding curve, theoretical points at 102 °C (375 K), 117 °C (390 K), and 127 °C (400 K) showing the maximum degree of unfolding were added to obtain a fit in addition to that obtained using only experimental points.

3.3 Results and Discussion

3.3.1 Apo-MT1a and apo-MT3 sequences predict ordered structures

Using Equation 3-1, MT's mean hydrophobicity relative to its mean net charge can be evaluated and compared to other IDPs.²⁵³ MT1a's calculated mean hydrophobicity based on the sequence is 0.50. Based on MT1a's mean net charge of +0.11, a mean hydrophobicity lower than 0.45 would indicate likely disorder. As MT1a has a mean hydrophobicity above this value, it is less likely to be a highly disordered protein.

Likewise, MT3 has a mean hydrophobicity of 0.47 and a mean net charge of +0.01, the latter of which is much lower than for MT1a. For this net charge, MT3 would require a mean hydrophobicity of lower than 0.42 to be considered likely disordered using this method. Based on these results, MT3 is predicted to be more ordered than MT1.

Mammalian MTs are rich in both cysteine and lysine. Cysteine is considered an order-promoting residue, while lysine is considered a disorder-promoting residue.²¹ Mutation of all of the cysteine residues in apo-MT1a to lysine residues result in a raised mean net charge of +0.37 and a lowered mean hydrophobicity of 0.30. This mean hydrophobicity is below the boundary line of 0.55 and thus predicts a random coil structure for this sequence.²⁵³

This mutated sequence provides an example of such a protein equal in size to MT which would theoretically adopt a random coil structure.

3.3.2 MD simulations of apo-MT1a reveal a compact structure

MD simulations were performed on apo-MT1a to probe the compactness of the structure and the cysteine exposure under native and denaturing conditions. Apo-MT1a adopts an ensemble of compact conformations with both buried and exposed cysteines at 300 K (Fig. 3-2 A-B). This compact but fluxional structure is seen whether the calculation was run beginning from a sequentially demetallated Cd₇MT structure as in Rigby et al.¹⁶⁴ (Fig. 3-2A) or by beginning with a linear sequence (Fig. 3-2B).

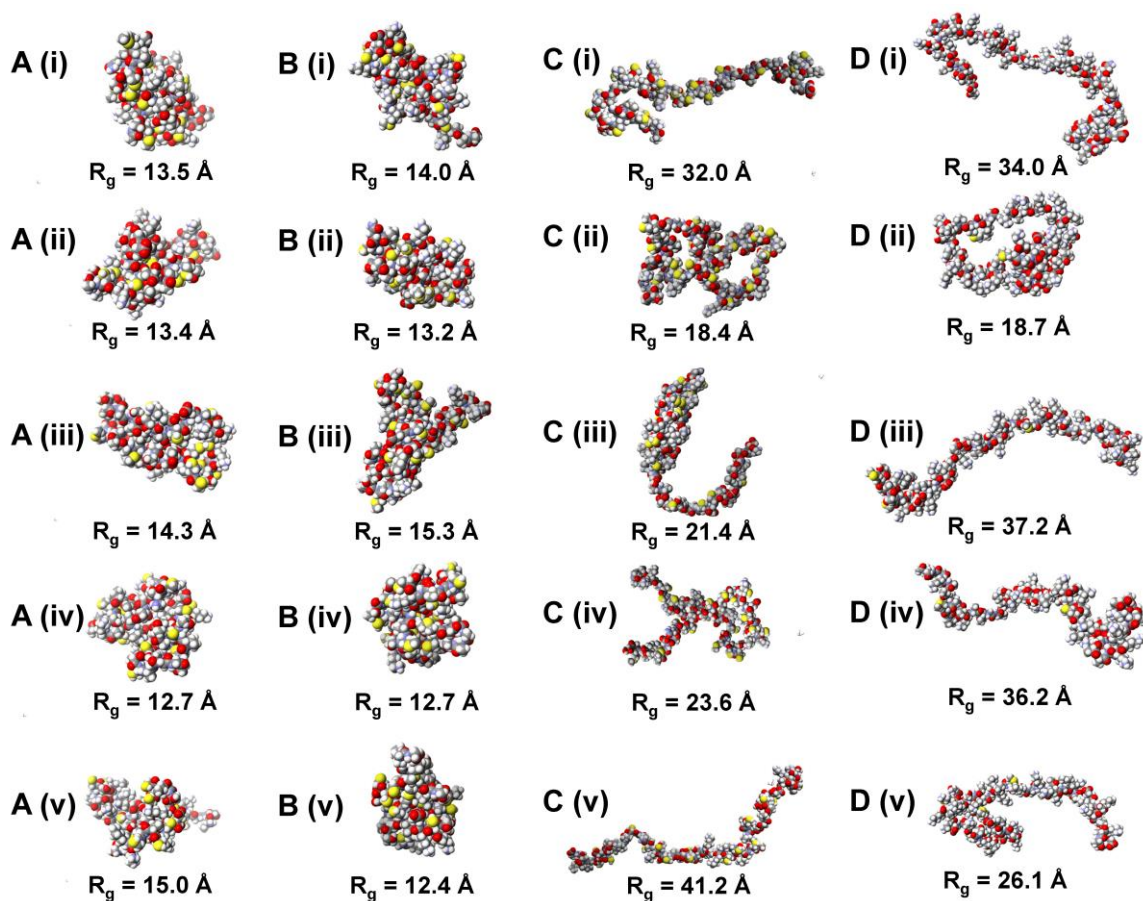


Figure 3-2. MD simulations of apo-MT. MD simulations of apo-MT represented by space-filling models at (A) 300 K after sequential demetallation, (B) 300 K beginning from a linear sequence, (C) 1000 K beginning from a linear sequence, and (D) 300 K where all cysteine residues in the sequence were replaced by lysine residues shown at time points of (i) 1000 ps (ii) 2000 ps, (iii) 3000 ps, (iv) 4000 ps, and (v) 5000 ps. The radius of gyration is shown under its respective structure.

This contrasts the previous results which found apo-MT1a displayed random coil behaviour when beginning from a linear sequence.¹⁶⁴ Under denaturing conditions, modelled by using a temperature of 1000 K, apo-MT1a takes on a structure similar to that of a random coil, with a variety of loosely compact and extended structures seen throughout the duration of the simulation. The sequence where all cysteines have been mutated to lysines run at 300 K produces very similar structures than those seen for the non-mutated sequence at 1000 K. The higher mean net charge and lower abundance of hydrophobic residues appears to prevent the collapse into a compact conformation even at non-denaturing temperatures. This suggests that the native apo-MT1a sequence promotes the collapse into a bundled structure, more so than the mutated sequence with a high net charge as predicted by Equation 3-1.

The radius of gyration (R_g) over time, calculated from the simulated structures is plotted in Fig. 3-3 for each condition. The average R_g for apo-MT1a at 300 K is 14 Å and the average R_g for apo-MT1a at 1000 K is 26 Å. The average R_g for apo-MT1a with the cysteines replaced by lysines is 30 Å. The R_g for the latter two conditions are much more variable than the others due to the greater heterogeneity of structures.

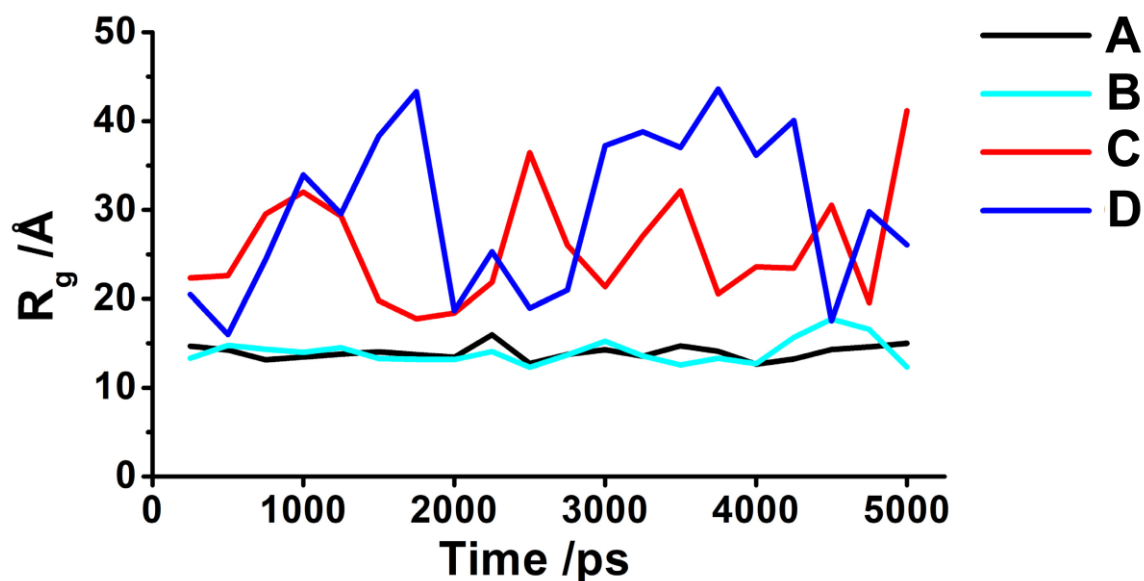


Figure 3-3. Radius of gyration for apo-MT MD simulations over time. The calculated radius of gyration over time for apo-MT at (A) 300 K after sequential demetallation, (B) 300 K beginning from a linear sequence, (C) 1000 K beginning from a linear sequence, and (D) 300 K where all cysteine residues in the sequence were replaced by lysine residues. The average R_g values are (A) 14.0 ± 0.8 Å, (B) 14 ± 1 Å, (C) 26 ± 6 Å, and (D) 30 ± 9 Å.

Analysis of the R_g further suggests that the denatured apo-MT1a is a random coil, while the native apo-MT1a is not. Using the linear relationship determined by Kohn et al. (Equation 3-2)²⁶³ the predicted R_g for a random coil of length 76 amino acids (the length of rhMT1a) would be 26.55 Å. This is near the average value obtained from the MD simulations for the denatured apo-MT1a at 1000 K.

Ubiquitin is a protein with a traditional ordered native structure that has the same number of amino acids as rhMT1a and a denatured R_g of 25.2 Å, similar to the simulated value obtained from MT.²⁶³ Additionally, the R_g of the native ubiquitin structure²⁷⁷ measured using PyMOL is 12.15 Å which is near the value obtained from apo-MT1a at 300 K. This suggests that the dimensions of apo-MT1a determined through MD simulations are only slightly larger than those expected of a natively folded protein rather than a random coil IDP. Additionally, the apo-MT1a with cysteines mutated to lysine formed structures similar to those of a random coil even at 300 K, further suggesting that the sequence of MT1a influences the formation of compact structures.

3.3.3 MD simulations indicate both buried and exposed cysteines in the apo-MT1a native structure

The cysteine exposure of the MT under different conditions was also analyzed (Fig. 3-4). Even in the apo-MT1a structures simulated at 300 K, the exposure of each cysteine residue was rather fluxional despite the compact structure, with many having a range from 0 to approximately 80 Å² (Fig. 3-4A). This was likely due to the overall fluxionality of the protein. Even while maintaining the compact structure, small expansions and contractions took place over the simulation, leading to changes in amino acid exposure. To avoid outliers due to occasional expansions of the protein, the median cysteinyl sulfur ASA was reported rather than the mean to investigate whether certain cysteines preferred the interior or exterior of the protein (Fig. 3-4A). The overall median cysteinyl sulfur exposure for the apo-MT1a structures at 300 K was between 20 and 30 Å², while this number was near 50 Å² for the 1000 K structures. This is consistent with the overall structure of the protein, with a more open and fluxional structure producing more exposed cysteines.

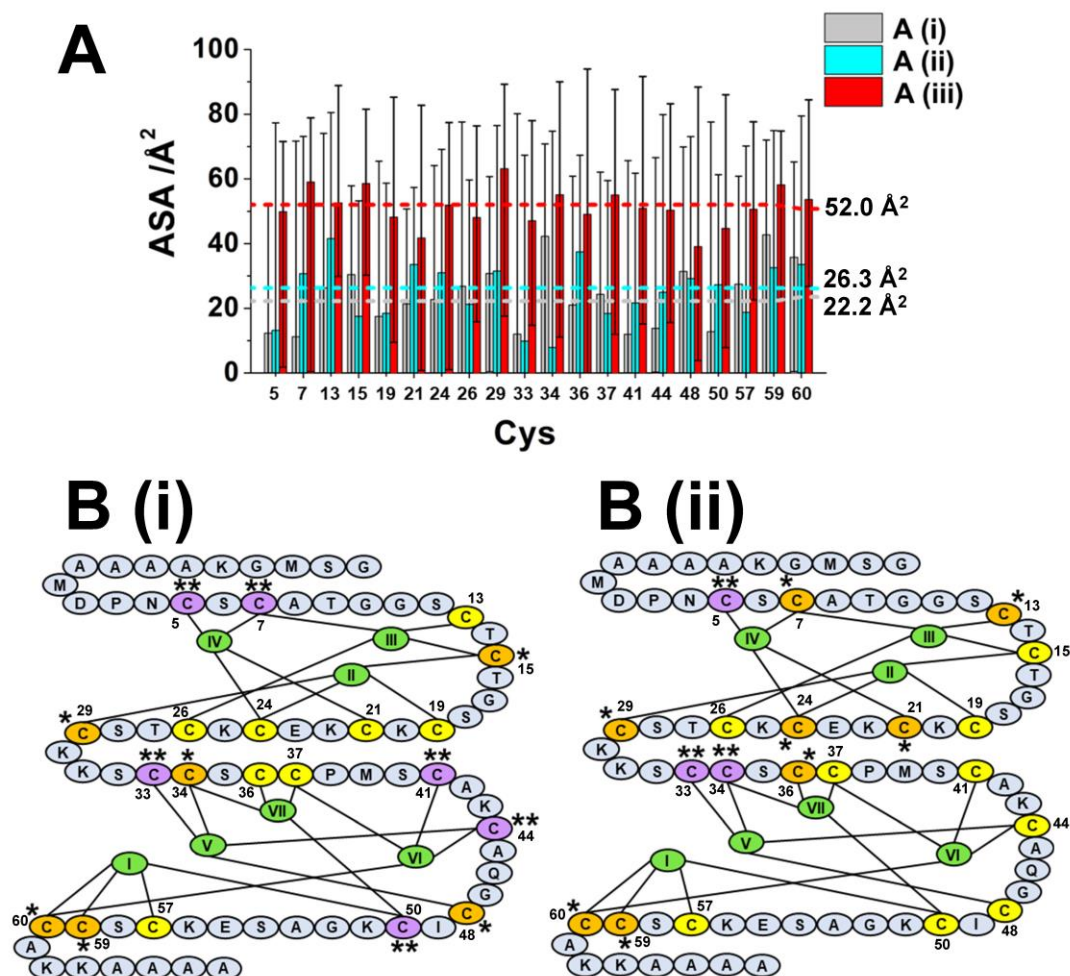


Figure 3-4. The median cysteine ASA based on MD simulations. (A) The median ASA for individual cysteinyl sulfurs calculated from MD simulations of apo-MT1a at (i) 300 K after sequential demetallation, (ii) 300 K beginning from a linear sequence, and (iii) 1000 K beginning from a linear sequence. The dotted lines indicate the median exposure of all cysteinyl sulfurs in the protein which are (i) 22.2 \AA^2 , (ii) 26.3 \AA^2 , and (iii) 52.0 \AA^2 . The error bars extend from the lowest observed ASA to the highest observed ASA for each cysteinyl sulfur. (B) The sequence of apo-MT1a showing the divalent metal connectivity and highlighting more exposed vs more buried cysteines for (i) 300 K after sequential demetallation and (ii) 300 K beginning from a linear sequence. Orange cysteines labeled with (*) indicate a median ASA of greater than 30 \AA^2 . Purple cysteines labeled with (**) indicate a median ASA of less than 15 \AA^2 .

Fig 3-4B summarizes the cysteinyl sulfur exposure of the “native” apo-MT1a structures at 300 K, showing the most exposed and the least exposed cysteines. The connectivity of the metals is also shown. In the apo-MT1a structure, which was demetallated from Cd₇MT (Fig. 3-4Bi), the most exposed cysteines are Cys 15, 29, 34, 48, 59, and 60. The most buried cysteines are Cys 5, 7, 33, 41, 44, and 50. Based off of the energy minimized structures from Rigby et al., Cd(II) I in the α -domain may be the first metal to bind. Two of the cysteines that bind this metal, Cys 59 and Cys 60 are exposed. In this model, Cd(II) VI, which is the last metal in the α -domain to bind, is connected to two cysteines, Cys 41 and Cys 44, which are buried in the apo-MT. Similarly in the β -domain, Cd(II) II is bound to the more exposed Cys 15 and Cys 29 and Cd(II) IV is bound to the more buried Cys 5 and Cys 7. This supports the idea that the apo-MT structure may be optimized to bind metals, with the metals binding initially to more exposed cysteines.

Analysis of the apo-MT1a beginning from a linear sequence at 300 K, without the bias of the fully metallate structure, reveals more exposed cysteines than buried cysteines (Fig. 3-4Bii). Cys 7, 13, 21, 24, 29, 36, 59, and 60 are more exposed. Cys 5, 33, and 34 are more buried. The exposure of Cys 59 and Cys 60 are consistent with the demetallated apo-MT1a. However, Cd(II) IV in the β -domain now binds to 1 buried cysteine and 3 exposed cysteines.

3.3.4 Cysteine modification and trypsin digestion experimentally monitor cysteine exposure in apo-MT1a

The MD simulations show that the cysteine residues in apo-MTs under native conditions are unequally exposed due to the collapsed structure of the protein. An experimental method for monitoring cysteine exposure is cysteine modification in combination with ESI-MS. In theory, an unfolded protein will have more equally exposed cysteines, which will be equally likely to be modified, and thus will exhibit a modification profile shaped like a Binomial distribution. Conversely, a protein with entirely buried cysteines will exhibit a cooperative modification profile as each bound NEM opens up the protein and triggers the binding of the subsequent NEM.

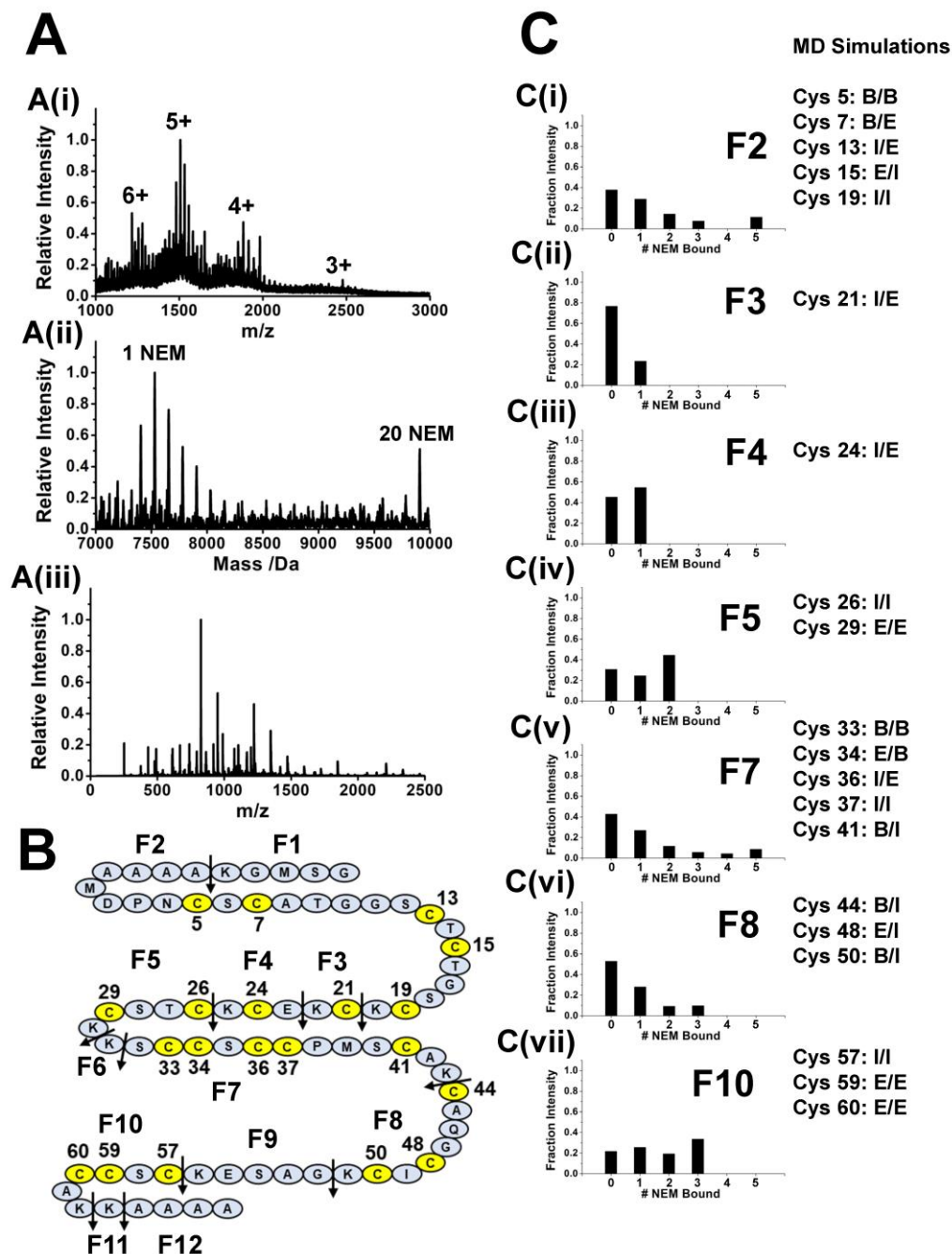


Figure 3-5. Apo-MT1a partially modified with NEM at pH 7.4 and digested by trypsin. (Ai) Charge state and (Aii) deconvoluted ESI mass spectra of MT1a with 6 mol. eq. NEM added. Note these spectra are the same as those from Fig. 3-2A and are shown here again for clarity. (Aiii) A mass spectrum of MT1a with 6 mol. eq. NEM added and then digested with trypsin (1:50 w/w) for 30 min. at 37 °C. (B) The sequence of apo-MT1a showing the trypsin cut sites (black arrows). (C) Bar graph representations of the data from (Aiii) showing the distribution of NEM modification within fragment (i) 2, (ii) 3, (iii) 4, (iv) 5, (v) 7, (vi) 8, and (vii) 10 of the MT1a. Next to each graph are the results from the MD simulations (demetallated/linear) showing the exposure of the cysteinyl sulfurs where B = buried, I = intermediate, and E = exposed.

The modification profile of apo-MT1a after the addition of 6 mol. eq. NEM results in a distribution from approximately apo-MT1a(NEM)₀₋₆ as well as cooperative formation of apo-MT1a(NEM)₂₀ (Fig. 3-5Ai-ii). It is hypothesized that the observed 0-6 modifications took place on exposed cysteines as the overall structure was not disturbed. After digestion of the apo-MT1a using trypsin (Fig. 3-5Aiii), the relative intensities of the modifications were normalized within each fragment and plotted in bar graphs for clarity (Fig. 3-5B). It is important to note that the peak intensities can only be meaningfully compared within the same fragment, as the large differences in peptide lengths lead to different ionization efficiencies in the ESI source.

Fig. 3-5C shows the representation of the modification distributions found within each fragment. It is important to note that due to the semi-cooperative nature of the modification profile, each fragment will have a portion where all of the available cysteines are modified regardless of the exposure of these cysteines. Additionally, it is important to note that due to the fluxional nature of the protein, a description of a cysteine or fragment to be more “exposed” or “buried” describes the behaviour on average compared to other cysteines or fragments. A proportionally higher number of cysteines modified indicates a generally more exposed fragment, while less modifications suggest a more buried fragment.

Fragment F2 contains 5 cysteines (Cys 5, 7, 13, 15, and 19). According to the MD simulations this fragment should contain a mixture of buried and exposed cysteines. The experimental data suggests that only one cysteine is easily modified in this fragment. Additionally, this fragment never displays four modifications at one time, potentially indicating two highly buried cysteines that only become modified once all 20 cysteines have bound NEM.

Fragment F3, which only contains Cys 21, appears to be quite buried with a very low abundance of modifications observed. However, this was not seen in the MD simulations, which predict either an intermediately exposed cysteine from the demetallated protein, or an exposed cysteine when beginning with the linear protein. For fragment F4 (Cys 21), MD simulations predict an intermediate (from the demetallated apo-MT1a) or exposed (from the linear apo-MT1a) Cys 24, while the experimental results predict an exposed

cysteine. Experimentally, the fragment F5 (Cys 26 and 29) modification profile indicates that both of these cysteines are exposed. MD simulations predict one intermediate and one exposed cysteine.

Fragment F7, like fragment F2, appears to contain a mixture of buried and exposed cysteines. The MD simulations also show that these cysteines (Cys 33, 34, 36, 37, and 41) are a mixture of two buried, one exposed, and two intermediate. Fragment F8 also experimentally shows more buried cysteines. The MD simulations for the demetallated protein agree with these results showing two buried and one exposed cysteine for those in this fragment (Cys 44, 48, and 50). The MD simulations beginning from the linear protein, however, suggests that these cysteines are intermediately exposed.

Finally, fragment F10 appears to be a more exposed fragment, with a similar modification abundance for each cysteine. The MD simulations agree with this, where Cys 57 is intermediately exposed and Cys 59 and 60 are exposed.

These results show that overall, the experimentally determined cysteine exposure is generally in agreement with the simulated data, with few results that deviate strongly between the two experiments. Future tandem MS studies will be required to see if individual cysteines agree with the simulated data.

3.3.5 Apo-MT1a and apo-MT3 exhibit different pH-dependent structures

The native structure of apo-MT1a involves more exposed cysteines than the native structure of apo-MT3. The titration of NEM in to apo-MT1a at pH 7.4 (Fig. 3-6) shows two distinct patterns. A Binomial-type distribution is seen ranging from 0-6 modifications (Fig. 3-6B-D). A cooperative modification pattern where apo-MT1a binds all 20 NEM with minimal intermediate species also occurs as more NEM is added (Fig. 3-6B-D).

Regardless of the mol. eq. NEM added, the distribution of lower modified species always remains centered around approximately 4 modifications. At 10 mol. eq. added, a higher proportion of intermediate species is seen, however the intensity remains low compared to the distribution and the cooperative formation of 20 (Fig. 3-6D).

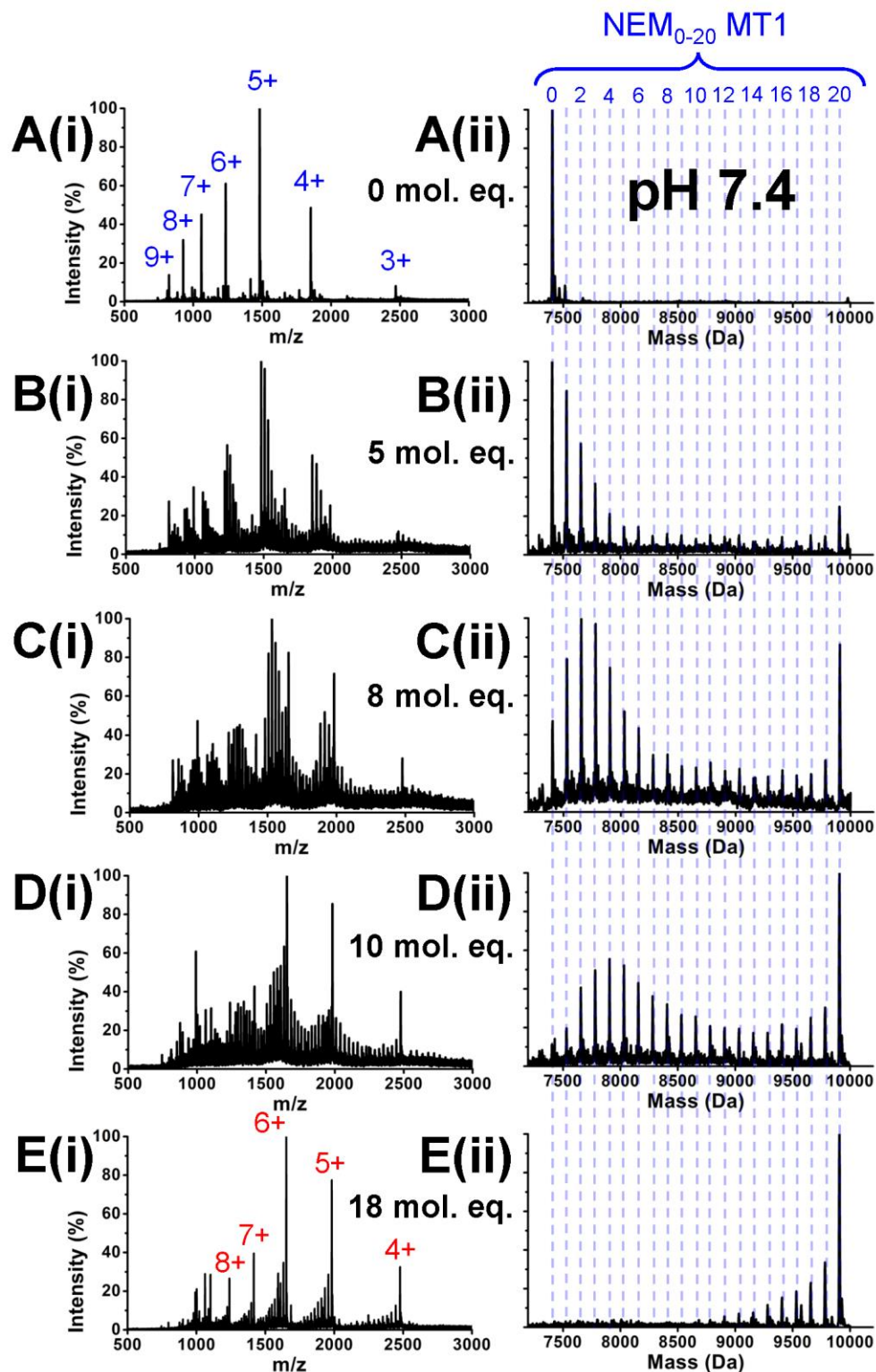


Figure 3-6. NEM titration into apo-MT1a at pH 7.4 monitored by ESI-MS. (i) Charge state and (ii) deconvoluted ESI mass spectra showing a titration of NEM into apo-MT1a at pH 7.4 at (A) 0, (B) 5, (C) 8, (D) 10, and (E) 18 mol. eq. NEM added. Figure adapted from Yuan et al., 2023 with permission.

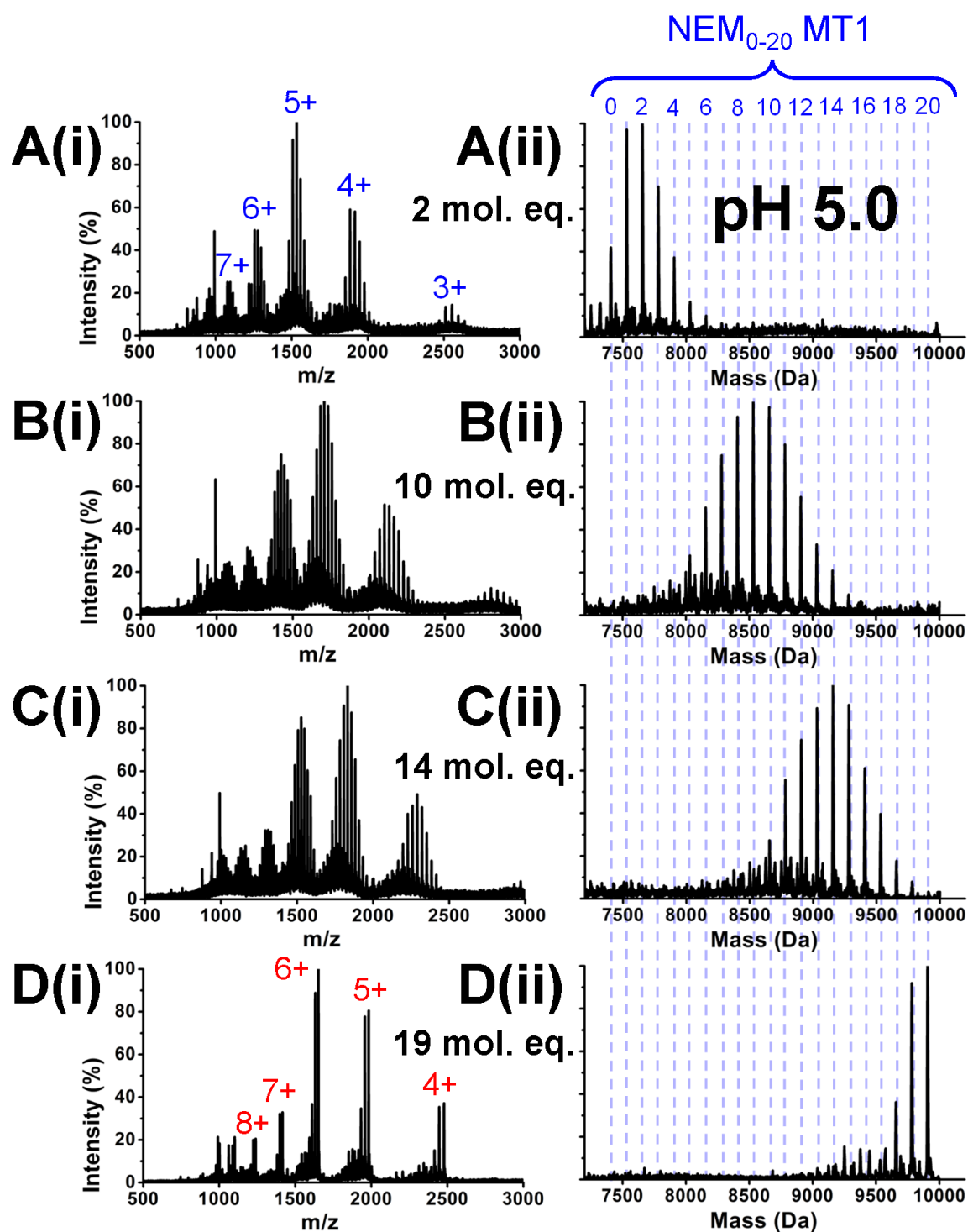


Figure 3-7. NEM titration into apo-MT1a at pH 5.0 monitored by ESI-MS.(i) Charge state and (ii) deconvoluted ESI mass spectra showing a titration of NEM into apo-MT1a at pH 5.0 at (A) 2, (B) 10, (C) 14, and (D) 19 mol. eq. NEM added. Figure adapted from Yuan et al., 2023 with permission.

The consistency in the shape of the modification pattern implies that there is consistency in the apo-MT1a structure. It is likely that at any time, approximately 6 of the cysteines are equally solvent exposed on the surface of the protein, allowing the distribution from 0-6 modifications to form. Binding more than this amount appears to trigger the apo-MT1a to open up and cooperatively bind all 20 cysteines.

Conversely, it is seen at pH 5.0 that the NEM binds entirely in a Binomial-type distribution (Fig. 3-7). The NEM binds in a distribution centered around the mol. eq. added, unlike at pH 7.4 where the distribution only occurred up to 6 modifications. This binding pathway implies that all cysteines are equally solvent exposed.

A titration of NEM into apo-MT3 at pH 7.4 shows that there are little to no exposed cysteines on the surface of the protein (Fig. 3-8). At any point in the titration, only apo-MT3 and apo-MT3(NEM)₂₀ species exist, with minimal abundance in the apo-MT3(NEM)₁₋₄ species seen in Fig. 3-8B-C. The implication is that after 1 NEM binds, this triggers the opening of the protein, exposing more cysteines to bind leading to a cooperative modification pathway. This shows that the native structure of apo-MT3 is very different from that of apo-MT1a. Apo-MT1a has approximately 6 cysteines exposed on the surface at one time, while apo-MT3 has no exposed cysteines on the surface.

In addition, the cysteines of apo-MT3 are only partially exposed at pH 5.0 (Fig. 3-9). A mixture of cooperative and non-cooperative modification pathways is seen in the mass spectra. The non-cooperative distribution shifts to the right as more species are added, suggesting that there is a population of apo-MT3 that is completely unfolded allowing this pathway and another folded population allowing the 20 to form. This is contrasted with the apo-MT1a at pH 7.4 where the non-cooperative distribution stays centered around 4 modifications, indicating it is all part of one structure. Apo-MT3 only exhibits the fully non-cooperative pathway at pH 2.9 (Fig. 3-10).

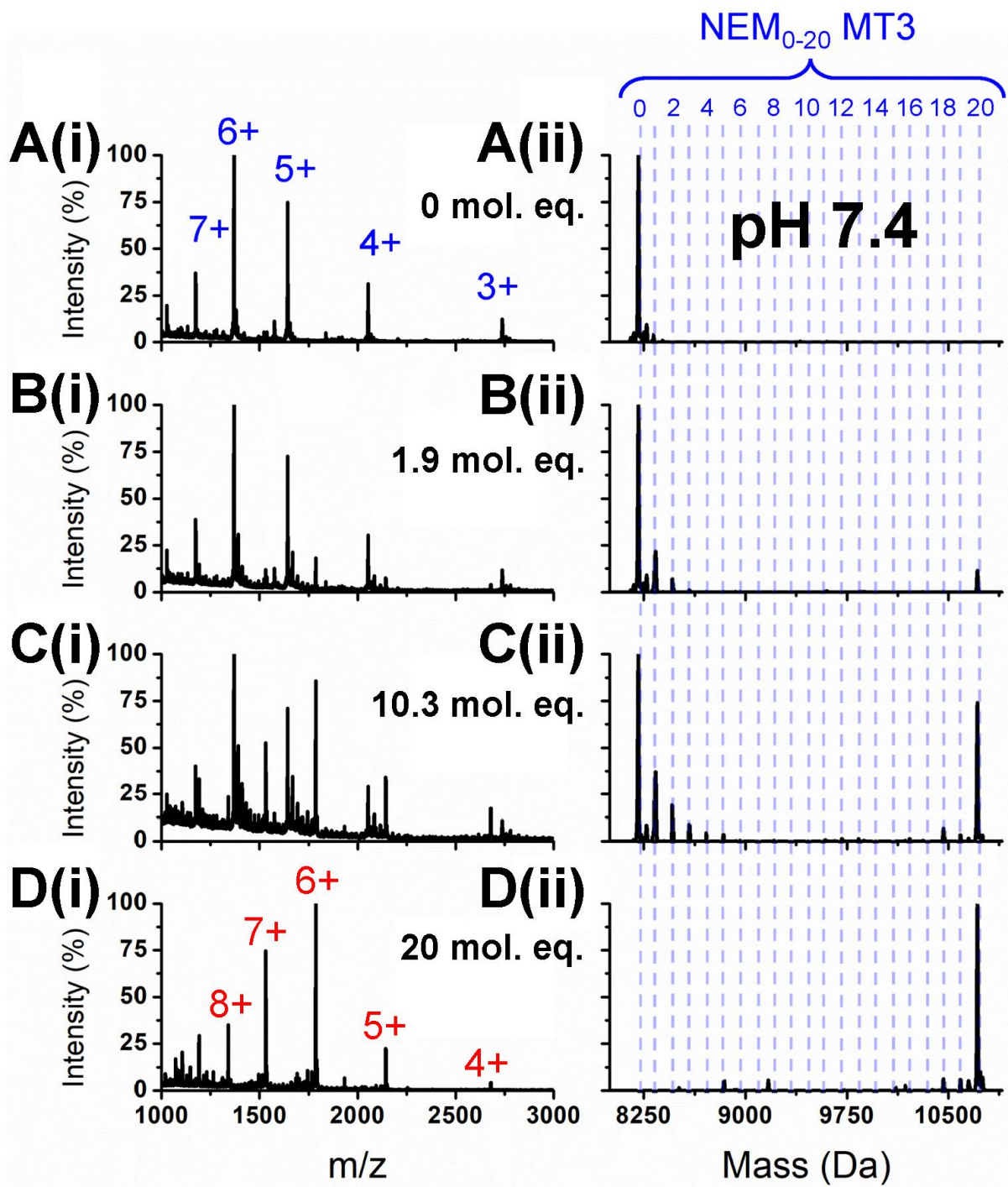


Figure 3-8. NEM titration into apo-MT3 at pH 7.4 monitored by ESI-MS.(i) Charge state and (ii) deconvoluted ESI mass spectra showing a titration of NEM into apo-MT3 at pH 7.4 at (A) 0, (B) 1.9, (C) 10.3, and (D) 20 mol. eq. NEM added. Figure adapted from Yuan et al., 2023 with permission.

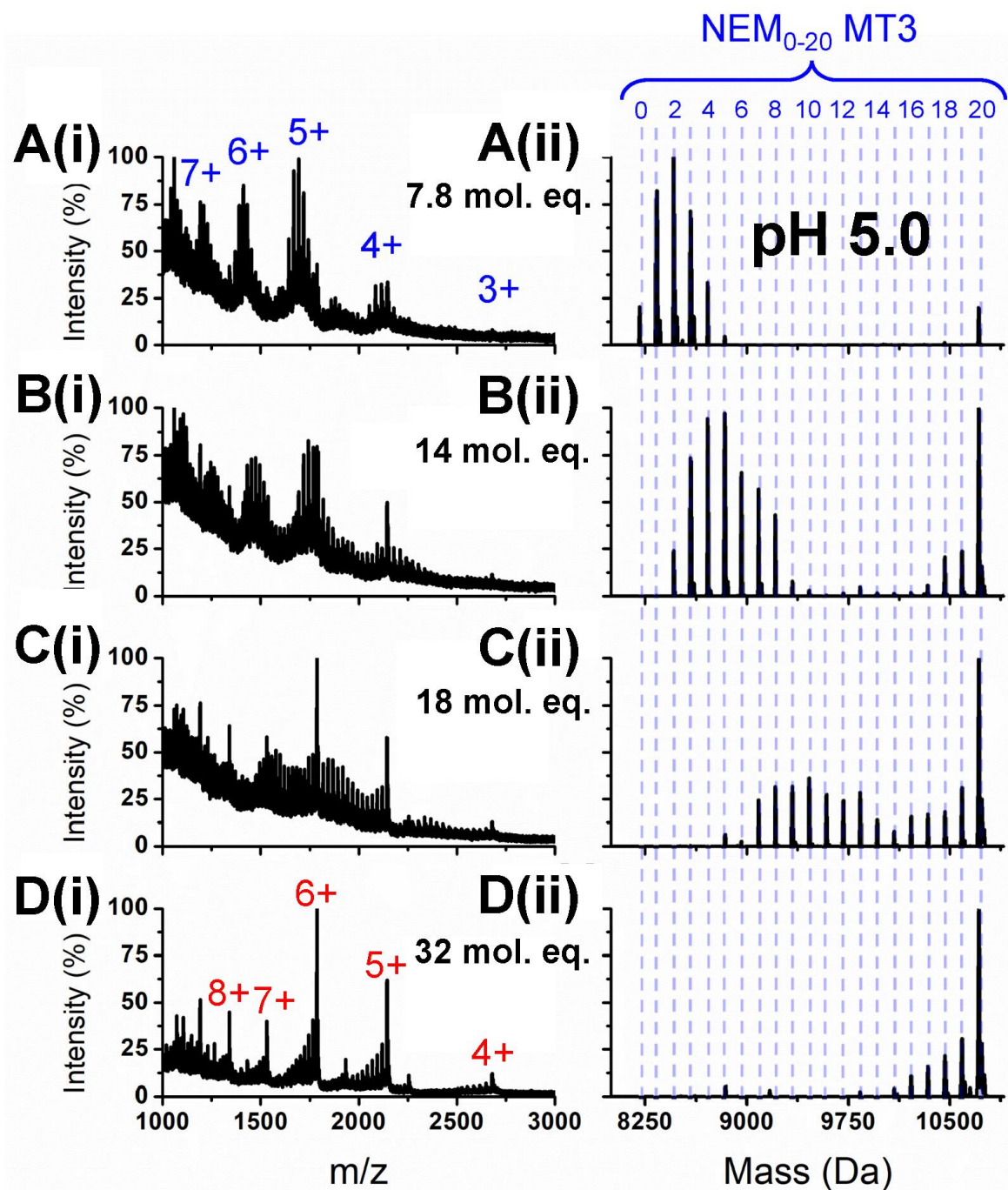


Figure 3-9. NEM titration into apo-MT3 at pH 5.0 monitored by ESI-MS.(i) Charge state and (ii) deconvoluted ESI mass spectra showing a titration of NEM into apo-MT3 at pH 5.0 at (A) 7.8, (B) 14, (C) 18, and (D) 32 mol. eq. NEM added. Figure adapted from Yuan et al., 2023 with permission.

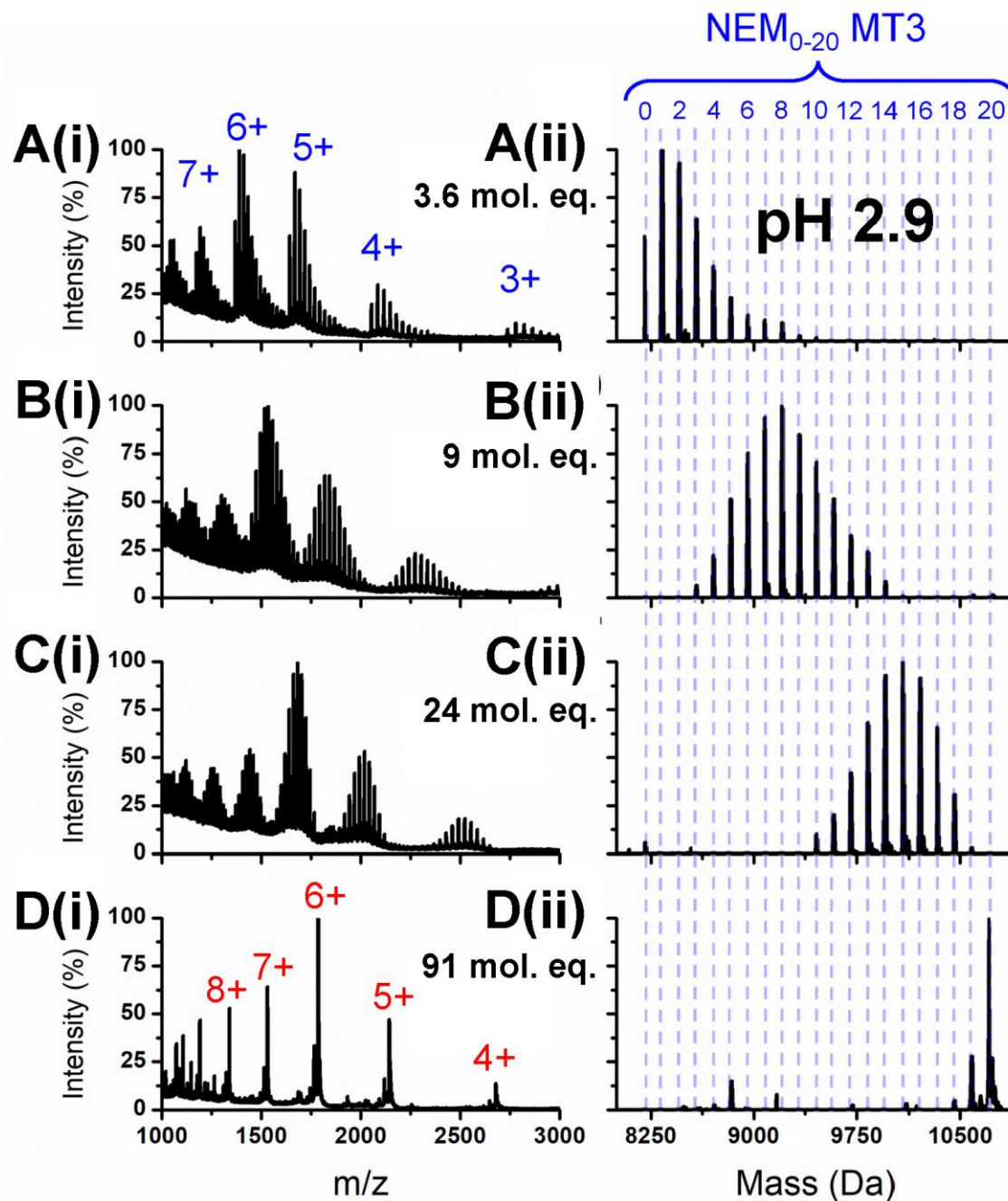


Figure 3-10. NEM titration into apo-MT3 at pH 2.9 monitored by ESI-MS. (i) Charge state and (ii) deconvoluted ESI mass spectra showing a titration of NEM into apo-MT3 at pH 2.9 at (A) 3.6, (B) 9, (C) 24, and (D) 91 mol. eq. NEM added. Figure adapted from Yuan et al., 2023 with permission.

3.3.6 The cooperative pH-dependent unfolding transition of apo-MT1a monitored using ESI-MS

The observation of a cooperative unfolding transition in apo-MT3 prompted study into the unfolding transitions of apo-MT1a. The pH-induced unfolding of apo-MT1a monitored using cysteine modification and ESI-MS is shown in Fig. 3-11. Apo-MT1a at pH 7.4 has the typical modification pattern of the native structure (Fig. 3-11A). Lowering the pH to 6.49, a change in the modification pattern can be seen (Fig. 3-11B). The semi-cooperative modification pattern to 20 still occurs, however the earlier distribution shifts from centering around 3 modifications to 8 modifications.

This is similar to apo-MT3 at pH 5.0, where two populations are observed. Since 8 mol. eq. NEM were added, this suggests that a population of the apo-MT1a has all of its cysteines equally available for binding and another population does not, leading to 20 modifications. At pH 6.09 the distribution is still centered around 8 modifications but also has a lower abundance of apo-MT1a(NEM)₂₀ (Fig. 3-11C). Below pH 5.84, the cysteines of apo-MT1a are fully exposed (Fig. 3-11D-E).

An unfolding curve, which was generated using Equations 3-3 through 3-6 based on the ESI-MS data and fit using Equation 3-7 is shown in Fig. 3-12 and shows a cooperative structural transition involving altered cysteine exposure. The curve fit indicates that the midpoint of this transition occurs at pH 5.8. This means that apo-MT1a is slightly less pH-stable in terms of structure compared to a protein like myoglobin, in which unfolding intermediates are observed near pH 4.²⁸¹

Apo-MT1a undergoing structural changes at different pH levels could indicate some sort of biological role. Lysosomes for example can have pH levels in the 4.5-5.0 region.²⁸² This means that lysosomal apo-MT1a may adopt different structures and thus potentially different functions than cytosolic apo-MT1a, which would be under more neutral pH conditions.

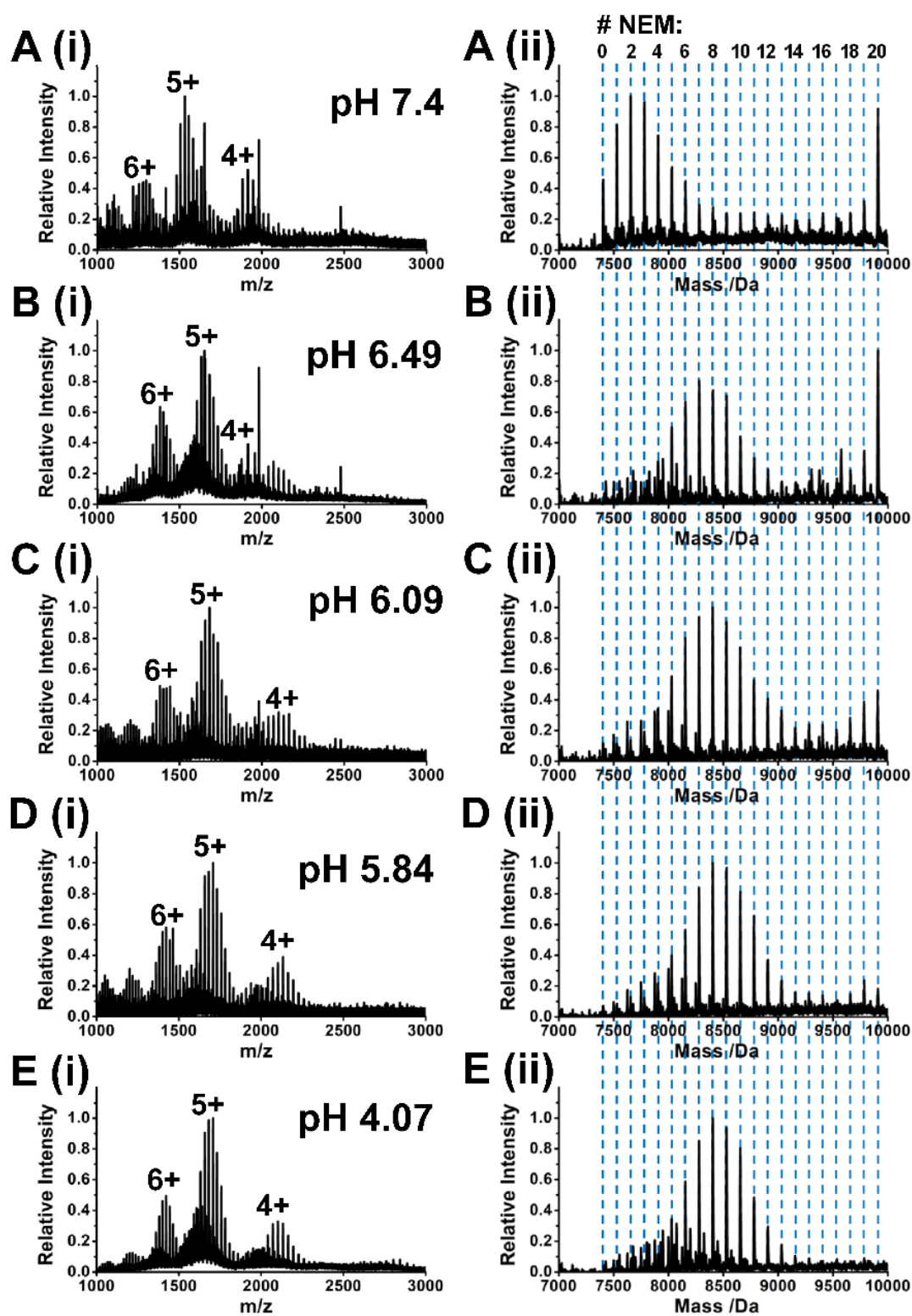


Figure 3-11. Effect of pH on apo-MT1a cysteine modification pattern monitored by ESI-MS. (i) Charge state and (ii) deconvoluted ESI mass spectra of apo-MT1a with 8 mol. eq. NEM added at pH (A) 8.2, (B) 6.49, (C) 6.09, (D) 5.84, and (E) 4.07.

As well, diseases can change the pH environment, such as cancer cells which can have pHs of 6.0 to 6.8.²⁸³ MTs are thought to be involved in tumor progression and drug resistance,²⁸⁴ which means that they may play altered roles compared to MTs in healthy cells due to a structural difference. Apo-MT1a also binds metals in a highly pH-dependent manner,¹⁷¹⁻¹⁷² which also potentially has implications on this function.

Additionally, these results have also shown that the apo-MT3 structures are more stable to harsh pH conditions than apo-MT1a. Unlike MT1 and MT2, MT3 is not induced by metals and its activity may be more due to its sequence differences rather than the metal-binding properties.²⁶⁶ It has been proposed MT3's growth inhibitory activity involves multiple protein-protein interactions.²⁸⁵⁻²⁸⁶ It is possible that the different structures of apo-MT1a and apo-MT3 play roles in their unique biological processes.

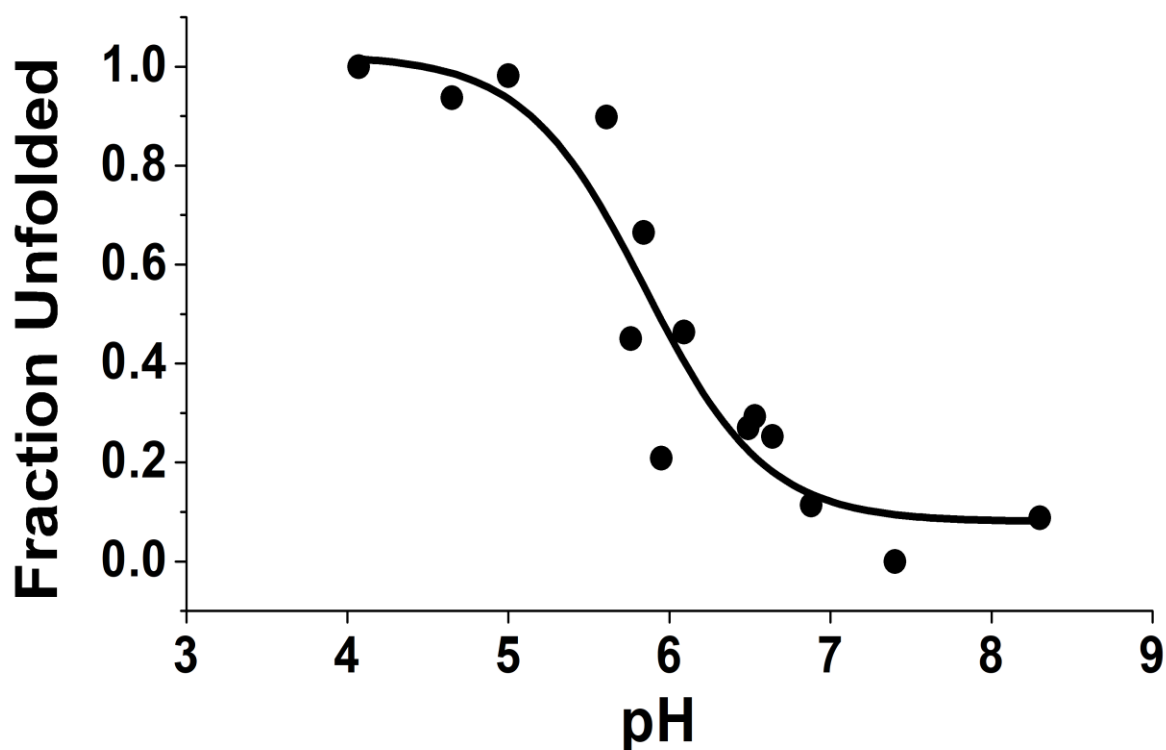


Figure 3-12. Fraction unfolded apo-MT1a vs pH monitored by ESI-MS. The fraction of unfolded apo-MT1a as a function of pH monitored by the NEM distribution in the ESI mass spectra (points) with a sigmoidal fit (line). The pH at the point of 50 % denaturation is 5.8.

3.3.7 The cooperative temperature-dependent unfolding transition of apo-MT1a monitored using ESI-MS

MT is highly thermally stable, and the complete exposure of cysteine residues only occurs by 99 °C. ESI-MS data showing partial cysteine modification with NEM are shown in Fig. 3-13. The expected semi-cooperative distribution is seen in Fig. 3-13A at 22 °C. It is interesting to note that at 45 °C, there is a higher proportion of 18 and 19 modified cysteines compared to at 22 °C where modification to that extent always reaches 20 (Fig. 3-13B). This effect is gradually exacerbated as the temperature is raised. The apo-MT1a with 17-20 modified cysteines change from greatly favouring 20 modifications to forming their own small distribution separate from the lower modified species with 0-6 modified cysteines (Fig. 3-13C-E). This effect appears to be unique to temperature denaturation.

At 97 °C, there are no longer any apo-MT1a molecules with 0 or 1 modifications which is also not typical of the native modification pattern (Fig. 3-13E). At 99 °C the Binomial-type distribution formed, indicating complete cysteine exposure (Fig. 3-13F.)

Fig. 3-14 shows the unfolding curve for the ESI-MS data in Fig. 3-13. A sharp unfolding curve is seen with an inflection point at 369 K or 96 °C, indicating the majority of the structure transition is cooperative. An experimental post-transition baseline is not seen as data above 99 °C was not possible to obtain. A gradual sloping pre-transition baseline is seen which likely corresponds to the change in distribution at the higher modified species seen in the ESI mass spectra.

3.3.8 The cooperative GdmCl-dependent unfolding transition of apo-MT1a monitored using ESI-MS

Partial cysteine modification of apo-MT1a under varying levels of the denaturant GdmCl shows that the cysteines are exposed at 2 M GdmCl (Fig. 3-15). Between 0 and 1.75 M denaturant the modification pattern is semi-cooperative, which indicates the native conformation of the apo-MT1a (Fig. 3-15A-D).

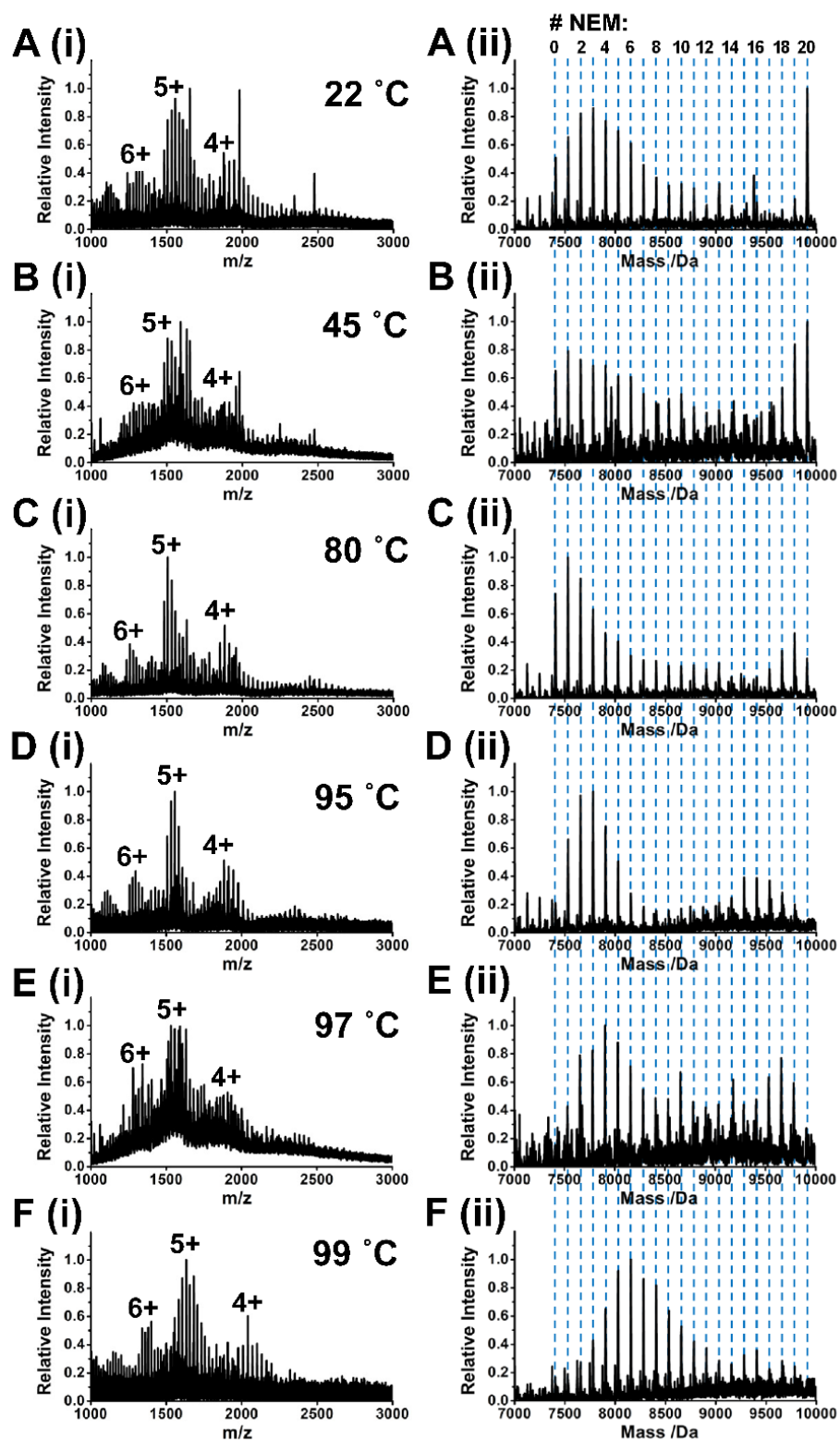


Figure 3-13. Effect of Temperature on apo-MT1a cysteine modification pattern monitored by ESI-MS. (i) Charge state and (ii) deconvoluted ESI mass spectra of apo-MT1a with 10 mol. eq. NEM added at (A) 22 °C, (B) 45 °C, (C) 80 °C, (D) 95 °C, (E) 97 °C, and (F) 99 °C at pH 8.3.

After the addition of NEM modifier in the presence of 2 M GdmCl, the cysteine modification pattern is completely non-cooperative, resembling a Binomial distribution. (Fig. 3-15E). Even in the presence of very high concentrations of GdmCl (7 M), the modification pathway remains non-cooperative (Fig. 3-15F). This Binomial-like distribution suggests that the cysteines are equally exposed and thus are modified in a random pattern distributed around the molar equivalence added.

A fraction unfolded vs. GdmCl concentration plot based on the ESI-MS data in Fig. 3-15 is shown in Fig. 3-16. From this data, the calculated ΔG_0 value is $15 \pm 12 \text{ kJmol}^{-1}$ and the calculated m-value is $9 \pm 7 \text{ kJmol}^{-1}\text{M}^{-1}$. It should be noted that the errors are quite high, therefore caution must be taken when interpreting these results as quantitative thermodynamic values. Rather, the fitting of the data points is better used to show a general trend.

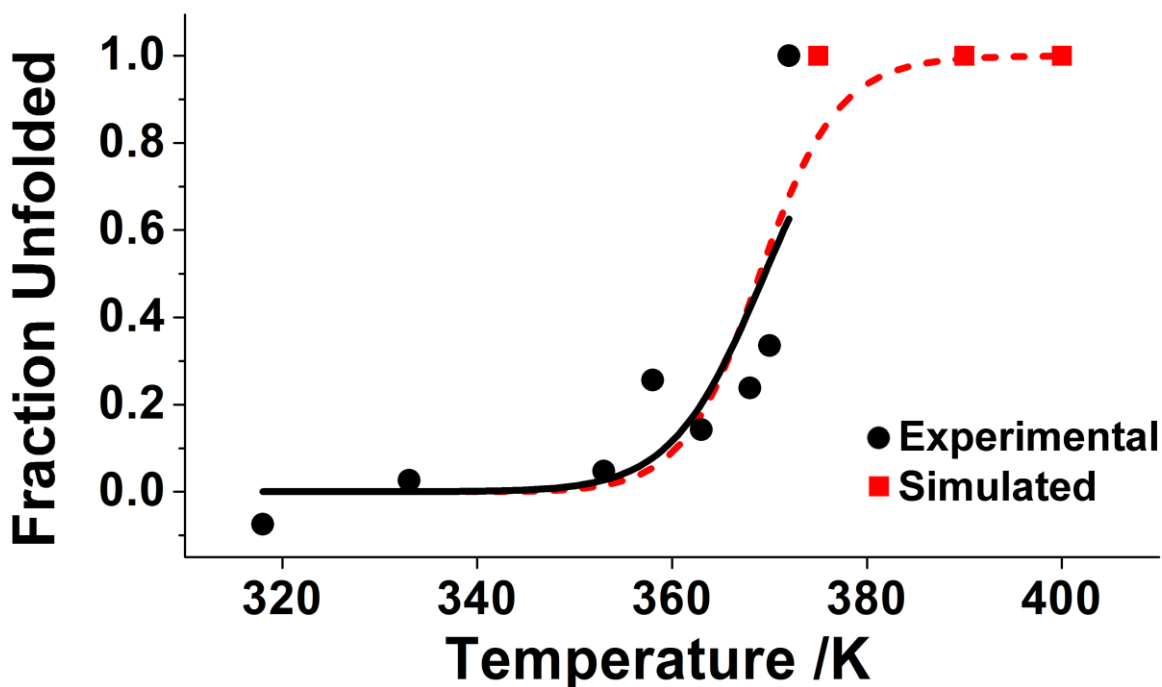


Figure 3-14. Fraction unfolded apo-MT1a vs Temperature monitored by ESI-MS. The fraction of unfolded apo-MT1a as a function of temperature monitored by the NEM distribution in the ESI mass spectra. The data points (circles) and fit (line) in black are experimental. The data points (square) and fit (line) in red are simulated to extrapolate beyond 373 K (100 °C). The temperature at the point of 50 % denaturation is 369 K (96 °C).

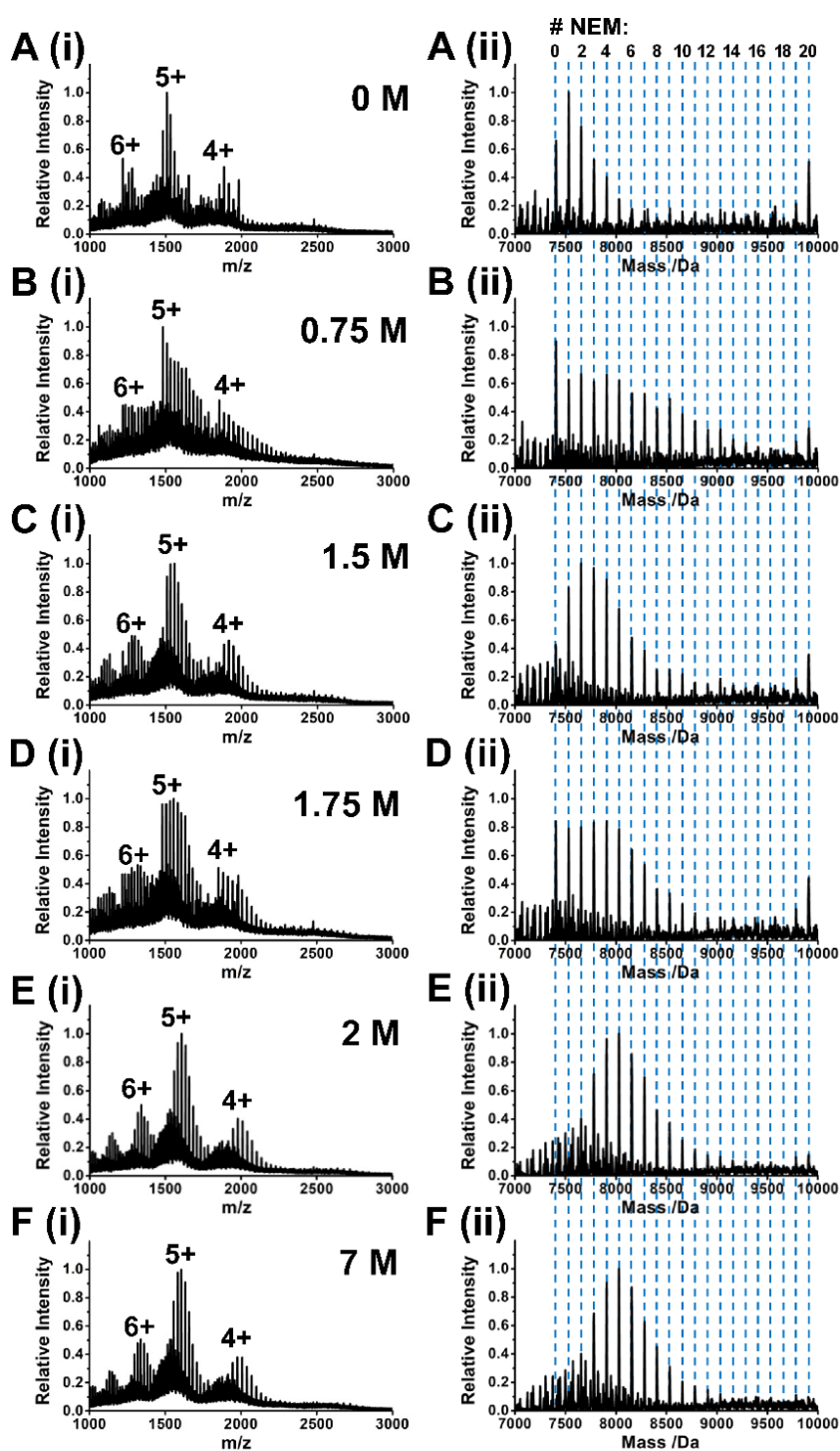


Figure 3-15. Effect of GdmCl on apo-MT1a cysteine modification pattern monitored by ESI-MS.(i) Charge state and (ii) deconvoluted ESI mass spectra of apo-MT1a with 6 mol. eq. NEM added in the presence of (A) 0 M, (B) 0.75 M, (C) 1.5 M, (D) 1.75 M, (E) 2 M, and (F) 7 M GdmCl at pH 7.4. The GdmCl was removed via buffer exchange prior to ESI-MS analysis.

It can be seen how the structure transition from folded to unfolded is very abrupt, with the inflection point occurring at 1.7 M GdmCl. Even small amounts of denaturant (0.75 M) appear to alter the structure compared to no denaturant. Looking at the ESI-MS spectra in Fig. 3-15B, the distribution of non-cooperative NEM is much broader than in Fig. 3-15A. Also, in Fig. 3-15C and 3-15D, the proportion of 20 modifications is suppressed.

The mass spectral results obtained here agree with those obtained for the isolated domains of apo-MT1a. In those studies, the β -domain fragment had fully exposed cysteines when modified in the presence of 1 M GdmCl, while the α -domain required 2 M to obtain the entirely non-cooperative modification pattern.²⁷³

The structural change from partially buried to more equally exposed cysteines under denaturing conditions (low pH, high temperature, and presence of GdmCl) occurred

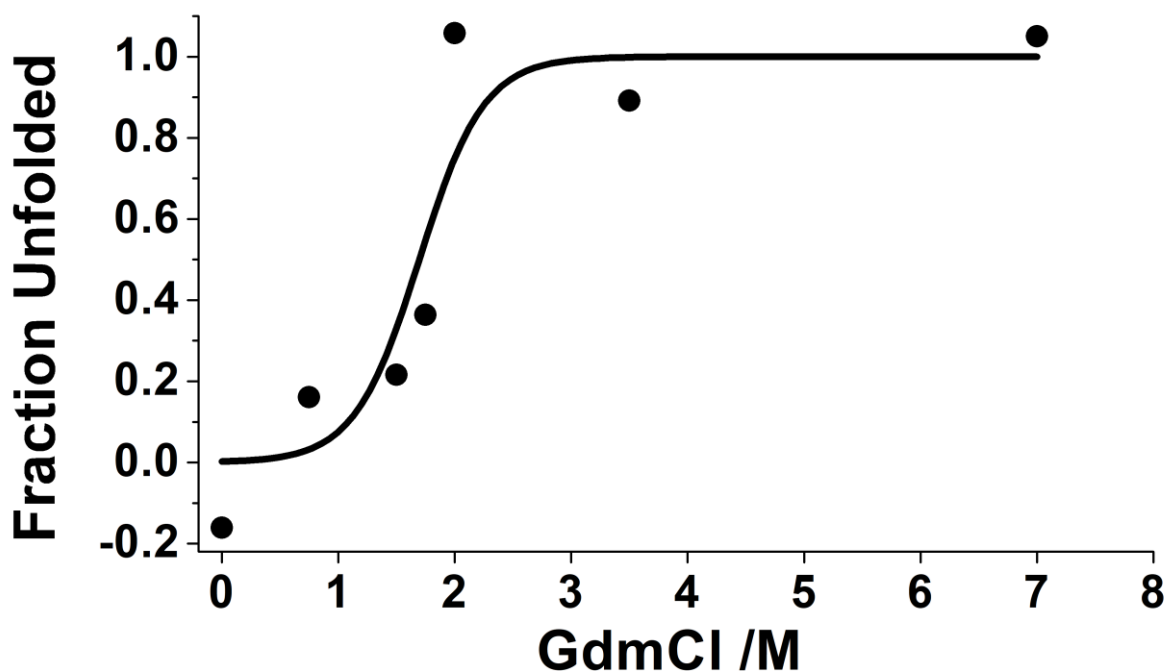


Figure 3-16. Fraction unfolded apo-MT1a vs GdmCl monitored by ESI-MS. The fraction of unfolded apo-MT1a as a function of GdmCl concentration monitored by the NEM distribution in the ESI mass spectra (points) with a sigmoidal fit (line). The parameters determined using the linear extrapolation method are $\Delta G_0 = 15 \pm 12 \text{ kJmol}^{-1}$ and $m = 9 \pm 7 \text{ kJmol}^{-1}\text{M}^{-1}$. The concentration of GdmCl at the point of 50 % denaturation is 1.7 M.

cooperatively for all conditions studied. This indicates that there is residual structure in apo-MT1a that can be unfolded.

For the temperature and GdmCl conditions, pre-unfolding transition changes in the modification distributions were observed. This may indicate that additional unfolding intermediates are present that may require other techniques to fully observe. It is also important to note that apo-MT1a did not aggregate at low pH conditions or high temperatures. This is an unusual property for a globular protein to possess but is rather common for IDPs.²⁶⁴

3.3.9 The cooperative GdmCl-dependent unfolding transition of apo-MT1a monitored using CD spectroscopy

The unfolding of apo-MT_a using GdmCl was also monitored using CD spectroscopy. This is a more traditional technique used to study protein folding, however, the difference between apo-MTs under native and denaturing conditions have not yet been studied in this manner.

The CD spectra of apo-MTs are typical for that of IDPs. However, the negative signal at 222 nm indicates some residual structure. Upon addition of the denaturant GdmCl, the ΔA at 222 nm is suppressed compared to the protein under native conditions and the resulting spectra is more like that of a random coil (Fig. 3-17A).

A titration of GdmCl monitored at 222 nm reveals a sigmoidal unfolding curve, with the melting point occurring at approximately 2.4 M GdmCl (Fig. 3-17B). The unfolding transition was fit to a two-state mechanism using Equations (3-3) to (3-9). A ΔG_0 of 10 ± 2 kJmol⁻¹ and an m-value of 4.3 ± 0.6 kJmol⁻¹M⁻¹ were obtained (Fig. 3-17C). These values have much smaller errors than those obtained using ESI-MS, therefore they will be discussed in further detail.

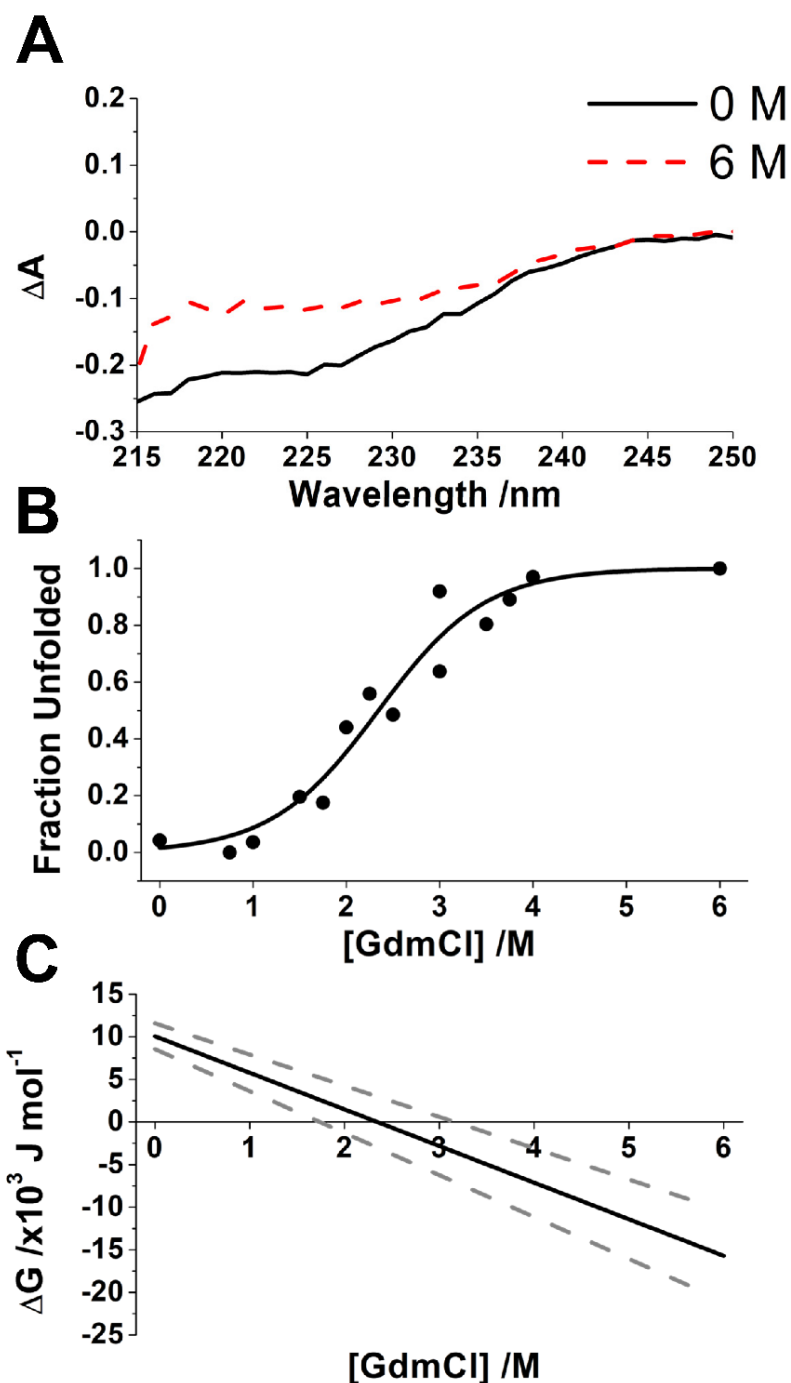


Figure 3-17. GdmCl-induced unfolding of apo-MT monitored by CD spectroscopy. (A) CD spectra of apo-MT1a in the presence of 0 M (black solid line) and 6 M (red dashed line) GdmCl at pH 7.4. (B) The fraction of unfolded apo-MT1a as a function of GdmCl concentration monitored by the molar ellipticity at 222 nm (points) with a sigmoidal fit (line). (C) A plot of the free energy of apo-MT1a as a function of GdmCl concentration. The parameters determined using the linear extrapolation method are $\Delta G_0 = 10 \pm 2 \text{ kJmol}^{-1}$ and $m = 4.3 \pm 0.6 \text{ kJmol}^{-1}\text{M}^{-1}$. The concentration of GdmCl at the point of 50 % denaturation is 2.3 M.

These thermodynamic parameters are on the low end compared to ordered globular proteins. A typical m -value for a protein of 60-70 residues has been shown to be approximately $7000 \text{ Jmol}^{-1}\text{M}^{-1}$.²⁸⁷ These data are from proteins with particularly ordered structures, as they all had available X-ray crystallography data. Proteins are marginally stable, with typical conformational stabilities between $20\,000$ - $60\,000 \text{ Jmol}^{-1}$.²⁸⁸⁻²⁸⁹ As apo-MT1a is fluxional in structure, it is not surprising that low thermodynamic values are obtained.

Comparing the CD data to the ESI-MS data, a structural change may occur by 0.75 M GdmCl that is detected in the mass spectra but not the CD spectra. Since the ESI-MS data shows full cysteine exposure under conditions of 2 M GdmCl with a much more abrupt transition, while the CD spectra shows full unfolding only at 4 M GdmCl with the inflection point occurring at 2.3 M GdmCl , it is possible that cysteine exposure is involved in an early intermediate step in the unfolding.

3.3.10 Metallothionein as an intrinsically disordered protein

Apo-MT1 possesses several features of an IDP. It has a high number of charged residues and a lack of bulky hydrophobic ones. It has no well-defined secondary structural features and has a very fluxional three-dimensional structure with unequal cysteine exposure. Apo-MTs also possess stability in extreme conditions such as high temperatures and low pH environments. Apo-MT1a is also highly sensitive to proteolysis, requiring it to be purified from *E. coli* in the fully metallated Cd_7MT form. However, none of these indicators allow differentiation between a random coil and a molten-globule type structure.

Where does apo-MT1a fit in the protein structural continuum? These results give evidence that although apo-MT1a is an IDP, it is not a random coil. MD simulations indicate dimensions more like a natively folded protein rather than a random coil. Both MD simulations and experimental results show an unequal cysteine exposure that potentially plays a role in optimal metal binding.

The cooperative sigmoidal shape seen in the unfolding transition monitored by CD spectroscopy and the calculated thermodynamic parameters are more in line with what

would be seen for a natively folded protein. Likewise, the abrupt exposure of the cysteines seen in response to GdmCl, heat, and reduced pH indicates an all-or-nothing structural change. These phenomena imply that in order for apo-MT1a to undergo a cooperative unfolding transition, it must have had a structure to be denatured in the first place. Additionally, differences are seen between apo-MT1 and apo-MT3, isoforms which play different biological functions. This suggests that apo-MTs have a structure-function relationship beyond flexible disorder.

Many IDPs lack cooperative structural transitions in response to denaturants. An example is prothymosin α , a random coil IDP which has a similar Stokes radius under native and denatured conditions.²⁹⁰⁻²⁹¹ Other IDP structures can be expanded upon addition of denaturant such as the unstructured cytoplasmic domain of the human neuronal adhesion protein neuroligin 3,²⁹² the N region of the yeast prion protein Sup35,²⁹³ and the ribosomal acidic protein YP2 β .²⁹⁴ In these examples, the expansion is non-cooperative.

However, some IDPs have similar structural transitions to apo-MT1a. Examples include small heat shock protein Hsp22,²⁹⁵ *BpUreG*,²⁹⁶ Genome-linked protein VPg of *Potato virus A*,²⁹⁷ osteopontin (OPN),²⁹⁸ and the nuclear coactivator binding domain (NCB) of CREB binding protein.²⁹⁹

OPN is comparable to apo-MT1a in the sense that it is fluxional while still able to be cooperatively unfolded, showing that this feature is not exclusive to well-defined structures. The structure ensemble of OPN involves both cooperatively folded and extended conformations.

NCB in the absence of a binding partner has also been shown to undergo cooperative unfolding modeled to a two-state process due to its collapsed core.²⁹⁹ This collapsed structure resembles a precursor to the complex of NCB with its binding partner ACTR, to which it undergoes coupled binding and folding.³⁰⁰ Interestingly, it resembles the complex with ACTR rather than that of its complex with IRF-3, another binding partner.²⁹⁹ Apo-MT1a could also have a collapsed structure that is optimal for binding certain metallated structures but is still fluxional enough to bind in the many diverse stoichiometries it is known to form.

3.4 Conclusions

The early structure-function paradigm put forth the thought that the rigid tertiary packing was the precursor for protein function. As more information about proteins that did not fit this model (IDPs) was reported, this paradigm was challenged. However, it is clear from numerous examples that IDPs still have a structure-function relationship, often using flexibility to bind multiple partners.

Apo-MTs are also flexible proteins which bind multiple partners in the form of metals. These results have demonstrated that apo-MT1a is not a random coil but is better described as a molten globule IDP. Through MD simulations, ESI-MS, and CD spectroscopy, it was found that apo-MT1a has a bundled structure more compact than a typical random coil which can be cooperatively unfolded. The native structure has a mixture of buried and exposed cysteine residues which can be equally exposed in the presence of a denaturant. Apo-MT3 has a different native structure than apo-MT1a with minimal cysteines exposed to the solvent, which may play impact its biological role. Conversely, the more exposed cysteines of apo-MT1a may play a role in optimally binding biologically relevant and toxic metals in a variety of tissues. The unique structures of apo-MTs further solidify the remarkable diversity in disordered protein structures that exist in nature.

Chapter 4

4 Structural Motifs in the Early Metallation Steps of Zn(II) and Cd(II) binding to Apo-Metallothionein 1a

In the previous chapter, the unique apo-MT1a structure was investigated and found to have a bundled “molten globule” structure which could be cooperatively unfolded. The structure was fluxional but distinct from a “random coil.” Apo-MTs have been previously described to undergo metal-induced folding from a disordered to ordered structure. However, few studies have considered the effect the apo-MT native structure has on the early metal-thiolate structures formed. In this chapter, the effect of the apo-MT1a structure on binding of Zn(II) and Cd(II) is described using stopped-flow kinetic methods and cysteine modification combined with ESI-MS.

4.1 Introduction

Metals are involved in many physiological processes, with many proteins requiring a metal cofactor to perform their functions.^{6, 9, 12-13, 161} The formation of a metal binding site is a result of the overall three-dimensional structure of the protein arranging in such a way to bring the required amino acids to the correct spatial orientation.¹ The metal cofactor can assist in the protein folding process³⁰¹⁻³⁰³ or can be required for formation of the tertiary structure.³⁰⁴⁻³⁰⁵ Metallothioneins (MTs) are specialist proteins that bind multiple metal ions in binding sites that only form upon the metallation.

MTs were initially discovered as an equine Cd(II)-binding protein⁶³ and isolated in humans as a Zn(II), Cd(II), and Cu(I) protein.⁶⁵ Since then, MTs have been isolated from numerous organisms and are now considered ubiquitous in life. MTs are cysteine-rich proteins thought to be involved in metal homeostasis and heavy metal detoxification^{113, 124}, with upregulation occurring via the MTF-1 pathway in some vertebrate isoforms.¹⁰⁹

MTs are intrinsically disordered in the absence of metals (apo-MTs) but will form more ordered structures in the presence of metals. Thus, the binding of metals is sometimes

referred to metal-induced folding.³⁰⁶ These structures formed depend on factors such as the species of MT, the metal identity, and the metal stoichiometry.

The most well-known structure comes from the single available mammalian MT crystal structure of Cd₅Zn₂MT, which exhibited a two-domain structure.^{140, 142-143} Mammalian MTs contain 20 conserved cysteine residues.⁶⁷ The N-terminal β -domain binds three divalent metals with an M₃S₉ stoichiometry and the C-terminal α -domain binds four divalent metals with an M₄S₁₁ stoichiometry. These cluster structures involve a network of both bridging (one cysteine bound to two metals) and terminal (one cysteine bound to only one metal) cysteines.¹⁴⁵⁻¹⁴⁷

Although mammalian MTs fully metallated with Zn(II) and Cd(II) have been studied extensively, very much less is known about the relevant apo-MT and partially metallated species that likely form *in vivo*.¹⁵³⁻¹⁵⁵ However, due to their fluxional nature, these structures are more difficult to characterize than those of fully metallated MTs. ESI-MS is a powerful technique to study partially metallated states of MT due to the ability to observe individual species and their relative abundances rather than an average in solution.

Through electrospray ionization mass spectrometry (ESI-MS) and circular dichroism (CD) spectroscopy methods, it has been shown that mammalian MTs can bind Zn(II) or Cd(II) in one of two different pathways.^{166-169, 171} The “cluster” pathway describes a cooperative formation of M₄S₁₁ in the α -domain, followed by M₃S₉ in the β -domain without the formation of any stable intermediates.^{169, 171} The non-cooperative pathway involves the sequential binding of each metal initially to terminal cysteines, where all intermediates are observed.^{166-168, 171} It has been proposed that up to five metals each coordinate to four separate terminally bound cysteines, forming Zn₅S₂₀ or Cd₅S₂₀ structures, followed by rearrangement into bridging metal-thiolate clusters upon further binding.^{168, 171}

These two pathways are highly pH dependent.¹⁷¹ Cd(II) binds in the cooperative pathway below pH 6, and in the non-cooperative pathway above pH 8. Between these pHs, a sigmoidal transition between these pathways is observed. A mixed pathway is observed in this range. Zn(II) binds in the cooperative pathway below pH 4, and in the non-cooperative pathway above pH 6. Again, a mixed pathway is observed between these pHs. At

physiological pH (7.4), Cd(II) binds in a mixed cooperative and non-cooperative pathway, while Zn(II) binds entirely non-cooperatively.

Tandem MS studies have been performed in an attempt to elucidate the partially metallated binding sites of Zn(II) and Cd(II).^{170, 176, 307} These studies suggest that Zn(II) and Cd(II) have different binding pathways, with Cd₄MT localized in the α -domain and Zn₄MT spanning both domains.^{170, 176, 307} Conversely, similar studies on Zn₄MT and Cd₄MT structures suggest higher affinities of these metals to the middle of the protein, between Asn18 to Cys38 in MT2.³⁰⁸

The change in metallation kinetics under various conditions can also provide insight into the binding reactions. The pH-dependent binding kinetics of both Zn(II) and Cd(II) to apo-MT, which occur on the millisecond timescale, have been observed previously using stopped flow methods at 25 °C.³⁰⁶ That study was concerned with describing the folding of MT in terms of the metal binding pathway, contrasting the formation of secondary structural elements and a hydrophobic core in typical proteins. At neutral pH, much of the binding reaction was completed within the dead time of the instrument used and thus no kinetic data at physiological pH (7.4) for apo- β MT were obtained.³⁰⁶

The knowledge of pH-dependent binding pathways as well as pH-dependent binding kinetics prompted our group to study the kinetics of non-cooperative binding at pH 8 and cooperative cluster formation at pH 5. Stopped-flow methods at low temperatures overcame the previous limitation preventing kinetic observation at high pHs.¹⁶¹ These results showed the non-cooperative Cd(II) binding at pH 8 was faster than the cooperative Cd₄MT cluster formation at pH 5. It was proposed that this difference in rate was due to the concerted cluster formation involving 4 Cd(II) requiring more time than the binding of individual Cd(II) non-cooperatively. However, the likely role of thiol protonation and solution H⁺ concentration driving this process was not thoroughly considered.

As well, Cd(II) metallation in the presence of a denaturant was shown slowed the binding, implying that the structure of the initial apo-MT is optimal for its metal-binding function.¹⁶⁰⁻¹⁶¹ This is significant, because apo-MT appears to take on a compact structure which can be unfolded by a denaturant.^{158-159, 164-165, 252, 272-273} The mammalian MT isoforms

MT1a and MT3 have recently been shown to have differences in their apo structures, with the cysteines of MT3 existing in a more collapsed conformation with the cysteines buried in the center of the protein.²⁵² Stopped-flow kinetic studies have shown that apo-MT3 binds Cd(II) with a rate constant approximately 1.7 times larger than apo-MT1a.²⁵² This also gives an indication that the apo-MT structure impacts the rate of metal binding.

Although changes in kinetics can indicate both structural changes in the protein and changes in the pathway of metal binding, the information gained using stopped-flow kinetics monitored by absorption spectroscopy alone is limited. This is because only a single kinetic trace is obtained, which corresponds to seven overlapping bimolecular reactions. Only an average of $M_{1-7}MT$ species is observed and only a single rate constant can be reported. For this reason, ESI-MS is an excellent technique to pair with stopped-flow methods. Stopped-flow provides quantitative data measured in the solution phase which can be combined with the level of detail seen using ESI-MS.

In this chapter, stopped-flow kinetics and ESI-MS are combined to probe the pH and structural dependence of apo-MT on the rates of Zn(II) and Cd(II) binding to apo-MT. The effect of different pH conditions from pH 5 to pH 7.4 and implications for the rate of different binding pathways are reported and discussed. The rates of Zn(II) and Cd(II) metallation as a function of GdmCl concentration are reported. The different structures formed during a titration of Zn(II) and Cd(II) into native and denatured apo-MT are monitored using CD spectroscopy. ESI-MS studies reveal the metal-thiolate stoichiometries in the first few metallation steps of Zn(II) and Cd(II) to native and denatured apo-MT.

To date, the dependence of Zn(II) and Cd(II) metallation properties on the initial apo-MT structure has not been studied using both stopped-flow kinetics to analyze the difference in rate constants and ESI-MS to visualize the individual M_xS_y formed. Additionally, the pH-dependence of both Zn(II) and Cd(II) binding to apo-MT has not been fully described.

4.2 Materials and Methods

Recombinant human metallothionein 1a (rhMT1a) was expressed and purified as described in Chapter 2. For the remainder of this chapter, rhMT1a will be referred to as MT. Apo-MT was prepared in Tris-HCl at pH 7.4 and its concentration was measured as described in Chapter 2.

4.2.1 Stopped flow methods

All stopped flow experiments were carried out at 7 °C. All reagents were prepared, and their pHs were measured and adjusted, at 7 °C.

For chemical denaturation experiments, the prepared apo-MT at pH 7.4 was diluted into solutions of 20 mM Tris-HCl and 8 M GdmCl in specific ratios to obtain a final concentration of 10 μ M apo-MT and 2 M, 3 M, 3.5 M, 4 M, 4.5 M, 5 M, 5.5 M, 6 M, 7 M GdmCl. Separate solutions of Zn(OAc)₂ and Cd(OAc)₂ were prepared to equal 70 μ M from 10 mM stock solutions, again in varying ratios of 20 mM Tris-HCl and 8 M GdmCl at pH 7.4 to match those of the MT samples. Solutions of 20 mM Tris-HCl at pH 7.4 were mixed in varying ratios with 8 M GdmCl at pH 7.4 to equal the concentrations of the apo-MT and metal solutions.

For pH dependence experiments, solutions of 20 mM Tris-HCl at varying pHs were prepared. The prepared apo-MT at pH 7.4 was diluted into these solutions of 20 mM Tris-HCl at varying pHs. Separate solutions of Zn(OAc)₂ and Cd(OAc)₂ were prepared to equal 70 μ M from 10 mM stock solutions by diluting into the 20 mM Tris-HCl at varying pHs matching those of the apo-MT solutions. The pHs were measured using a micro pH electrode and adjusted using dilute ammonium hydroxide and formic acid if necessary, using extremely small volumes to avoid further dilution of the sample.

The four syringes of the SFM-400 instrument were loaded with Tris-HCl (S1), apo-MT (S2), water (S3), and Zn(OAc)₂ or Cd(OAc)₂ (S4) with matching GdmCl concentrations or matching pH. The syringes were initially programmed to deliver 150 μ L each of Tris-HCl and apo-MT at a flow rate of 3.75 mLs⁻¹ (total flow rate of 7.5 mLs⁻¹) per shot to establish a baseline. Three shots were obtained per experiment. Then the program was altered to

deliver 150 μL each of apo-MT and either $\text{Zn}(\text{OAc})_2$ or $\text{Cd}(\text{OAc})_2$ at a flow rate of 3.75 mLs^{-1} (total flow rate of 7.5 mLs^{-1}). Five to ten shots were obtained per experiment. For $\text{Zn}(\text{II})$ experiments, the reaction was monitored at 230 nm. For $\text{Cd}(\text{II})$ experiments, the reaction was monitored at 250 nm. The kinetic traces were collected for either every 100 μs for 0.6 s for all GdmCl denaturation experiments, or 200 μs for 1.2 s, 500 μs for 3 s, or 1 ms for 6 s for the pH dependence experiments depending on the time required for the reaction to reach completion.

4.2.2 Analysis of kinetic Data

The kinetic traces for each experiment were averaged and the baselines were subtracted. The kinetic traces were converted from absorbance vs time to concentration vs time using Equation 4-1, where C_t is the concentration of M_7MT forming at a particular time t , A_t is the absorbance observed at time t , C_0 is the initial concentration of apo-MT (5 μM after a 50:50 dilution with the metal solution), and A_∞ is the maximum observed absorbance.

$$C_t = \frac{A_t C_0}{A_\infty} \quad (4-1)$$

The kinetic traces were fit using Complex Pathway Simulator (COPASI) version 4.27 to a single bimolecular second order reaction. As discussed in Chapter 2, the actual kinetics are much more complicated, consisting of seven consecutive metal binding reactions that overlap in the observed kinetic traces. Therefore, during the fitting process, the reactions were each simplified to a single bimolecular reaction, approximating one step of the metallation as follows in Equation 4-2 for $\text{Zn}(\text{II})$ and Equation 4-3 for $\text{Cd}(\text{II})$.



The metal stoichiometry is not specified as it cannot be determined by absorbance alone the identity of the species observed at a given time point. In reality, a mixture of species would be present at any time throughout the reaction. During the fitting process, the concentration of metal was varied within reason to produce the fit with the lowest root

mean square error. The fitting requirements are further discussed in the Results and Discussion section.

The rate constants obtained from the GdmCl denaturation experiments were taken as a measure of the apo-MT folded status and converted to a fraction unfolded curve using Equation 4-4, where f_u is the fraction of the protein that is unfolded and where k represents the observed rate constant. In cases where there was a high deviation between baseline points, the average minimum and maximum rate constants were used.

$$f_u = \frac{(k - k_{max})}{(k_{min} - k_{max})} \quad (4-4)$$

The calculated fraction unfolded curves were fit using Origin Pro 8.5 to a two-state sigmoidal curve. Equations 4-5 through 4-8 were used to find the protein stability, ΔG_0 , and the m-value for GdmCl using the linear extrapolation method.²⁷⁸⁻²⁷⁹ The reported errors were the standard errors on the fit.

$$K = \frac{[U]}{[N]} \quad (4-5)$$

$$K = \frac{e^{\left(\frac{-\Delta G}{RT}\right)}}{1 + e^{\left(\frac{-\Delta G}{RT}\right)}} \quad (4-6)$$

$$\Delta G = -RT \ln K \quad (4-7)$$

$$\Delta G = \Delta G_0 - m[GdmCl] \quad (4-8)$$

4.2.3 Circular dichroism methods

The prepared apo-MT at pH 7.4 was diluted to a concentration of 25 μ M in either only 5 mM Tris-HCl at pH 7.4 or a mixture of 5 mM Tris-HCl at pH 7.4 and 8 M GdmCl at pH 7.4 to equal a final concentration of 7 M GdmCl.

Either Zn(OAc)₂ or Cd(OAc)₂ was titrated stepwise into the apo-MT without denaturant and the apo-MT in the presence of 7 M GdmCl. The samples were measured using a Jasco J-810 spectropolarimeter after each addition of Zn(II) or Cd(II). A water baseline was

collected and subtracted automatically from each sample by the instrument. The samples were run between 200 and 310 nm in a 0.2 cm cuvette with a data pitch of 1 nm, a response of 2 s, and a band width of 2 nm. Two accumulations were made. The ellipticity (θ) was measured by the spectropolarimeter in units of mdeg. The relationship $\theta = 32.98(\Delta A)$ was used to convert the units to absorbance.

4.2.4 ESI-MS methods

The prepared apo-MT at pH 7.4 was diluted to a concentration of 70 μM in either only 20 mM Tris-HCl at pH 7.4 or a mixture of 20 mM Tris-HCl at pH 7.4 and 8 M GdmCl at pH 7.4 to equal a final concentration of 7 M GdmCl. Either 3 mol. eq. $\text{Zn}(\text{OAc})_2$ or 3 mol. eq. $\text{Cd}(\text{OAc})_2$ was added to apo-MT without denaturant and the apo-MT in the presence of 7 M GdmCl. These samples were allowed to equilibrate for 10 min after which 16.5 mol. eq. NEM modifier was added to bind free cysteines. The samples were once again allowed to equilibrate for 10 min and then buffer exchanged with 20 mM ammonium formate at pH 7.4 using an Amicon centrifugal filter tube with a 3 kDa cut-off 5 times at 4000 rpm for 30 min each to prepare for ESI-MS analysis.

The samples were measured using the Bruker MicroTOF II ESI mass spectrometer using the parameters described in Chapter 2 and the spectra were deconvoluted between 7000 and 11000 Da. Species were identified that corresponded to various $\text{Cd}_x\text{NEM}_y\text{MT}$ and $\text{Zn}_x\text{NEM}_y\text{MT}$ stoichiometries. It is important to note that Zn(II) is nearly half the mass of NEM, which made analysis of the Zn(II) spectra more complicated. However, in cases where the identity of the observed species was unclear by mass alone, a decision was made based on both patterns observed in the $\text{Cd}_x\text{NEM}_y\text{MT}$ (i.e. decreasing NEM as metal content increased) and logic about the realistic combinations that Zn(II) and NEM can form in the 20-cysteine MT. Once the number of bound metal and NEM molecules were determined, the number of NEM was subtracted from 20 to obtain the number of cysteines involved in the metal binding.

4.3 Results and Discussion

4.3.1 The nature of the observed kinetic traces

The data presented in this section were obtained using stopped-flow kinetic methods, CD spectroscopy, and ESI-MS. It is important to comment on the nature of the resulting kinetic data, as MT presents a unique case in regard to kinetic analysis.

The binding of seven metals to apo-MT is described by seven consecutive bimolecular reactions. However, it is not possible to resolve all seven individual reactions using stopped flow methods as each step of the reaction contributes to the observed LMCT band absorbance. This results in a single kinetic trace which, in this study, was fit to a singular bimolecular reaction. The slowest step, or the rate determining step (RDS) will influence the observed kinetic trace in terms of both the observed rate constants and the parameters required to fit the trace. It is expected that the seventh metal to bind will be the rate determining step due to the limited binding sites available.

Additionally, as 4 ms of the reaction is lost in the dead time, the observable trace is likely more characteristic of later steps. Any initial rapid steps which may reveal a biphasic reaction are lost in this time. Reaction conditions which change the rate of the final step will also impact earlier steps. Therefore, although the other steps are not directly observable, the RDS will be influenced by the first and subsequent reaction steps, thus providing information about the beginning of the reaction.

4.3.2 The effect of multistep reactions on the kinetic fitting parameters

It is important to comment on the molar ratio of Zn(II) or Cd(II) required to fit the data because, in each experiment, 7 mol. eq. of Zn(II) or Cd(II) were used to fully metallated the protein. In other words, the concentration of metal in the reaction cuvette was seven times that of the MT.

Under neutral pH or low denaturant conditions, a metal molar equivalence near equal to the MT concentration resulted in the best fit. However, under lower pH or high denaturant concentrations, a larger concentration of metal was required to be used in the fitting

parameters, despite the same concentration being used experimentally. If the slower steps are at the end, then the observed kinetic traces will be more characteristic of the end steps. By the end of the reaction, when only one metal is left to bind, there is no more excess in solution. There will be one mole of metal per mole of protein. Thus, a one-to-one fitting makes sense. However, when the slower steps are at the beginning, possibly due to needing to overcome thiol protonation or an unfolded protein structure, more of the initial steps will be observed. At the beginning, when the first metal binds, there will be seven times excess of metals in solution. This is the reason for requiring a higher concentration of metal in the fit.

4.3.3 The rate of Zn(II) and Cd(II) metallation is pH-dependent

The rate of Zn(II) binding to apo-MT is highly pH dependent. The kinetic traces resulting from reactions of apo-MT with Zn(II) at various pHs are shown in Fig. 4-1. A clear difference in the rate of reaction can be seen from the kinetic traces. At pH 7.4, the trace plateaus by 0.05 s (Fig. 4-1A). When the pH is lowered to a range between 7.26-6.38, the plateau does not occur until approximately 0.5 s (Fig. 4-1B-E). At pH values below 6, the reaction takes over 1 s to complete (Fig. 4-1F-H).

The rate of Cd(II) metallation of apo-MT is also pH dependent, although less so than Zn(II) metallation. The kinetic traces of these pH-dependent reactions are shown in Fig. 4-2. Although there is very little visual difference between the kinetic traces from pH 7.85 to pH 6.38, which appear to plateau between 0.05 and 0.1 s (Fig. 4-2A-E), all analyses show a significant decrease in the rate below pH 7.40 (Table 4-1). Below pH 6, the reaction takes closer to 0.15 s to reach completion (Fig. 4-2F-H), signaling the reduced rate.

The rate constants resulting from the fit of the kinetic traces are shown in Table 4-1 and plotted in Fig. 4-3. At physiological pH, Zn(II) and Cd(II) metallate apo-MT at a very similar rate, with Cd(II) being slightly faster. The rate of Zn(II) metallation slows dramatically from pH 7.4 to pH 7.26, with the rate constant decreasing by a factor of approximately five. From this point the rate constant is lowered much more gradually, approximately halving in value upon each next pH measured until pH 5.51.

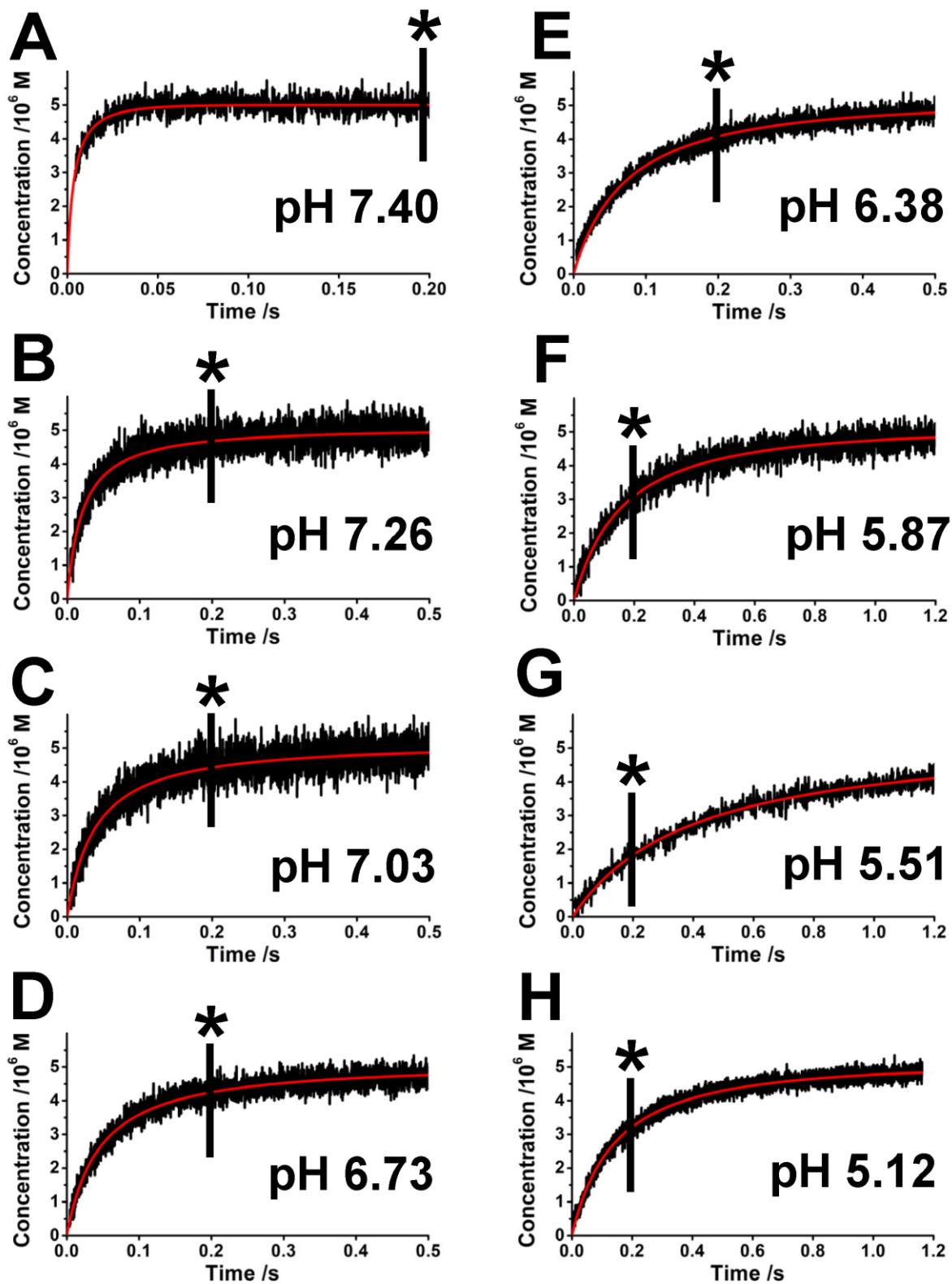


Figure 4-1. pH-dependent kinetic traces of Zn(II) binding to apo-MT. Kinetic traces resulting from a reaction of 5 μ M apo-MT and 35 μ M Zn(II) at various pHs monitored at 230 nm. Kinetic traces are shown for pH (A) 7.40, (B) 7.26, (C) 7.03, (D) 6.73, (E) 6.38, (F) 5.87, (G) 5.51, (H) 5.12. Reactions were performed at 7 $^{\circ}$ C. The line with (*) is placed at 0.2 s into the reaction.

Between the fastest and slowest reaction, the rate constant is decreased by a factor of approximately 100. The rate of Cd(II) metallation also follows the trend of slowing down under more acidic conditions. However, unlike Zn(II) where the rate dropped dramatically between pH 7.4 and pH 7.26, the change is much more gradual over all pHs measured.

The observed Cd(II) rate constants can be sorted into three groups similar in magnitude over pH 7.85 to pH 7.4, pH 7.26 to pH 6.38, and pH 5.87 to pH 5.12. The rate constants in the highest pH group are approximately one and a half to two times higher than those in the middle group. The rate constants in the middle group are approximately two times higher than those in the lowest pH group. Overall, the rate constant is decreased by a factor of approximately five from the fastest to slowest condition.

4.3.4 The difference in metallation rates of Zn(II) and Cd(II) to apo-MT is amplified under acidic conditions.

These results reveal a difference in the metallation rate of Zn(II) or Cd(II) binding to apo-MT as a function of pH. The Zn(II) metallation rate undergoes a sharp decrease below physiological pH, a phenomenon that was not observed for Cd(II), where the rate decreases gradually and stays generally constant within pH ranges above 7.4, between 6.3 and 7.3, and below 6. Under physiological pH conditions, Cd(II) metallation is approximately 1.5 faster than Zn(II) metallation. Under the lowest pH conditions, Cd(II) metallation is approximately 10 times faster than Zn(II) metallation. The faster reaction between Cd(II) and MT than Zn(II) and MT is unsurprising. As Cd(II) is a softer metal than Zn(II), the change in affinity from M–O to M–S increases more for Cd(II) than for Zn(II). A larger affinity constant results in a larger rate constant and thus a faster reaction.

The pH-dependence of these reactions is also expected due to increased thiol protonation at lower pH levels. Deprotonation of the thiol is required for metal binding. If this is a rate determining step, then the thiol protonation status will impact the rate of metal binding. The pKa of a cysteine thiol is 8.3, implying that at pH 7.4, approximately 2 of the 20 cysteines in apo-MT remain deprotonated. However, the pKa can be lowered if the negatively charged thiolate is stabilized by a nearby positive charge such as on a lysine side chain, which are abundant in the MT sequence.

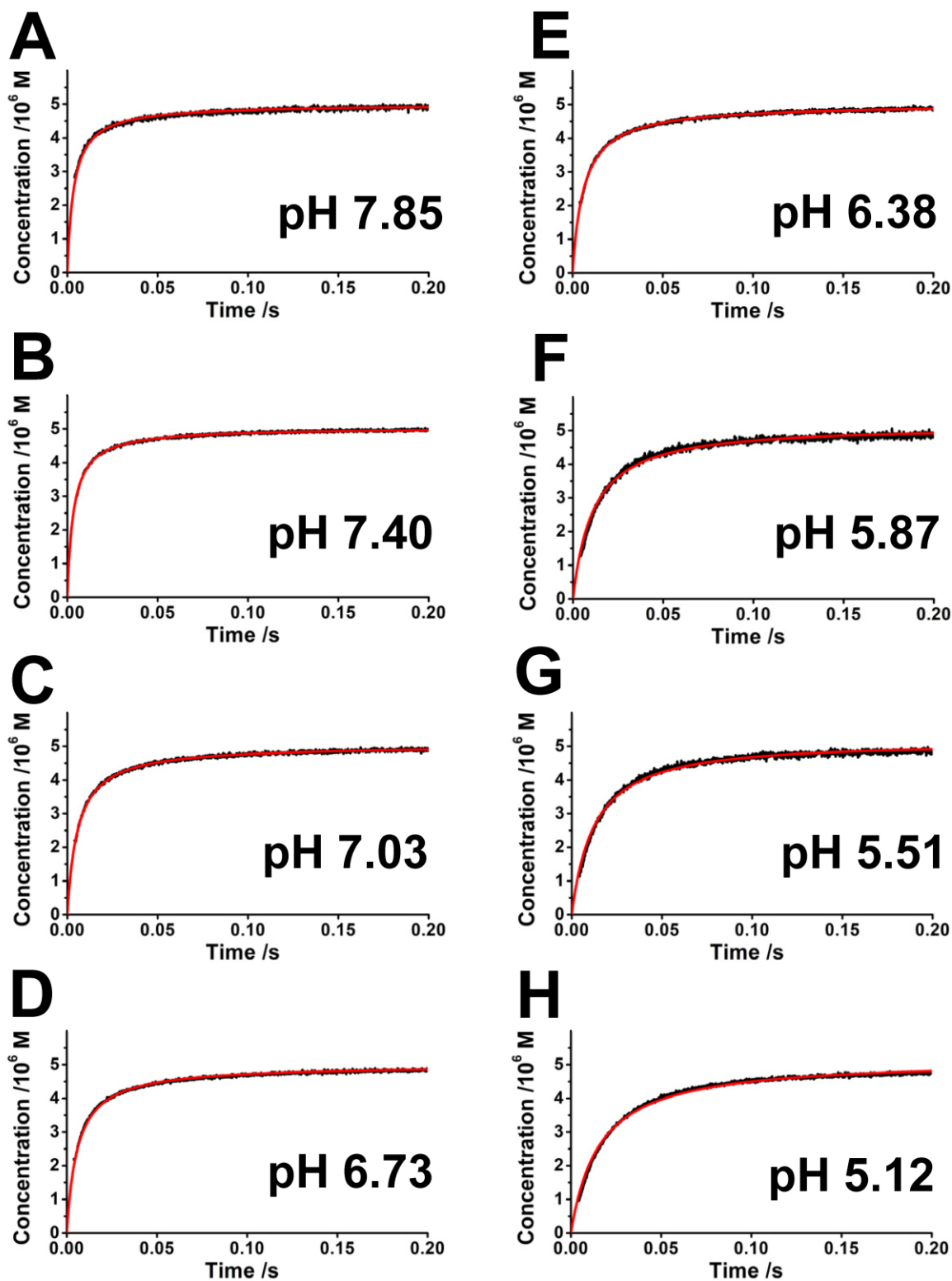


Figure 4-2. pH-dependent kinetic traces of Cd(II) binding to apo-MT. Kinetic traces resulting from a reaction of 5 μ M apo-MT and 35 μ M Cd(II) at various pHs monitored at 250 nm. Kinetic traces are shown for pH (A) 7.85, (B) 7.40, (C) 7.03, (D) 6.73, (E) 6.38, (F) 5.87, (G) 5.51, and (H) 5.12. Reactions were performed at 7 $^{\circ}$ C.

It is currently unknown whether this phenomenon occurs in MTs. Nevertheless, a pH-dependence in the thiol protonation status near physiological pH cannot be discounted for apo-MTs. This would provide an explanation for the lower reaction rates at lower pHs.

This protonation is also likely responsible for the two different pH-dependent metal binding pathways observed for Zn(II) and Cd(II), as the non-cooperative formation of intermediates may be unfavourable when thiols are protonated. Due to its softer character, Cd(II) forms cooperative clusters more readily than Zn(II), which is known to have intermediate properties. For Cd(II), the non-cooperative pathway dominates above pH 7.4 and the cooperative pathway dominates below pH 6.¹⁷¹

Table 4-1. Table of pH-dependent rate constants of Zn(II) and Cd(II) binding to apo-MT. The rate constants resulting from the reaction between 5 μM apo-MT and 35 μM Zn(II) or Cd(II) at various pHs. The concentrations of the apo-MT and Zn(II) or Cd(II) required to fit the kinetic traces are shown. The errors are a result of the standard deviation between 3 replicates at pH 7.4 for each metal. The percent standard deviation was applied to other samples.

pH	Zn(II) / $\mu\text{M}^{-1}\text{s}^{-1}$	k	[MT] _{Fit} / μM	[Zn] _{Fit} / μM	Cd(II) / $\mu\text{M}^{-1}\text{s}^{-1}$	k	[MT] _{Fit} / μM	[Cd] _{Fit} / μM
7.85	-	-	-	-	55 \pm 7	5	5	5
7.40	44* \pm 10	-	-	-	64* \pm 8	-	-	-
	51 \pm 11	5	5	6	57 \pm 7	5	5	5.1
	38 \pm 8	5	5	6	62 \pm 8	5	5	5.15
	-	-	-	-	72 \pm 9	5	5	5.05
7.26	9 \pm 2	5	5	5.4	-	-	-	-
7.03	5 \pm 1	5	5	5.7	34 \pm 4	5	5	5.1
6.73	4.1 \pm 0.9	5	5	5.5	34 \pm 4	5	5	5
6.38	2.2 \pm 0.5	5	5	6.7	32 \pm 4	5	5	5.05
5.87	1.0 \pm 0.2	5	5	6.8	17 \pm 2	5	5	5.6
5.51	0.4 \pm 0.1	5	5	6.2	15 \pm 2	5	5	5.7
5.12	1.2 \pm 0.3	5	5	6.5	12 \pm 1	5	5	5.5

*Obtained by averaging all rate constants obtained at the specified pH

The change in rate constants of Cd(II) binding at varying pH levels generally correspond to the pH ranges where pathway changes are observed, with fast binding seen for the non-cooperative pathway, slow binding for the cooperative pathway, and an intermediate rate for the mixed pathway. This agrees with the previous study suggesting that the formation of the non-cooperative intermediates is fast, while formation of the cluster is slow.¹⁶¹

This however, is not the case for Zn(II). Zn(II) follows an entirely non-cooperative binding pathway above pH 6.0 and a mixed pathway between pH 4.0 and pH 6.0.¹⁷¹ The Zn(II) binding rate is dramatically reduced from pH 7.4 to pH 7.26, well within the non-cooperative binding range, suggesting that the binding pathway alone is not influencing the rate. Rather, the significant drop in the rate of Zn(II) binding below pH 7.4 may be the result of thiol protonation.

Nevertheless, the binding pathway may be influencing the extent of the pH-dependent rate reduction. The reduction of the Cd(II) binding constant is not as drastic as for Zn(II) below

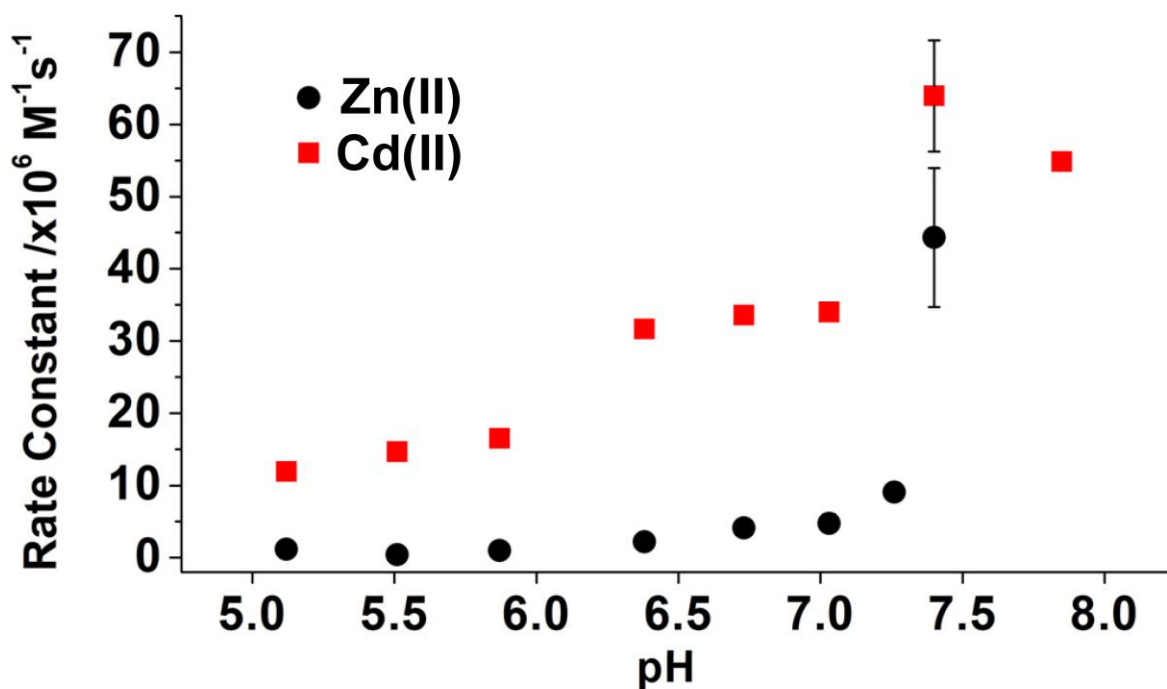


Figure 4-3. Plot of pH-dependent rate constants of Zn(II) and Cd(II) binding to apo-MT. A plot of rate constants resulting from a reaction of 5 μM apo-MT and either 35 μM Zn(II) (black circles) or 35 μM Cd(II) (red squares) versus pH.

pH 7.4. This may be due to the protonated thiols more greatly preventing non-cooperative intermediates from forming with Zn(II) than the cooperative cluster with Cd(II).

Previous studies have reported that there are differences in apo-MT structure,^{165, 252} Zn(II) and Cd(II) binding pathways,¹⁷¹ and Zn(II) and Cd(II) binding rates at different pHs.³⁰⁶ This highly pH-dependent behaviour may have biological implications. Apo-MT1a has been shown to bind Cd(II) in the proximal tubular lysosomes³⁰⁹ and mobilize Zn(II) in various organelles including lysosomes, mitochondria, nucleus, endoplasmic reticulum, cytosol, and the Golgi apparatus.³¹⁰ The pH environment of different organelles can vary. For example, the proximal tubules can have environments from pH 6.7–6.8³¹¹ and the lysosomes pH 4.5–5.0.²⁸²

Based on Hard Soft Acid Base Theory,⁷ Cd(II) will preferentially bind sulfur ligands over Zn(II). Cd(II) has no known biological role and is toxic, often by route of displacing Zn(II) from enzymes, which leads to disfunction of the affected protein.⁶⁰ However, in the case of MT, the displacement of Zn(II) by Cd(II) results in both sequestration of the toxic metal and upregulation of MT via the MTF-1 pathway.^{108-109, 113} Lower pH conditions may enhance the MT's preference for Cd(II) binding over Zn(II) binding, such as in the sequestration to the kidneys where the Cd(II) is stored in the cluster.¹¹³

4.3.5 The rates of Zn(II) and Cd(II) metallation slow under denaturing conditions.

Metallation of apo-MT with both Zn(II) and Cd(II) is slower when carried out in the presence of GdmCl. The kinetic traces resulting from the metallation of apo-MT with Zn(II) in the presence of increasing concentrations of GdmCl are shown in Fig. 4-4. Between 0 and 3.5 M GdmCl, approximately 40% of the reaction is complete within the dead time of the instrument (Fig.4A-C). Under conditions of 4 M GdmCl, this number decreases to around 20%, indicating a slower reaction (Fig. 4-4D).

An interesting observation is that some of the kinetic traces plateau rather suddenly rather than gradually despite the earlier part of the reaction slowing, which is normally consistent with a first order or pseudo first order reaction rather than the second order reaction that is

taking place (Fig.4D-G). At 6 M and 7 M GdmCl, the kinetic traces look visibly slower than the preceding ones (Fig. 4-4H-I).

The kinetics of Cd(II) binding to apo-MT under denaturing conditions show similar trends to that of Zn(II) (Fig. 4-5). From 0 M to 3.5 M, approximately 60% of the reaction is completed in the dead time (Fig. 4-5A-D). From 4 M to 7 M, approximately 40% of the reaction occurs in the dead time (Fig. 4-5E-I). In contrast to the Zn(II) reactions, the visual difference in the kinetic traces is not as clear due to more of the reaction occurring within the dead time. It does appear however, like with Zn(II), that the largest change in the kinetic trace occurs in the early part of the reaction, as the reactions appear to plateau at approximately the same time independent of denaturant concentration.

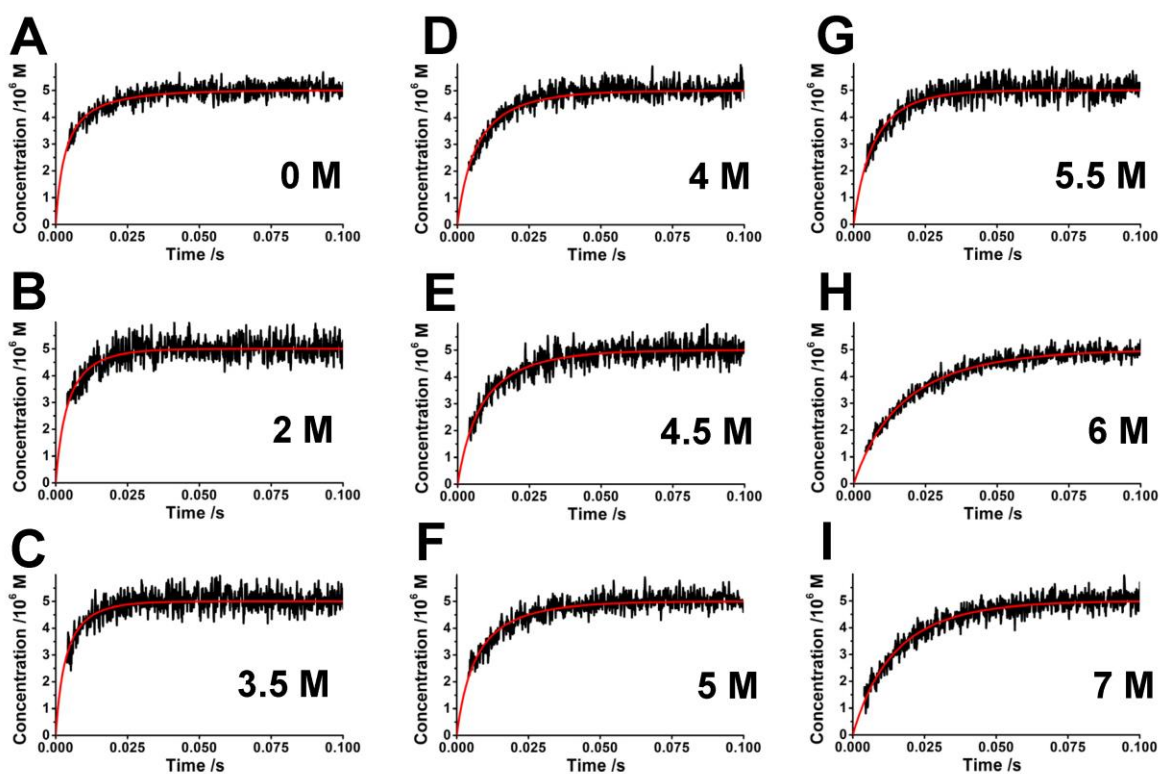


Figure 4-4. GdmCl-dependent kinetic traces of Zn(II) binding to apo-MT. Kinetic traces resulting from a reaction of 5 μ M apo-MT and 35 μ M Zn(II) at various GdmCl concentrations monitored at 230 nm. Kinetic traces are shown for GdmCl concentrations of (A) 0, (B) 2, (C) 3.5, (D) 4, (E) 4.5, (F) 5, (G) 5.5, (H) 6, and (I) 7 M. Reactions were performed at 7 $^{\circ}$ C.

The rate constants obtained from the fitting of the kinetic traces are summarized in Table 4-2 and Fig. 4-6. Fig. 4-6A shows the plotted rate constants for Zn(II) (Fig. 4-6Ai) and Cd(II) (Fig. 4-6Aii) as a function of GdmCl concentration.

For both Zn(II) and Cd(II), the rate constants between 0 M and 3.5 M GdmCl remain relatively unchanged. At 4 M GdmCl, the Zn(II) rate constant has reduced by approximately half. It then gently decreases until reaching a value at 6 M about 8 times smaller than its original value at 0 M.

For Cd(II), the rate constant is also halved by 4 M GdmCl. Beyond 4 M GdmCl, the Cd(II) rate constant does not appear to decrease anymore. Fig. 4-6B clearly shows that the inflection point for Zn(II) is at 4.3 M GdmCl while the inflection point for Cd(II) is at 3.7 M. Interestingly, higher concentrations of GdmCl are required to fully slow the Zn(II)

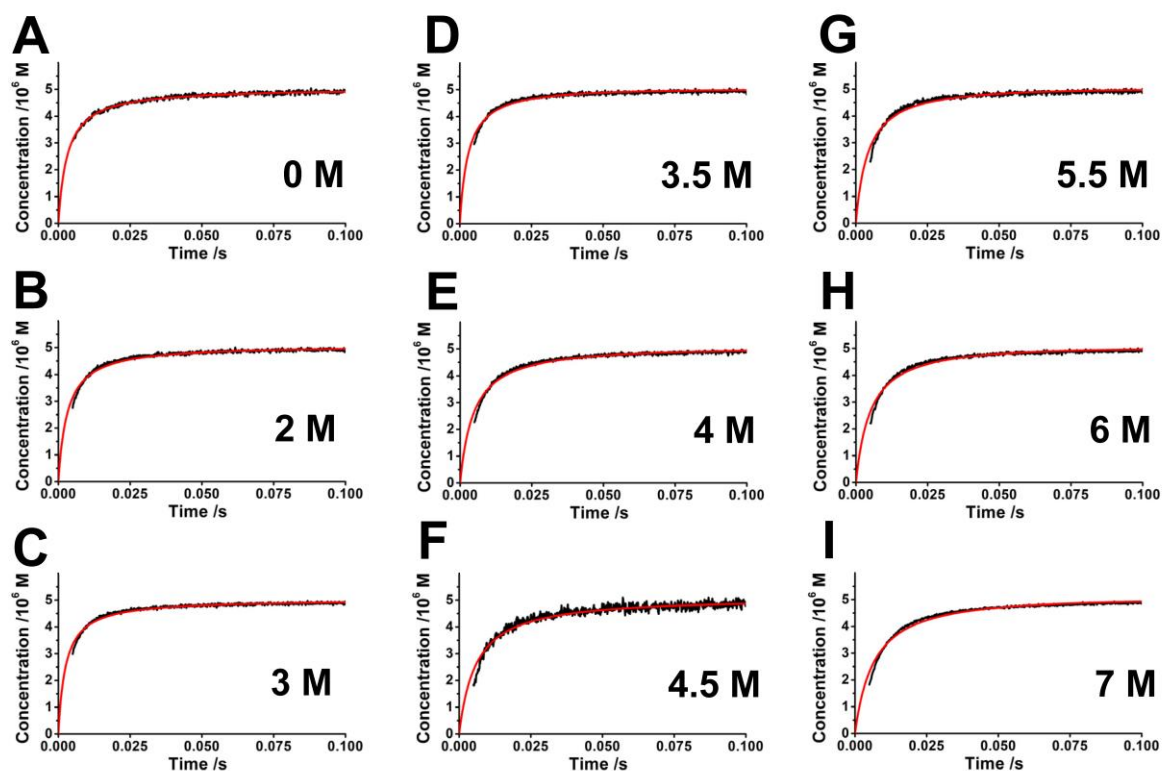


Figure 4-5. GdmCl-dependent kinetic traces of Cd(II) binding to apo-MT. Kinetic traces resulting from a reaction of 5 μ M apo-MT and 35 μ M Cd(II) at various GdmCl concentrations monitored at 250 nm. Kinetic traces are shown for GdmCl concentrations of (A) 0, (B) 2, (C) 3, (D) 3.5, (E) 4, (F) 4.5, (G) 5.5, (H) 6, and (I) 7 M. Reactions were performed at 7 $^{\circ}$ C.

binding compared to the Cd(II) binding, but the actual rate of Zn(II) binding is still much slower compared to the rate for Cd(II). The change in the metallation rate constants between native and denaturing conditions provides insight into how the compact apo-MT structure, which can be disrupted using GdmCl,¹⁶¹ impacts some of the metal binding steps. If we take this change in metal binding rate as a measure for protein unfolding, the thermodynamic parameters can be calculated using Equations 4-4 through 4-8. The protein stability ΔG_0 is 13 ± 6 kJmol⁻¹ for Zn(II) and 15 ± 13 kJmol⁻¹ for Cd(II).

Table 4-2. Table of GdmCl-dependent rate constants of Zn(II) and Cd(II) binding to apo-MT. The rate constants resulting from the reaction between 5 μ M apo-MT and 35 μ M Zn(II) or Cd(II) at various GdmCl concentrations. The concentrations of the apo-MT and Zn(II) or Cd(II) required to fit the kinetic traces are shown. The errors are a result of the standard deviation between 3 replicates at pH 7.4 for each metal. The percent standard deviation was applied to other samples.

[GdmCl] /M	Zn(II) k / μ M ⁻¹ s ⁻¹	[MT] _{Fit} / μ M	[Zn] _{Fit} / μ M	Cd(II) k / μ M ⁻¹ s ⁻¹	[MT] _{Fit} / μ M	[Cd] _{Fit} / μ M
0	44* \pm 10			64* \pm 8		
	51 \pm 11	5	6	57 \pm 7	5	5.1
	38 \pm 8	5	6	62 \pm 8	5	5.15
				72 \pm 9	5	5.05
2	33 \pm 7	5	8	61 \pm 7	5	5.3
3	-	-	-	77 \pm 9	5	5.1
3.5	40 \pm 9	5	7.7	63 \pm 8	5	5.5
4	21 \pm 5	5	8	40 \pm 5	5	5.5
4.5	15 \pm 3	5	8.8	33 \pm 4	5	5.4
5	22 \pm 5	5	7.6	-	-	-
5.5	14 \pm 3	5	11	42 \pm 5	5	5.7
6	5 \pm 1	5	13	36 \pm 4	5	5.8
				42 \pm 5	5	5.6
7	5 \pm 1	5	16	27 \pm 3	5	5.9

*Obtained by averaging all rate constants obtained at the specified GdmCl concentration

4.3.6 Denaturation of the apo-MT structure reduces the rate of the early Zn(II) and Cd(II) metallation steps

The report that apo-MT adopts a compact structure under native conditions prompted investigation into whether this structure is optimal for metal binding. Based on these results, both Zn(II) and Cd(II) binding are affected by the apo-MT structure.

The profile of the kinetic traces obtained as well as the required fitting parameters implies that, in the case of Zn(II), it is the first few steps of metallation that are most affected by the structure of the apo-MT. This potentially means that once enough metals bind to

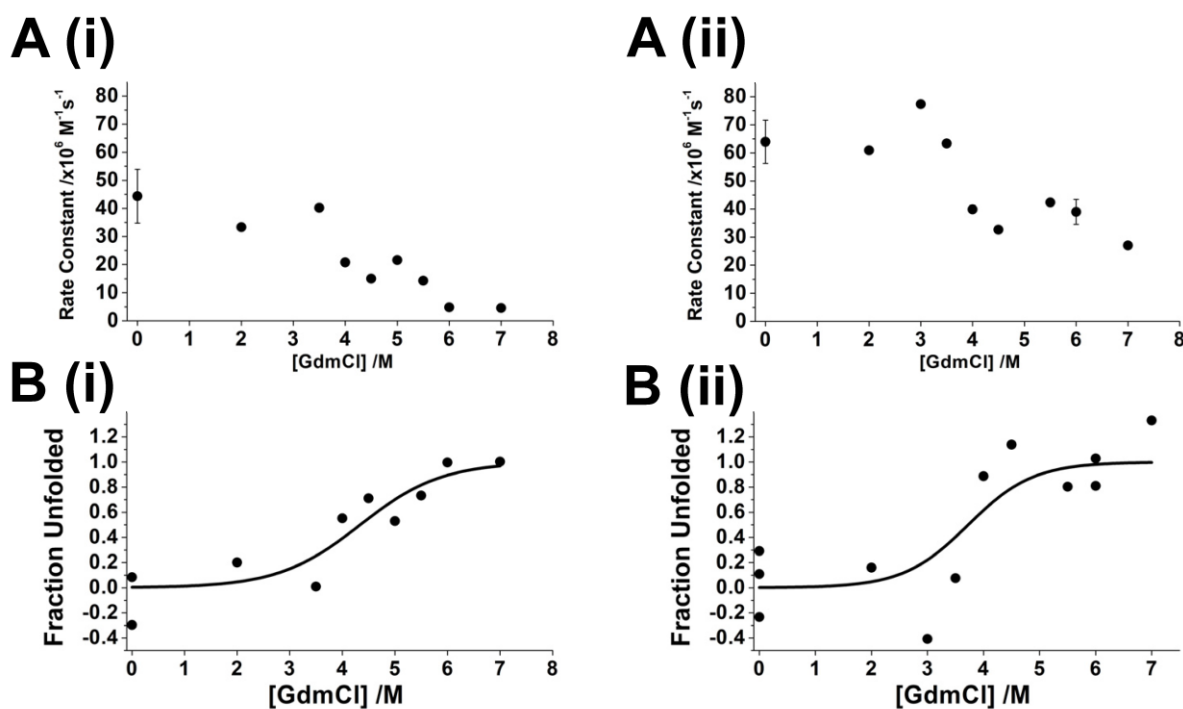


Figure 4-6. Plots of GdmCl-dependent rate constants of Zn(II) and Cd(II) binding to apo-MT with fraction unfolded curves. The rate constants and unfolding curves resulting from a reaction of 5 μM apo-MT and either 35 μM Zn(II) or 35 μM Cd(II) under various GdmCl concentrations. (A) The rate constants versus GdmCl concentration for (i) Zn(II) and (ii) Cd(II). (B) The fraction unfolded curves derived from the rate constants with the fit for (i) Zn(II) and (ii) Cd(II). The parameters determined using the linear extrapolation method are (A) $\Delta G_0 = 13 \pm 6 \text{ kJmol}^{-1}$ and $m = 3 \pm 1 \text{ kJmol}^{-1}\text{M}^{-1}$ and (B) $\Delta G_0 = 15 \pm 13 \text{ kJmol}^{-1}$ and $m = 4 \pm 3 \text{ kJmol}^{-1}\text{M}^{-1}$. The concentration of GdmCl at the point of 50 % denaturation is (A) 4.3 M and (B) 3.7 M.

overcome the denatured state and form a backbone structure close to the fully metallated protein, the remaining metals can bind more quickly.

The protein folding based on the reduction of the rate constant was fit to a two-state folding model as a function of GdmCl concentration, as was possible with the α -domain of MT.¹⁶⁰ The inflection point seen here is consistent with the reduction in rate constants seen in the α -domain of apo-MT when metallated with Cd(II), which occurs at approximately 4 M GdmCl.¹⁶⁰ This, as well as the thermodynamic parameters obtained, are also consistent with those obtained for the GdmCl denaturation of apo-MT monitored using CD spectroscopy. This suggests that the backbone unfolding of apo-MT as observed using CD spectroscopy is indeed the reason for the reduced metal binding rate.

At the greatest extent of denaturation, the rate constant for the Zn(II) binding is reduced by a factor of approximately 8, while the rate constant for the Cd(II) binding is only approximately half of the one measured under native conditions. The proposal that the first few metallation steps are most affected by GdmCl-induced denaturation may also explain this. As much of the Cd(II) metallation reaction is complete within the dead time of the instrument, the earlier steps which are slowed by the denaturant may not contribute to the observed kinetic trace as much as the less affected later steps. The rate of Cd(II) metallation of the isolated α -domain of apo-MT slows approximately ten-fold under denaturing conditions.¹⁶⁰ This is further evidence that the later metallation steps are obscuring the observed kinetic trace. Based on this analysis, it is possible that the Zn(II) binding is impacted by the denaturation of apo-MT for more of the later metallation steps than for the Cd(II) binding. This would explain the greater effect on the rate constants.

4.3.7 Stepwise Zn(II) and Cd(II) titrations monitored using CD spectroscopy suggest different pathways under native and denaturing conditions

A stepwise titration of Zn(II) and Cd(II) into apo-MT in the absence and presence of 7 M GdmCl was monitored by CD spectroscopy to investigate the structural changes in the protein during different metallation steps (Fig. 4-7). Apo-MT has a CD spectrum characteristic of an intrinsically disordered protein lacking formal secondary structure,

shown by a negative signal in the near-UV region. However, in the presence of a chemical denaturant, the CD spectrum resembles a protein that is more unfolded and disordered, with a suppression of the strong negative signal at 222 nm (Fig. 4-7A,F).

The titration of Zn(II) into apo-MT under native and denaturing conditions shows that the denatured MT backbone fold and metallated structures do not resemble those of the native MT until full metallation. After additions of 2.5, 4, and 6.5 mol. eq. Zn(II), the spectra of the MT in the presence of GdmCl produces different signals than those in the absence of GdmCl (Fig. 4-7B-D). The native MT spectra are characteristic of non-cooperative Zn(II) binding after 2.5 and 4 mol. eq. added, with a slightly less negative signal near 230 nm (Fig. 7B-C). After 6.5 mol. eq. Zn(II) has been added, the characteristic derivative-shaped signal with maxima at 230 nm (-) and 245 nm (+) indicating a cluster structure is observed (Fig. 4-7D).

During the titration of the denatured apo-MT, a positive signal at 225 nm is observed upon addition of 2.5 and 4 mol. eq. (Fig. 7B-C). A weak derivative-shaped signal is seen after 6.5 mol. eq. of Zn(II) has been added, however it is distorted compared to the one seen for the native MT with the negative maximum around 235 nm rather than 230 nm and still with a raised 225 nm peak not seen in the native protein (Fig. 4-7D). Only after 7.5 mol. eq. Zn(II) added do the two spectra overlap, indicating formation of the final Zn₇MT two-domain structure (Fig. 4-7E) and identical backbone folds.

The results of the Cd(II) titration into native and denatured apo-MT show that the metallated structures of the denatured MT resemble those formed in the native MT at an earlier stage in the titration compared to Zn(II). At 2.5 mol. eq. Cd(II) added, the typical non-cooperative spectrum expected for this step in the titration is seen for the native protein with a maximum at 245 nm (Fig. 4-7G).

Likewise, a similar spectrum is seen for the denatured protein with the negative signal at 225 nm slightly suppressed (Fig. 4-7G). At 4 mol. eq. added a weak derivative-shaped signal is observed in both the native and denatured MT, indicating cluster formation in both samples (Fig. 7H). However, the two spectra do not quite overlap at this point with the signal for the denatured MT being less pronounced.

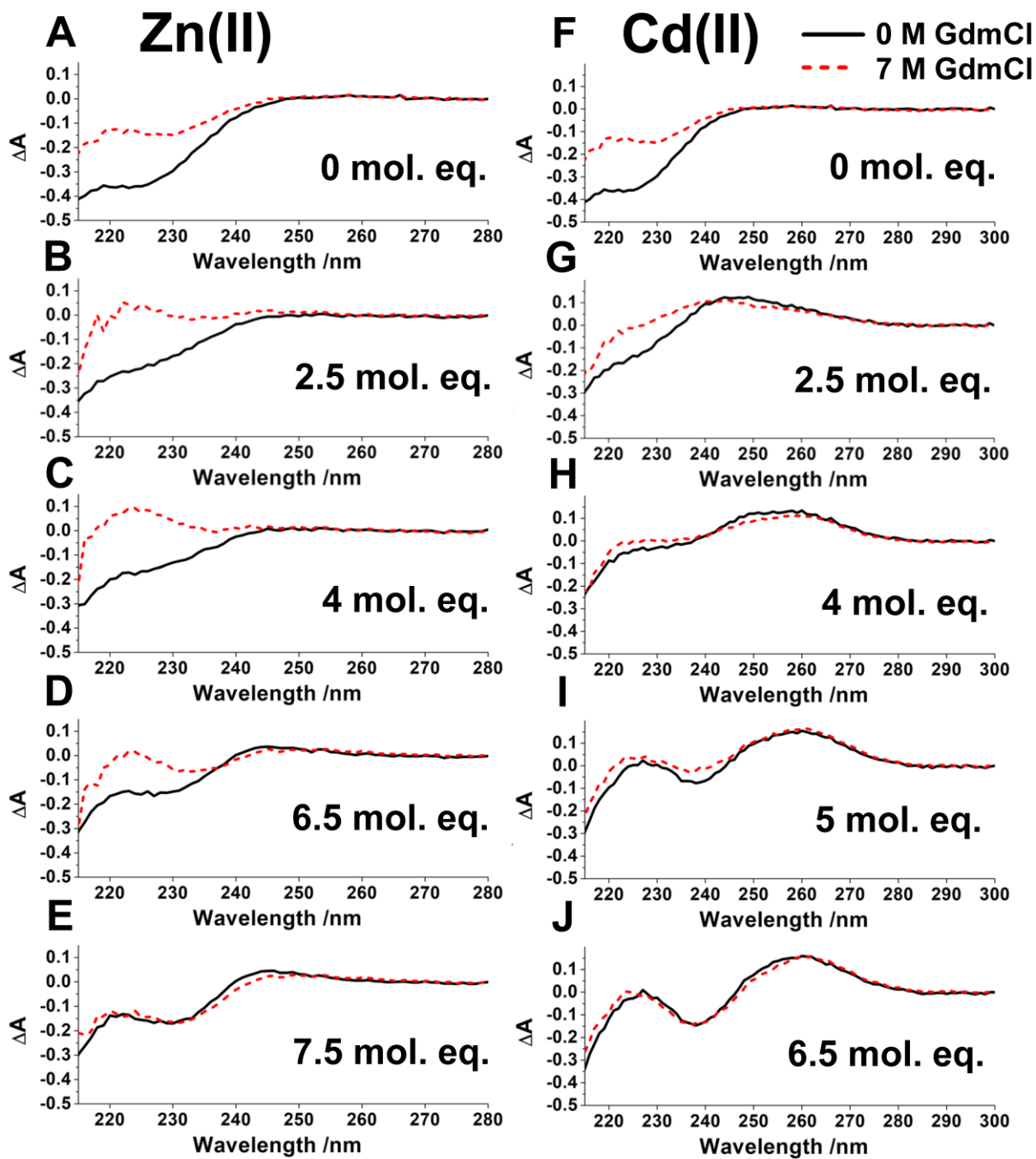


Figure 4-7. Titrations of Zn(II) or Cd(II) into apo-MT under native and denaturing conditions monitored by CD spectroscopy at pH 7.4. (A-E) A titration of (A) 0, (B) 2.5, (C) 4, (D) 6.5, and (E) 7.5 mol. eq. Zn(II) into apo-MT. (F-J) A titration of (F) 0, (G) 2.5, (H) 4, (I) 5, and (J) 6.5 mol. eq. Cd(II) into apo-MT. Both titrations were performed in the absence of GdmCl and in the presence of 7 M GdmCl.

By 5 mol. eq. Cd(II) added the derivative shape in both samples is more pronounced (Fig. 4-7I). Finally, at 6.5 mol. eq. Cd(II) added, the clear derivative shape with a minimum at 240 nm (-) and a maximum at 260 nm (+) is observed and the two spectra overlap, showing that they have the same structure (Fig. 4-7J).

Although the starting apo-MT in these titrations displayed different backbone structures (Fig. 4-7A,F), they each displayed the same characteristic derivative-shaped signal indicating formation of the two-domain cluster structure upon full metallation (Fig. 4-7E,J). Additionally, these spectra overlap regardless of whether the Zn(II) or Cd(II) is titrated into native or denatured apo-MT. This shows that not only are the same metallated structures formed upon full metallation, but the overall backbone fold of the Zn₇MT or Cd₇MT is the same.

In both the Zn(II) and Cd(II) titrations, the observed differences in the CD spectra in the first few metallation steps indicate that the structures formed in the native and denatured MTs are different despite the same average number of metals being bound. This could mean that either the metals are binding using different cysteines between the native and denatured MTs, or that the few metals bound are not enough to alter the overall protein backbone fold from its apo form.

The Zn(II)-bound MT under denaturing conditions does not resemble the Zn(II)-bound MT under native conditions until full metallation to Zn₇MT. This means that even at Zn₆MT, differences in structure between the two conditions still exist despite the presence of a cluster structure in both. Conversely, for Cd(II)-bound MTs, the structure of the native and the denatured proteins are nearly identical after addition of 4 mol. eq. Cd(II) and exactly overlap after 6.5 mol. eq. Cd(II) is added.

This suggests differences in how chemical denaturation of apo-MT protein affects Zn(II) and Cd(II) binding and is consistent with the results obtained from kinetic studies. In Zn(II) binding, nearly all metallation steps are affected, while only the first few metallation steps are affected in Cd(II) binding.

It is interesting to note that even under denaturing conditions, the same two-domain structure is able to form after addition of enough metal. This suggests that it is the primary structure of the MT that dictates the fully metallated structures that form, contrasting the effect of the compact apo-MT structure on the initial metallation steps. This concept of metal-induced folding was previously discussed following computational analysis by Rigby et al. in 2006.³¹²

4.3.8 Specific bridging thiolate structures form in metal-unsaturated Zn(II) and Cd(II) MTs

To characterize the individual M_xS_y species formed in native and denatured apo-MTs during metallation using Zn(II) or Cd(II), cysteine modification in combination with ESI-MS methods were performed. 3 mol. eq. Zn(II) or Cd(II) was added to apo-MT in the presence of either 0 M or 7 M GdmCl, followed by 16.5 mol. eq. NEM modifier to bind the free cysteines. The resulting ESI mass spectral data is shown in Fig. 4-8.

The possible metal-thiolate structures formed based on the ESI-MS data are shown in Fig. 4-9. As multiple connectivities for certain bridging metal-thiolate clusters are possible, particularly for the higher metallated species, only one possible structure is shown for simplicity. However, it is important to note that the exact structures are not known. Rather, the structures in Fig. 4-9 are intended as a visual aid.

As expected at pH 7.4, multiple intermediate species are observed for each condition. Specific metal-thiolate stoichiometries form for each metallated species. When either Zn(II) or Cd(II) is bound to apo-MT under native conditions, similar stoichiometries are observed. These stoichiometries imply a mixture of terminally bound metals as well as structures with bridging cysteines previously only associated with the M_4S_{11} and M_3S_9 clusters in the fully metallated protein.

A mixture of Zn_2S_6 and Zn_2S_8 are seen in the mass spectra (Fig. 4-8A), while only Cd_2S_6 forms (Fig. 4-8C). M_2S_8 describes a structure with two metals bound to only terminal cysteines. Conversely, M_2S_6 is a structure that can only form if two thiols participate in bridging.

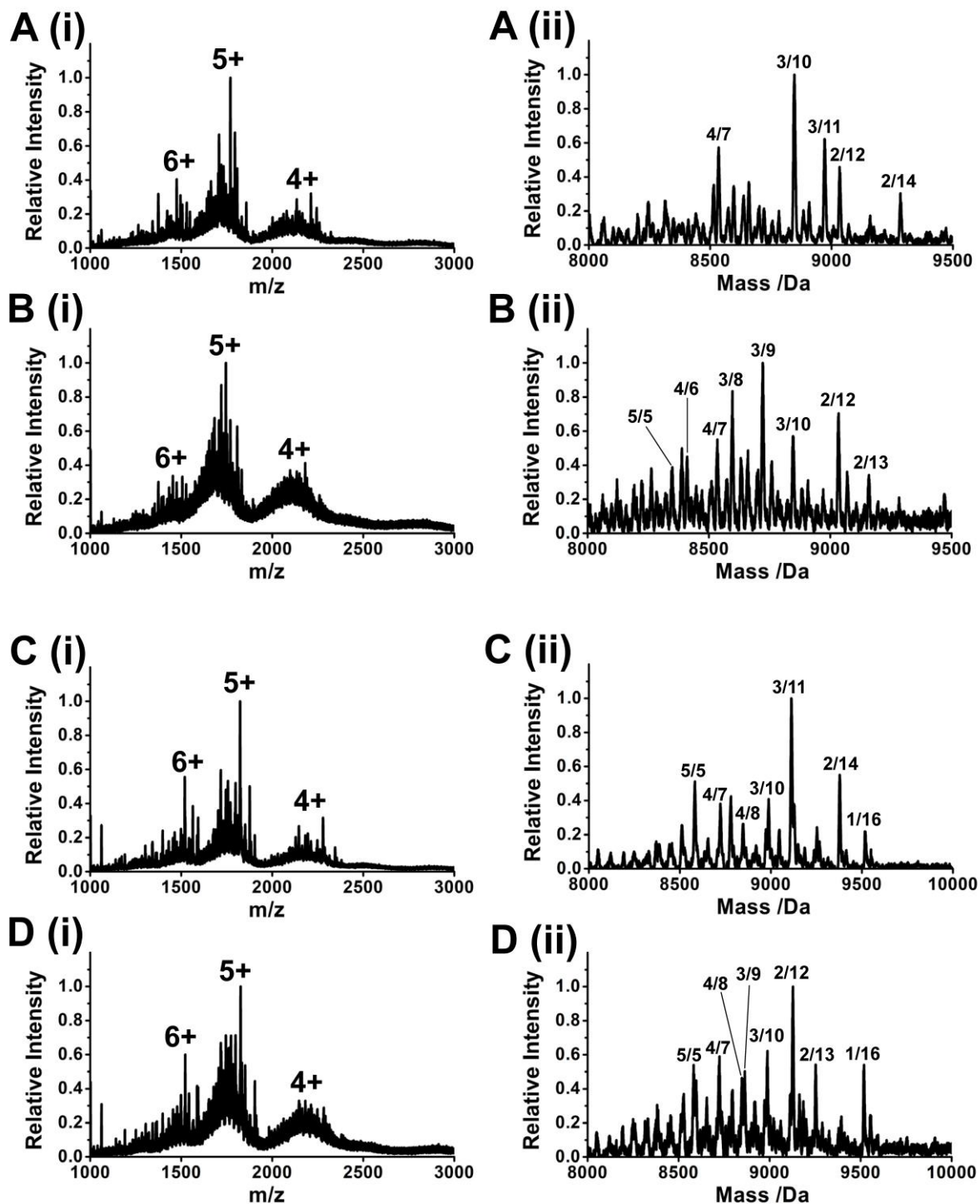


Figure 4-8. The early metallation steps of Zn(II) and Cd(II) to apo-MT at pH 7.4 under native and denaturing conditions monitored using ESI-MS. (i) Charge state and (ii) deconvoluted ESI mass spectra of (A-B) Apo-MT with 3 mol. eq. Zn(II) followed by 16.5 mol. eq. NEM (A) in the absence of GdmCl and (B) in the presence of 7 M GdmCl and (C-D) Apo-MT with 3 mol. eq. Cd(II) followed by 16.5 mol. eq. NEM (A) in the absence of GdmCl and (B) in the presence of 7 M GdmCl.

The metal-thiolate stoichiometries observed when three metals are bound are the same for both Zn(II) and Cd(II). Zn_3S_{10} and Zn_3S_9 as well as Cd_3S_{10} and Cd_3S_9 form. However, the ratios of these species formed are different for Zn(II) and Cd(II). The Zn_3S_{10} species is favoured (Fig. 4-8A) while the Cd_3S_9 is favoured (Fig. 4-8C). M_3S_{10} describes a structure where a single metal with all terminally bound cysteines exists alongside the M_2S_6 structure seen in the previous metallation step.

As no structure with only terminal cysteine exists when three metals are bound, the Zn_2S_8 structure must rearrange to form a structure with bridging cysteines upon the binding of a third metal. M_3S_9 involves three bridging cysteines. The structure is either an addition to M_2S_6 where the new metal shares one cysteine from the intact M_2S_6 structure or a rearranged structure potentially resembling the M_3S_9 cluster seen in the β -domain of the fully metallated protein. Based on ESI-MS experiments alone, it is not possible to tell which of these structures form or if the same structure forms for Zn_3MT and Cd_3MT .

After 4 metals have bound, Zn_4S_{13} , Cd_4S_{13} , and Cd_4S_{12} stoichiometries are observed. It is interesting to note that the M_4S_{11} cluster is not seen at this stage, indicating that it forms at

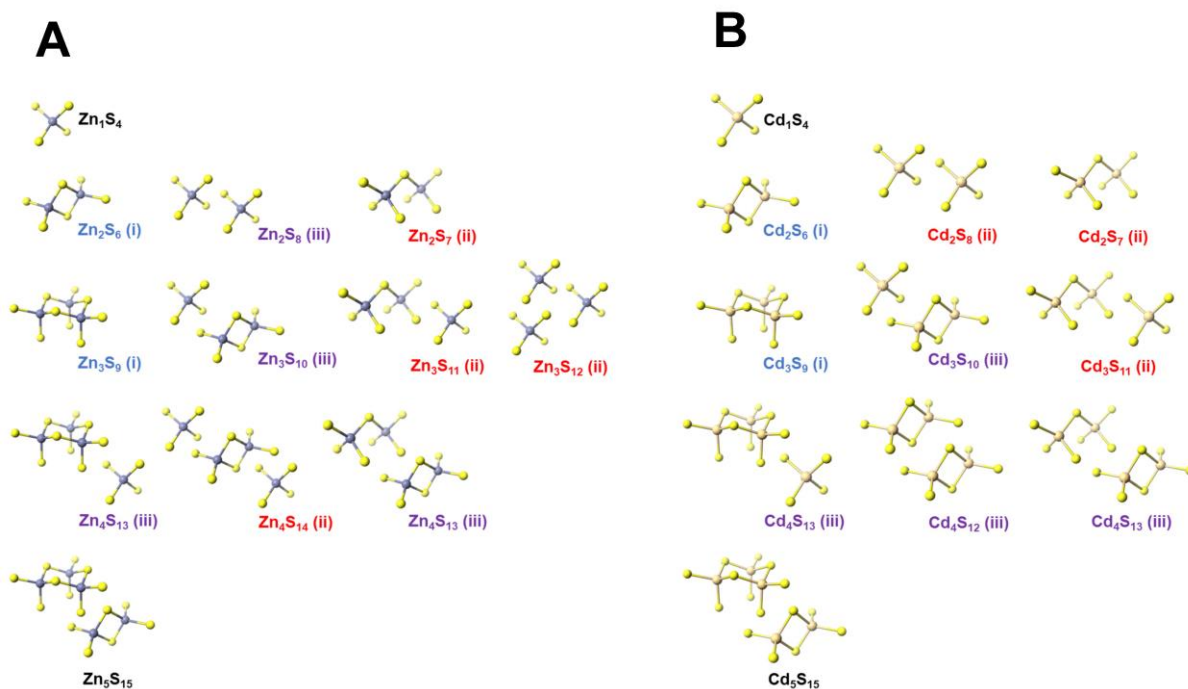


Figure 4-9. Intermediate Zn_xS_y and Cd_xS_y structures formed. Models of possible metal-thiolate structures formed during (A) Zn(II) and (B) Cd(II) metallation of apo-MT under (i) only native, (ii) only denaturing, or (iii) both native and denaturing conditions.

a later step in the metallation. Following the pattern of M_3S_{10} , the structure of M_4S_{13} can be described as the addition of one metal with all terminally bound cysteines to the M_3S_9 structure. Again, any metals in the M_3S_{10} structure would need to rearrange as the fourth metal is added. Cd_4S_{12} , which requires four bridging cysteines, likely describes two M_2S_6 structures, with the newly added Cd(II) binding to the terminally bound Cd(II) from the M_3S_{10} structure. This could also be a Cd(II) with a single bridging cysteine connecting to the M_3S_9 structure and three terminal cysteines.

Only a Cd_5MT species is observed with a stoichiometry of Cd_5S_{15} . This could describe the Cd_4S_{11} cluster in the α -domain plus a single Cd_1S_4 in the β -domain. It could also describe separate Cd_3S_9 and Cd_2S_6 structures.

The observed results establishes a loosely followed pattern for Zn(II) and Cd(II) binding under native conditions. It is commonly observed that for each metallation step, a single metal binds using only terminally bound structures for a single one terminally bound cysteine adds and is incorporated into a bridging structure upon binding to the next metal. This follows for $M_2S_6 \rightarrow M_3S_{10} \rightarrow M_4S_{13}$, all of which are observed for both Zn(II) and Cd(II) metallation. In some cases, formation of the bridging structure occurs without the additional terminally bound metal, as is the case for $M_2S_6 \rightarrow M_3S_9$. For this step, Zn(II) strongly prefers to form Zn_3S_{10} , while Cd(II) prefers to form Cd_3S_9 . Additionally, only Zn(II) forms the terminally bound Zn_2S_8 structure, while only Cd(II) forms the more bridging Cd_4S_{12} structure.

It has previously been suggested that under conditions where non-cooperative metal binding takes place, the metals bind using only terminal cysteines in a pathway of $M_1S_4 \rightarrow M_2S_8 \rightarrow M_3S_{12} \rightarrow M_4S_{16} \rightarrow M_5S_{20}$ before formation of any bridging thiolate structures.^{168,}
¹⁷¹ However, it can be seen from these ESI-MS data that specific bridging thiolate structures are seen after only two metals have bound. The only terminally bound structure observed at this step is Zn_2S_8 . It should be noted that although the structures formed during the Zn(II) and Cd(II) binding are very similar, their relative abundances observed in the ESI mass spectra show that Zn(II) prefers to form structure with less bridging thiolates, while Cd(II) tends to prefer the structures with more bridging thiolates. Cd(II) is known to

prefer cooperative binding to M_4S_{11} compared to Zn(II), a structure which involves formation of a network of bridging thiolate structures.¹⁷¹ Therefore it makes sense that Cd(II) forms bridging thiolate structures more easily than Zn(II).

4.3.9 Denaturation of apo-MT disrupts formation of bridging metal-thiolate structures

Under denaturing conditions, the Zn(II) and Cd(II) species that form generally contain less bridging cysteines than those formed under native conditions. When two Zn(II) are bound, higher abundances of Zn_2S_8 are formed as well as a new Zn_2S_7 species (Fig. 4-8B). Zn_3S_6 is no longer observed. Likewise, Cd_2S_8 , which was not observed in the native MT, forms in high abundance under denaturing conditions (Fig. 4-8D). Cd_2S_7 also forms. The newly observed M_2S_7 structure describes 2 metals with only one bridging cysteine between them.

Both Zn_3S_{10} and Cd_3S_{10} species are still observed under denaturing conditions (Fig. 4-8B,D). Zn_3S_9 and Cd_3S_9 however, do not appear to be able to form as these species are no longer observed. Rather, peaks corresponding to new species of Zn_3S_{11} , Zn_3S_{12} , and Cd_3S_{11} are seen in the ESI mass spectra. An M_3S_{11} structure is likely a terminally bound metal added to the M_2S_7 structure and M_3S_{12} describes three metals bound to only terminal cysteines each with M_1S_4 stoichiometry. With a mixture of three possible M_xS_y structures for Zn_3MT under denaturing conditions, this is the step of the metallation with the most diversity in structures seen.

When four metals are bound, the Zn_4S_{13} and Cd_4S_{13} species observed under native conditions still form under denaturing conditions. Additionally, Cd_4S_{12} still forms as well. These two Cd(II) bound species have similar relative intensities to each other compared to in the native spectra. This implies that the Cd_4MT structure is not as affected by denaturant compared to previous metallation steps. Conversely, a new Zn_4S_{14} structure is seen, which corresponds to a Zn_2S_6 structure plus two terminally bound metals. Also, Zn_4S_{13} and Cd_4S_{13} may consist of an M_2S_6 plus an M_2S_7 structure. This structure is more likely to form under denaturing conditions than under native conditions due to the presence of an M_2S_7 precursor.

Zn₅S₁₅ and Cd₅S₁₅ stoichiometries are both seen under denaturing conditions as the only species where five metals are bound. The identical stoichiometries suggest that both the Zn(II) and Cd(II)-bound MT structures are the same. However, the results from the CD spectra imply that Zn(II)-bound MTs still have a different backbone structure at this step. Previous research has suggested that Zn₅MT consists of three Zn(II) in the α -domain and two Zn(II) in the β -domain, while Cd₄MT is localized to the α -domain.¹⁷⁶ This could imply that Zn(II) forms two clusters, possibly consisting of an M₃S₉ and an M₂S₆ structure, stoichiometries which were both observed in MTs with a lower metal loading status. The Cd(II) structure may consist of an M₄S₁₁ cluster in the alpha domain and one terminally bound M₁S₄ in the beta domain, corresponding to the first cluster formed in the fully metallated, two-domain protein. However, other structures corresponding to an M₅S₁₅ stoichiometry are also possible, such as a single M₅S₁₅ cluster not localized to a single domain.

These results have shown that the partially metallated Zn(II) and Cd(II) bound MT species formed differ from those formed under native conditions. A trend is seen where the structures formed under denaturing conditions generally consist of more terminally bound cysteines and less bridging cysteines. As in the native protein, Zn(II) tends to prefer terminally bound species compared to Cd(II), forming structures such as Zn₃S₁₂ which contain no bridging structures.

Overall, the results combined from stopped-flow kinetics, CD spectroscopy, and ESI-MS show that the native structure of apo-MT does indeed impact the Zn(II) and Cd(II) metallation. Under native conditions, the binding is fast and specific bridging metal-thiolate structures are formed which form a scaffold for which more complicated structures can form. Under denaturing conditions, the binding is slow, and the bridging metal-thiolate structures are not able to form as efficiently, rather forming simpler structures. The initial denaturation of the apo-MT appears to impact the Cd(II) binding up to approximately 4 Cd(II) bound. The binding of additional Cd(II) does not seem to be affected by a high denaturant concentration, implying that sufficient metal-induced folding has taken place to overcome the unfolded MT backbone. The Zn(II) binding pathway under denaturing conditions is different. Evidence of MT backbone denaturation is detected at all Zn(II)

binding steps, suggesting that altered structures are forming under denaturing conditions compared to under native conditions. This suggests an amplified preference for Cd(II) binding over Zn(II) binding under denatured conditions.

4.4 Conclusions

MTs are resilient proteins that can bind a wide variety of metals under many different conditions. However, these results have shown that the metal binding pathways can be altered by changing the conditions under which the metallation takes place. Zn(II) and Cd(II) metallation rates responded differently to various pH conditions. The pH sensitivity to Zn(II) binding was justified by the inability of Zn(II) to form the Zn_4S_{11} cluster unless at very low pH levels. This differential pH sensitivity in Zn(II) and Cd(II) binding may have biological implications for the ubiquitously expressed MTs, potentially prioritizing Cd(II) cluster formation over Zn(II) homeostasis under lower pH conditions.

Unfolding the apo-MT impacted the rate of Zn(II) and Cd(II) metallation, the structure of the protein backbone during the metallation, and the specific metal-thiolate structures formed. The impact was greater on the Zn(II) binding than the Cd(II) binding, which can be related to the preference of Zn(II) to form structures with less bridging cysteines than Cd(II). This not only implies that the structure of the native apo-MT is important for Zn(II) binding, but also potentially gives insights into protein disfunction and misfolding as the apo-MT with the unfolded MT binds toxic Cd(II) more readily than essential Zn(II).

Chapter 5

5 The pH and Structure-Dependent Binding of Bismuth to Metallothionein 1a*

In the previous chapters, it was established that the compact structure of apo-MT as well as pH conditions impact the Zn(II) and Cd(II) metallation. MTs evolved in the presence of metals such as Zn(II) and Cu(I) which may have helped shape the binding properties.³¹³ The fully metallated Zn(II) and Cu(I) bound MT structures involve domain specific cluster structures.

This chapter focuses on bismuth, a xenobiotic metal with pharmaceutical applications.³¹⁴ Bismuth has no role in normal physiology and it would not have been present to influence the evolution of MTs. The binding of Bi(III) to MTs provides an interesting model to study the non-traditional metal-thiolate structures that can form in MTs.

Portions of this chapter have been previously published (Korkola et al. 2020³¹⁵ and Korkola et al. 2021³¹⁶). Data from previous publications are indicated in the appropriate figure captions.

5.1 Introduction

Bismuth is a group 15 metal known for its uses in the pharmaceutical industry. Its most well-known use is as an antimicrobial agent against *Helicobacter pylori* with medications such as De-Nol™, Tritec™/Pylorid™, and Pepto-Bismol.^{314, 317-320} Additionally, bismuth has potential for roles in cancer therapy, with recent studies using bismuth nanoparticles to

* A portion of this chapter has been published:

Korkola, N. C.; Scarrow, P. M.; Stillman, M. J., pH dependence of the non-cooperative binding of Bi³⁺ to human apo-metallothionein 1A: kinetics, speciation, and stoichiometry. *Metallomics* **2020**, *12* (3), 435-448.

Reproduced with permission from: The Royal Society of Chemistry

Korkola, N. C.; Hudson, E.; Stillman, M. J., Structurally restricted Bi(III) metallation of apo-βMT1a: metal-induced tangling. *Metallomics* **2021**, *13* (5).

Reproduced with permission from: Oxford University Press

increase the effect of radiation in tumours.³²¹⁻³²⁴ Other potential uses in cancer treatment include using bismuth to relieve side effects of cancer drugs such as cisplatin and doxorubicin.³²⁵ Recently, a study has suggested that ranitidine bismuth citrate may relieve symptoms of Sars-Cov-2 in hamsters.³²⁶

In treatments against *Helicobacter pylori*, bismuth inhibits the growth of the bacteria³²⁷ through a variety of mechanisms, some which may involve binding to cysteine residues.³²⁸⁻³²⁹ For example, bismuth may bind to the cysteine in the active sites of urease, and displace zinc from the cysteine in the binding sites of alcohol dehydrogenase.³³⁰⁻³³¹

Administered alongside anticancer drugs cisplatin and doxorubicin, bismuth counteracts the nephrotoxic and cardiotoxic effects of these drugs, respectively by inducing the cysteine-rich metallothionein (MT) in the kidney and heart tissues.^{187, 325, 332-338} Considering that the uses of bismuth compounds in medicine often involve cysteine residues in proteins, it is important to study the interactions of bismuth with cysteine-rich proteins, such as metallothioneins (MTs).

MTs *in vivo* maintain homeostasis of essential metals, bind and sequester toxic heavy metals, and provide protection against oxidative stress.³³⁹⁻³⁴² Although MTs are most well-known as Zn(II)-binding proteins, they have also been shown to bind to a variety of “non-traditional” metals not usually found in biology such as Ag(I) or Pt(II).^{187, 197} Mammalian isoforms MT1 and MT2 are upregulated by a variety of metals including Bi(III).³⁴³⁻³⁴⁶

Mammalian MTs are most well-known for their two-domain structure formed upon metallation with seven Cd(II) or Zn(II).^{143, 146, 171, 272, 276, 347-351} The apo-MT at physiological pH is intrinsically disordered with a bundled structure in which the cysteines are not uniformly solvent accessible, unless unfolded using a denaturant.^{160-161, 252} In Chapter 4, it was shown that the structure of apo-MT impacted the partially metallated Zn(II) and Cd(II) bound MT structures formed.

The stepwise metallation pathways followed when Bi(III) binds to MTs have not been widely studied, even though the protective effects of MT against nephrotoxicity after induction by Bi(III)³⁵²⁻³⁵⁴ suggests the formation of Bi-MT species.¹⁸⁷

Sun et al.²⁰², using UV-visible absorption, ¹H NMR, and extended X-ray absorption fine structure (EXAFS) spectroscopic methods determined that Bi(III) bound to rabbit liver Zn₇β α MT₂, displacing the Zn(II), with a 7:1 ratio. The coordination of the Bi(III) was found to be Bi(S_{cys})₃ with an occasional fourth bond to oxygen. The clusters were described to be “distorted compared to those of Cd₇MT and Zn₇MT”.²⁰² It was also reported that [Bi(cit)]⁻ and [Bi(EDTA)]⁻ displaced Cd(II) from Cd₇MT and Zn(II) from Zn₇MT.²⁰²

An electrospray ionization (ESI) mass spectral study by Ngu et al.¹⁷⁸ of Bi(OAc)₃ binding to β α MT, βMT, and α MT at pH 2.3–2.7 showed species forming up to Bi₇β α MT, Bi₃βMT, and Bi₄ α MT upon addition of excess Bi(OAc)₃. A unique feature of ESI-MS is that the individual species can be observed, and thus information about the binding pathway can be obtained. The binding pathways were shown to be non-cooperative, favouring no specific species, rather forming a Binomial-type distribution of species before saturation.¹⁷⁸ This non-cooperative binding pathway has also been observed for the trivalent metal As(III). However, As(III) only binds up to As₃βMT, As₃ α MT, and As₆β α MT.^{177, 355} These binding pathways contrast the cooperativity seen under certain conditions for metals such as Cd(II), Zn(II), Cu(I), and Ag(I) binding to MT.^{171, 179, 182, 356}

Although it has been established that Bi(III) will bind to MTs, there are still questions about the exact pathway and stoichiometry of the binding to MT1a and its fragments. Throughout the limited research on Bi(III) binding to MTs, reaction conditions have varied greatly. The binding of Bi(III) to Zn₇MT, and Zn₂Cd₅MT have been studied using [Bi(cit)]⁻ and [Bi(EDTA)]⁻ at neutral pH,²⁰² while the binding to apo-MT has been studied using Bi(OAc)₃ at low pH.¹⁷⁸ The possibility of structural differences, pH, or Bi(III) salt affecting the binding has been largely neglected.

In this chapter, a description of Bi(III) binding to MT1a under a variety of conditions using ESI-MS methods is provided. First, the dependence of Bi(III) salt and pH on Bi_nMT species formation was explored. It was found that up to Bi₇MT formed only using [Bi(cit)]⁻ at pH 2.6 with a weakly bound adduct forming Bi₈MT. When using [Bi(EDTA)]⁻, up to Bi₇MT was formed at pH 2.6, while only Bi₆MT was formed at pH 7.4. Due to competition from the EDTA ligand, much larger stoichiometric amounts of Bi(III) were required to saturate

the MT, particularly under low pH conditions. The binding constants for these three conditions were determined. Cysteine modification experiments were performed to probe the proposed Bi_1S_3 structure. The binding pathway and binding constants were also determined for the titration of $[\text{Bi}(\text{EDTA})]^-$ into the fragments βMT and αMT at pH 7.4, which aligned closely with the results observed for the full $\beta\alpha\text{MT}$ protein.

Using βMT , the effect of protein denaturation on $\text{Bi}(\text{III})$ binding was studied. It was found that a higher proportion of Bi_3MT formed under denaturing conditions. Finally, $[\text{Bi}(\text{EDTA})]^-$ was titrated into Zn_7MT . Under this condition, Bi_7MT formed after only adding 8 molar equivalents of $\text{Bi}(\text{III})$. These studies suggest that the structure and the initial metal-loading status of MT is important for the binding pathway of $\text{Bi}(\text{III})$.

5.2 Materials and Methods

5.2.1 Protein expression, purification, and preparation for experiments

Recombinant human (rh) $\beta\alpha\text{MT}$, βMT , and αMT were expressed and purified as described in Chapter 2. Apo- $\beta\alpha\text{MT}$, apo- βMT , and apo- αMT at pH 7.4 were prepared as described in Chapter 2. Apo- $\beta\alpha\text{MT}$ at pH 2.6 was also prepared as described in Chapter 2, using ammonium formate at pH 2.6 in place of the ammonium formate at pH 7.4. $\text{Zn}_7\beta\alpha\text{MT}$ was prepared by adding 7 mol. eq. $\text{Zn}(\text{OAc})_2$ to apo- $\beta\alpha\text{MT}$ at pH 7.4. The pH of the $\text{Zn}_7\beta\alpha\text{MT}$ was measured and adjusted back to pH 7.4 using dilute ammonium hydroxide. This step was necessary due to a reduction in pH caused by proton displacement upon $\text{Zn}(\text{II})$ binding.

5.2.2 Electrospray ionization mass spectrometry experiments

All mass spectrometric data was collected on a Bruker MicroTOF II electrospray ionization mass spectrometer using the parameters described in Chapter 2. The data were collected and averaged over 1-2 min. The data were deconvoluted over the range 7000-10000 Da for $\beta\alpha\text{MT}$, 3500-5000 Da for βMT , and 3800-5800 for αMT .

5.2.3 Titrations of $[\text{Bi}(\text{cit})]^-$ into apo-MT at pH 2.6

$[\text{Bi}(\text{cit})]^-$ was added to solutions of 50 μM apo- $\beta\alpha\text{MT}$ in varying molar equivalences at pH 2.6. The samples were allowed to equilibrate for 10 min before measurement on the mass

spectrometer. A sample with 7.5 mol. eq. $[\text{Bi}(\text{cit})]^-$ was centrifuged for 1 h after the initial MS measurement to observe the loss of the Bi_8MT species. $[\text{Bi}(\text{cit})]^-$ titrations were only performed at pH 2.6, as $[\text{Bi}(\text{cit})]^-$ was insoluble at higher pH levels.

5.2.4 Titrations of $[\text{Bi}(\text{EDTA})]^-$ into apo-MT at pH 2.6

$[\text{Bi}(\text{EDTA})]^-$ is an ideal Bi(III) compound with which to study the interactions of Bi(III) and MTs at physiological pH because unlike other Bi(III) compounds, it is soluble at neutral pH. It is important to note here that because EDTA has 4 acidic protons, a distribution of protonated species will always exist. To calculate that distribution at any pH, one needs to use the 4 pKa's, which is described in more detail when the determination of conditional binding constants is discussed later in this section (5.2). Throughout this chapter, "EDTA" is used when referring to the ligand alone as an abbreviation for the multiple protonated species that exist. For consistency with previous literature,²⁰² the formula $[\text{Bi}(\text{EDTA})]^-$ is used for the coordinated Bi(III) complex.

$[\text{Bi}(\text{EDTA})]^-$ was added to solutions of 50 μM apo- $\beta\alpha\text{MT}$ in varying molar equivalences at pH 2.6. As the binding of $[\text{Bi}(\text{EDTA})]^-$ is slow at pH 2.6, The samples were allowed to equilibrate for 6 h before measurement on the mass spectrometer. Samples with over 20 mol. eq. or 100 mol. eq. $[\text{Bi}(\text{EDTA})]^-$ added were centrifuged for 1 h or 2 h, respectively prior to MS measurement. This step was required because the excess $[\text{Bi}(\text{EDTA})]^-$ overwhelmed the spectrum, obscuring the MT peaks.

5.2.5 Titrations of $[\text{Bi}(\text{EDTA})]^-$ into apo-MT at pH 7.4

$[\text{Bi}(\text{EDTA})]^-$ was added to solutions of either 50 μM apo- $\beta\alpha\text{MT}$, apo- βMT , or apo- αMT in varying molar equivalences at pH 7.4. The samples were allowed to equilibrate for 10 min before measurement on the mass spectrometer. $[\text{Bi}(\text{EDTA})]^-$ was also added to solutions of 50 μM $\text{Zn}_7\beta\alpha\text{MT}$ in varying molar equivalences at pH 7.4. The samples were allowed to equilibrate for 16 h before measurement on the mass spectrometer.

5.2.6 Trypsin digestion experiments

Samples of apo- $\beta\alpha\text{MT}$ and $\text{Bi}_2\beta\alpha\text{MT}$ at pH 7.4 were digested with trypsin in a 1:20 w/w ratio at 37 °C for 30 min. The samples were analysed on the mass spectrometer without

quenching the reaction by reducing the pH to avoid rearrangement of the $\text{Bi}_2\beta\alpha\text{MT}$ structure. The fractional contribution of each fragment peak to the total intensity of the spectrum was determined. The matching fragment peaks in both spectra were then normalized to each other between 0 and 1 to compare the gain or loss in fractional intensity in the different conditions.

5.2.7 Cysteine modification experiments

$\beta\alpha\text{MT}$ with a mixture of 6 and 7 Bi(III) bound was prepared at pH 2.6 via a titration of $[\text{Bi(cit)}]^-$ into apo- $\beta\alpha\text{MT}$ and measured using ESI-MS. 12 mol. eq. of benzoquinone (Bq) was added to this sample and allowed to equilibrate for 10 min before measurement on the mass spectrometer. $\text{Bi}_2\beta\alpha\text{MT}$ formed from a titration of $[\text{Bi(EDTA)}]^-$ into apo- $\beta\alpha\text{MT}$ at pH 7.4 was measured using ESI-MS. 14 mol. eq. N-ethylmaleimide (NEM) was added to this sample and allowed to equilibrate for 10 min before measurement on the mass spectrometer. Apo- βMT was prepared at pH 6.9 in the same manner as for all other experiments, with pH 6.9 ammonium formate used instead of pH 7.4. The cysteine modifier Bq is ineffective above neutral pH, requiring the pH to be lowered for this experiment. 1.5 mol. eq. $[\text{Bi(EDTA)}]^-$ was initially titrated in and measured on the ESI mass spectrometer to confirm that the binding pathway was like that at pH 7.4. Another 0.5 mol. eq. of $[\text{Bi(EDTA)}]^-$ was added to bring the total to 2 mol. eq. and this sample was measured on the ESI mass spectrometer. Excess 10 mM Bq (40 mol. eq.) was added to this sample and allowed to equilibrate for 10 min before obtaining a mass spectrum.

5.2.8 Metallation of denatured apo- βMT with $[\text{Bi(EDTA)}]^-$

Apo- βMT at pH 7.4 was split into 2 samples. 8 M GdmCl was added to one of the samples to make a final concentration of 4 M GdmCl. The solutions were allowed to equilibrate for 30 min. A 5-mol. eq. aliquot of $[\text{Bi(EDTA)}]^-$ was added to each sample. Since metallation of MT has been shown to be slower in the presence of denaturants, the samples were both allowed 1 hour to equilibrate after addition of the $[\text{Bi(EDTA)}]^-$ to ensure complete metallation. The sample containing the GdmCl was passed down a PD-10 column and buffer exchanged using the centrifugal filter units at 3901 g (4500 rpm) for 30 min. The purpose of this step was to remove the GdmCl, as its presence would overwhelm the mass

spectral signal. Following this step, both samples were measured on the ESI mass spectrometer.

5.2.9 pH dependence of Bi₂βMT

A 2-mol. eq. aliquot of [Bi(EDTA)]⁻ was added to apo-βMT at pH 7.4. The sample was measured on the ESI mass spectrometer. Dilute formic acid was added to the Bi₂βMT solution to bring the pH to 5, and then to pH 2. Mass spectra were measured after both pH changes.

5.2.10 Metal exchange between Bi₂βMT, Cd₃βMT, and Zn₃βMT

2 mol. eq. [Bi(EDTA)]⁻, 3 mol. eq. Cd(OAc)₂, and 3 mol. eq. Zn(OAc)₂ were added to separate samples of apo-βMT at pH 7.4 to make Bi₂βMT, Cd₃βMT, and Zn₃βMT, respectively. An ESI mass spectrum was obtained for each sample to ensure the desired product was made. 1:1 mixtures of Bi₂βMT and Cd₃βMT, Bi₂βMT and Zn₃βMT, and Cd₃βMT and Zn₃βMT were prepared and allowed to equilibrate for 12 h. Each sample was measured on the ESI mass spectrometer to determine the extent of metal exchange.

5.2.11 Titration simulations and determination of conditional binding constants

The species formed from the experimental titrations of [Bi(cit)]⁻ and [Bi(EDTA)]⁻ into apo-MTs were plotted as a function of the mol. eq. [Bi(EDTA)]⁻ added. The Hyperquad Simulation and Speciation (HySS) program was used to simulate the titrations and to determine the relative conditional binding constants of Bi(III) to apo-MTs.³⁵⁷

The use of conditional binding constants is necessary because the proton competition for the EDTA ligand directly modifies the binding constant $K_{[Bi(EDTA)]^-}$. To obtain the correct value for the conditional binding constant, we must adjust for the fraction of EDTA⁴⁻ available for binding at pH 7.4. This is achieved using the fractional composition parameter α_4 , described generally in the literature.³⁵⁸ The value of α_4 for EDTA at pH 7.4 was calculated to be 1.3×10^{-3} using the 4 pKa values for protonation of EDTA⁴⁻: 1.99, 2.67, 6.16, 10.26.³⁵⁸⁻³⁵⁹ The conditional binding constant $K'_{[Bi(EDTA)]^-}$ was calculated using α_4

and the known binding constant $\log K_{[\text{Bi}(\text{EDTA})]^-} = 27.8^{359-360}$ using Equation 5-1. At pH 7.4, $\alpha_4 = 1.3 \times 10^{-3}$ and at pH 2.6, $\alpha_4 = 2.4 \times 10^{-12}$.

$$K'(\text{pH}7.4) = \alpha_4 \times K_{[\text{Bi}(\text{EDTA})]^-} \quad (5-1)$$

The conditional binding constants K' were determined using this method for the titration of $[\text{Bi}(\text{EDTA})]^-$ into apo- $\beta\alpha$ MT, apo- β MT, and apo- α MT at pH 7.4 and apo- $\beta\alpha$ MT at pH 2.6. The conditional binding constants for the titration of $[\text{Bi}(\text{cit})]^-$ into apo- $\beta\alpha$ MT at pH 2.6 were estimated by scaling the first binding constant to K_1' of the titration of $[\text{Bi}(\text{EDTA})]^-$ into apo- $\beta\alpha$ MT at pH 2.6.

5.2.12 UV-Visible absorption experiments

Apo-MT samples were diluted to 5 μM . UV-visible absorption spectra were obtained using a Cary-60 spectrometer. The spectra were scanned between 200 and 600 nm with a scan rate of 600 nm/min. Prior to each experiment, an air baseline, a spectrum of 20 mM ammonium formate (pH 7.4 or pH 2.6), and spectrum of the starting MT (apo- $\beta\alpha$ MT at pH 2.6, apo- $\beta\alpha$ MT at pH 7.4, or $\text{Zn}_7\beta\alpha$ MT at pH 7.4) prior to addition of Bi(III) were obtained. All resulting spectra from these experiments were manually subtracted from the ammonium formate spectrum of the appropriate pH.

Spectra at each step of a titration of $[\text{Bi}(\text{cit})]^-$ into apo- $\beta\alpha$ MT at pH 2.6 and $[\text{Bi}(\text{EDTA})]^-$ into apo- $\beta\alpha$ MT at pH 7.4 were obtained with 10 min between each new addition and measurement. The UV-visible absorption spectra over time were measured for a reaction of 200 mol. eq. $[\text{Bi}(\text{EDTA})]^-$ and apo- $\beta\alpha$ MT at pH 2.6. Spectra were collected every 2 min for 20 min, and then every 5 min for 800 min. The UV-visible absorption spectra over time were also measured for a reaction of 8 mol. eq. $[\text{Bi}(\text{EDTA})]^-$ and $\text{Zn}_7\beta\alpha$ MT at pH 7.4. Spectra were collected every 0.5 min for 20 min, and then every 5 min for 800 min.

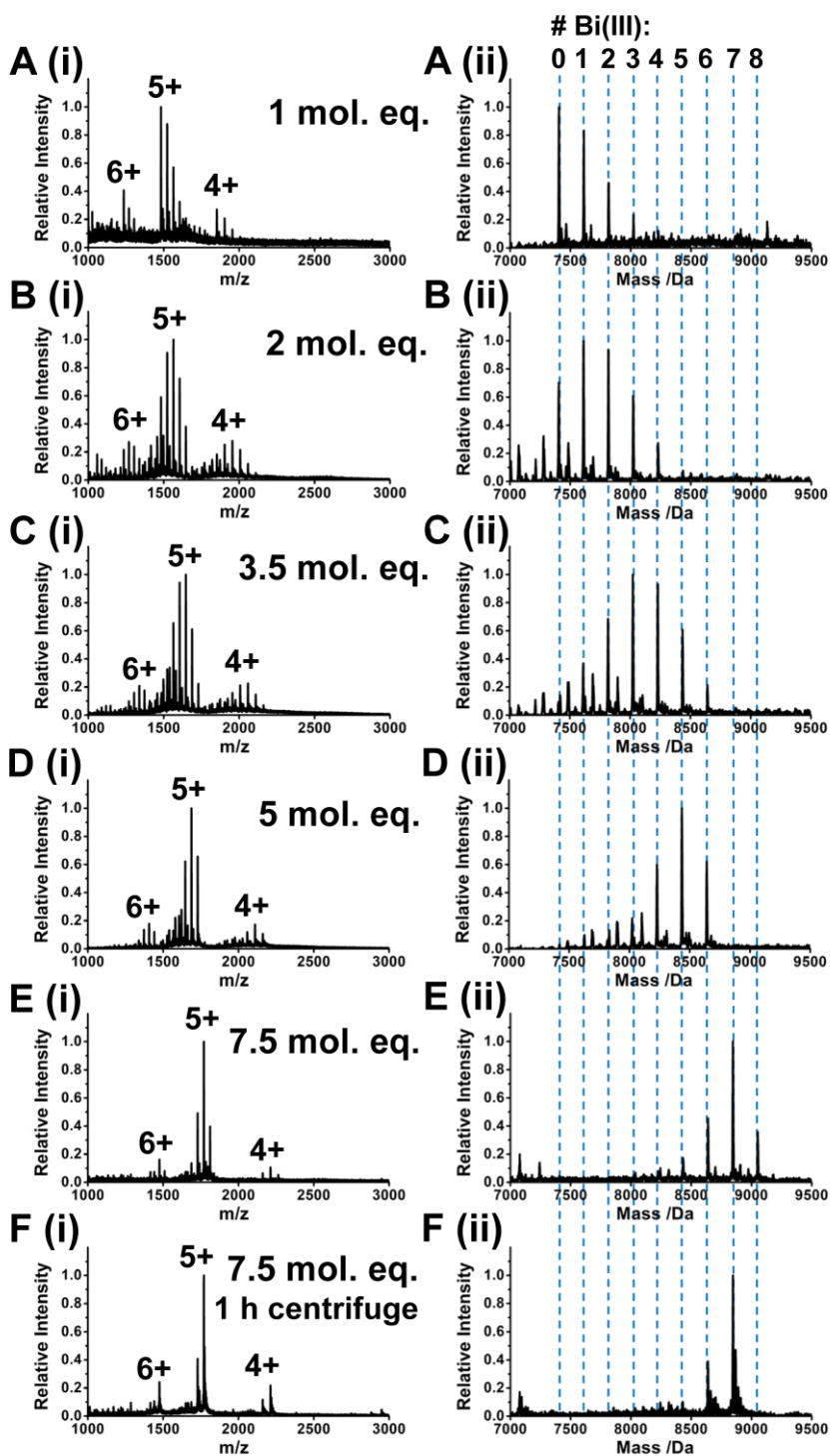


Figure 5-1. A titration of $[\text{Bi}(\text{cit})]^-$ into apo- $\beta\alpha\text{MT}$ at pH 2.6 monitored using ESI-MS. (i) Charge state and (ii) deconvoluted ESI mass spectra show the stepwise reaction after (A) 1, (B) 2, (C) 3.5, (D) 5, and (E) 7.5 mol. eq. $[\text{Bi}(\text{cit})]^-$ added. (F) shows the resulting spectra after 1 h centrifugation of the sample shown in (E). Adapted from Korkola et al., 2020 with permission from The Royal Society of Chemistry to include updated data.

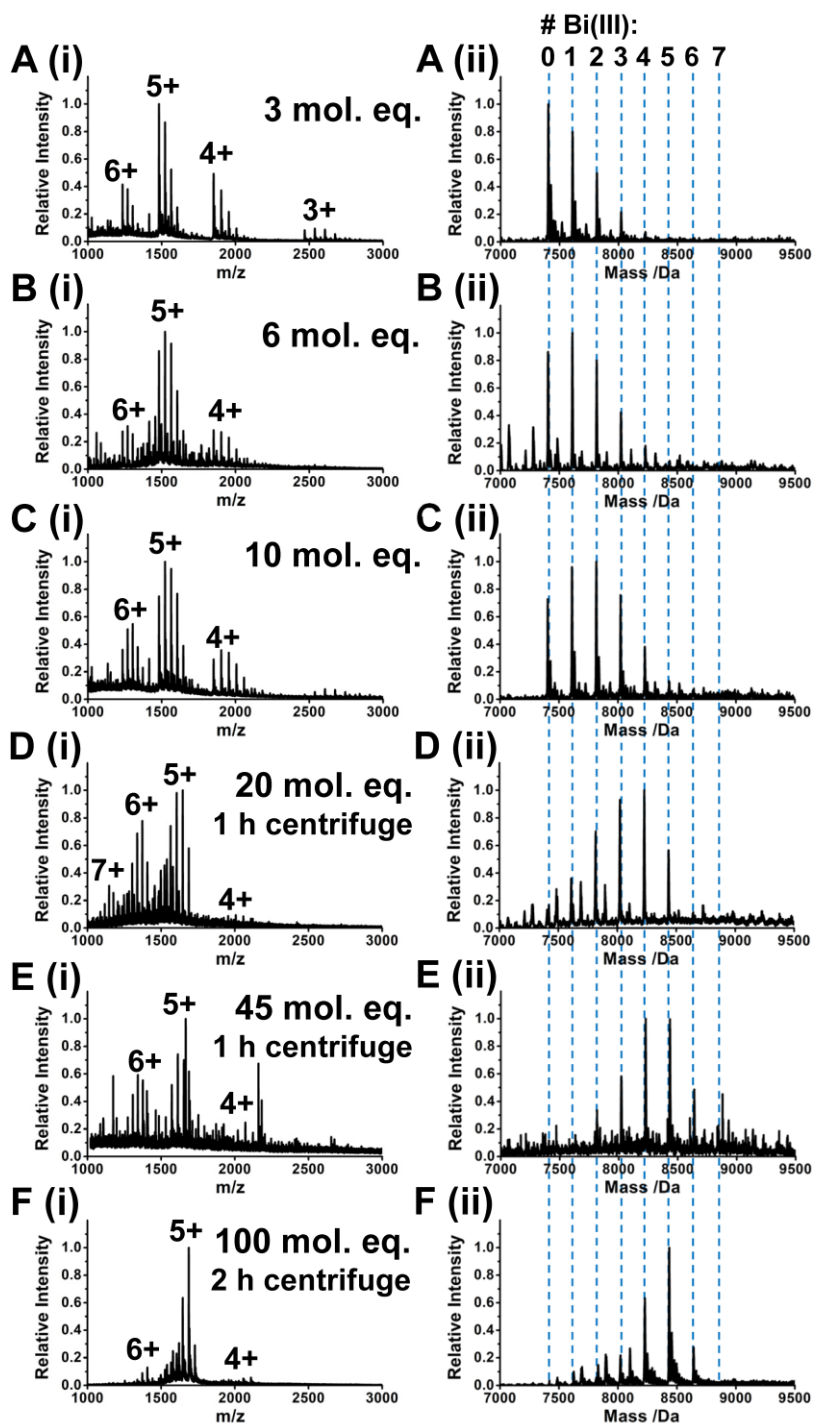


Figure 5-2. A titration of $[\text{Bi}(\text{EDTA})]^-$ into apo- $\beta\alpha\text{MT}$ at pH 2.6 monitored using ESI-MS. (i) Charge state and (ii) deconvoluted ESI mass spectra show the stepwise reaction after (A) 3, (B) 6, (C) 10, (D) 20, (E) 45, and (F) 100 mol. eq. $[\text{Bi}(\text{EDTA})]^-$ added. Spectra were measured 6 h after addition of $[\text{Bi}(\text{EDTA})]^-$. The spectra in (D) and (E) were collected after after 1 h centrifugation of the sample. The spectra in (F) were collected after 2 h centrifugation of the sample. Adapted from Korkola et al., 2020 with permission from The Royal Society of Chemistry to include updated data.

5.3 Results and Discussion

5.3.1 The pH and anion dependence of Bi(III) binding to apo-MT

The binding pathway of Bi(III) to apo-MT was probed through titrations of $[\text{Bi}(\text{cit})]^-$ into apo-MT at pH 2.6 (Fig. 5-1) and $[\text{Bi}(\text{EDTA})]^-$ into at pH 2.6 (Fig. 5-2) and pH 7.4 (Fig. 5-3) using ESI-MS. The binding of $[\text{Bi}(\text{cit})]^-$ to apo-MT at pH 2.6 is entirely non-cooperative (Fig. 5-1). The Bi(III) bound in a 1:1 ratio to amount added, meaning the citrate anion provided minimal competition. From Fig 5-1E, it appears as if the stoichiometry forms up to Bi_8MT . However, upon centrifugation of the sample, the Bi_8MT species is no longer observed (Fig. 5-1F). This suggests that the eighth Bi(III) is an adduct resulting from excess amounts of Bi(III) in solution.

Titrations with $[\text{Bi}(\text{EDTA})]^-$ at pH 2.6 result in a similar outcome as with citrate (Fig. 5-2). A non-cooperative pathway was observed. However, much larger stoichiometric amounts of $[\text{Bi}(\text{EDTA})]^-$ were required to saturate the MT compared to when $[\text{Bi}(\text{cit})]^-$ was used. Even after addition of 45 mol. eq., only a small fraction of Bi_6MT , and an even smaller fraction of Bi_7MT forms (Fig. 5-2E). At this point in the titration, species with a metal saturation as low as Bi_2MT remain. After 100 mol. eq. $[\text{Bi}(\text{EDTA})]^-$ added, Bi_5MT is the major species with a lower fraction of the lesser metallated species remaining (Fig. 5-2F). However, Bi_6MT still does not form in a significant fraction. Interestingly, the Bi_7MT peak is not observed. This is potentially due to the seventh Bi(III) being removed during the longer centrifugation process, much like with the Bi_8MT species during the $[\text{Bi}(\text{cit})]^-$ titration.

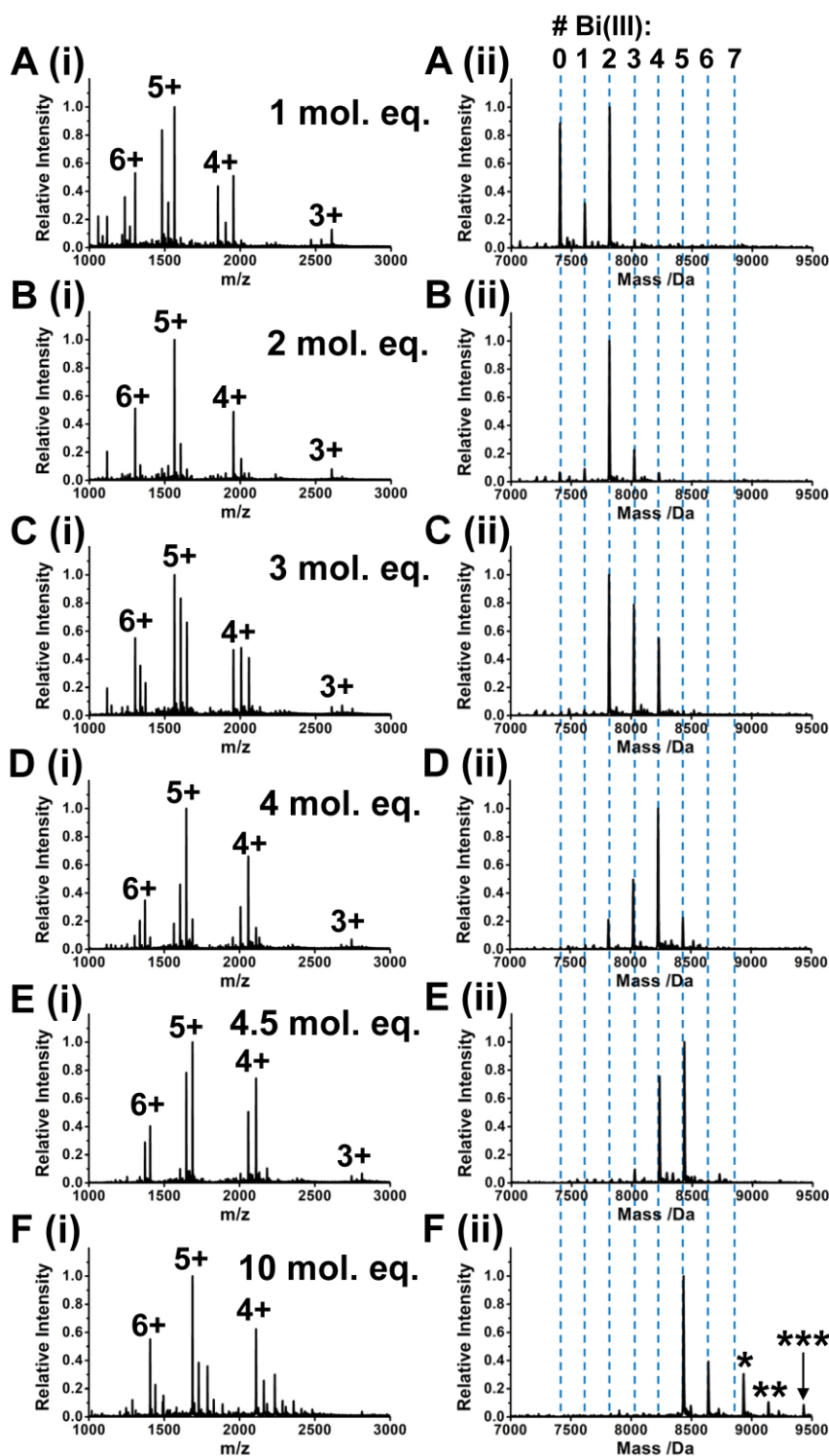


Figure 5-3. A titration of $[\text{Bi}(\text{EDTA})]^-$ into apo- $\beta\alpha\text{MT}$ at pH 7.4 monitored using ESI-MS. (i) Charge state and (ii) deconvoluted ESI mass spectra show the stepwise reaction after (A) 1, (B) 2, (C) 3, (D) 4, (E) 4.5, and (F) 10 mol. eq. $[\text{Bi}(\text{EDTA})]^-$ added. Species corresponding to $\text{Bi}_6\text{MT-EDTA}$, $\text{Bi}_7\text{MT-EDTA}$, and $\text{Bi}_7\text{MT-EDTA}_2$ are denoted (*), (**), and (***), respectively.

A different binding pathway is observed during a titration of $[\text{Bi}(\text{EDTA})]^-$ into apo-MT at pH 7.4 (Fig. 5-3). The binding of Bi(III) is cooperative to Bi_2MT , as shown by significant fractions of apo-MT and Bi_2MT existing in the sample after addition of 1 mol. eq. $[\text{Bi}(\text{EDTA})]^-$ (Fig. 5-3A). Comparatively, the Bi_1MT species is not favoured. After addition of 2 mol. eq. $[\text{Bi}(\text{EDTA})]^-$, the Bi_2MT species dominates the spectrum, with only small fractions of Bi_1MT and Bi_3MT (Fig. 5-3B). The formation of Bi_4MT is semi-cooperative. Bi_3MT is never the most abundant species but still forms in significant fractions compared to Bi_1MT (Fig. 5-3C-D). After the addition of 4.5 mol. eq. $[\text{Bi}(\text{EDTA})]^-$, only Bi_4MT and Bi_5MT are observed in the spectrum (Fig. 5-3E).

Bi_{1-5}MT species are formed from stoichiometric additions of $[\text{Bi}(\text{EDTA})]^-$ at pH 7.4, contrasting the titration at pH 2.6. where excess $[\text{Bi}(\text{EDTA})]^-$ was required to form the higher metallated species. However, only after addition of excess $[\text{Bi}(\text{EDTA})]^-$ (10 mol. eq.), does Bi_6MT form at pH 7.4 (Fig. 5-3F). In this spectrum, species corresponding to $\text{Bi}_6\text{MT-EDTA}$, $\text{Bi}_7\text{MT-EDTA}$, and $\text{Bi}_7\text{MT-EDTA}_2$ are observed, labelled as (*), (**), and (***) respectively. In the case of $\text{Bi}_6\text{MT-EDTA}$, this is likely an intermediate species that forms before the EDTA ligand dissociates, forming Bi_6MT . Conversely, since Bi_7MT alone is never observed in this titration, the formation of $\text{Bi}_7\text{MT-EDTA}$, and $\text{Bi}_7\text{MT-EDTA}_2$ may be the result of excess $[\text{Bi}(\text{EDTA})]^-$ in solution forming adducts on the protein. The seventh Bi(III) may bind to a sulfur or oxygen ligand on Bi_6MT while still remaining bound to the EDTA. If not enough sites on MT are available, it may not be able to dissociate from the EDTA ligand.

The experimental and simulated speciation curves allow for the determination of the relative binding constants for the titration of Bi(III) into apo-MT using $[\text{Bi}(\text{cit})]^-$ at pH 2.6 (Fig. 5-4A), $[\text{Bi}(\text{EDTA})]^-$ at pH 2.6 (Fig. 5-4B), and $[\text{Bi}(\text{EDTA})]^-$ at pH 7.4 (Fig. 5-4C). Both speciation distributions at pH 2.6 possess the pattern of a typical non-cooperative binding pathway, where the formation of no particular species is favoured over another. In the speciation distribution for the $[\text{Bi}(\text{cit})]^-$ addition to apo-MT, for approximately 0-4 mol. eq. added the distribution is quite broad, with multiple overlapping species from Bi_{0-5}MT observed at a single point. This indicates a pattern of gently, rather than sharply, decreasing binding constants (Table 5-1).

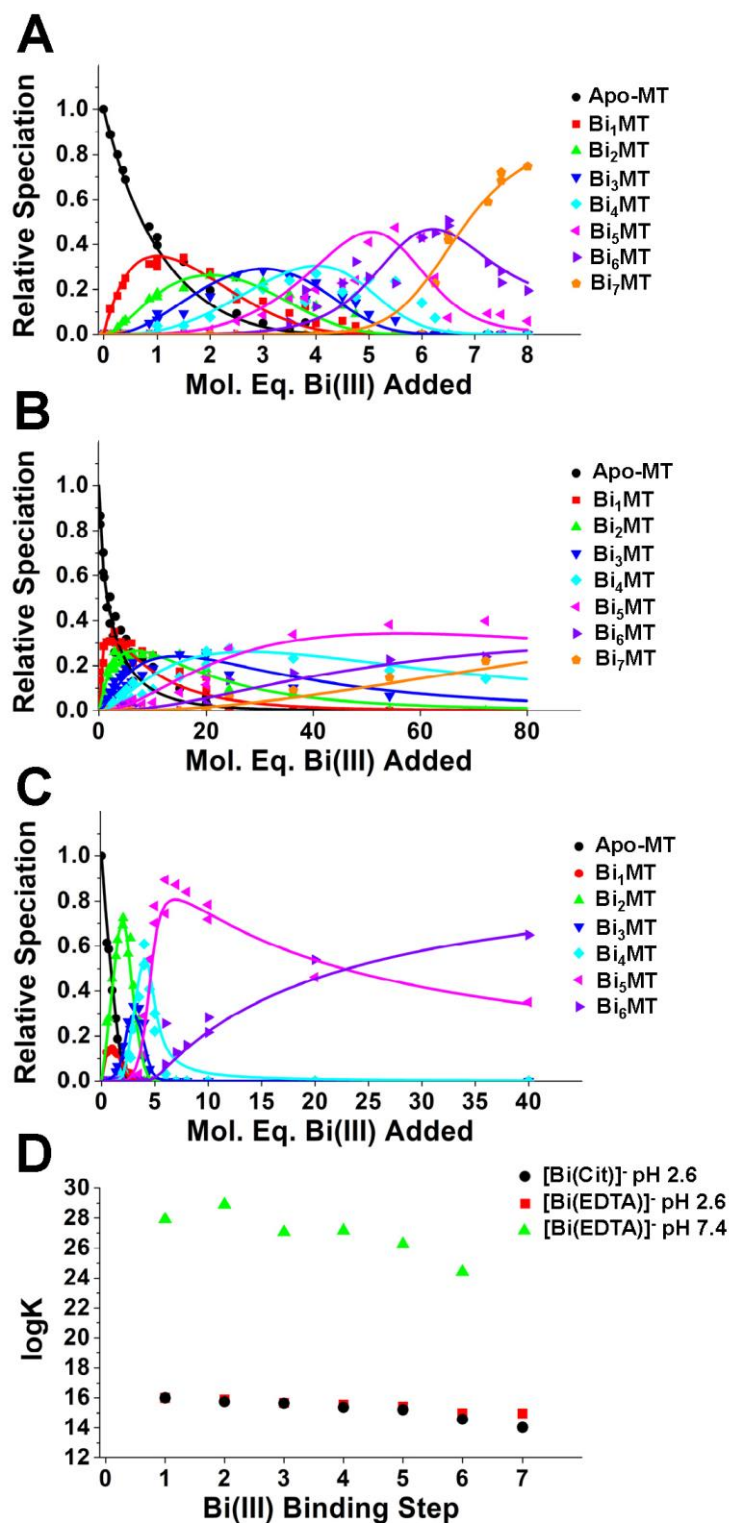


Figure 5-4. Speciation curves and calculated binding constants for the titration of Bi(III) into apo- $\beta\alpha$ MT. Experimental (points) and simulated (lines) speciation distributions showing the titration of (A) [Bi(cit)]⁻ at pH 2.6, (B) [Bi(EDTA)]⁻ at pH 2.6, and (C) [Bi(EDTA)]⁻ at pH 7.4 into apo- $\beta\alpha$ MT. (D) A plot of the binding constant for each titration at each step.

Towards the end of the titration, between 5 and 8 mol. eq. added, the Bi₂₋₄MT species disappear and Bi₆₋₇MT dominate the speciation without the broad overlap from other species. This pattern indicates more sharply decreasing binding constants. This suggests that beyond Bi₅MT, a conformational change may be required in the MT to accommodate more Bi(III). This effect is not observed as strongly in the titration of [Bi(EDTA)]⁻ at pH 2.6, with Bi₆MT and Bi₇MT appearing while Bi₁₋₃MT are still seen in the speciation curve.

The cooperative nature of the [Bi(EDTA)]⁻ binding to apo-MT at pH 7.4 is apparent in the speciation distribution. Bi₂MT at its peak represents approximately 75% of the species observed. The semi-cooperative formation of Bi₄MT is also seen with it reaching 50% of all species at its peak. The formation of Bi₁MT and Bi₃MT are relatively low, reaching 10% and 35% of species at their peaks, respectively. Between 5 and 10 mol. eq. [Bi(EDTA)]⁻ added, approximately 80-90% of the species in solution are Bi₅MT. At first glance, this makes the formation of Bi₅MT appear strongly cooperative. However, this is not the case. The build-up of the Bi₅MT species is in fact due to the low binding constant of Bi₆MT.

Table 5-1. Relative Bi(III)-MT binding constants. The relative Bi(III)-MT binding constants determined from the fit of a titration of [Bi(cit)]⁻ at pH 2.6, [Bi(EDTA)]⁻ at pH 2.6, and [Bi(EDTA)]⁻ at pH 7.4.

	[Bi(cit)] ⁻ pH 2.6	[Bi(EDTA)] ⁻ pH 2.6	[Bi(EDTA)] ⁻ pH 7.4
logK ₁	15.99	15.99	27.92
logK ₂	15.74	15.87	28.92
logK ₃	15.64	15.67	27.07
logK ₄	15.37	15.55	27.17
logK ₅	15.21	15.42	26.27
logK ₆	14.57	14.97	24.42
logK ₇	14.03	14.96	-

The binding constants relative to $K_{[\text{Bi}(\text{EDTA})]^-}$ for each step resulting from the fit of the speciation are plotted in Fig. 5-4D and listed in Table 5-1. Immediately apparent is the reduction of binding constants at pH 2.6 compared to pH 7.4. The binding constants for the titrations at pH 2.6 both follow a gently decreasing pattern, indicating non-cooperativity. $\text{Log}K_6$ and $\text{log}K_7$ decrease more sharply, although this is more apparent for $[\text{Bi}(\text{cit})]^-$ than for $[\text{Bi}(\text{EDTA})]^-$. With $[\text{Bi}(\text{EDTA})]^-$ at pH 7.4 $\text{log}K_2$ and $\text{log}K_4$ are both elevated, indicating cooperativity with the rest of the binding constants following the trend of a gentle decrease. $\text{Log}K_6$ is nearly two orders of magnitude lower than $\text{log}K_5$.

The UV-visible absorption spectra of Bi(III)-bound MTs are pH-dependent (Fig. 5-5). The spectra formed at low pH, shown in Fig. 5-5Ai using $[\text{Bi}(\text{cit})]^-$ and Fig. 5-5Bi using $[\text{Bi}(\text{EDTA})]^-$ show a $\text{S} \rightarrow \text{Bi}$ LMCT band at 368 nm that increases as more Bi(III) bind. The absorbances at 368 nm as a function of Bi(III) added (for $[\text{Bi}(\text{cit})]^-$) or time (for $[\text{Bi}(\text{EDTA})]^-$) are plotted in Fig. 5-5Aii and Bii, respectively. For $[\text{Bi}(\text{cit})]^-$, this absorbance increases stoichiometrically and plateaus above additions of 7-8 mol. eq. Bi(III), agreeing with the ESI-MS results. The absorbance monitoring the addition of $[\text{Bi}(\text{EDTA})]^-$ is near its maximum by 100 min of reaction. However, despite the similarity of the spectra to the one obtained with a titration of $[\text{Bi}(\text{cit})]^-$, this absorbance plateaus much lower, corresponding to an average only of 4-5 mol. eq. bound despite the addition of 200 mol. eq. $[\text{Bi}(\text{EDTA})]^-$.

The UV-visible spectra obtained during a titration of $[\text{Bi}(\text{EDTA})]^-$ into apo-MT at pH 7.4 are quite different than those obtained at pH 2.6. (Fig. 5-5Ci). From 1-6 mol. eq. $[\text{Bi}(\text{EDTA})]^-$ added, the spectra have two maxima at 319 nm and 466 nm. The latter maximum produces a visible yellow colour in the solution. Beyond the addition of 6 mol. eq. $[\text{Bi}(\text{EDTA})]^-$, the maxima begin to decrease, forming a flatter looking shoulder band. This may be due to the rearrangement of the metal-thiolate structures to accommodate more Bi(III). The absorbance at 319 nm, 368 nm, and 466 nm are plotted as a function of mol. eq. $[\text{Bi}(\text{EDTA})]^-$ added in Fig. 5-5Cii. The gentle decrease after 6 mol. eq. is seen for 319 nm and 466 nm, while the 368 nm plateaus after this point.

5.3.2 Determination of free cysteines in Bi(III)-bound $\beta\alpha$ MT species

The Bi_xS_y stoichiometries were investigated in the Bi_2MT species formed from addition of $[\text{Bi}(\text{EDTA})]^-$ at pH 7.4 and the Bi_6MT and Bi_7MT species formed from addition of $[\text{Bi}(\text{cit})]^-$ at pH 2.6 using cysteine modification methods (Fig. 5-6). When 12 mol. eq. Bq were added to a mixture of Bi_6MT and Bi_7MT at pH 2.6 (Fig. 5-6A), a single $\text{Bi}_6\text{Bq}_2\text{MT}$ species was formed (Fig. 5-6B). Two remaining free cysteines indicates that the Bi_6MT structure is

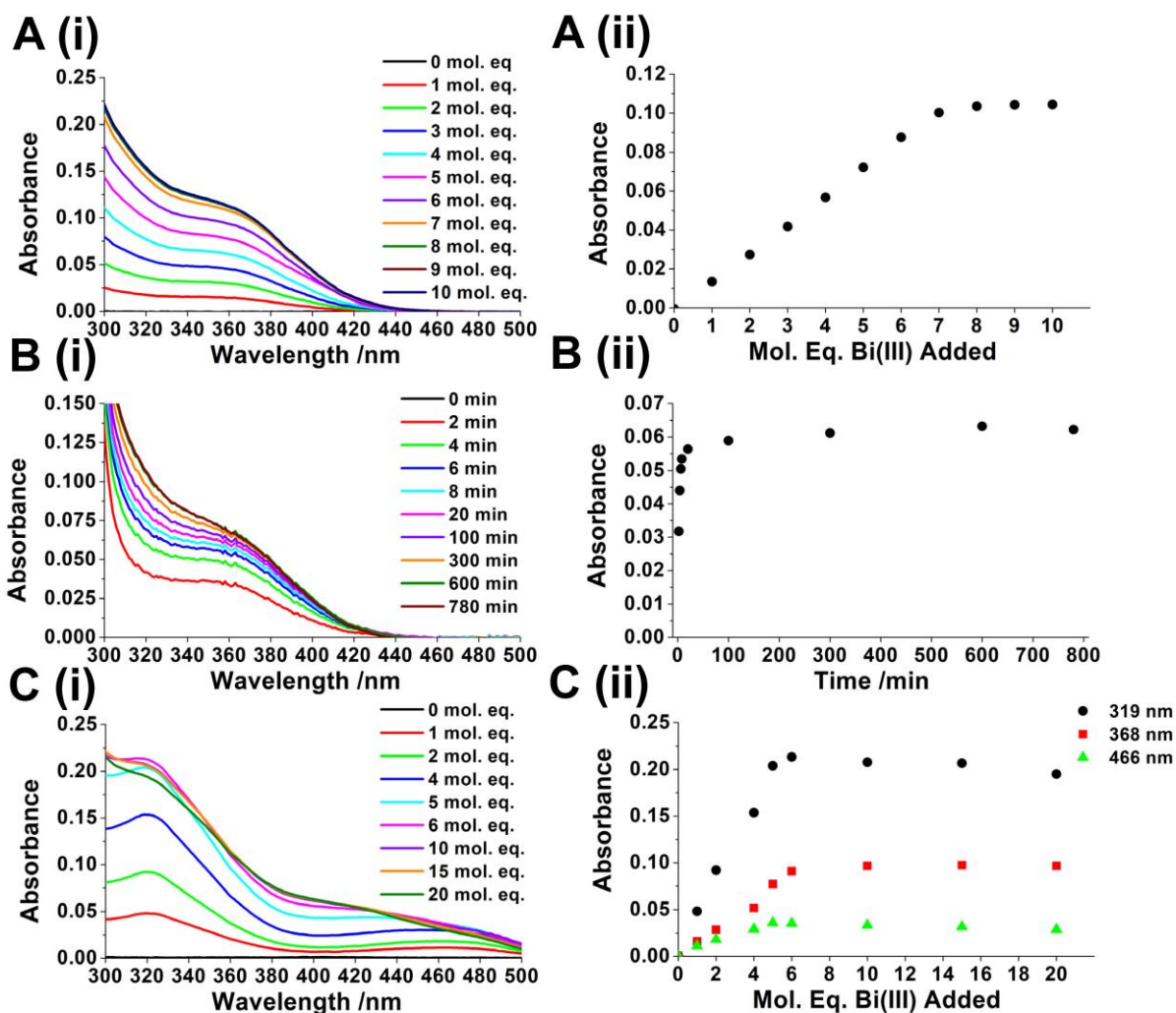


Figure 5-5. UV-visible absorption spectra of $\text{Bi}(\text{III})$ -bound $\beta\alpha$ MT. (i) UV-visible absorption spectra of (A) a stepwise titration of $[\text{Bi}(\text{cit})]^-$ into 5 μM apo-MT at pH 2.6, (B) a time-dependent reaction of 200 mol. eq. $[\text{Bi}(\text{EDTA})]^-$ with 5 μM apo-MT at pH 2.6, and (C) a stepwise titration of $[\text{Bi}(\text{EDTA})]^-$ into 5 μM apo-MT at pH 7.4. (ii) A plot of (A) the absorbance at 368 nm from (Ai) as a function of mol. eq. $[\text{Bi}(\text{cit})]^-$ added, (B) the absorbance at 368 nm from (Bi) as a function of time, and (C) the absorbances at 319 nm, 368 nm, and 466 nm from (Ci) as a function of mol. eq. $[\text{Bi}(\text{EDTA})]^-$ added.

using 18 cysteines to bind the Bi(III). In other words, each Bi(III) is bound to three cysteines each with no cluster formation. The Bi₇MT species is not stable towards reaction with Bq, and the seventh Bi(III) is displaced before any Bq binds. This indicates that Bi₇MT uses all 20 cysteines with none remaining to participate in modification.

If the Bi₁S₃ stoichiometry is consistent at different pH levels, one would expect for the Bi₂MT species at pH 7.4 to have 14 free cysteines. However, with the addition of 14 mol. eq. NEM to a solution of Bi₂MT at pH 7.4 (Fig 5-6C), two clear species are seen corresponding to Bi₂NEM₁₁MT and NEM₂₀MT (Fig. 5-6D). The formation of NEM₂₀MT is due to some of the Bi(III) being displaced by the NEM. 11 free cysteines would mean an average of 4.5 cysteine residues per Bi(III), which is not logical based on previous results which indicate trigonal binding.²⁰² The more likely explanation is that the Bi₂MT species is wrapping the protein in such a way where at least three free cysteines are inaccessible to the modifier. The lack of a Bi₁NEM_xMT species also suggests that the presence of both Bi(III) in the Bi₂MT is integral to the stability of the structure. Displacement of one via NEM results in displacement of both.

Overall, the Bi(III) binding to apo-β₂MT displays a strong dependence on Bi(III) salt used and pH conditions. The use of [Bi(cit)]⁻ or [Bi(EDTA)]⁻ at low pH produced the same binding pathway. However, [Bi(cit)]⁻ provided much less competition for the Bi(III) and thus the titration did not require excess Bi(III) to fully metallate the protein. With [Bi(cit)]⁻, Bi₇MT was formed as the major species upon full metallation with a Bi₈MT adduct. Conversely, when [Bi(EDTA)]⁻ was used, Bi₅MT was the major species formed despite a large excess of Bi(III) added, although Bi₆MT and Bi₇MT were also observed.

Bi(III) binding to apo-MT under low pH conditions results in an entirely non-cooperative distribution with binding constants over ten orders of magnitude lower than those obtained at neutral pH. The non-cooperative pathway at low pH is consistent with the report by Ngu et al.¹⁷⁸ The binding stoichiometry appears to be Bi₁S₃.

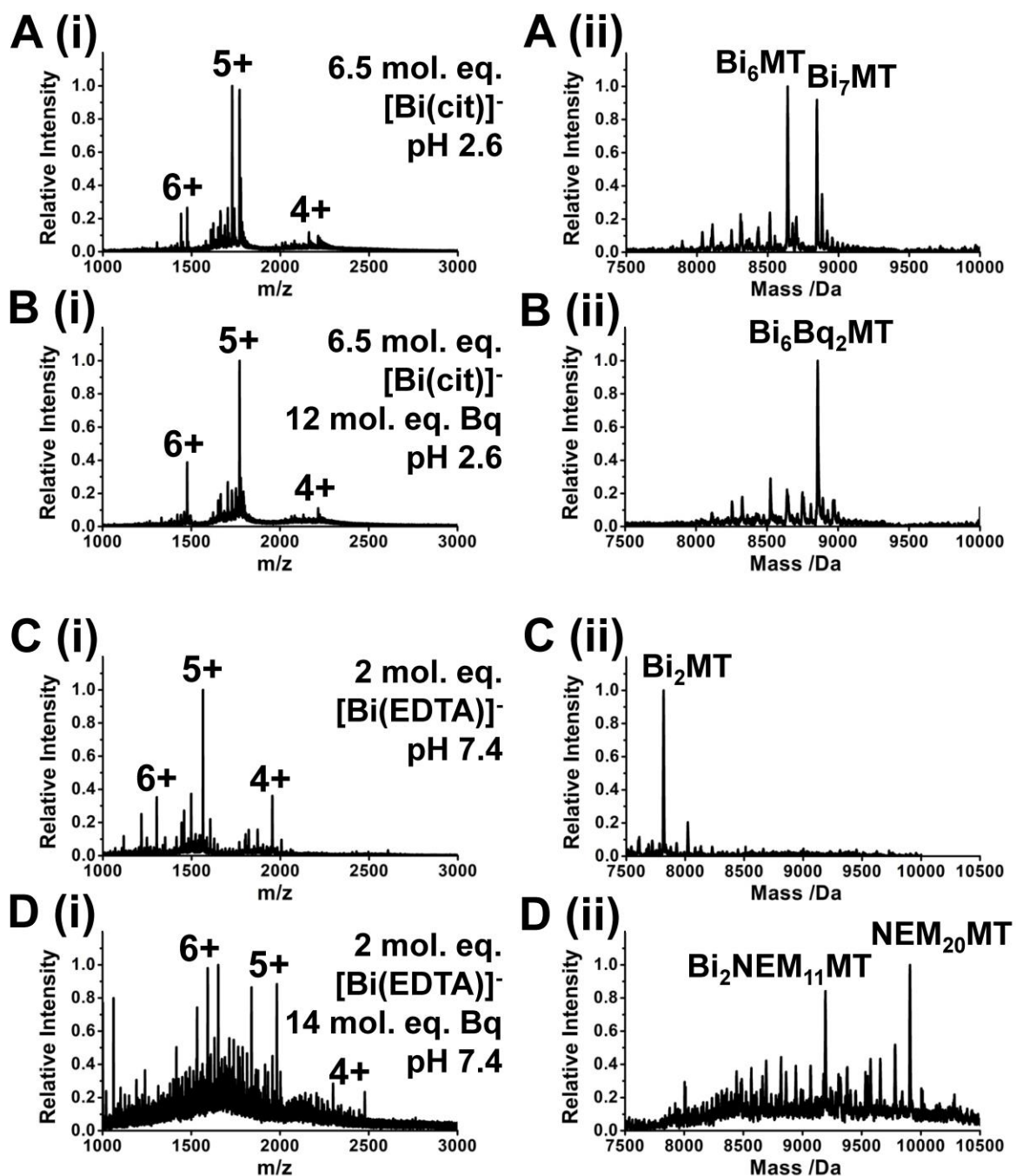


Figure 5-6. Cysteine modification of Bi(III)-bound apo $\beta\alpha$ -MT species monitored using ESI-MS. (i) Charge state and (ii) deconvoluted ESI-MS spectra showing (A) A mixture of Bi₆MT and Bi₇MT formed via addition of 6.5 mol. eq. [Bi(cit)]⁻ at pH 2.6, (B) the sample shown in (A) with 12 mol. eq. Bq added, (C) A sample of Bi₂MT formed via addition of 2 mol. eq. [Bi(EDTA)]⁻ at pH 7.4, and (D) the sample shown in (C) with 14 mol. eq. NEM added.

Under neutral pH conditions, Bi₂MT and Bi₄MT form semi-cooperatively. Species up to Bi₆MT are observed, however a low binding constant for the formation of Bi₆MT is calculated compared to other species, suggesting a structural rearrangement must occur to accommodate a sixth Bi(III). The maximum stoichiometry of Bi₆MT contrasts the Bi₇MT species observed by Sun et al. obtained upon titration of Bi(III) into Zn₇MT.²⁰² The implication is that binding Bi(III) into apo-MT and Zn₇MT at neutral pH results in different outcomes, a concept which will be explored later in this chapter. Based on cysteine modification studies, the Bi₂MT species wraps the protein in such a way where at least three free cysteines are inaccessible to modifier. This wrapping may impede further binding of Bi(III) to the MT.

5.3.3 Studies of the [Bi(EDTA)]⁻ binding pathways in apo-βMT and apo-αMT.

In the previous section, it was determined that two structures cooperatively form during the titration of Bi(III) into apo-MT at pH 7.4: Bi₂MT and Bi₄MT. This finding prompted the study into whether these structures display domain specificity, as has been observed in Zn(II), Cd(II), and Cu(I) MTs using ESI-MS.^{166-168, 179} In this section, the binding pathway and binding constants of the titration of [Bi(EDTA)]⁻ into the fragments apo-βMT and apo-αMT pH 7.4 is described as a method to probe the possible domain specificity of Bi₂MT.

The stepwise titration of [Bi(EDTA)]⁻ into apo-βMT at pH 7.4 monitored using ESI-MS is shown in Fig. 5-7. The binding appears to follow the same pathway as the full βαMT. Apo-βMT (Fig. 5-7A) binds up to two Bi(III) stoichiometrically as a function of the added mol. eq. of [Bi(EDTA)]⁻ (Fig. 5-7B-C). In detail, addition of 1 mol. eq. [Bi(EDTA)]⁻ results in Bi(III) distributing mostly as Bi₂βMT, while much of the MT remains metal free with a small fraction of Bi₁βMT forming (Fig. 5-7B). Addition of 2 mol. eq. [Bi(EDTA)]⁻ results in the single Bi₂βMT species forming (Fig. 5-7B). Apo-βMT binds up to three Bi(III) when excess [Bi(EDTA)]⁻ is added (Fig. 5-7D). Specifically, addition of 5 mol. eq. [Bi(EDTA)]⁻ results in a small fraction of Bi₃βMT forming. At this point in the titration, the amount of Bi(III) bound to the βMT is significantly less than the amount of Bi(III) added. Upon addition of 100 mol. eq. of [Bi(EDTA)]⁻, a large fraction of Bi₃βMT is formed; however, a significant amount of Bi₂βMT remains (Fig. 5-7E).

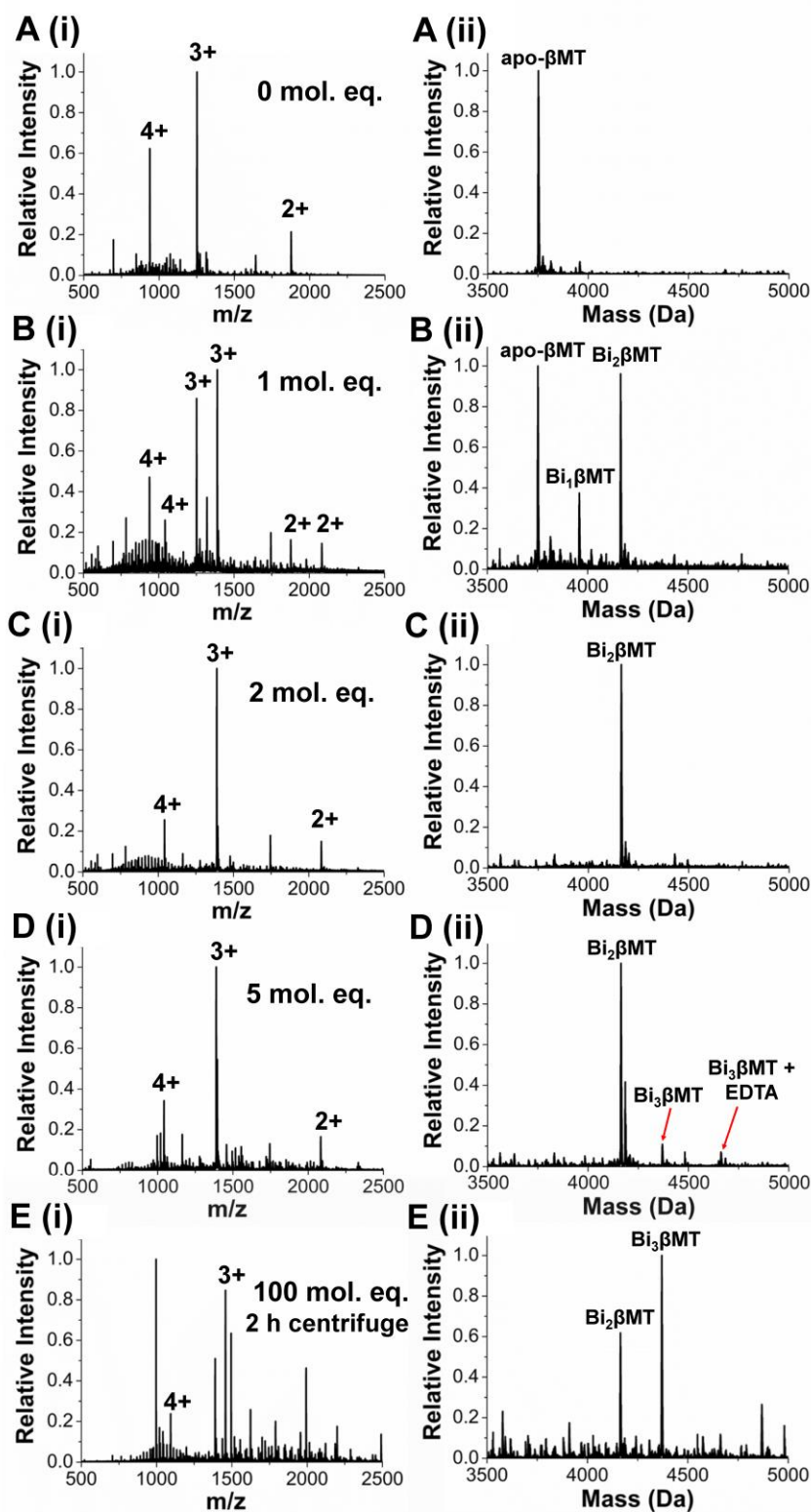


Figure 5-7. A titration of $[\text{Bi}(\text{EDTA})]^-$ into apo- βMT at pH 7.4 monitored using ESI-MS. (i) Charge state and (ii) deconvoluted ESI mass spectra show the stepwise reaction after (A) 0, (B) 1, (C) 2, (D) 5, and (E) 100 mol. eq. $[\text{Bi}(\text{EDTA})]^-$ added. The spectra in (E) were collected after 2 h centrifugation of the sample. Reproduced from Korkola et al., 2021 with permission from Oxford University Press.

The stepwise titration of $[\text{Bi}(\text{EDTA})]^-$ into apo- α MT at pH 7.4 monitored using ESI-MS is shown in Fig. 5-8. As with apo- β α MT and apo- β MT, the formation of $\text{Bi}_2\alpha$ MT is semi-cooperative with only small fractions of $\text{Bi}_1\alpha$ MT forming (Fig. 5-8A-B). However, like with β α MT and unlike β MT, the $\text{Bi}_2\alpha$ MT species never makes up 100% of the speciation. At 1.7 mol. eq. added, small fractions of apo- α MT and $\text{Bi}_1\alpha$ MT remain and a small fraction of $\text{Bi}_3\alpha$ MT has already formed. The α MT forms a single species of $\text{Bi}_3\alpha$ MT stoichiometrically with no excess $[\text{Bi}(\text{EDTA})]^-$ required (Fig. 5-8C-D). Upon addition of excess $[\text{Bi}(\text{EDTA})]^-$ (10 mol. eq.), very small fractions of $\text{Bi}_4\alpha$ MT-EDTA and $\text{Bi}_5\alpha$ MT-EDTA₂ are observed (Fig.5-8F).

Based on the determined stoichiometries of $\text{Bi}_6\beta\alpha$ MT and Bi_1S_3 , it would be expected for apo- β MT and apo- α MT to form $\text{Bi}_3\beta$ MT and $\text{Bi}_3\alpha$ MT, respectively at pH 7.4. β MT has 9 cysteines, therefore forming $\text{Bi}_3\beta$ MT would require use of all cysteines if no clustering occurs. α MT has 11 cysteines and would have 2 remaining free cysteines after forming $\text{Bi}_3\alpha$ MT.

The β MT requiring all 9 cysteines to bind 3 Bi(III) could be a reason why it resists full metallation to $\text{Bi}_3\beta$ MT. If the first two Bi(III) bind in such a way that makes formation of a third Bi_1S_3 structure unfavourable, such as folding the protein to where available cysteines either become buried or unable to form the trigonal pyramidal structures, then a third Bi(III) may not bind. As the $\text{Bi}_2\beta$ MT structure forms cooperatively, it may be particularly stable and thus unfavourable to rearrange until significant amounts of $[\text{Bi}(\text{EDTA})]^-$ are in solution.

The α MT forms up to $\text{Bi}_3\alpha$ MT rather easily. In theory this structure would have the same number of remaining free cysteines as $\text{Bi}_6\beta\alpha$ MT. However, $\text{Bi}_3\alpha$ MT forms stoichiometrically, while $\text{Bi}_6\beta\alpha$ MT requires excess $[\text{Bi}(\text{EDTA})]^-$ to bind the final Bi(III). As proposed for the β MT, the difficulty could be a result of the $\beta\alpha$ MT folding in such a way that restricts access for the sixth Bi(III) to bind. It is possible that the first two Bi(III) bind to apo- α MT in a way that allows for easy access of the third Bi(III).

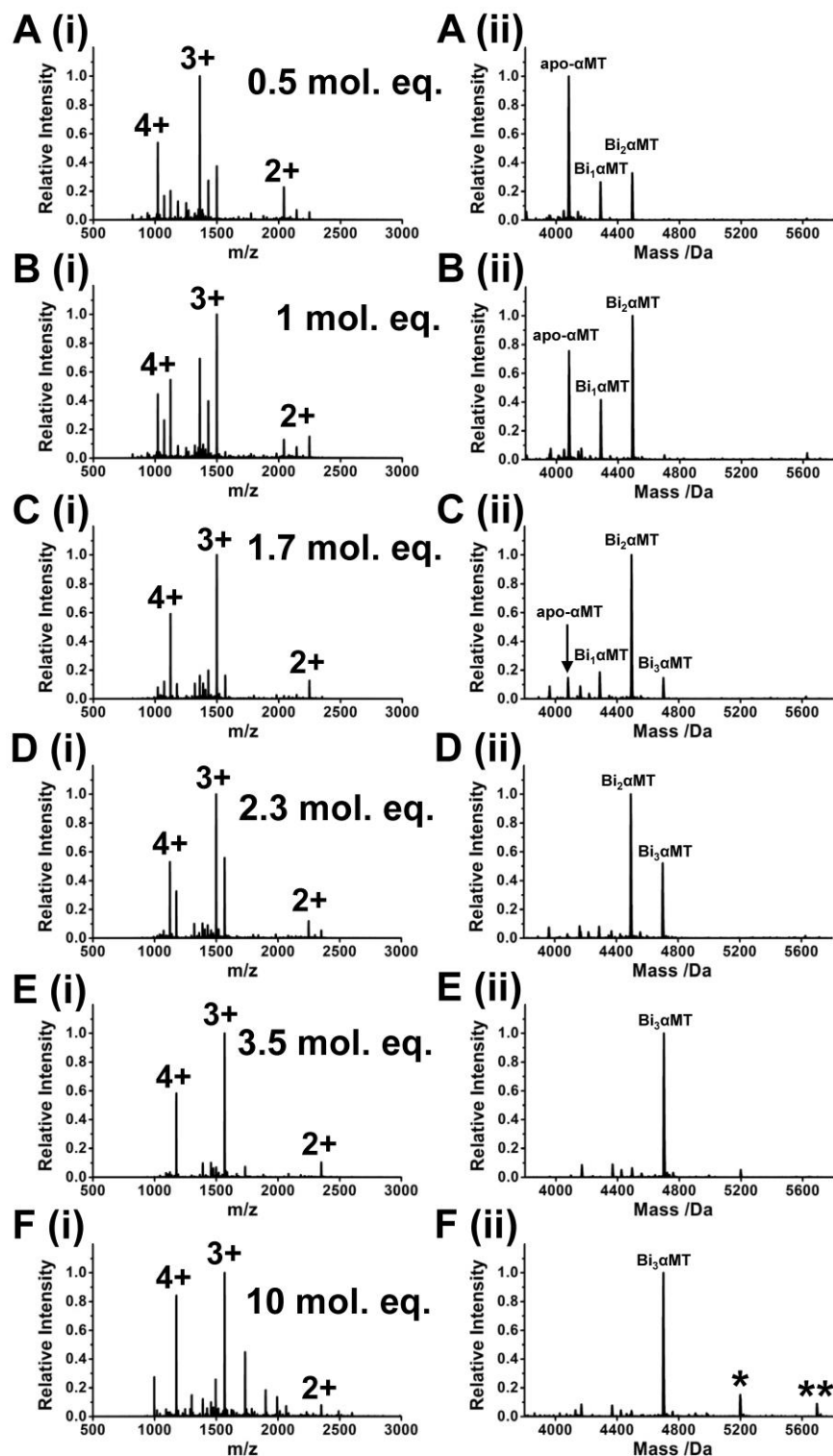


Figure 5-8. A titration of $[\text{Bi}(\text{EDTA})]^-$ into apo- αMT at pH 7.4 monitored using ESI-MS. (i) Charge state and (ii) deconvoluted ESI mass spectra show the stepwise reaction after (A) 0.5, (B) 1, (C) 1.7, (D) 2.3, (E) 3.5, and (F) 10 mol. eq. $[\text{Bi}(\text{EDTA})]^-$ added. Species corresponding to $\text{Bi}_4\alpha\text{MT-EDTA}$ and $\text{Bi}_5\alpha\text{MT-EDTA}_2$ are denoted (*) and (**), respectively.

The speciation distributions for $[\text{Bi}(\text{EDTA})]^-$ binding to apo- $\beta\alpha\text{MT}$, apo- βMT , and apo- αMT are shown in Fig. 5-9A, Fig. 5-9B, and Fig. 5-9C, respectively. The speciation curves for $\beta\alpha\text{MT}$ are the same as those shown in Fig. 5-4C but only showing up to 8 mol. eq. added here for easier observation of the early species. Fig. 5-9D shows a plot of each of the binding constants calculated relative to $K_{[\text{Bi}(\text{EDTA})]^-}$. The binding constants are also listed in Table 5-2.

It is apparent from the speciation curves that the formation of Bi_2MT is favoured in all three proteins. The first two binding constants compared between each protein are all within one order of magnitude of each other. This is also true for the $\log K_3$ of $\beta\alpha\text{MT}$ and αMT but not βMT , which is over three orders of magnitude smaller. Interestingly, $\log K_3$ for βMT is on a similar scale to $\log K_6$ for $\beta\alpha\text{MT}$. This potentially implies that $\text{Bi}_2\beta\text{MT}$ and $\text{Bi}_5\beta\alpha\text{MT}$ share similar structural properties that make binding of the final $\text{Bi}(\text{III})$ unfavourable. The ease of forming $\text{Bi}_3\alpha\text{MT}$ and $\text{Bi}_3\beta\alpha\text{MT}$ combined with the difficulty in forming $\text{Bi}_3\beta\text{MT}$ and $\text{Bi}_6\beta\alpha\text{MT}$ may imply the $\text{Bi}(\text{III})$ binds in the α -domain first and that the $\text{Bi}_2\beta\text{MT}$ species may correspond to the $\text{Bi}_4\beta\alpha\text{MT}$.

However, this does not explain the strong cooperativity of the $\text{Bi}_2\beta\text{MT}$ species formation. It could be argued that the apparent lowered binding constant for the $\text{Bi}_4\beta\alpha\text{MT}$ species is simply due to a statistical decrease in available binding sites compared to the formation of $\text{Bi}_2\beta\alpha\text{MT}$. However, the individual fragments already have a lower number of cysteines than the full $\beta\alpha\text{MT}$. Therefore, they should already have lowered binding constants, which is not observed in this case. Another possible explanation is, as mentioned previously, that the binding of $\text{Bi}(\text{III})$ crosslinks the protein in such away that makes subsequent binding unfavourable. If the binding to the $\beta\alpha\text{MT}$ was taking place in the individual domains, this should not occur, as the remaining free domain should not be involved in binding any preceding $\text{Bi}(\text{III})$. The possibility that $\text{Bi}(\text{III})$ binds across domains to the most readily available cysteines rather than into specific domains is explored in the next section.

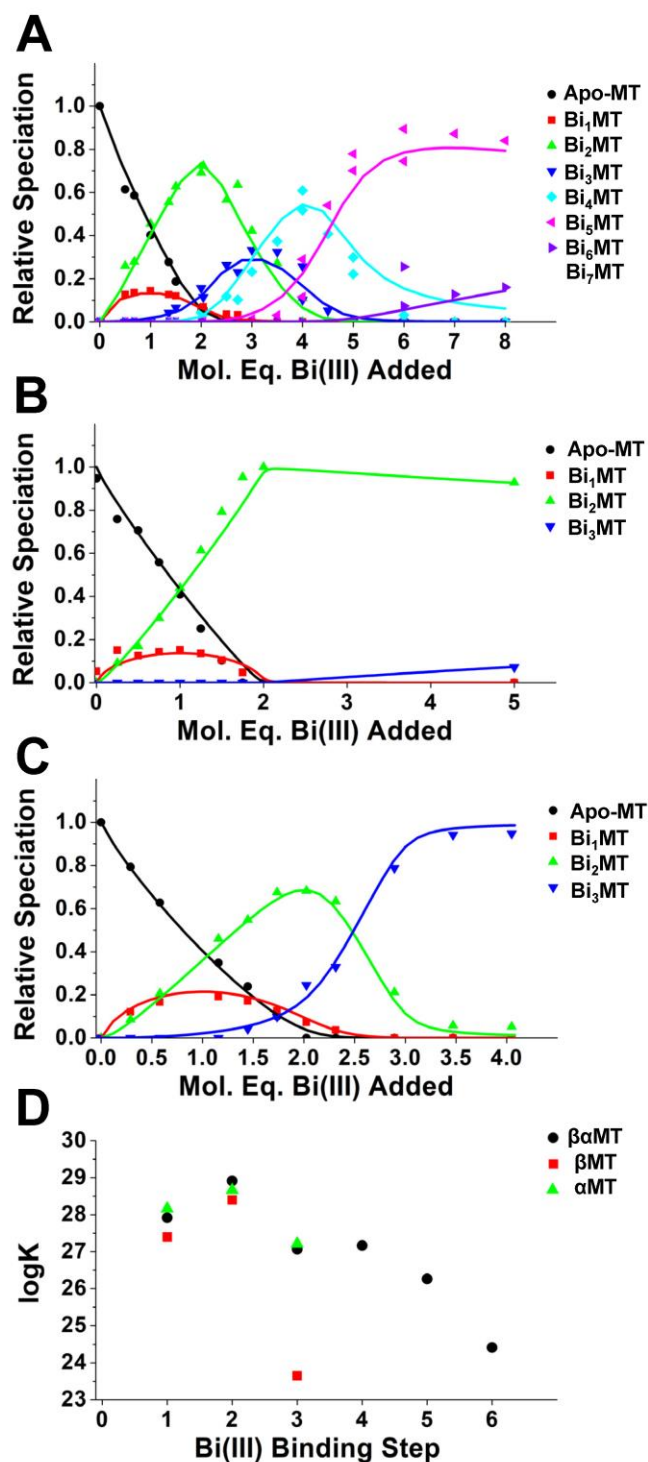


Figure 5-9. Speciation curves and calculated binding constants for the titration of Bi(III) into apo- $\beta\alpha$ MT, apo- β MT, and apo- α MT. Experimental (points) and simulated (lines) speciation distributions showing the titration of $[\text{Bi}(\text{EDTA})]^-$ into (A) apo- $\beta\alpha$ MT, (B) apo- β MT, and (C) apo- α MT at pH 7.4. (D) A plot of the binding constant for each titration at each step. Panel B adapted from Korkola et al., 2021 with permission from Oxford University Press to include additional data.

Table 5-2. Relative Bi(III)-MT binding constants of $\beta\alpha$ MT and fragments. The relative Bi(III)-MT binding constants determined from the fit of a titration of $[\text{Bi}(\text{EDTA})]^-$ at pH 7.4 into apo- $\beta\alpha$ MT, apo- β MT, and apo- α MT.

	$\beta\alpha$ MT	β MT	α MT
logK ₁	27.92	27.40	28.17
logK ₂	28.92	28.40	28.67
logK ₃	27.07	23.65	27.22
logK ₄	27.17	-	-
logK ₅	26.27	-	-
logK ₆	24.42	-	-

5.3.4 Investigating the location of Bi(III) in the Bi₂ $\beta\alpha$ MT structure

The location of the two Bi(III) in Bi₂ $\beta\alpha$ MT was studied by digesting a solution of primarily Bi₂ $\beta\alpha$ MT with trypsin and comparing the resulting fragments to a solution of trypsin-digested apo- $\beta\alpha$ MT (Fig. 5-10). The first thing to note is that the ESI-MS digestion profiles for apo- $\beta\alpha$ MT (Fig. 5-10A) and Bi₂ $\beta\alpha$ MT (Fig. 5-10B) are different. This implies that some trypsin cut sites are more shielded by the presence of the Bi-S structures and thus protected from digestion. A single large fragment of MT containing 2 Bi(III) is also seen in the mass spectra of the trypsin-digested Bi₂ $\beta\alpha$ MT (Fig. 5-10C-D).

These data are further analyzed in Fig. 5-11. In Fig. 5-11A the intensities of each fragment from Fig. 5-10A and Fig. 5-10B relative to the total intensity of all fragments their corresponding spectrum are compared between apo- $\beta\alpha$ MT and Bi₂ $\beta\alpha$ MT. It can be seen that fragments 4(β), 5(β), 6(β), and 9(α) are much less susceptible to digestion in the Bi₂ $\beta\alpha$ MT sample based on their lowered relative intensities. Fragments 2(β) and 11/12(α) are slightly less susceptible. Conversely, fragments 3(β) and 7(α) appear to have increased susceptibility to digestion in Bi₂ $\beta\alpha$ MT compared to apo- $\beta\alpha$ MT, which could be due to a structural change causing exposure of different sites. Only fragments 1(β), 8(α), and 10(α) have minimal to no change between the two conditions. From this analysis, it appears that both domains of the protein are involved in the binding of Bi₂ $\beta\alpha$ MT.

Fig. 5-11B shows the sequence of MT with the trypsin cleavage sites. Green boxes are drawn around the ends of the protein not part of the Bi₂MT-containing fragment shown in

Fig. 5-10C. The middle portion of the protein without green boxes, which spans all 9 cysteines of the β -domain and the first 5 cysteines of the α -domain, corresponds to the intact Bi_2MT fragment peak seen in the mass spectrum (Fig. 5-10C).

The three cysteines highlighted in pink indicate those in fragments 4 and 5, which were the cysteine-containing fragments with the most decreased susceptibility to digestion and include Cys 24, 26, and 29. These are likely the cysteines that are the most involved in the $\text{Bi}_2\beta\alpha\text{MT}$ structure, either binding the Bi(III) directly or forming an integral part of the backbone fold. It should also be reiterated that the cysteine modification of $\text{Bi}_2\beta\alpha\text{MT}$ shown in Fig. 5-6D suggests free but buried cysteines that are not available for binding. These cysteines would also likely not be susceptible to trypsin digestion.

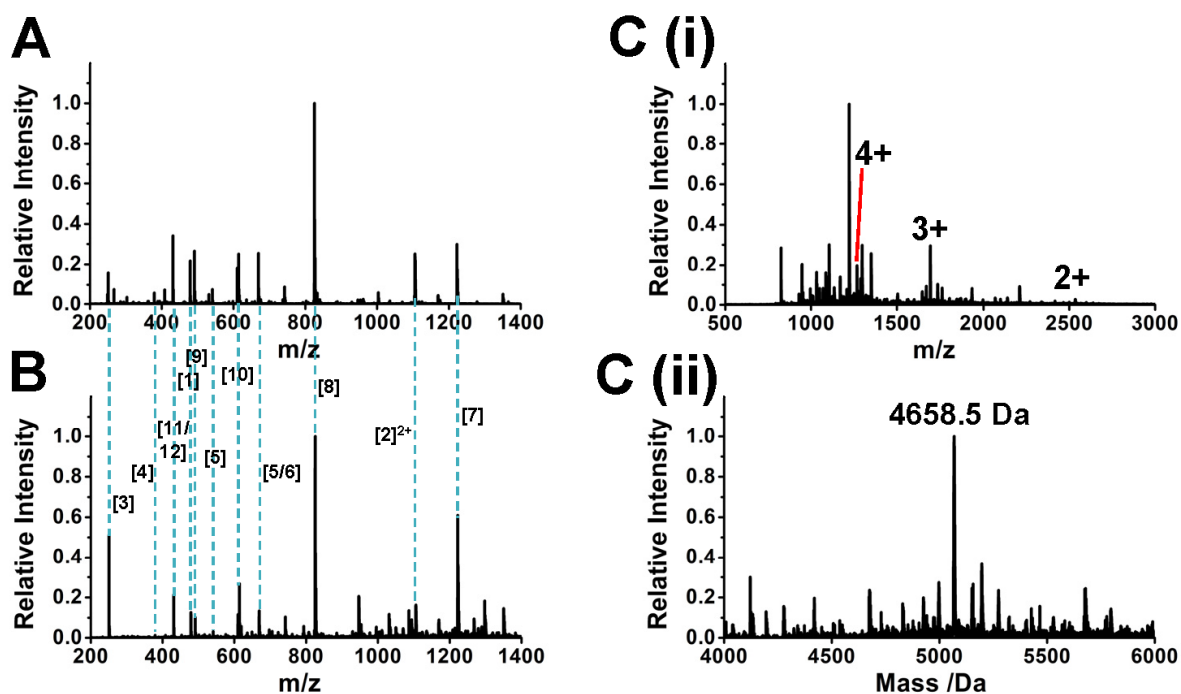


Figure 5-10. Trypsin digestion of apo- $\beta\alpha\text{MT}$ and $\text{Bi}_2\beta\alpha\text{MT}$ monitored by ESI-MS. ESI mass spectral data showing a trypsin digestion of (A) apo- $\beta\alpha\text{MT}$, (B) $\text{Bi}_2\beta\alpha\text{MT}$, and (C) $\text{Bi}_2\beta\alpha\text{MT}$ with the ESI-MS parameters tuned for large molecules. (C) shows (i) charge state and (ii) deconvoluted mass spectra.

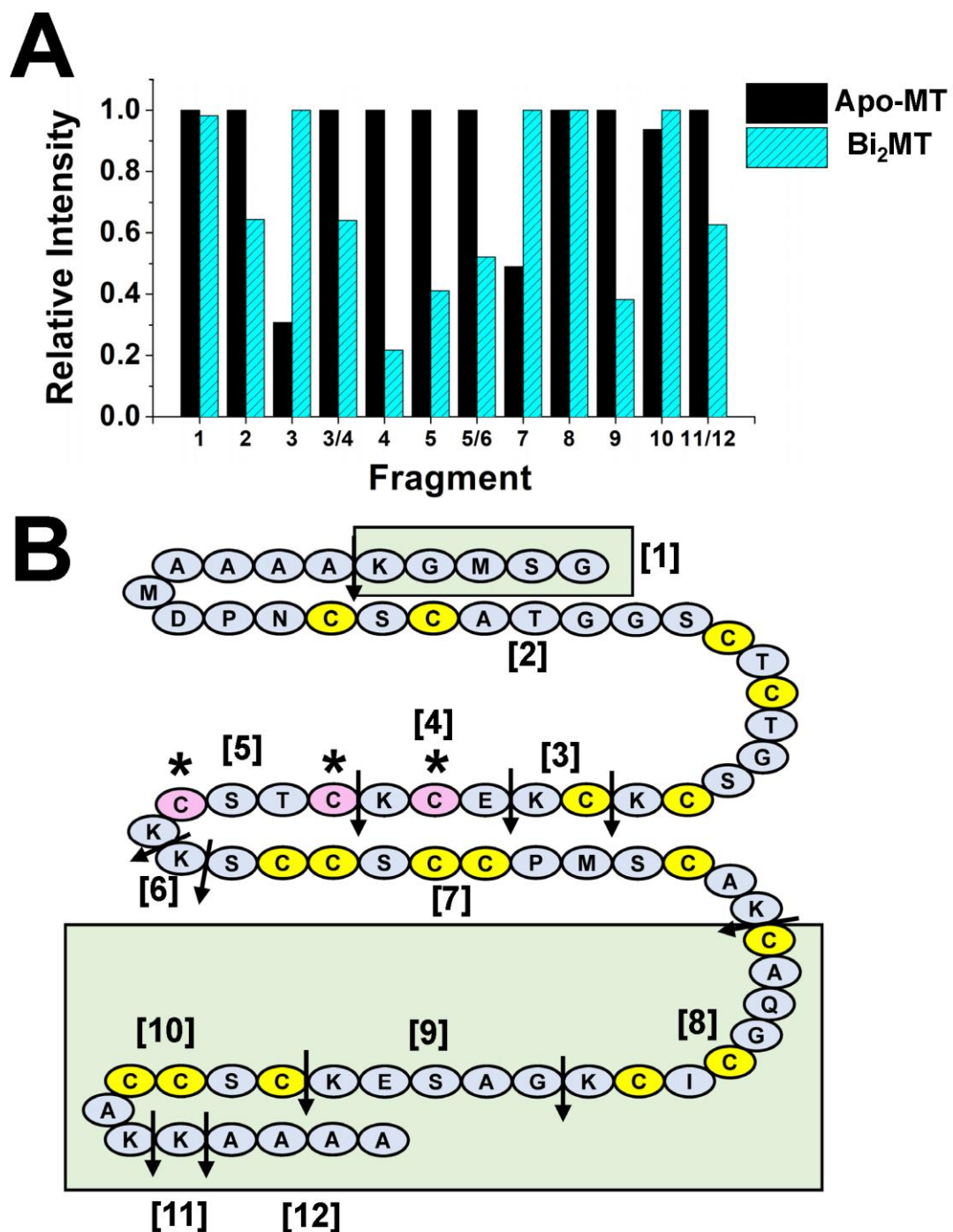


Figure 5-11. Analysis of the trypsin digestion of apo- β MT and Bi₂ β MT. (A) The relative intensities of each fragment peak relative to the total intensity of all fragment peaks within the spectrum. The relative intensities are normalized between 0 and 1 within the same fragment. (B) The sequence of MT showing trypsin cleavage sites and numbered fragments. Green boxes show the fragments that were successfully cleaved by the trypsin without disruption of the Bi₂ β MT species. Cysteines in pink are within the fragments most shielded from trypsin digestion.

From this data, it is not clear if the Bi(III) binding sites are consistent. Given that only one Bi(III)-containing fragment was observed in the mass spectra, the Bi(III) binding is likely at least localized within this fragment. As the fragments with reduced susceptibility and the Bi(III)-containing fragment span both domains, this is further evidence that Bi(III) binding to apo- β MT is not domain specific.

5.3.5 Bi(III) binding to apo-MT does not display domain specificity

Based on the ESI-MS titrations and trypsin digestion, it does not appear that Bi(III) has a domain preference. This may be considered unsurprising, as the two domains of mammalian MTs are mostly associated with the formation of specific metal-thiolate cluster structures such as with Zn(II), Cd(II), and Cu(I).^{147, 179, 361} Zn(II) and Cu(I) are biologically important metals and MT is thought to be involved in their homeostasis. Cd(II) is a toxic metal found in the environment that can often displace Zn(II) from proteins due to its high binding constant to sulfur. The semi-cooperative formation to Cd₄MT in the α -domain may play a role in protecting the cell against these toxic mechanisms. The coupled binding and folding of these biologically and environmentally relevant metals may have been tuned by evolutionary sequence changes to perform these functions.

Bi(III) is not toxic but also has no biological role and is not abundant in the environment. Only relatively recently have Bi(III) therapeutic agents been used.³¹⁴ Therefore, although MT can bind Bi(III) with high affinity, it would not have evolved to use the potential two-domain structure when binding Bi(III), especially since the two domains are only separated with a three amino acid linker in the primary structure. Given that Bi(III) forms the same Bi₂MT structure in both isolated fragments, Bi(III) may only require any sequence of cysteine residues to form this structure.

5.3.6 The structure of apo- β MT inhibits the formation of Bi₃ β MT

In previous sections, it was shown that the binding constant for the formation of Bi₃ β MT is approximately four orders of magnitude lower than that for the formation of Bi₂ β MT. It was hypothesized that this was due to the limited available cysteine residues making rearrangement of the Bi₂ β MT structure unfavourable. The sequence of β MT having nine cysteines which is just enough to bind three Bi(III) in a Bi₁S₃ stoichiometry makes this

fragment an interesting model for which to study the effect of protein structure on metal-loading ability. In the previous sections, it has been shown that β MT can in fact bind up to 3 Bi(III) upon addition of excess $[\text{Bi}(\text{EDTA})]^-$ at pH 7.4, however, formation of this $\text{Bi}_3\beta\text{MT}$ species is unfavourable compared to the semi-cooperative formation of $\text{Bi}_2\beta\text{MT}$.

Initially, the free cysteines remaining in $\text{Bi}_2\beta\text{MT}$ were determined using cysteine modification. At pH 6.9, apo- β MT binds in the same pathway as at pH 7.4 and forms a single species of $\text{Bi}_2\beta\text{MT}$ (Fig. 5-12A). $\text{Bi}_2\beta\text{MT}$ binds up to 3 molecules of Bq at pH 6.9 (Fig. 5-12B). The single peak observed in the ESI-mass spectrum indicates that $\text{Bi}_2\text{Bq}_3\text{MT}$ forms and thus least three cysteines remain free. This result is consistent with the Bi_1S_3 stoichiometry seen at pH 2.6 in $\text{Bi}_6\beta\alpha\text{MT}$. It does however contrast the $\text{Bi}_2\beta\alpha\text{MT}$ species

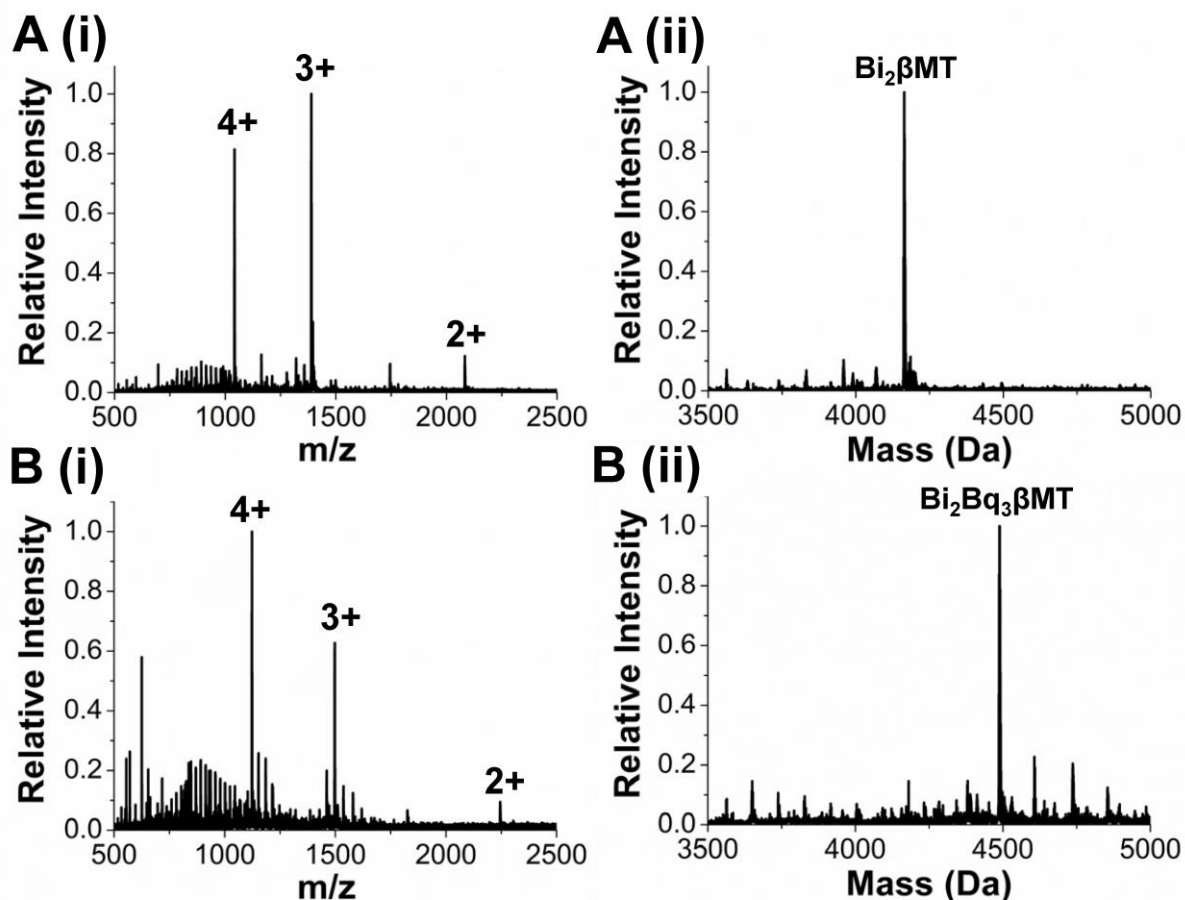


Figure 5-12. Cysteine modification of $\text{Bi}_2\beta\text{MT}$ with Bq monitored using ESI-MS. (i) Charge state and (ii) deconvoluted ESI mass spectra of (A) $\text{Bi}_2\beta\text{MT}$ at pH 6.9 and (B) $\text{Bi}_2\beta\text{MT}$ with 40 mol. eq. Bq added at pH 6.9. Reproduced from Korkola et al., 2021 with permission from Oxford University Press.

only having 11 free cysteines available to bind modifier. This could either be due to use of a different modifier or because the $\text{Bi}_2\beta\alpha\text{MT}$ wraps in such a way that obscures the cysteines, while $\text{Bi}_2\beta\text{MT}$ does not. There may also be free cysteines buried within the $\text{Bi}_2\beta\text{MT}$ structure that are inaccessible to the modifier.

At neutral pH, the apo- βMT peptide exists in a wrapped conformation in which the some of the cysteines are inaccessible to the solvent.^{161, 362} The first two Bi(III) may bind to the protein and wrap in in such a way that the remaining free cysteines are in an unfavourable conformation to bind additional Bi(III) . The bulky EDTA ligand likely exacerbates this effect. The resistance to binding the third Bi(III) may be a result of the “tangling” of the

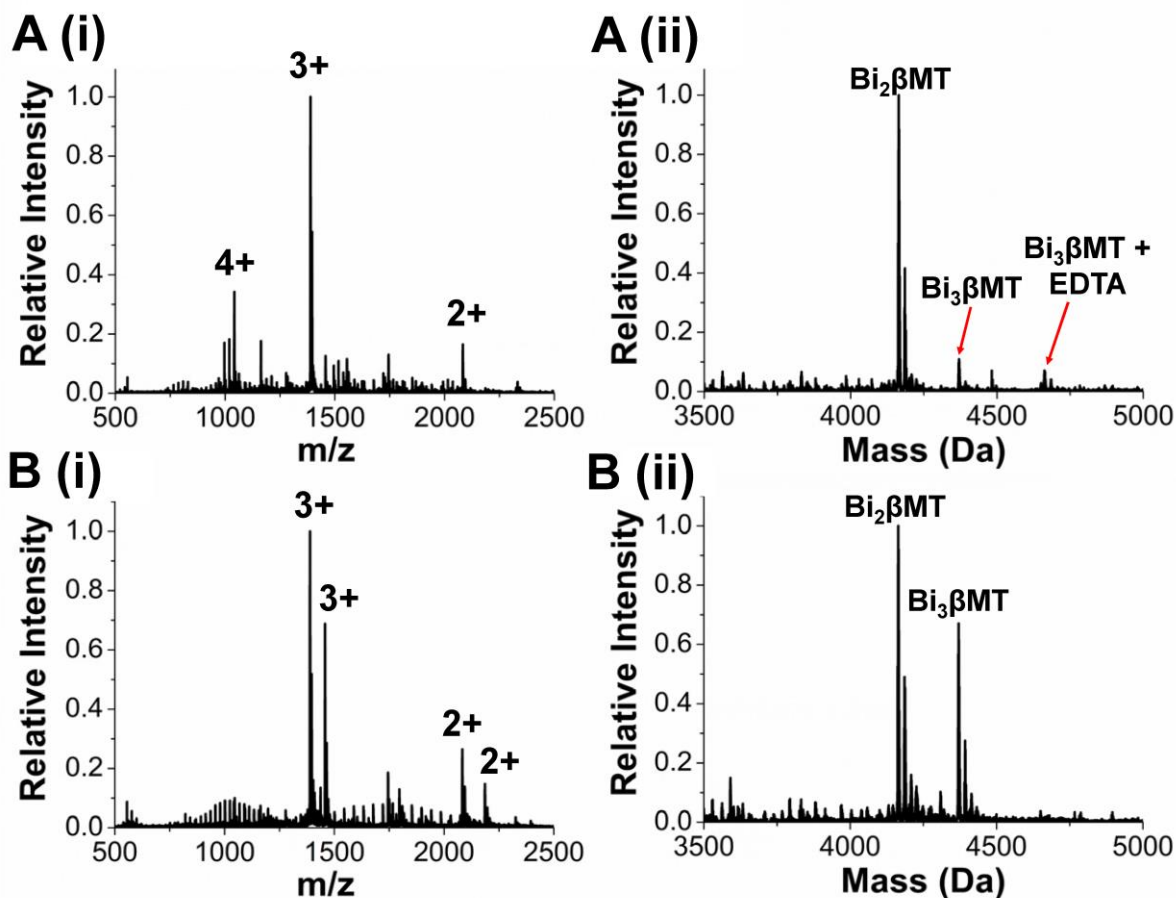


Figure 5-13. Bi(III) binding to apo- βMT in the absence and presence of 4 M GdmCl monitored using ESI-MS. (i) Charge state and (ii) deconvoluted ESI mass spectra of (A) apo- βMT with 5 mol. eq. $[\text{Bi(EDTA)}]^-$ added at pH 7.4 in the absence of GdmCl and (B) apo- βMT with 5 mol. eq. $[\text{Bi(EDTA)}]^-$ added at pH 7.4 in the presence of 4 M GdmCl. The spectra in (A) are also depicted in Fig. 5-7D. Reproduced from Korkola et al., 2021 with permission from Oxford University Press.

peptide chain due to the crosslinking of the first two Bi(III). This can be probed by making all nine cysteines equally accessible at pH 7.4 by using a denaturing agent before binding Bi(III).

Apo- β MT will bind more $[\text{Bi}(\text{EDTA})]^-$ when the cysteines are more accessible in an extended conformation than when the cysteines are less accessible in its native conformation (Fig. 5-13). In the absence of a denaturing agent at pH 7.4, only a small fraction of $\text{Bi}_3\beta\text{MT}$ forms in addition to $\text{Bi}_2\beta\text{MT}$ upon addition of 5 mol. eq. $[\text{Bi}(\text{EDTA})]^-$ to a solution of apo- β MT (Fig. 5-13A). A separate sample of apo- β MT in the presence of 4 M formed a much greater fraction of $\text{Bi}_3\beta\text{MT}$ upon addition of 5 mol. eq. $[\text{Bi}(\text{EDTA})]^-$ (Fig. 5-13B).

The data in Fig. 5-13 clearly show that a greater Bi(III) saturation is achieved when the cysteines of apo- β MT are more solvent accessible. This result suggests that the lesser degree of cysteine accessibility at pH 7.4 significantly impedes metallation with this xenobiotic metal.

5.3.7 There is a pH dependence in the competition between the EDTA and the nine cysteines of β MT for the Bi(III).

At pH 7.4, when 2 mol. eq. of $[\text{Bi}(\text{EDTA})]^-$ are added, all the Bi(III) binds, forming a single species of $\text{Bi}_2\beta\text{MT}$ (Fig. 5-14A). When the pH of this solution is lowered to pH 5.0 or pH 2.3, the speciation becomes a distribution centred around Bi_1MT (Fig. 5-14B). The average mol. eq. of Bi(III) bound is lower than the amount added, meaning that $[\text{Bi}(\text{EDTA})]^-$ forms in competition with the $\text{Bi}_n\beta\text{MT}$. The data in Fig. 5-14 show that $\log K([\text{Bi}(\text{EDTA})]^-) / \log K(\text{Bi}_n\beta\text{MT})$ favours Bi(III) binding to EDTA to a larger extent at lower pH levels in comparison with β MT. It is interesting to note that cooperativity for Bi_2MT is lost at pH 5.0 and 2.3. A non-cooperative, sequential demetallation takes place.

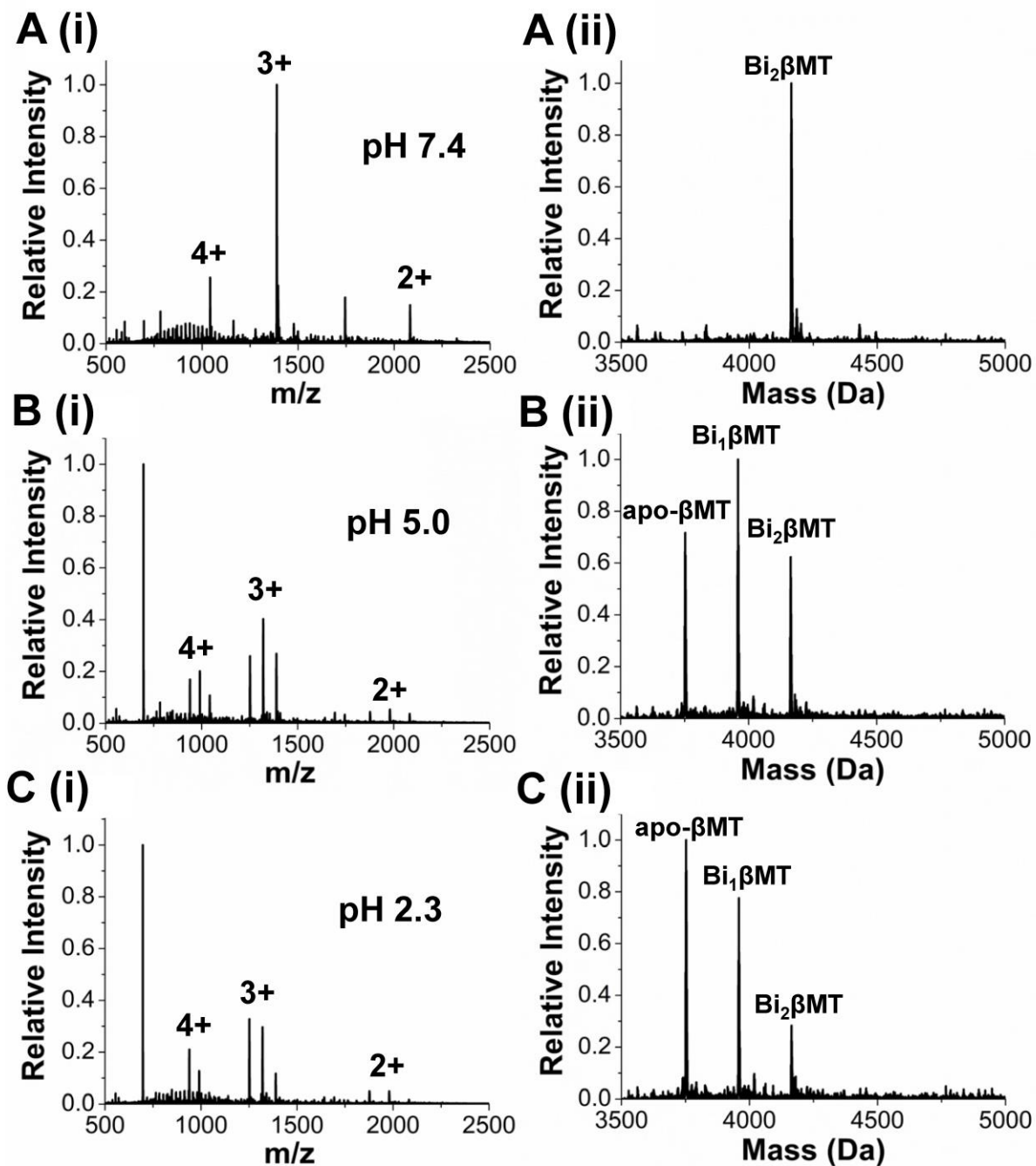


Figure 5-14. The pH dependence of $\text{Bi}_2\beta\text{MT}$ cooperativity monitored using ESI-MS. (i) Charge state and (ii) deconvoluted ESI mass spectra of apo- βMT with 2 mol. eq. $[\text{Bi}(\text{EDTA})]^-$ added at pH 7.4 then adjusted to pH (A) 7.4, (B) 5.0, and (C), 2.35. The spectrum in (A) is also depicted in Fig. 5-7C. Reproduced from Korkola et al., 2021 with permission from Oxford University Press.

5.3.8 Bi₂βMT will not exchange metals with Cd₃βMT and Zn₃βMT.

The mobility of Bi(III) in the Bi₂βMT species was further tested through competition with Cd₃βMT and Zn₃βMT (Fig. 5-15). The ESI mass spectral data show that Bi₂βMT did not exchange metals with Cd₃βMT (Fig. 5-15A) or Zn₃βMT (Fig. 5-15B) at pH 7.4. The mass spectra show separate Bi₂MT and Cd₃MT peaks in Fig. 5-15A and separate Bi₂βMT and Zn₃βMT in Fig. 5-15B. No mixed metals species were present in significant amounts. However, when Cd₃βMT and Zn₃βMT were mixed, there was exchange of metals, forming Cd₁Zn₂βMT and Cd₂Zn₁βMT (Fig. 5-15C).

This is surprising, as Bi(III) has a much higher binding affinity to sulfur compared to Cd(II) or Zn(II), making an exchange thermodynamically favourable.^{135, 363} Thus, it is likely a high transition state energy kinetically inhibiting exchange between the trigonally coordinated Bi(III) in the Bi₂βMT and the tetrahedrally coordinated Cd₃βMT or Zn₃βMT.

5.3.9 Studies of [Bi(EDTA)]⁻ binding to Zn₇βαMT

This chapter thus far has focused on Bi(III) binding to apo-MTs. However, the lack of Bi₇MT formation at pH 7.4 in apo-βαMT contrasts previous results,²⁰² which studied Bi(III) binding to Zn₇MT and Zn₂Cd₅MT. Therefore, the hypothesis is that apo-MT and fully metallated MT produce Bi_nMT species with different stoichiometries. This section describes the binding of [Bi(EDTA)]⁻ to Zn₇MT at pH 7.4 and the individual Zn_xBi_yMT species formed.

A stepwise titration of [Bi(EDTA)]⁻ into Zn₇MT at pH 7.4 monitored using ESI-MS is shown in Fig. 5-16. It is important to note that Zn(II)-bound MTs and Bi(III)-bound MTs do not have the same ionization efficiencies. It is likely that mixed metal species of a similar Zn(II)/Bi(III) composition will have comparable ionization efficiencies, and thus species at similar points in the titration may be compared. Nevertheless, information gained from the relative peak intensities in this ESI-MS experiment should only be taken as an approximation.

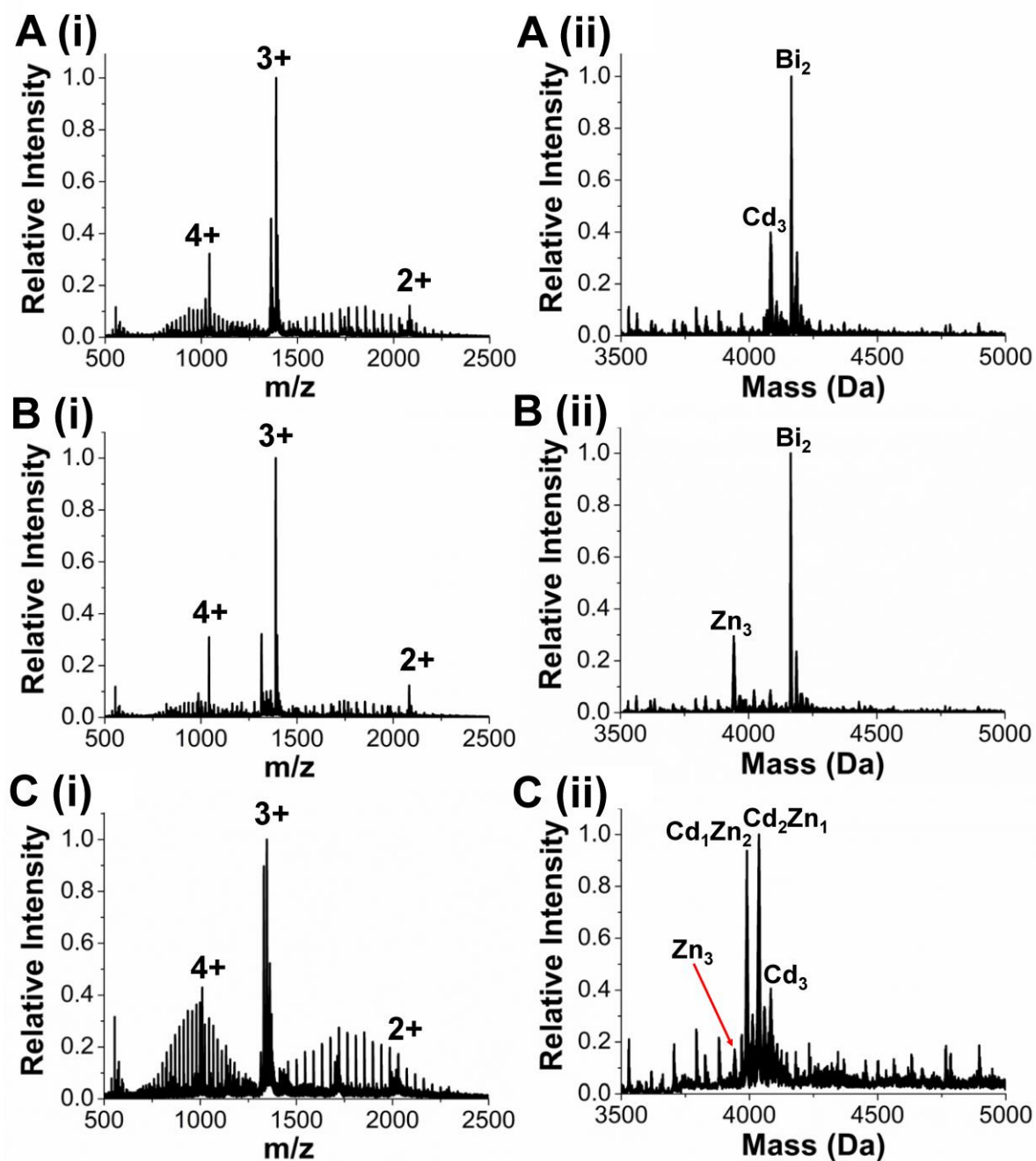


Figure 5-15. Test of metal exchange between Bi₂MT, Cd₃MT, and Zn₃MT monitored using ESI-MS. (i) Charge state and (ii) deconvoluted ESI mass spectra of a 1:1 ratio of (A) Bi₂MT and Cd₃MT, (B) Bi₂MT and Zn₃MT, and (C), Cd₃MT and Zn₃MT at pH 7.4. Reproduced from Korkola et al., 2021 with permission from Oxford University Press.

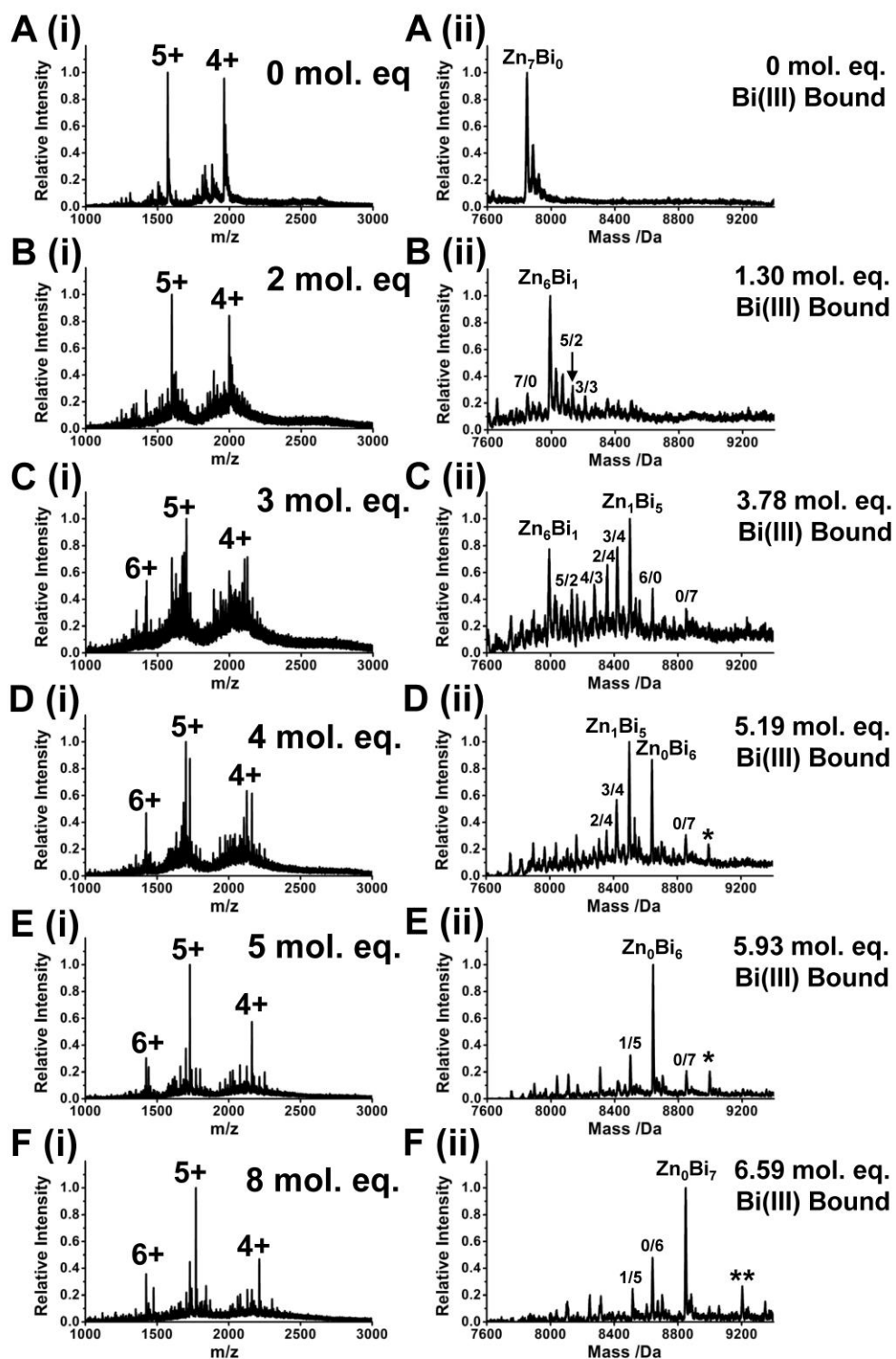


Figure 5-16. A titration of [Bi(EDTA)]⁻ into Zn₇βaMT at pH 7.4 monitored using ESI-MS. (i) Charge state and (ii) deconvoluted ESI mass spectra show the stepwise reaction after (A) 0, (B) 2, (C) 3, (D) 4, (E) 5, and (F) 8 mol. eq. [Bi(EDTA)]⁻ added. Spectra were measured 16 h after addition of [Bi(EDTA)]⁻. Species corresponding to Bi₆MT-EDTA and Bi₇MT-EDTA are denoted (*) and (**), respectively.

Upon addition of 2 mol. eq. $[\text{Bi}(\text{EDTA})]^-$ to Zn_7MT , one $\text{Zn}(\text{II})$ is displaced, and the major species formed is $\text{Zn}_6\text{Bi}_1\text{MT}$ (Fig. 5-16B). Peaks of lower intensity corresponding to $\text{Zn}_5\text{Bi}_2\text{MT}$ and $\text{Zn}_3\text{Bi}_3\text{MT}$ are also observed at this step. After 3 mol. eq. $[\text{Bi}(\text{EDTA})]^-$ are added, $\text{Zn}_6\text{Bi}_1\text{MT}$, $\text{Zn}_5\text{Bi}_2\text{MT}$, $\text{Zn}_4\text{Bi}_3\text{MT}$, $\text{Zn}_2\text{Bi}_4\text{MT}$, $\text{Zn}_3\text{Bi}_4\text{MT}$, $\text{Zn}_1\text{Bi}_5\text{MT}$, Bi_6MT , and Bi_7MT species are seen (Fig. 5-16C). $\text{Zn}_6\text{Bi}_1\text{MT}$ and $\text{Zn}_1\text{Bi}_5\text{MT}$ are the most abundant species at this step. This could imply semi-cooperativity, or it could be due to these species having a higher ionization efficiency than the others.

In the next step, after addition of 4 mol. eq. $[\text{Bi}(\text{EDTA})]^-$, only the $\text{Zn}_2\text{Bi}_4\text{MT}$, $\text{Zn}_3\text{Bi}_4\text{MT}$, $\text{Zn}_1\text{Bi}_5\text{MT}$, Bi_6MT , and Bi_7MT species remain with a new peak corresponding to $\text{Bi}_6\text{MT-EDTA}$ (Fig. 5-16D). At this point, the Bi_6MT species has a much greater peak intensity. At 5 mol. eq. added, Bi_6MT is the major species with small amounts of $\text{Zn}_1\text{Bi}_5\text{MT}$, Bi_7MT , and $\text{Bi}_6\text{MT-EDTA}$ (Fig. 5-16E) Finally, after the addition of 8 mol. eq., Bi_7MT is the major species, with small fractions of $\text{Zn}_1\text{Bi}_5\text{MT}$, Bi_6MT , and $\text{Bi}_7\text{MT-EDTA}$ (Fig. 5-16F).

It is interesting to note that in this titration, Bi_1MT in the form of $\text{Zn}_6\text{Bi}_1\text{MT}$ is a major species. This is unlike the titration of $[\text{Bi}(\text{EDTA})]^-$ into apo-MT where the formation of Bi_1MT was significantly less favoured than the formation of Bi_2MT . The Bi_2MT species, in the form of $\text{Zn}_5\text{Bi}_2\text{MT}$ is also much less abundant in the titration of $[\text{Bi}(\text{EDTA})]^-$ into Zn_7MT . $\text{Zn}_1\text{Bi}_5\text{MT}$ is another dominant species and stable species that is not normally favoured over others for the apo-MT titration.

The most notable thing observed in this titration, however, is that $\text{Bi}(\text{III})$ binds to the MT stoichiometrically as it displaces the $\text{Zn}(\text{II})$. After only 8 mol. eq. $[\text{Bi}(\text{EDTA})]^-$ have been added, Bi_7MT is the major species. In the titration using apo-MT at pH 7.4, Bi_6MT resists formation until a large excess of $[\text{Bi}(\text{EDTA})]^-$ is added and Bi_7MT does not form at all. This finding agrees with the work by Sun et al. and reconciles the differences between these works seen thus far, confirming that the differences observed are due to the use of either Zn_7MT or apo-MT.²⁰²

A speciation plot of the titration is shown in Fig. 5-17. To reiterate, the exact speciation should be taken as an approximation due to the different ionization efficiencies of $\text{Zn}(\text{II})$ -MTs and $\text{Bi}(\text{III})$ -MTs. All mixed $\text{Zn}(\text{II})/\text{Bi}(\text{III})$ species are shown in Fig. 5-17A.

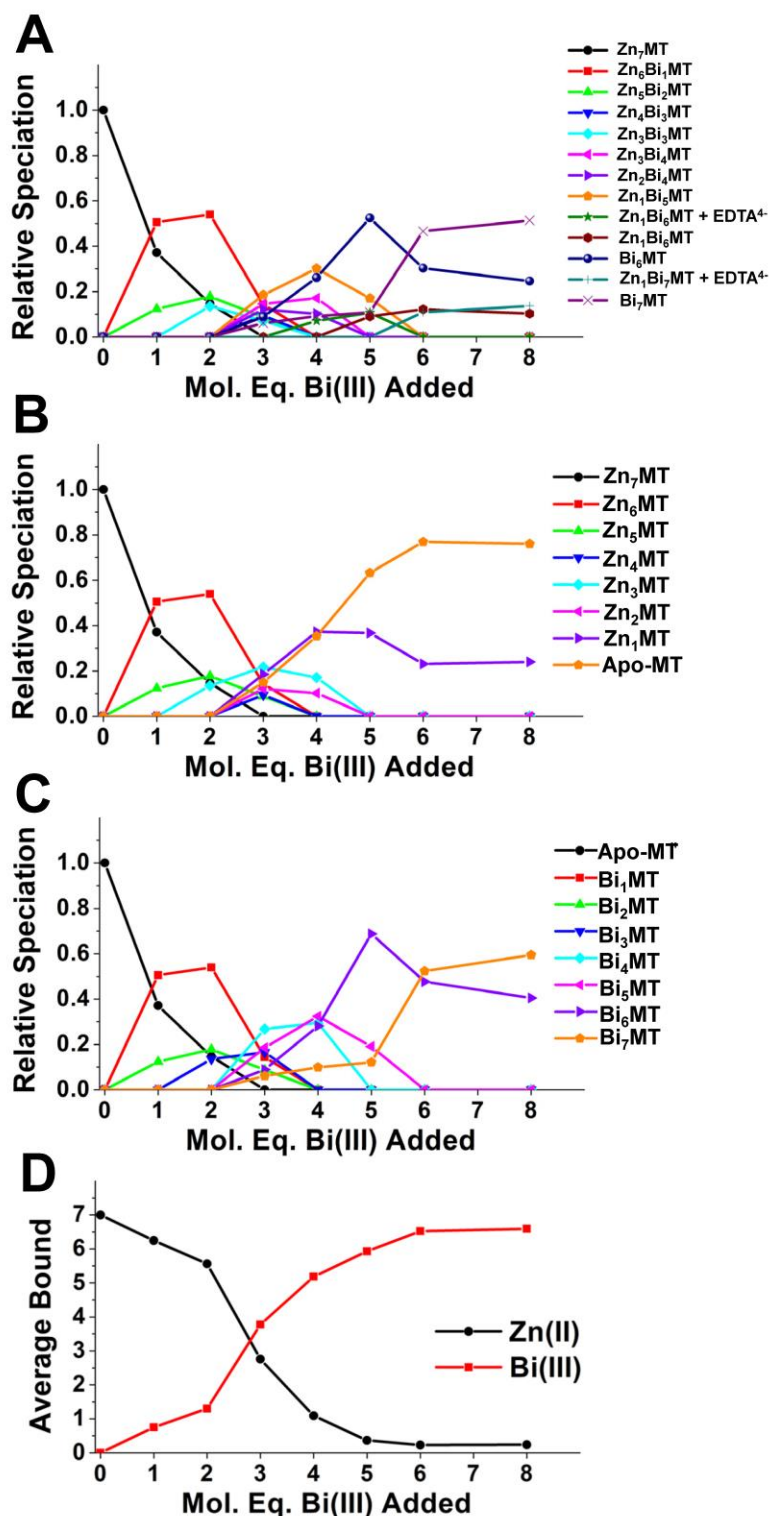


Figure 5-17. Speciation curves for the titration of $[\text{Bi}(\text{EDTA})]^-$ into $\text{Zn}_7\beta\alpha\text{MT}$. Experimental speciation distributions with the points connected showing the titration of $[\text{Bi}(\text{EDTA})]^-$ into Zn_7MT showing (A) the mixed metal species, (B) only the Zn(II) content in each species, (C) only the Bi(III) content in each species, and (D) the average Zn(II) and Bi(III) bound at each step.

Zn_6Bi_1MT , Zn_1Bi_5MT , Bi_6MT , and Bi_7MT are apparent as major species with other intermediate species remaining low in relative speciation. Fig. 5-17B shows the calculated speciation showing only the Zn(II) content of each species. Zn_6MT , Zn_1MT , and Zn_0MT are the major species. The calculated speciation showing only the Bi(III) content is shown in Fig. 5-17C. Bi_1MT , Bi_6MT , and Bi_7MT are the major species. Fig. 5-17D shows the average number of Bi(III) and Zn(II) bound as a function of $[Bi(EDTA)]^-$ added. Beyond 3 mol. eq. the number Bi(III) bound exceeds the number added by approximately 1 mol. eq., indicating that the Bi(III)-bound species have a higher ionization efficiency than the Zn(II)-bound species, as expected.

As the structures formed from titrating $[Bi(EDTA)]^-$ into Zn_7MT are quite different than those formed from titrating $[Bi(EDTA)]^-$ into apo-MT, UV-visible spectra were measured to see if the shape of the $S \rightarrow Bi$ LMCT bands remain consistent with other conditions studied (Fig. 5-18). The UV-visible spectrum monitored over time after addition of 8 mol. eq. $[Bi(EDTA)]^-$ into Zn_7MT shows a steadily rising band. The shape of the band somewhat resembles that of the apo-MT at pH 7.4 metallated with excess $[Bi(EDTA)]^-$. The band is much flatter without the distinct peaks at 319 nm and 466 nm. It is also flatter than the absorption spectra collected at pH 2.6, which have a distinct shoulder at 368 nm. This suggests that the coordination of the Bi(III) when titrated into Zn_7MT has a structure in between those of the higher metallated species of Bi(III)-bound apo-MTs at pH 7.4 and those of the species measured at pH 2.6.

Structural differences between the apo-MT and Zn_7MT provides a possible explanation for the observed differences. It is possible that because in Zn_7MT the cysteines are already arranged in such a way to accommodate seven metals, the sequential displacement by Bi(III) may yield Bi(III) in binding sites like those of Zn(II). Sun et al. concluded in that Bi_7MT binds using an occasional fourth bond to an oxygen ligand and is bound in “distorted” clusters compared to Zn(II).²⁰² Therefore, it could be possible that the seven Bi(III) binding sites are mimicking the Zn(II) it displaced.

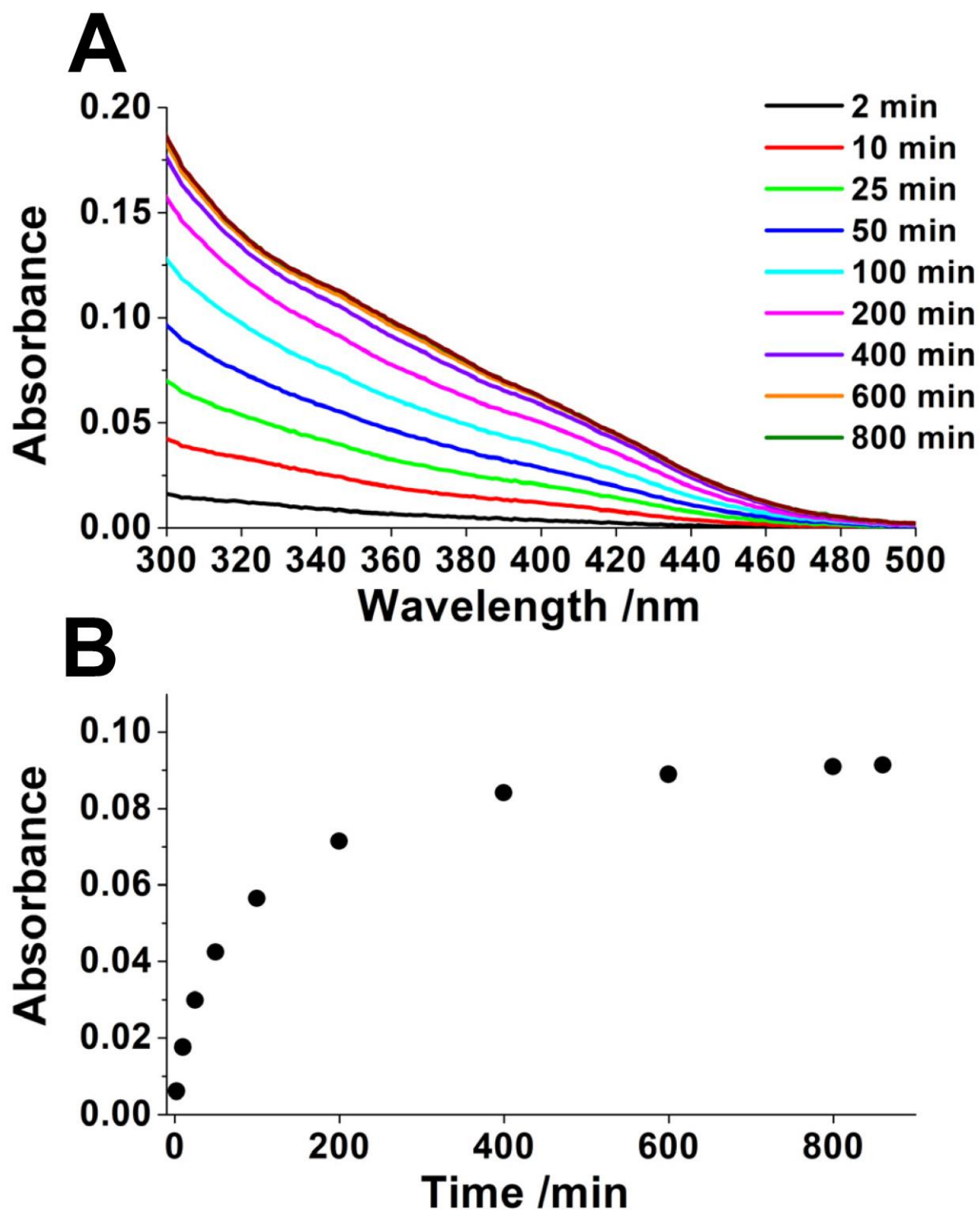


Figure 5-18. UV-visible absorption spectra of $[\text{Bi}(\text{EDTA})]^-$ binding to $\text{Zn}_7\beta\alpha\text{MT}$. (A) UV-visible absorption spectra of a time-dependent reaction of 8 mol. eq. $[\text{Bi}(\text{EDTA})]^-$ with $5 \mu\text{M}$ $\text{Zn}_7\beta\alpha\text{MT}$ at pH 7.4. (B) A plot of the absorbance at 368 nm from (A) as a function of time.

Conversely, when beginning from apo-MT the Bi₂MT and Bi₄MT structures form most readily and metallation beyond Bi₅MT is resisted. As seen with the β MT fragment, changing the cysteine exposure using denaturant resulted in a greater fraction of Bi(III) bound. Therefore, the formation of these structures within the MT is likely impacted by the unequal cysteine exposure.

By examining other literature, the same phenomenon can be observed in other metals binding to MTs. For example, Ag(I) forms Ag₆MT and Ag₁₂MT cooperatively in apo-MT, with up to Ag₁₇₋₁₈MT forming non-cooperatively.¹⁸¹⁻¹⁸² When Ag(I) is titrated into Zn₇MT, Ag₁₈MT is the dominant species formed. The intermediate Ag₆MT no longer forms and Ag₁₂MT only forms under high temperature conditions.³⁶⁴ When Hg(II) is titrated into apo-MT, Hg₇MT is the major species formed with a distinct CD signal.¹⁹⁶ However, titrations of Hg(II) into Zn₇MT produce a signal corresponding to Hg₁₁MT in addition to the one at Hg₇MT.¹⁹⁶

Zn₇MT sometimes accommodates incoming metals in a domain-specific fashion. When Cu(I) binds to apo-MT, Cu₄MT and then Cu₆MT preferentially form in the β -domain, followed by Cu₄MT in the α -domain to form a total of Cu₁₀MT. An additional three Cu(I) can then bind in the α -domain to form Cu₁₃MT.¹⁷⁹ When Cu(I) is added to Zn₇MT, Zn₄Cu₆MT (Cu₆ β MT and Zn₄ α MT) and Zn₂Cu₁₀MT (Cu₆ β MT + Cu₄Zn₂ α MT).³⁶¹ However, the formation of these species is less cooperative. As Zn(II) and Cu(I) are both biologically relevant metals, it is possible that MT evolved to bind them both simultaneously without losing the domain specificity and ability to form clusters. Overall, these results combined with studies of other metals show insight into how MTs deal with the many essential and xenobiotic metals it may encounter in physiology.

5.4 Conclusions

In this chapter, the binding pathways of Bi(III) to MT1a were characterized. The binding was found to be highly dependent on pH, Bi(III) salt used, MT structure, and metal-loading status.

The binding pathways of Bi(III) to apo- β MT1a using two different Bi(III) salts ($[\text{Bi}(\text{cit})]^-$ and $[\text{Bi}(\text{EDTA})]^-$) and two different pH environments (pH 7.4 and pH 2.6) were characterized. The binding constants were determined and compared.

Under low pH conditions, the binding was entirely non-cooperative, while at neutral pH, Bi_2MT and Bi_4MT formed cooperatively. Apo-MT resisted metallation past Bi_5MT at neutral pH, only forming Bi_6MT upon addition of excess Bi(III). This is hypothesized to be due an unfavourable structural rearrangement needing to occur. Additionally, metallation past $\text{Bi}_2\beta\text{MT}$ is unfavourable but can be enhanced by unfolding the protein with a chemical denaturant, suggesting that the cysteines are becoming tangled.

The cooperative formation occurs in both MT fragments but trypsin digestion suggests the binding is not domain specific, meaning that the formation of Bi_2MT may not be highly structure dependent, unlike other metals such as Zn(II), Cd(II), and Cu(I).

When Zn_7MT is used as the starting point, Bi_7MT is able to form at neutral pH, which did not occur in the apo protein. This may occur because the Bi(III) displaces the Zn(II) in a stepwise manner, forming similar binding site locations that would not form in the apo-MT.

Bi(III) provides a model for a xenobiotic metal that MT would not have evolved to bind. The observed “tangling” effect where metal-saturation is resisted in apo-MT contrasted with the readily formed high Bi(III)-loading species in Zn_7MT may prompt further research into the structural dependence of MT for the binding of other xenobiotic metals.

Chapter 6

The Chapters in this thesis so far have focused on metals binding to MTs and their pathways' dependence on aspects such as apo-MT structure and pH environment. In the previous chapter, it was shown that the binding pathway of Bi(III) to MTs was altered depending on the initial metallated status of the MT. This finding suggests that the functions of MT may be altered depending on the metal loading status.

In this chapter, MT's redox abilities are investigated by observing various apo, Cd(II), and Zn(II) metallated MTs' response to oxidative stress. The results show that the metal-loading status has an impact on the cysteinyl thiols' susceptibility to reactive oxygen species.

6 The Structural Role of Cadmium And Zinc In Metallothionein Oxidation By Hydrogen Peroxide: The Resilience of Metal-Thiolate Clusters*

6.1 Introduction

An overabundance of reactive oxygen species in a cell can lead to oxidative stress,⁴³⁻⁴⁵ which is a concern because of its link to many diseases.⁴⁶⁻⁵¹ Healthy cells have many defenses against ROS, many of which are proteins.⁴⁰⁻⁴³

Cysteine residues are common targets for both one and two electron ROS, both resulting in disulfide bond formation. The thiol group will form a sulfenic acid intermediate with two-electron oxidants such as H₂O₂ before forming a disulfide with another cysteine. Disulfide bond formation is a reversible process, thereby providing a controlled pathway linking oxidation and reduction without permanent damage to the protein.^{52-53, 56-57}

* A version of this chapter has been published:

Korkola, N. C.; Stillman, M. J., Structural Role of Cadmium and Zinc in Metallothionein Oxidation by Hydrogen Peroxide: The Resilience of Metal-Thiolate Clusters. *J. Am. Chem. Soc.* **2023**, *145* (11), 6383-6397.

Reproduced with permission from: The American Chemical Society

Metallothioneins (MTs) are a family of small proteins (usually 6–7 kDa) with an unusually high cysteine content and no traditional secondary structural elements. They are thought to be involved in the homeostasis of Zn(II) and Cu(I), the detoxification of heavy metals such as Cd(II), and in the protection against oxidative stress.³³⁹ MT's redox role has been supported by MT production being upregulated by various sources of oxidative stress,^{101-108, 365} the overexpression of MT providing protective effects to cells under oxidative stress,^{118-121, 366-367} and the observation that MTs form both intramolecular and intermolecular disulfide bonds upon oxidation.²¹¹⁻²¹⁴

Apo-MTs bind a wide range of metals in a variety of different structures. The most widely recognized structure of mammalian MTs involves the binding of seven divalent metals such as Cd(II) or Zn(II) into two distinct domains using 20 cysteine residues. Nine thiols bind three metals in the N-terminal β -domain and eleven thiols bind four metals in the C-terminal α -domain using a mix of bridging and terminally bound thiolates.^{110, 143, 146-147, 339}

Metal displacement from MT can result from exposure to ROS as thiols form disulfide bonds and become unavailable for binding. Multiple studies have investigated the mobilization of Zn(II) and Cd(II) from MT due to reaction with various ROS. This process has been monitored via atomic absorption spectrometry^{117, 211}, UV-visible absorption spectroscopy^{116, 136, 211, 215-217}, measurement of ⁶⁵Zn and ¹⁰⁹Cd radioactivity^{128, 218}, fluorescence spectroscopy²¹⁹⁻²²¹, circular dichroism spectroscopy,²²²⁻²²³ and nuclear magnetic resonance (NMR) spectroscopy^{211, 224}. Additionally, redox agents such as glutathione disulfide facilitate Zn(II) transfer from MT to enzymes with lower Zn(II) binding constants,¹³⁶ suggesting MT's involvement in Zn(II) distribution was related to the redox state of the cell.^{116, 128, 136}

Kinetic evidence suggests that the two domains of Cd₇MT and Zn₇MT have different reactivity towards ROS, chelators, and cysteine modifiers.^{175, 209, 224, 368-369} The reaction with each of these different agents results in demetallation. The three metals from the more labile β -domain cluster are the first to be released, followed by the four metals from the more stable α -domain cluster.^{175, 209, 368-369} This sequence of metal release has been

supported by ^{113}Cd NMR spectroscopy, showing selective release of only the three Cd(II) from the β -domain upon exposure to nitric oxide.²²⁴

A limitation of many of the previous studies is that they do not consider the intermediate $\text{M}_x(\text{SH})_y\text{MT}$ species formed as the metals are displaced from the Cd_7MT and Zn_7MT structures ($x = 0-7$, $y = 0-20$). Most spectroscopic methods can only show the average number of cysteines oxidized and the average number of metals bound to MT, so information about these individual species is lost.

Additionally, minimal consideration has been given to the effect of ROS on MTs with a lower metal-loading status that have not yet formed the two-domain structure. Although Cd_7MT and Zn_7MT are the most well-studied forms of MT, reports of partially metallated and oxidized MTs in biological tissue suggest that the most relevant structures of MTs *in vivo* are more complicated.^{225, 370} These structures are not well-defined and thus are difficult to study using typical structural methods like NMR spectroscopy.

A simulation of the release of Zn(II) from the β -domain of MT found that the terminally bound cysteines were more susceptible to oxidation than bridging cysteines within the cluster.²²⁶ This suggests that there may be a difference in susceptibility to oxidation between the fully metallated two-domain structure and a partially metallated structure that has not yet formed the complete network of bridging cysteines.

In order to obtain details of the reaction products following oxidation of these complicated systems, identities of all the products of reaction must be determined. As we mentioned above, optical spectroscopic methods typically provide only averages of the species present rather than the identities of all species in the mixture. Electrospray ionization mass spectrometry is an ideal technique to bridge the gap in knowledge as it can distinguish between individual species in a solution and it is not limited to studying rigid well-defined structures. ESI-MS has been a successful technique for studying MT metallation and demetallation kinetics.^{175, 177} Matrix-assisted laser desorption/ionization MS-MS was used to study the disulfide bond structures formed in the γ -domain of the wheat E_c-1 MT upon oxidation with H_2O_2 . However, this protein has a dissimilar sequence to mammalian MTs and only binds 2 Zn(II).²²³ Additionally, a study on MT exposed to ROS and extracted

from mouse hearts showed by mass spectrometry that disulfide bonds formed in both the β and α domains.²²⁵ However, the metallated structures were not investigated. Overall, the use of MS in studying the simultaneous disulfide bond formation and metal release due to oxidation in mammalian MT structures has been limited.

In this chapter, I characterize the oxidation-induced demetallation pathways of fully and partially metallated Cd(II)-bound and Zn(II)-bound recombinant human MT1a. Using electrospray ionization mass spectrometry (ESI-MS), we identified many intermediate $M_x(\text{SH})_y\text{MT}$ ($x = 0-7$, $y = 0-20$) species formed upon oxidation of apo-MT, Cd_xMT , and Zn_xMT , ($x = 1-7$) by H_2O_2 . The rate constants for each individual metal displacement step measured by ESI-MS were calculated to determine the sensitivity of each species to oxidation. We also investigated the reversibility of the MT oxidation using ESI-MS methods. The reaction rates of apo-MT, Cd_7MT , and Zn_7MT with H_2O_2 were also measured using UV-visible absorption spectroscopy to further compare the susceptibility of the fully metallated and apo-MTs to oxidation by H_2O_2 . Circular dichroism spectroscopy was used to determine the presence of the Cd_4S_{11} and Zn_4S_{11} cluster structures in the partially oxidized MTs from the characteristic cluster derivative signal. Finally, density functional theory calculations were used to show the differences in electron density between terminally bound and bridging cysteines in order to identify the more likely nucleophilic thiol that attacks the H_2O_2 . Together, these data allow comparison between the reactivities of apo-MT, Cd(II)-bound and Zn(II)-bound MTs with different metal-loading statuses towards H_2O_2 and reveal that there are many intermediate $M_x(\text{SH})_y\text{MT}$ species formed during oxidation.

6.2 Materials and Methods

6.2.1 Expression, purification, and preparation of apo-MT

The rhMT1a was expressed and purified as described in Chapter 2. The apo-MT was prepared and the concentration was determined as described in Chapter 2.

6.2.2 Preparation of Cd₇MT, Zn₇MT, Cd₃MT, and Zn₃MT

The apo-MT was metallated to varying degrees using Cd(II) and Zn(II). Solutions of Cd(II) and Zn(II) were prepared by dissolving either solid cadmium acetate (Cd(OAc)₂) or zinc acetate (Zn(OAc)₂) (Fisher) in water to a concentration of 10 mM.

The apo-β_αMT was metallated with either 3 molar equivalents or 8 molar equivalents of the 10 mM Cd(OAc)₂ solution or the 10 mM Zn(OAc)₂ solution and then buffer exchanged by centrifugation with ammonium formate at pH 7.6 containing 0.5 mM TCEP in the same manner that was used to prepare the apo-β_αMT. The pH was confirmed to be 7.6 by measuring the flow-through of the centrifugal filter unit.

It is important to note that the resulting metallated MT samples do not consist of a single species of one particular metal-loading status. In reality, a distribution of species centered around the stoichiometric amount of metal added will be present. However, for simplicity, the partially metallated samples prepared here will be referred to using only the identity of the major species (Cd₃MT and Zn₃MT).

6.2.3 Creation of the oxidizing environment

The oxidation experiments were designed in a way to provide a controlled oxidation that would result in sequential metal release that can be observed on a realistic timescale. Due to this, higher concentrations were used than would be expected *in vivo*. Hydrogen peroxide (H₂O₂) was chosen as an oxidizing agent because it is readily available, stable, and provides a steady reliable source of oxidation whose effects can be observed without interference on the mass spectrometer.

All the MT solutions were prepared in ammonium formate containing 0.5 mM of the reducing agent TCEP. The purpose of this was to ensure no oxidation took place during the preparation of the apo-β_αMT, where the cysteines are extremely vulnerable to oxidation. This allows equal comparison of more stable fully metallated species with more vulnerable partially metallated species. Although GSH would be a more biologically relevant reducing agent, even in stoichiometric amounts to MT it overwhelms the ESI-MS

signal, making it unsuitable for these studies. Additionally, GSH and GSSG would provide significant competition for the Cd(II) and Zn(II).

The samples were prepared at pH 7.6. Mixing MT solutions of this pH with 150 mol. eq. H₂O₂ resulted in solutions of pH 7.4, which was the desired pH for the experiments.

6.2.4 Electrospray ionization mass spectral studies

The ESI-MS parameters used were described in Chapter 2, with a capillary exit voltage of 220.0 V.

Samples of 90 μM apo-MT, Cd₇MT, Zn₇MT, Cd₃MT, and Zn₃MT at pH 7.6 were measured at equilibrium before addition of H₂O₂. The data were collected for and averaged over 1–2 min using the Compass DataAnalysis software. These spectra were deconvoluted over the range 7000–9000 Da using the MaxEnt software package.

Mass spectral kinetic experiments were performed at 25 °C using a temperature controlled syringe pump connected to a water bath. 150 mol. eq. of 0.2 M H₂O₂ was added to either 90 μM apo-MT, Cd₇MT, Zn₇MT, Cd₃MT, or Zn₃MT at pH 7.6, mixed rapidly and thoroughly, quickly transferred to a Hamilton 250 μL syringe, and placed on the temperature controlled syringe pump. The pump was set at a flow rate of 10 μL/min. Once the signal was stable, the flow rate was lowered to 5 μL/min. Data were collected until the oxidation and/or de-metallation had reached equilibrium. Kinetic data were averaged every 2.0 min over time intervals of 1.0 min and deconvoluted over the range 7000–9000 Da. These reactions were performed in triplicate.

In the case of the apo-MT, Cd₇MT, and Zn₇MT, the remaining sample was incubated at 25 °C until the reaction time had reached 120 min. At this point, ESI mass spectra were collected again in the same manner as for the initial equilibrium conditions.

The masses of the peaks in the deconvoluted ESI-mass spectra from the kinetic reactions were obtained and averaged over the whole reaction. These masses were subtracted from the theoretical masses of their corresponding Cd_nMT and Zn_nMT species. The number obtained was taken as the average number of cysteines oxidized for that particular

metallated species. The number of remaining reduced cysteines was calculated by subtracting the number of oxidized cysteines from 20.

Additionally, a series of 30 μM Cd₇MT samples were reacted with 0, 2, 4, 6, 8, and 10 mol. eq. H₂O₂ at pH 7.4. The reagents were mixed and the samples were measured on the ESI mass spectrometer after 24 h, in the same manner as for the other equilibrium samples.

6.2.5 Reversibility experiments

To investigate the reversibility of the oxidation and the ability of MT to regain its metal-binding function after reversal, the 90 μM apo-MT, Cd₇MT, and Zn₇MT reactions with 150 mol. eq. H₂O₂ were quenched after 120 min using pH 2.6 ammonium formate. The samples were buffer exchanged in the same manner as used to prepare the apo-MT. The ammonium formate at pH 7.6 containing 0.5 mM TCEP was used to bring the pH back up and to reverse the oxidation. The samples were measured on the ESI mass spectrometer to verify that full reduction of the MT had been achieved. Cd(OAc)₂ and Zn(OAc)₂ were titrated into the samples that were once Cd₇MT and Zn₇MT, respectively to evaluate the metal-binding function of MT whose oxidation had been reversed. 20 mol. eq. of 10 mM N-ethylmaleimide (NEM) were added to the newly reduced apo-MT to quantify the number of reduced cysteines.

6.2.6 Proteolysis experiments

Proteolysis experiments were carried out on the apo-MT to investigate the source of irreversible oxidation. Trypsin was added to a sample of apo-MT that had never been oxidized and to the oxidized and reversed apo-MT sample described above (without addition of NEM) in a 1:50 w/w ratio. The mixture was incubated in a water bath for 30 min and the resulting peptide fragments were measured on the ESI mass spectrometer.

6.2.7 UV-visible absorption spectroscopy experiments

Kinetic experiments were carried out and measured using UV-visible absorption spectroscopy. 10 μM apo-MT, Cd₇MT, and Zn₇MT at pH 7.6 were measured on a Cary-60 UV-visible spectrometer between 200 and 300 nm using a 1 cm cuvette. For each kinetic run, 150 mol. eq. H₂O₂ was added to the sample in the cuvette (10 μM apo-MT, Cd₇MT,

or Zn₇MT), rapidly mixed, and placed in the cuvette holder. Scans were recorded every 0.2 min for 10 min, then every 1.0 min for 300 min for the apo-MT samples. Scans were recorded every 0.2 min for 10 min, every 1.0 min for 60 min, then every 5.0 min for 600 min in the case of the Cd₇MT and Zn₇MT samples.

To obtain the kinetic trace, absorbance over time at the wavelength of interest over time was extracted. The wavelengths used were that of the disulfide bond formation at 280 nm band for apo-MT, the S→Cd LMCT band at 250 nm for Cd₇MT, and the S→Zn LMCT at 230 nm for Zn₇MT.

6.2.8 Quantification of Zn(II) release

To validate the concentration of metal released over time during the ESI-MS kinetic experiments, a reaction between 17 μM Zn₇MT and 200 mol. eq. H₂O₂ in the presence of 1.2 mM zincon (ZI), a Zn(II)-sensor that forms a Zn-ZI complex absorbing at 618 nm with a molar extinction coefficient of 24 200 M⁻¹cm⁻¹ was monitored by absorption spectroscopy.³⁷¹ The reaction took place in a 0.2 cm cuvette and was measured between 500 and 700 nm every 0.2 min for 10 min, then every 1.0 min for 200 min. The total free Zn(II) was measured by scanning a sample of 119 μM Zn(OAc)₂ and 1.2 mM ZI in the absence of MT and the 0 min time point was measured by scanning the 17 μM Zn₇MT and 1.2 mM zincon (ZI) before the addition of H₂O₂. A parallel reaction was performed using the same concentrations but in the absence of ZI and measured on the ESI mass spectrometer at various time points (5 min, 15 min, 24 min, 38 min, 67 min, and 117 min) to compare the ability of the two methods to measure metals bound to MT. At 24, 38, and 67 min, a portion of the sample was acidified to demetallate the MT and obtain the average number of reduced cysteine residues for the whole protein.

6.2.9 Determination of the rate constants

For the kinetic reactions monitored by ESI-MS, the peak integrals over time were extracted using the Data Analysis software. All observed m/z peaks were extracted, including any adduct formations, and compiled to form a list of metallated species with their intensities as a function of time. The baseline was subtracted, and the intensity vs time was converted into concentration vs time using the known total concentration of MT (90 μM) and the

fractional intensities of each peak. These kinetic traces were modelled as multiple bimolecular reactions and fit using COPASI version 4.27.³⁷² An in depth explanation of the reactions used to fit the traces is presented in the Results and Discussion section. For the case of the kinetic traces obtained through UV-visible absorption experiments, the reaction was fit to a single bimolecular reaction.

6.2.10 Circular dichroism spectroscopy experiments

Circular dichroism spectroscopy measurements were made on a J-810 spectropolarimeter (Jasco, USA). All the samples were measured between 200 and 350 nm using a 0.2 cm cuvette with a data pitch of 1 nm and a response of 2 s. Two accumulations were collected. The MT samples were prepared as previously described with a few changes. All samples were prepared in 5 mM ammonium formate to minimize the absorbance near 200 nm. The Cd₇MT and Zn₇MT samples were prepared without the use of TCEP. Additional Cd₃MT and Zn₃MT samples in pH 5.0 ammonium formate were prepared and measured. The concentration of all MT samples was 25 μM.

The MT samples were incubated with 5 mol. eq. or 10 mol. eq. H₂O₂ at room temperature for either 40 h (for Cd₇MT and Zn₇MT) or 1 h (for Cd₃MT and Zn₃MT), respectively. CD spectra were measured before and after oxidation. For each CD spectrum obtained, the corresponding ESI-MS spectra was also obtained to identify the species in solution.

A reaction between 25 μM Cd₇MT and 150 mol. eq. H₂O₂ was monitored kinetically using CD spectroscopy. The CD spectra were measured before addition of H₂O₂, and then at 3, 11, 18, 33, 84, and 145 min after addition of H₂O₂. The spectra were scanned between 200 and 350 nm using a 0.2 cm cuvette with a data pitch of 2 nm and a response of 0.5 s. One accumulation was collected.

6.2.11 Theoretical calculations

Ground state geometries of molecular models of [Cd₃(CH₃S)₉]³⁻ and [Zn₃(CH₃S)₉]³⁻ mimicking the β-domain of fully metallated MT were optimized using the molecular mechanics and dynamics application in the Scigress software package (Fujitsu, Poland). A MeSH model mimicking a free sulfur on the apo-MT was also generated using the same

method. Molecular orbitals (MOs) were calculated using density functional theory (DFT) from Gaussian G09 with water as a solvent. The basis sets 6-31g(d,p) and lan12dz and the functional B3LYP were used. The frequencies were calculated, and all were positive.

6.3 Results and Discussion

The following data describe the effects of oxidation by H_2O_2 on recombinant human MTs with different metal-loading statuses. I start with a description of the reaction products of apo-MT to provide a baseline for how the cysteines in MT and the other amino acids that are part of the peptide respond to this particular oxidizing environment. Oxidation of the fully metallated Cd_7MT and Zn_7MT provides information about metal displacement from the well-known 2-domain cluster structure.

Cd_3MT and Zn_3MT model MT's response to oxidation with the more biologically relevant metal-deficient state, where the two-domain cluster structure has not formed. Under

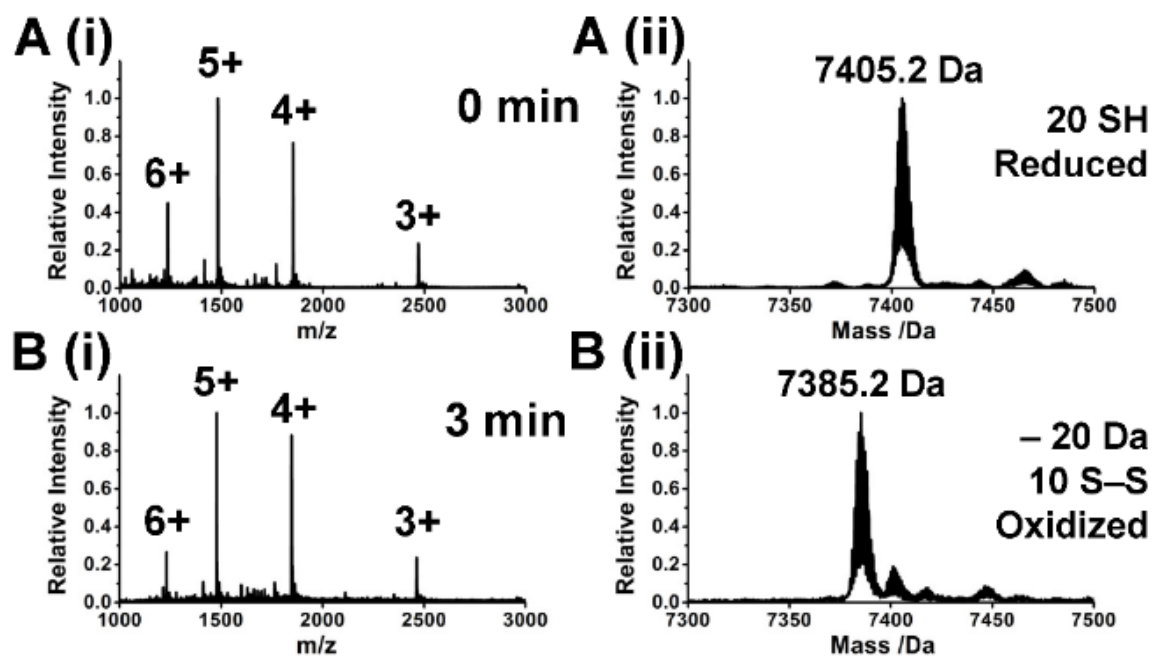


Figure 6-1. Oxidation of apo-MT monitored using ESI-MS. A reaction of $90\ \mu\text{M}$ apo-MT with $13.5\ \text{mM}$ H_2O_2 (150 mol. eq.) at pH 7.4 monitored over time using ESI-MS. (i) Charge state and (ii) deconvoluted ESI mass spectra show the reaction at (A) 0 min and (B) 3 min. The weighted average charge state is 4.7 for the fully reduced apo-MT and 4.6 for the fully oxidized apo-MT. Reproduced from Korkola and Stillman, 2023 with permission from The American Chemical Society.

physiological conditions (pH 7.4), Zn(II) will bind to apo-MT in a non-cooperative manner, where terminal metal-thiolate bonds form before the Zn_4S_{11} and Zn_3S_9 bridging cluster structures at metal saturation. At physiological pH, Cd(II) will bind to apo-MT in a mixed cooperative and non-cooperative pathway, where the majority of Cd(II) binds terminally but some will bind cooperatively to form Cd_4S_{11} .¹⁷¹

6.3.1 H_2O_2 selectively oxidizes the cysteine and methionine residues of apo-MT

The cysteines of apo-MT reversibly form disulfide bonds when exposed to H_2O_2 . A 20 Da decrease in mass after 3 min of reaction of 90 μ M apo-MT with 13.5 mM (150 mol. eq.) H_2O_2 is seen in the ESI mass spectral data (Fig. 6-1), corresponding to the loss of 2 H^+ for each disulfide formed. The loss of 20 H^+ indicate all 20 cysteines have formed disulfide bonds. The change in the surface area between the fully reduced and oxidized protein is minimal, with the weighted average charge state changing from +4.6 to +4.7 (Fig. 6-1).

Methionine sulfoxide formation occurs in later stages of the reaction, as seen in the ESI mass spectrum as a mass increase of 16 Da (Fig. 6-2Aii).³⁷³ This result is further supported by the trypsin digestion data, where a 16 Da mass increase is found on each of the three methionine-containing fragments (fragments [1], [2], and [7]) (Fig. 6-2D and Table 6-1).

The cysteine residues do not undergo irreversible sulfinic acid or sulfonic acid formation under these conditions. Upon buffer exchange with TCEP-containing ammonium formate, all the cysteine residues are reduced and therefore accessible, as indicated by a mass increase of 20 Da and the binding of 20 N-ethylmaleimide (NEM), a cysteine modifier (Fig 6-2B-C). However, the methionine sulfoxides remain, despite this being a reversible modification *in vivo*.⁵²

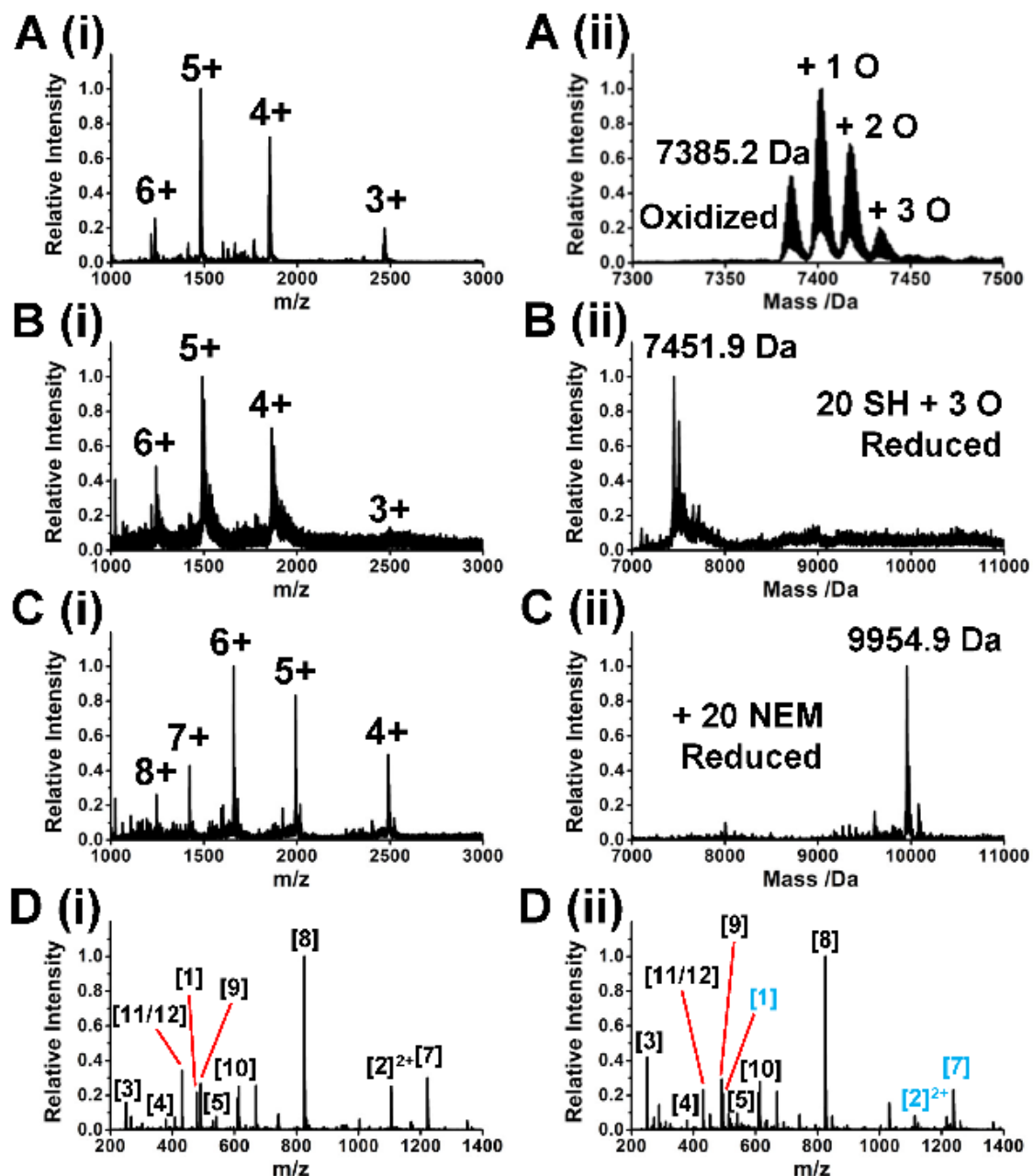


Figure 6-2. Oxidation, reduction, and trypsin digestion of apo-MT. A reaction of 90 μM apo-MT with 13.5 mM H_2O_2 (150 mol. eq.) at pH 7.4 monitored using ESI-MS. (i) Charge state and (ii) deconvoluted ESI mass spectra show (A) the oxidized apo-MT after 120 min, (B) the reduced apo-MT after reversing the reaction with TCEP, and (C) the reduced apo-MT after addition of 20 mol. eq. NEM. (D) ESI mass spectra after a 1:50 reaction of trypsin with (i) reduced apo-MT or (ii) oxidized apo-MT that was reduced with TCEP. The light blue labels indicate the fragments where the +16 oxygen addition was found. The x-axis ranges are (A) 7300 – 7500 Da, (B) and (C) 7000 – 11000 Da, and (D) 200 – 1400 m/z. Reproduced from Korkola and Stillman, 2023 with permission from The American Chemical Society.

6.3.2 Metal-thiolate bonds provide protection against MT oxidation

H₂O₂ oxidizes apo-MT, Cd₇MT, and Zn₇MT at different rates as determined by UV-visible absorption spectroscopy (Fig. 6-3). The rate constants describing the overall reaction of 1.5 mM H₂O₂ with 10 μM apo-MT, Cd₇MT, and Zn₇MT are $2.6 \pm 0.2 \text{ M}^{-1}\text{s}^{-1}$ (Fig. 6-3A), $0.08 \pm 0.01 \text{ M}^{-1}\text{s}^{-1}$ (Fig. 6-3B), and $0.10 \pm 0.01 \text{ M}^{-1}\text{s}^{-1}$ (Fig. 6-3C), respectively. The rate constant for apo-MT oxidation is 33 times higher than that of Zn₇MT demetallation and 26 times higher than that of Cd₇MT demetallation. However, the rate constant for Zn₇MT demetallation is only 1.25 times higher than that of Cd₇MT, showing that the presence of metal-thiolate bonds is more important for protecting the thiols over the identity of the metal.

Table 6-1. Apo-MT tryptic peptides. Peptide fragments resulting from a 1:50 reaction of trypsin with apo-MT. Reproduced from Korkola and Stillman, 2023 with permission from The American Chemical Society.

Fragment	Sequence Position	Peptide Sequence	Mass (Da)
1	1–5	GSMGK	479.6
2*	6–29	AAAAMDPNCSCATGGSCTCT GSCK*	2211.5
3	30–31	CK	250.3
4	32–34	ECK	379.5
5	35–39	CTSCK	541.7
6**	40–40	K	147.2
7	41–52	SCCSCCPMSCAK	1223.5
8	53–60	CAQGCICK	826.0
9	61–65	GASEK	491.5
10	66–71	CSCCAK	614.8
11**	72–72	K	147.2
12	73–76	AAAA	303.3
11 + 12***	72–76	KAAAA	431.512
1****	1–5	GSMGK	495.6
2* ****	6–29	AAAAMDPNCSCATGGSCTCT GSCK	2219.5
7****	41–52	SCCSCCPMSCAK	1239.5

*Peak appears as the 2+ charge state (m/z 1106.8)

**Peak does not appear in ESI-mass spectra

***Peak arises due to a missed cleavage

****Peak contains a +16 Da modification

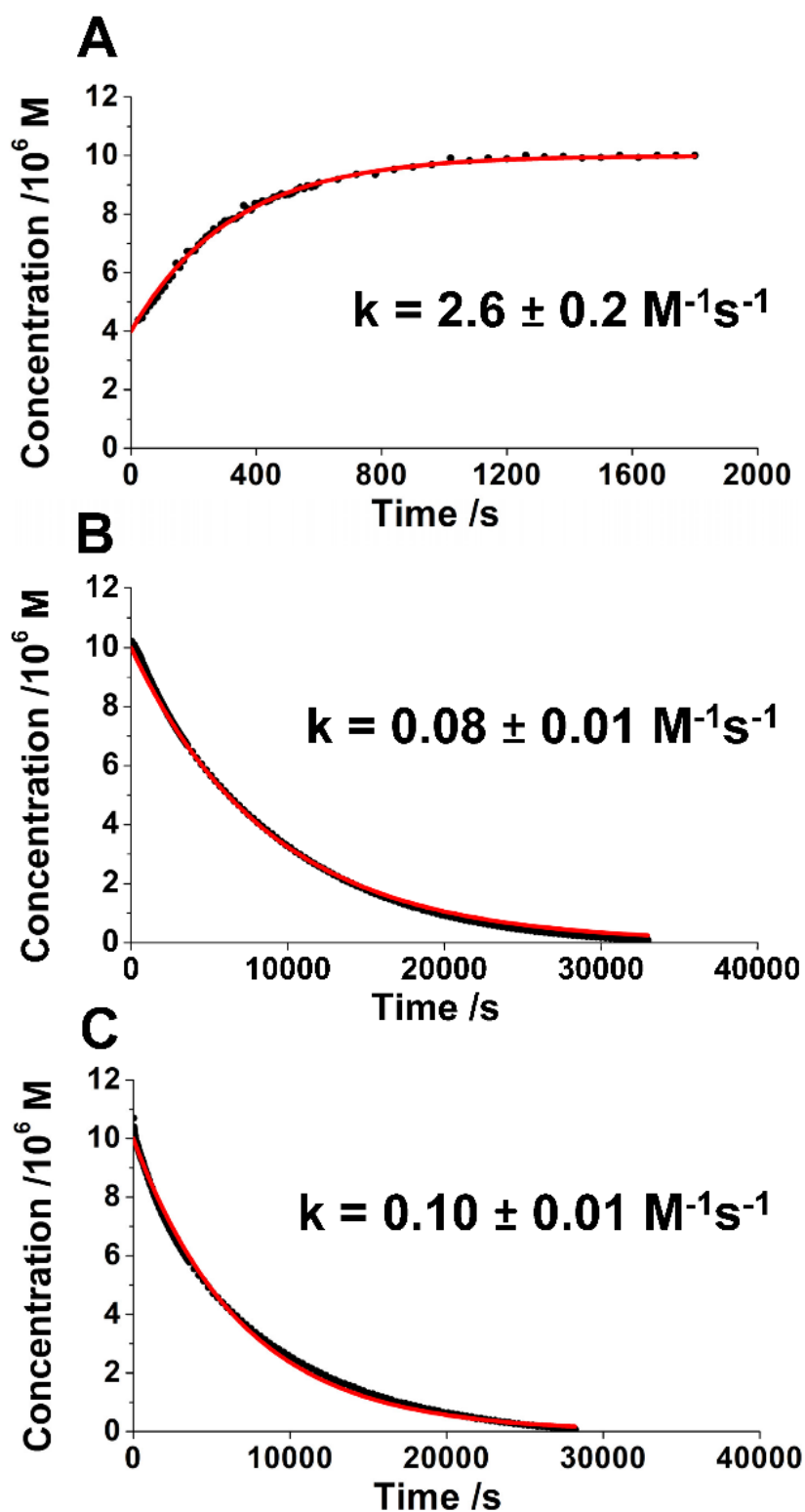


Figure 6-3. Oxidation of apo-MT, Cd₇MT, and Zn₇MT monitored using absorption spectroscopy. Kinetic traces for a reaction of 10 μM (A) apo-MT, (B) Cd₇MT, or (C) Zn₇MT with 150 mol. eq. H₂O₂ at pH 7.4 monitored by UV-visible absorption spectroscopy at (A) 280 nm, (B) 250 nm, or (C) 230 nm showing errors over three experiments. Reproduced from Korkola and Stillman, 2023 with permission from The American Chemical Society.

6.3.3 Individual metallated and oxidized species are identified using ESI-MS

ESI mass spectra from selected time points in the kinetic reaction of 90 μM Cd₇MT with 13.5 mM H₂O₂ and 90 μM Zn₇MT with 13.5 mM H₂O₂ are shown in Fig. 6-4. Both the metal-loading status and extent of disulfide formation are identified in the reaction intermediates by their masses. Before addition of H₂O₂, a distribution of Cd₇₋₉(SH)₂₀MT (Fig. 6-4Aii) and a single peak of Zn₇(SH)₂₀MT (Fig. 6-4Aiv) are seen in the respective

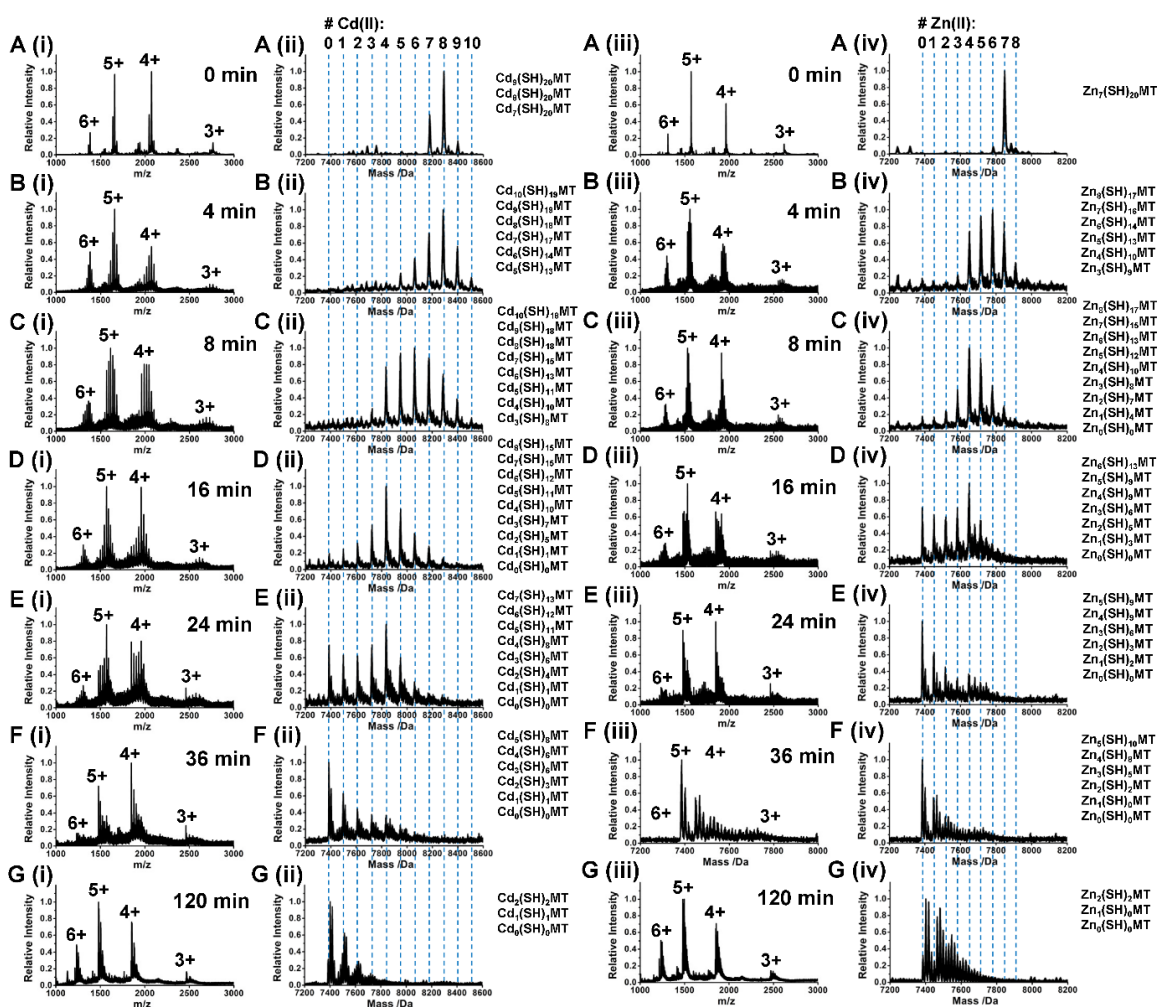


Figure 6-4. Oxidation of Cd₇MT and Zn₇MT monitored using ESI-MS. Reactions of either (i, ii) 90 μM Cd₇MT or (iii, iv) 90 μM Zn₇MT with 13.5 mM H₂O₂ (150 mol. eq.) at pH 7.4 monitored over time using ESI-MS. (i, iii) Charge state and (ii, iv) deconvoluted ESI mass spectra show the reaction at (A) 0 min, (B) 4 min, (C) 8 min, (D) 16 min, (E) 24 min, (F) 36 min, and (G) 120 min. To the right of each deconvoluted spectrum is a list of all the M_x(SH)_yMT species present in that spectrum. Adapted from Korkola and Stillman, 2023 with permission from The American Chemical Society.

deconvoluted ESI mass spectra. In both cases, all 20 cysteine residues are in the reduced state. We will use the nomenclature of $M_x(\text{SH})_y\text{MT}$ to indicate the number of bound metals (where $M = \text{Cd(II)}$ or Zn(II)) and the number of reduced thiols ($\text{SH} = \text{reduced thiol}$) in each species.

The starting Cd_7MT sample is not a pure species of only Cd_7MT . Cd_8MT formation is favourable under conditions of metal-saturation and has been reported.¹⁴⁸ Based on preliminary experiments, the presence of this species does not alter the pathway of metal release or the rate constants obtained. In fact, it allows more precision in determining the Cd_7MT to Cd_6MT demetallation step, as less of the reaction takes place in the dead time. Zn_7MT does form a significant fraction Zn_8MT , therefore a pure species of Zn_7MT is observed.

4 min. after the addition of H_2O_2 to Cd_7MT , a distribution of $\text{Cd}_{5-10}(\text{SH})_{13-19}\text{MT}$ is apparent in the mass spectra (Fig. 6-4Bii). After 8 min, a distribution of $\text{Cd}_{4-10}(\text{SH})_{10-18}$ is observed. A distribution of $\text{Zn}_{4-8}(\text{SH})_{10-16}\text{MT}$ forms 4 min after addition of H_2O_2 to Zn_7MT (Fig. 6-4Biv).

After 16 min (Fig. 6-4Dii) and 8 min (Fig. 6-4Civ), $\text{Cd}_4(\text{SH})_{10}\text{MT}$ and $\text{Zn}_4(\text{SH})_{10}\text{MT}$ dominate the spectra. The lower metallated species $\text{Cd}_{0-4}(\text{SH})_{1-8}\text{MT}$ and $\text{Zn}_{0-4}(\text{SH})_{0-8}\text{MT}$ are seen at 24 min (Fig. 6-4Eii) and 16 min (Fig. 6-4Div), respectively. Methionine sulfoxide adducts begin to form by 36 min for both the Cd(II) and Zn(II) reactions (Fig. 6-4F). After 120 min of reaction, the fraction of adduct formation is greater and it can be seen that significant amounts of $\text{Cd}_1(\text{SH})_1\text{MT}$ and $\text{Zn}_1(\text{SH})_0\text{MT}$ remain (Fig. 6-4G).

The oxidation reactions of the partially metallated MTs Cd_3MT and Zn_3MT were also kinetically monitored by ESI-MS. ESI mass spectra from selected time points in the kinetic reaction of $90 \mu\text{M}$ Cd_3MT with 13.5 mM H_2O_2 and Zn_3MT with 13.5 mM H_2O_2 are shown in Fig. 6-5.

Apo-MT with 3 mol. eq. Cd(II) or Zn(II) added results in distributions ranging from $\text{Cd}_{0-6}(\text{SH})_{20}\text{MT}$ (Fig. 6-5Aii) or $\text{Zn}_{0-6}(\text{SH})_{20}\text{MT}$ (Fig. 6-5Aiv), respectively. For both conditions, a weighted average of three metals are bound. 4 min after the addition of H_2O_2 ,

a distribution of $\text{Cd}_{2-6}(\text{SH})_{6-17}\text{MT}$ is seen (Fig. 6-5Bii). A distribution of $\text{Zn}_{0-6}(\text{SH})_{4-17}\text{MT}$ forms 2 min after the addition of H_2O_2 to Zn_3MT (Fig. 6-5Biv). After 12 min, the remaining $\text{Cd}(\text{II})$ now is now distributed between $\text{Cd}_{0-5}(\text{SH})_{1-12}\text{MT}$ (Fig. 6-5Cii). For Zn_3MT , the species range is $\text{Zn}_{0-5}(\text{SH})_{0-11}\text{MT}$ at 6 min (Fig. 6-5Civ).

Greater fractions of fully oxidized apo $(\text{SH})_0\text{MT}$ are seen at 16 min for $\text{Cd}(\text{II})$ and 8 min for $\text{Zn}(\text{II})$ (Fig. 6-5D). The reaction is complete by 30 min and 14 min for $\text{Cd}(\text{II})$ and $\text{Zn}(\text{II})$, respectively (Fig. 6-5E). A much smaller fraction of $\text{Cd}_1(\text{SH})_1\text{MT}$ and $\text{Zn}_1(\text{SH})_1\text{MT}$ remain at this point than was seen in the reaction with fully metallated MTs.

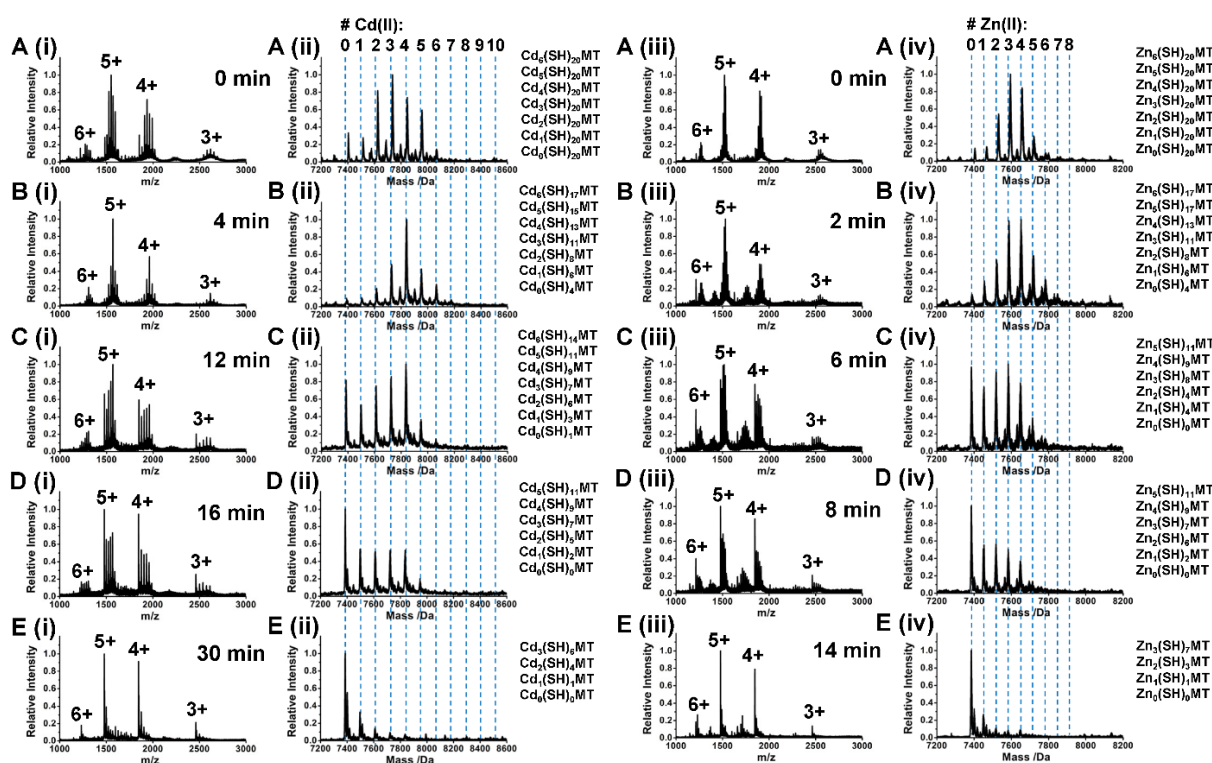


Figure 6-5. Oxidation of Cd_3MT and Zn_3MT monitored using ESI-MS. Reactions of either (i, ii) 90 μM Cd_3MT or (iii, iv) 90 μM Zn_3MT with 13.5 mM H_2O_2 (150 mol. eq.) at pH 7.4 monitored over time using ESI-MS. (i, iii) Charge state and (ii, iv) deconvoluted ESI mass spectra show the reaction at (A) 0 min, (B) 4 min, (C) 12 min, (D) 16 min, and (E) 30 min for the Cd_3MT reaction and at (A) 0 min, (B) 2 min, (C) 6 min, (D) 8 min, and (E) 14 min for the Zn_3MT reaction. To the right of each deconvoluted spectrum is a list of all the $\text{M}_x(\text{SH})_y\text{MT}$ species present in that spectrum. Adapted from Korkola and Stillman, 2023 with permission from The American Chemical Society.

6.3.4 The extent of disulfide bond formation predicts the metal-loading status

For both partially and fully metallated Cd(II) and Zn(II) MTs, the species with a lower metal-loading status have a greater extent of disulfide bond formation. This links the oxidation of the cysteine residues by H₂O₂ with the release of the metals from the metal-thiolate bonds.

The number of remaining reduced cysteine residues as a function of metal-loading status (M₀₋₁₀(SH)₀₋₂₀MT) obtained from the mass spectra and averaged over the duration of each reaction is shown in Table 6-2. One disulfide bond is formed on average for each metal displaced from Cd₇MT, Zn₇MT, or Cd₃MT, while an average of 1.5 disulfide bonds are formed for each metal displaced from Zn₃MT. The greatest variation between the different starting conditions occurs at M₆MT and M₅MT, where the MT starting from Zn₃MT has an average of four more reduced cysteines at these points than the MT starting from Cd₇MT. As well, the number of disulfide bonds formed over the duration of the reaction varies only by an average of ± 1 disulfide for fully metallated MTs, and by an average of ± 2 for partially metallated MTs. The greater variation for the partially metallated MTs is

Table 6-2. Number of oxidized and reduced cysteines throughout oxidation reactions.

The averaged number of reduced and oxidized cysteines per each metalated state over the reaction between 90 μ M Cd₇MT, Zn₇MT, Cd₃MT, or Zn₃MT and 13.5 mM H₂O₂ (150 mol. eq.) at pH 7.4 monitored using ESI-MS. The numbers were averaged over three experiments. The errors show the range of reduced/oxidized cysteines for that metalated species over the whole reaction. Reproduced from Korkola and Stillman, 2023 with permission from The American Chemical Society.

	Cd ₇ MT		Zn ₇ MT		Cd ₃ MT		Zn ₃ MT	
	# CYS _{red}	# CYS _{ox}	# CYS _{red}	# CYS _{ox}	# CYS _{red}	# CYS _{ox}	# CYS _{red}	# CYS _{ox}
M ₁₀ MT	19 \pm 1	1 \pm 1	-	-	-	-	-	-
M ₉ MT	19 \pm 1	1 \pm 1	-	-	-	-	-	-
M ₈ MT	17 \pm 1	3 \pm 1	18 \pm 1	2 \pm 1	-	-	-	-
M ₇ MT	15 \pm 2	5 \pm 2	16 \pm 1	4 \pm 1	-	-	-	-
M ₆ MT	12 \pm 1	8 \pm 1	14 \pm 1	6 \pm 1	15 \pm 2	5 \pm 2	18 \pm 2	2 \pm 2
M ₅ MT	10 \pm 2	10 \pm 2	10 \pm 2	10 \pm 2	12 \pm 2	8 \pm 2	14 \pm 2	6 \pm 2
M ₄ MT	9 \pm 1	11 \pm 1	10 \pm 1	10 \pm 1	10 \pm 2	10 \pm 2	11 \pm 2	9 \pm 2
M ₃ MT	6 \pm 1	14 \pm 1	7 \pm 1	13 \pm 1	8 \pm 2	12 \pm 2	9 \pm 2	11 \pm 2
M ₂ MT	4 \pm 1	16 \pm 1	4 \pm 1	16 \pm 1	5 \pm 1	15 \pm 1	5 \pm 2	15 \pm 2
M ₁ MT	2 \pm 1	18 \pm 1	2 \pm 1	18 \pm 1	2 \pm 2	18 \pm 2	2 \pm 2	18 \pm 2
Apo-MT	0 \pm 1	20 \pm 1	0 \pm 1	20 \pm 1	1 \pm 2	19 \pm 2	0 \pm 1	20 \pm 1

likely due to the fact that for the first few minutes of the reaction, the free cysteines are oxidized before metal displacement begins, therefore allowing a wider variety of species.

6.3.5 The metals in MT are remarkably resistant to displacement

The data in Table 6-2 for each oxidized state shows that more metals remain bound than should be theoretically possible based on the number of reduced thiols remaining after the disulfide bonds have been formed. Usually, Cd(II) or Zn(II) bind tetrahedrally using four cysteine thiols, while multiple Cd(II) or Zn(II) share bridging cysteines, such as in the M_4S_{11} and M_3S_9 clusters. However, species such as $M_2(SH)_4MT$ and $M_1(SH)_2MT$ are observed in the ESI mass spectral data. At this point in the oxidation, these two metals share just four cysteines between them. M_4MT , which normally utilizes the 11 cysteines of the α -domain, remains bound even when only 9-10 cysteines remain reduced. M_7MT remains with only 14 reduced cysteines, even though it normally binds using all 20 cysteines. This is likely due to the metals using other ligands on the protein backbone and the solvent to remain bound.

It is, however, important to note that the number of disulfides formed for each metallated species is not an exact number, but rather a small distribution. This is due to the width of the MT peak making the mass decrease of 2 Da per disulfide bond formed difficult to resolve.

6.3.6 Metal redistribution occurs upon exposure to H_2O_2

Upon the initial change from a reducing environment to an oxidizing one due to addition of H_2O_2 , peaks indicating a higher metal-loading status than normally observed appear in the mass spectra. Specifically, the small Cd_9MT peak increases in intensity and a $Cd_{10}MT$ peak appears as the Cd(II) begins to be displaced (Fig. 6-4Bii). Zn_8MT also appears in the Zn_7MT spectrum as the reaction begins (Fig. 6-4Biv). The presence of these species can be explained by the initially displaced metals binding to the less oxidized MTs, possibly as adducts.

A similar phenomenon is observed for the partially metallated MTs where the species shift to favour higher metal-loading statuses upon oxidation. However, the distributions formed

for Cd₃MT and Zn₃MT are different. When H₂O₂ is introduced to Cd₃MT, the distribution of Cd(II) species narrows and shift to center around Cd₄MT (Fig. 6-5Bii). Conversely, for Zn₃MT, there is a non-specific increase in the Zn₄₋₆MT species (Fig. 5Biv), without favouring the formation of Zn₄MT. The favouring of Cd₄MT suggests that this species is particularly stable towards oxidation.

6.3.7 The species distributions following oxidation depend on the metal-loading status of the MT

The distribution of oxidized species formed at different times gives insight into the stability of various metallated structures. For the fully metallated MTs, the distribution of oxidized species has two distinct profiles that appear throughout the reaction. When $M_{avg} > 4$, the distribution does not favour any particular species (Fig. 6-4B–C). However, when $M_{avg} < 4$ the distribution profile changes and favours those profiles of M₄MT and apo-MT (Fig. 6-4D–F). This again highlights how M₄MT is a particularly stable structure. The ESI-MS profiles for Cd₇MT and Zn₇MT are remarkably similar in their oxidation-induced metal displacement profiles.

The partially metallated MTs that have not yet formed the two-domain structure display some differences in their distributions compared with the changes seen with their fully metallated counterparts. The displacement of Cd(II) from Cd₃MT still favours a mixture of the Cd₄MT and apo-MT species (Fig. 6-5Cii). However, there is an increased abundance of the Cd₃MT and Cd₂MT species compared to the reaction products when Cd₇MT is the starting material. The Zn₃MT displacement distribution does not display the high abundance of the Zn₄MT species. Instead, the species remain in a non-specific distribution, centered around Zn₃MT (Fig. 6-5Civ). These results further suggest that the displacement pathways of Cd₇MT and Zn₇MT depend on the two-domain structure but the partially metallated Cd₃MT and Zn₃MT follow a different pathway.

It is important to reiterate that the experimental concentrations of H₂O₂ were chosen to allow observation of the demetallation pathways on a reasonable timescale rather than to mimic *in vivo* conditions. To verify that the same metal-release pathway results from other concentrations of H₂O₂, a series of 30 μM Cd₇MT samples were reacted with 2, 4, 6, 8, and

10 mol. eq. H_2O_2 and measured after 24 h (Appendix D, Fig. D-1). Under these conditions, the reaction does not go to completion, rather forming species between Cd_{2-8}MT with an extremely similar distribution to the kinetic pathway (Fig. S3). Most notably, the non-specific distribution at $\text{Cd}(\text{II}) > 4$ and the favourable formation of Cd_4MT is evident.

Additionally, to verify that the data obtained from the mass spectrometric studies reflect the solution conditions, a reaction of $17 \mu\text{M Zn}_7\text{MT}$ with 200 mol. eq. H_2O_2 in the presence of 0.5 mM TCEP and 1.2 mM ZI at pH 7.4 was monitored by absorption spectroscopy to quantify the $\text{Zn}(\text{II})$ release (Appendix D, Fig. D-2A). The average number of $\text{Zn}(\text{II})$ remaining bound to MT was calculated using the absorption spectroscopic data (Appendix D, Fig. D-2A) and mass spectrometric data (Appendix D, Fig. D-3) at various time points. The resulting values were found to be within 0.5 mol. eq. of each other, verifying that the species distributions in the mass spectrometer reflect solution-phase data (Appendix D, Fig. D-2B). At selected time points during this reaction, portions of the MT sample were acidified to induce demetallation to verify the overall disulfide bond formation (Appendix D, Fig. D-3C-E). The total number of reduced cysteines at each time point was calculated from both the weighted average of each metallated species in the spectrum and the average mass of the demetallated MT. These values are plotted in Fig. D-2C (Appendix D) and are within one cysteine of each other for both methods.

6.3.8 Circular dichroism spectroscopy reveals the presence of α -domain cluster structures in partially oxidized MTs

CD spectra of different metallated MT samples are shown in Fig. 6-6. Corresponding ESI mass spectra are shown in Fig. 6-7.

Before exposure to H_2O_2 , Cd_7MT and Zn_7MT show the characteristic derivative bands indicating the two-domain cluster structure. The Cd_7MT spectrum shows peaks at 260 nm (+) and 240 nm (-) with a crossover at 250 nm (Fig. 6-6Ai). The Zn_7MT spectrum shows peaks at 245 nm (+) and 235 nm (-) with a crossover at 240 nm (Fig. 6-6Bi). After 40 h of exposure to 5 mol. eq. H_2O_2 , partial demetallation has occurred and the derivative band is weakened in both Cd_7MT (Fig. 6-6Aii) and Zn_7MT (Fig. 6-6Bii) but is still present. In these spectra, Cd_4MT and Zn_4MT are the major species, as confirmed by ESI-MS as shown

in Fig. 6-7Bii and Fig. 6-7Biv, respectively. The CD spectra of Cd₃MT (Fig. 6-6Aiii and Ciii) and Zn₃MT (Fig. 6-6Biii and Diii) at pH 5.0 are also shown. At pH 5.0, the Cd₄S₁₁ cluster forms cooperatively and the Zn₄S₁₁ cluster forms semi-cooperatively. These data at pH 5.0 provide a reference for the CD spectra of the partially metallated cluster structure, allowing for comparison to the structures present in the partially oxidized samples.

The partially metallated Cd₃MT and Zn₃MT CD spectra at pH 7.4 before addition of H₂O₂ do not show the presence of cluster structures. Instead, the maximum at 245 nm (+) for Cd₃MT (Fig. 6-6Ci) and the lack of a peak at 235 nm (-) for Zn₃MT (Fig. 6-6Di) indicate non-specific terminally bound structures. Upon 1 h of reaction with 10 mol. eq. H₂O₂, the maximum of the Cd₃MT CD spectral band shifts from 245 nm (+) to 260 nm (+) (Fig. 6-6Cii). However, under the same conditions, the Zn₃MT CD spectrum remains largely

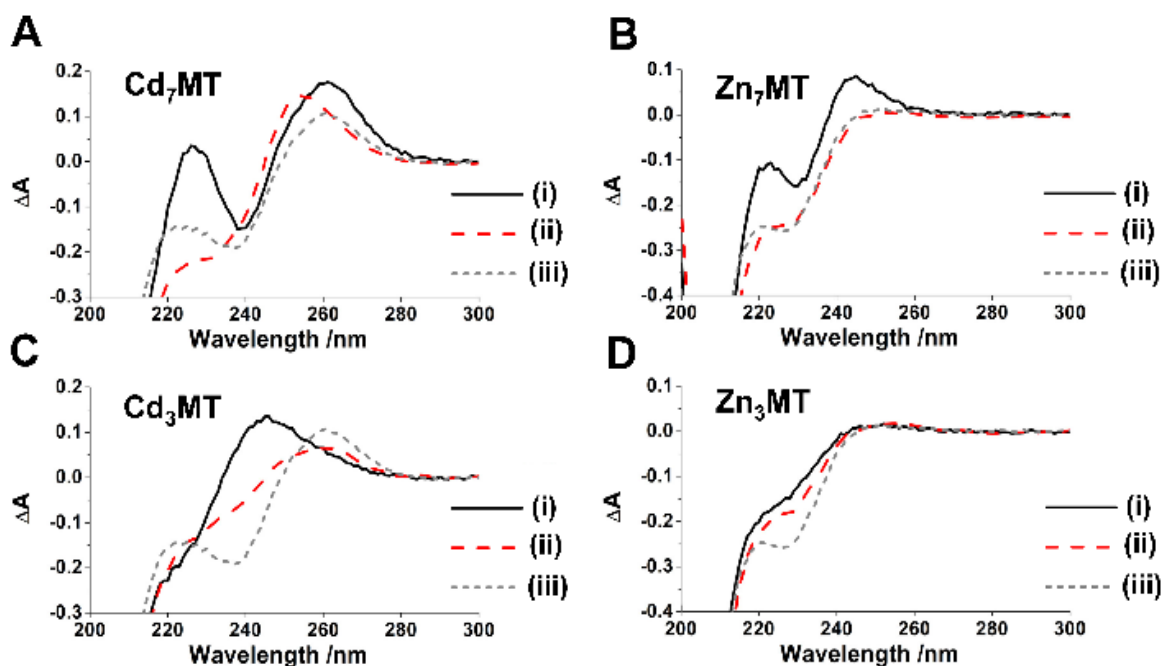


Figure 6-6. Reduced and oxidized MTs monitored using circular dichroism spectroscopy. Circular dichroism spectra of (A) 25 μ M Cd₇MT, (B) 25 μ M Zn₇MT, (C) 25 μ M Cd₃MT and (D) 25 μ M Zn₃MT (i) before reaction with H₂O₂ and (ii) after either (A-B) 40 h reaction with 0.125 mM (5 mol. eq. H₂O₂) at pH 7.4 or (C-D) 1 h reaction with 0.25 mM (10 mol. eq. H₂O₂) in the presence of 0.5 mM TCEP at pH 7.4. (iii) Circular dichroism spectra of (A, C) Cd₃MT at pH 5.0 and (B, D) Zn₃MT at pH 5.0. Reproduced from Korkola and Stillman, 2023 with permission from The American Chemical Society.

unchanged (Fig. 6-6Dii). As with the fully metallated samples, CD spectra of Cd₃MT (Fig. 6-6Ciii) and Zn₃MT (Fig. 6-6Diii) at pH 5.0 are shown.

These results show that the cluster structure still remains after partial oxidation of Cd₇MT and Zn₇MT to Cd₄MT and Zn₄MT, respectively. Based on comparisons with CD spectra of the α -domain cluster as well as the stability of the M₄MT structure, it can be concluded that the metals in the β -domain are the first to be released, leaving the α -domain largely intact. However, the M₄MT species never exists in isolation as shown by the ESI-MS

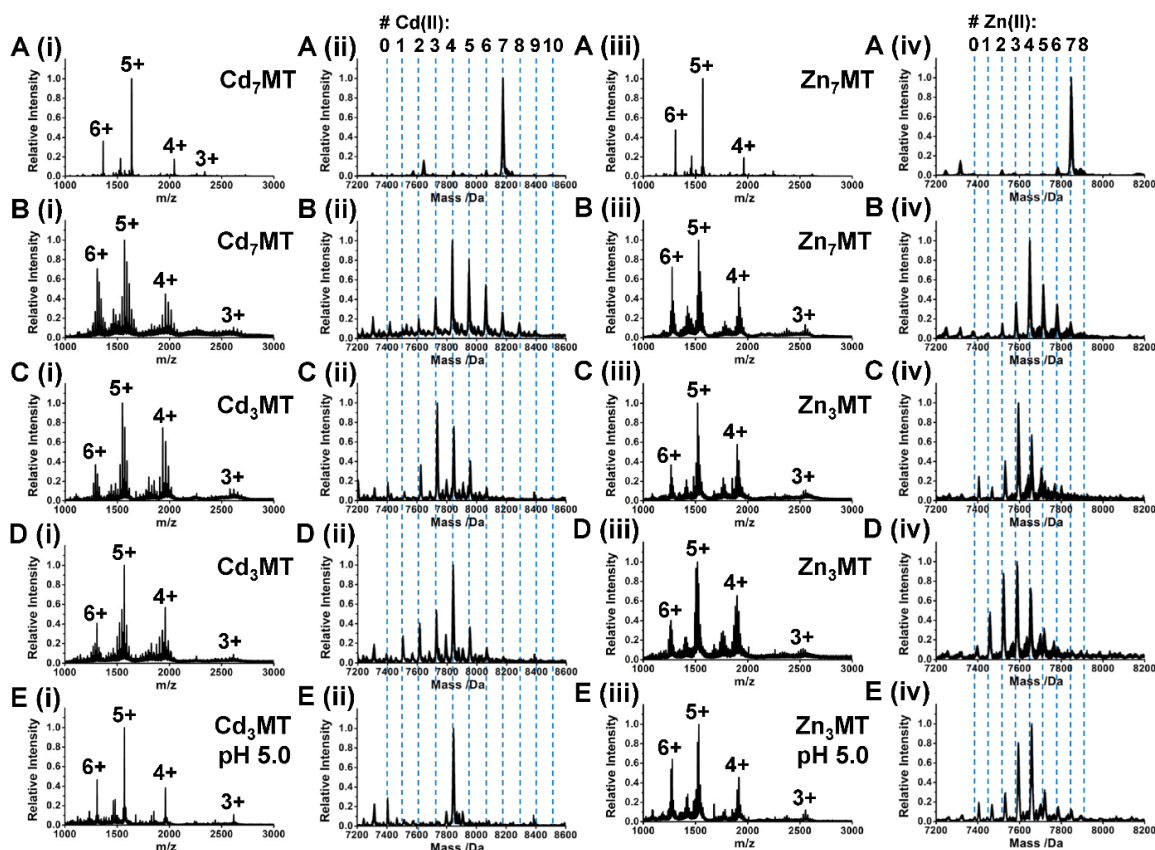


Figure 6-7. Reduced and oxidized MTs monitored using ESI-MS. (i) Charge state and (ii) deconvoluted ESI mass spectra of (A) 25 μ M Cd₇MT at pH 7.4, (B) 25 μ M Cd₇MT after 40 h reaction with 0.125 mM (5 mol. eq. H₂O₂) at pH 7.4, (C) 25 μ M Cd₃MT at pH 7.4, (D) 25 μ M Cd₃MT after 1 h reaction with 0.25 mM (10 mol. eq. H₂O₂) in the presence of 0.5 mM TCEP at pH 7.4, and (E) 25 μ M Cd₃MT at pH 5.0. (iii) Charge state and (iv) deconvoluted ESI mass spectra of (A) 25 μ M Zn₇MT at pH 7.4, (B) 25 μ M Zn₇MT after 40 h reaction with 0.125 mM (5 mol. eq. H₂O₂) at pH 7.4, (C) 25 μ M Zn₃MT at pH 7.4, (D) 25 μ M Zn₃MT after 1 h reaction with 0.25 mM (10 mol. eq. H₂O₂) in the presence of 0.5 mM TCEP at pH 7.4, and (E) 30 μ M Zn₃MT at pH 5.0. Adapted from Korkola and Stillman, 2023 with permission from The American Chemical Society.

results. Although it is often the major species, in reality a range from M_2MT – M_7MT exists. This mixture of species could explain the weakening of the derivative band characteristic of the cluster because only the Cd_4S_{11} and Zn_4S_{11} α -domain structures exhibit the derivative shape CD spectral band.

For Cd_3MT , exposure to H_2O_2 results in some of the $Cd(II)$ shifting to form the Cd_4MT cluster in the α -domain. This is consistent with the ESI mass spectra where the metallation status in the species shift to favour Cd_4MT rather than a non-cooperative species distribution. The shape of the derivative signal in the CD spectrum is weaker than what one would expect for the Cd_4MT cluster. This is possibly due to the presence of lower metallated species as well as disulfide bonds disrupting the structure.

The stoichiometry in the initial Zn_3MT does not change to form a cluster structure upon exposure to H_2O_2 . The CD spectrum resembles the non-specific terminally bound $Zn(II)$ -MT structures rather than the cooperative Zn_4MT structure.

As additional validation, a reaction of 25 μM Cd_7MT with 3.75 mM (150 mol. eq.) H_2O_2 was monitored kinetically throughout the entire reaction by CD spectroscopy (Appendix D, Fig. D-4). At the 3 min time point, the formation of some Cd_8MT as observed in the mass spectral data can be seen as a shift of the maximum from 260 nm (+) to 255 nm (+), as noted previously in the literature.¹⁴⁸ Throughout the reaction, the peak maximum slowly shifts closer towards 260 nm (+) and becomes weaker as the $Cd(II)$ is displaced, resembling Fig. 6-6Aii and Fig. 6-6Cii, until disappearing completely. The CD spectral band never resembles Fig. 6-6Ci, indicating that the Cd_4MT cluster remains present throughout the reaction.

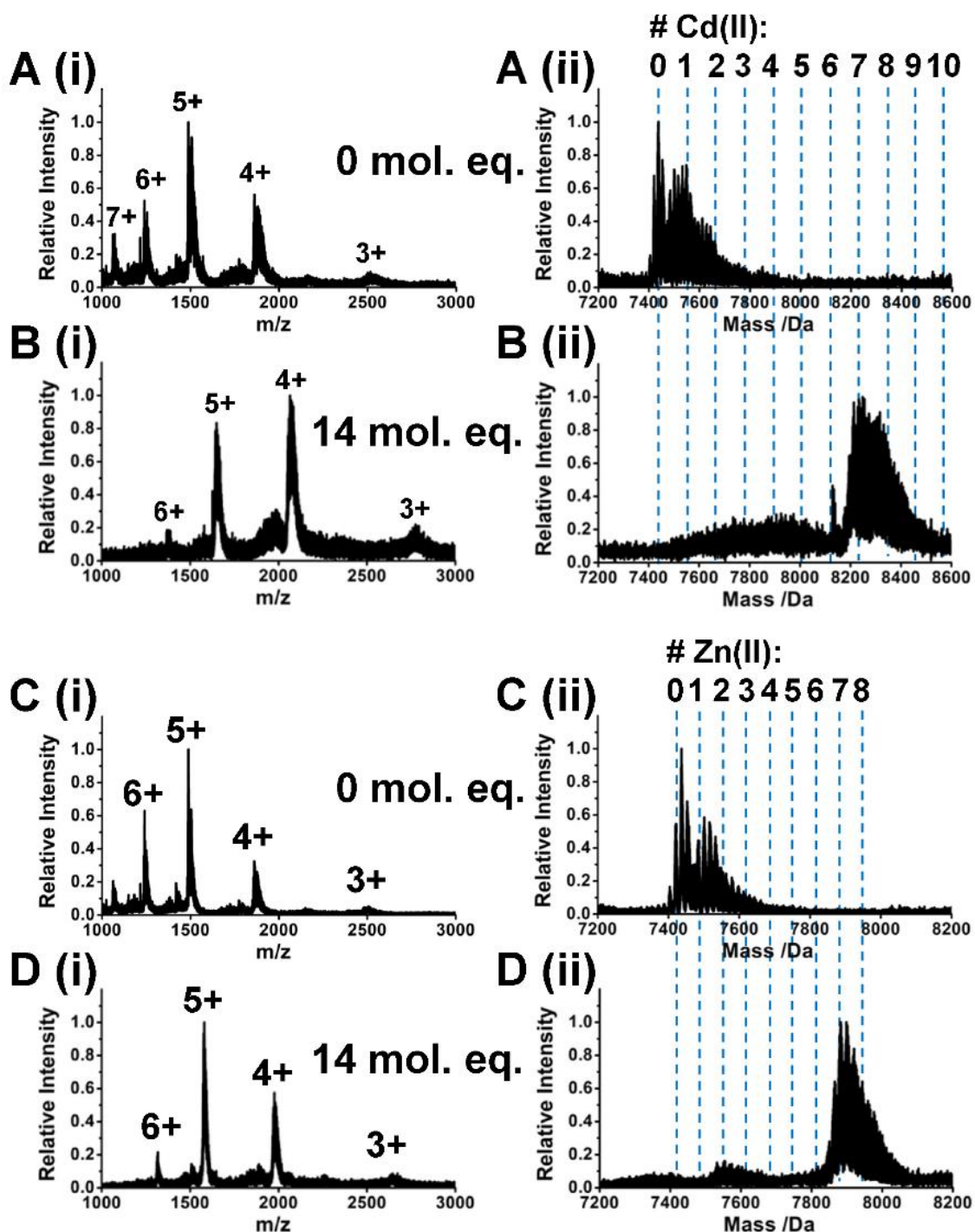
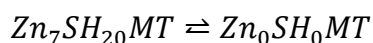


Figure 6-8. Cd(II) and Zn(II) binding to MTs after reversal of oxidation. 90 μ M (A, B) Cd₇MT or (C, D) Zn₇MT reacted with 13.5 mM H₂O₂ (150 mol. eq.) at pH 7.4 for 120 min, then reversed with TCEP. (i) Charge state and (ii) deconvoluted ESI mass spectra show (A, C) before and (B, D) after addition of 14 mol. eq. Cd(OAc)₂ to re-bind the metals. Adapted from Korkola and Stillman, 2023 with permission from The American Chemical Society.

6.3.9 MT regains its metal-binding ability upon reduction of disulfide bonds

Cd₇MT and Zn₇MT that have had all of their cysteines oxidized to disulfide bonds by H₂O₂ regain their ability to bind metals after reduction. Thorough buffer exchange with TCEP-containing ammonium formate results in full reduction of the 20 cysteines for both the Cd₇MT (Fig. 6-8A) and Zn₇MT (Fig. 6-8C) samples that had been demetallated by the addition of H₂O₂. Addition of Cd(II) and Zn(II) re-forms up to Cd₇₋₈MT (Fig. 6-8B) and Zn₇MT (Fig. 6-8D), respectively, showing that the MT can still bind the same number of metals as before. This highlights the reversible property of the oxidation of Zn₇MT suggested previously by Maret¹¹⁶ shown in the following reaction:



Overall, the observed mass differences in the ESI mass spectral data confirm the oxidation of apo-MT and various M₁₋₇MT species via disulfide bond formation. The reversibility of this process shows that the metal-binding function of MT can be regained even after severe oxidative damage. This strongly suggests that MT could function in a redox cycle where it is oxidized and repaired. The fully oxidized γ -domain of the wheat Ec-1 MT has been shown to resist proteolysis, also suggesting that oxidized MT would not be a target for degradation and could still be functional.²²³

6.3.10 The demetallation pathways are dependent on the metal-loading status of the MT

Complicated metallation pathways for the oxidation of various metallated MTs by H₂O₂ are required to fit the kinetic data. These pathways depend on the number of metals bound to MT prior to oxidation. The demetallation of the fully metallated Cd₇MT and Zn₇MT (Fig. 6-9A) begins with a sequential metal release up until M₇MT. Then, M₇MT either releases one metal to form M₆MT, or releases two metals rapidly in succession to produce M₅MT. The latter process is so fast that it is approximated in the fit as a two-metal release. Then, in a similar process, M₆MT will form only M₄MT without any observable release to M₅MT.

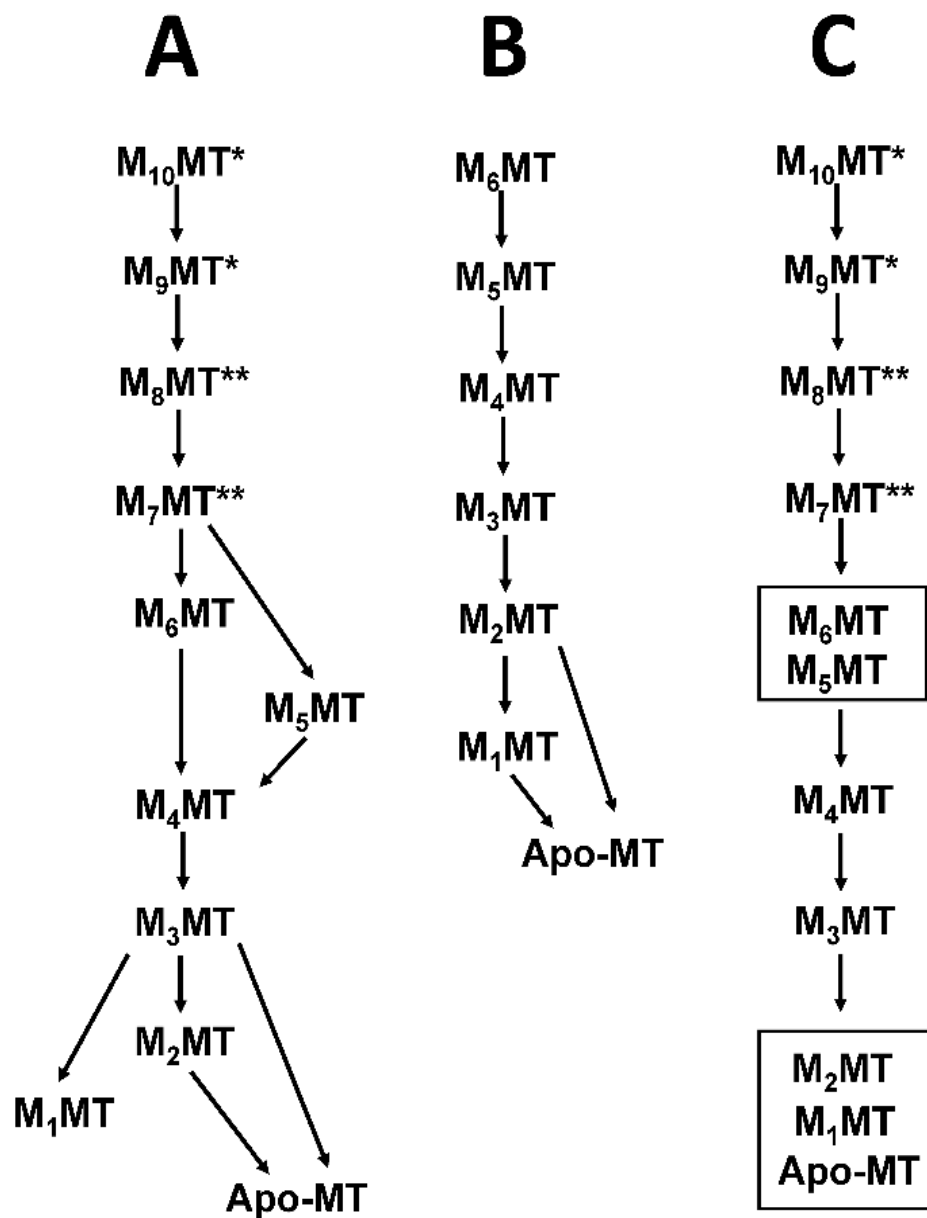


Figure 6-9. Oxidation-induced MT demetallation pathways. The demetallation pathway of (A) Cd_7MT , Zn_7MT , (B) Cd_3MT , and Zn_3MT upon oxidation with 150 mol. eq. H_2O_2 at pH 7.4 determined through the pathway required to fit the kinetic traces from ESI-MS experiments. (C) The demetallation pathway with M_6MT/M_5MT and $M_2MT/M_1MT/apo-MT$ each considered as one species to allow for comparison of the rate constants between the pathways of fully metallated and partially metallated MT. Species labeled with * are only observed with Cd_7MT and species labeled with ** are only observed with Cd_7MT and Zn_7MT . Note that for some steps where a single metal release is too fast to observe, the data were fit to only the following step, resulting in some pathways where multiple metals are released at once. Reproduced from Korkola and Stillman, 2023 with permission from The American Chemical Society.

The M_5MT formed from M_7MT will then form M_4MT directly. M_4MT releases one metal to form M_3MT , which can subsequently lose one, two, or three metals in a concerted process to form M_2MT , M_1MT , or apo-MT. Two metals displaced from M_2MT can also form apo-MT. If M_1MT is formed, it will not release the last metal to form apo-MT. This complexity shows that demetallation of fully metallated MTs do not occur in a simple sequential pathway. The disruption of the network of bridging cysteines in the cluster structures appears to result in multiple metals being simultaneously displaced from that cluster. This is consistent with previous ^{113}Cd NMR spectroscopic data, where the loss of the three β -domain $Cd(II)$ signals occurred simultaneously rather than sequentially.²²⁴In contrast, the metal release pathway for partially metallated MT is less complicated (Fig. 6-9B). The demetallation is sequential until M_2MT , when at that point it can release either to M_1MT or apo-MT. In the partially metallated samples, the two-domain cluster structure has not yet formed and therefore formation of a disulfide bond is less likely to disrupt multiple metals.

As the metal-release pathways between fully metallated and partially metallated MTs are different, a pathway where the complicating species are combined is used to fit the experimental data (Fig. 6-9C). This allows the obtained rate constants to be compared across fully and partially metallated MTs.

6.3.11 Major species from the metal-release are identified from the kinetic traces

The kinetic traces extracted from the mass spectral data from the oxidation of the $90\ \mu M$ Cd_7MT , Zn_7MT , Cd_3MT , and Zn_3MT show the concentration of individual species as a function of time (Fig. 6-10). The traces show the individual species in Fig. 6-10i and the combined species (from the pathway in Fig. 6-9C) in Fig. 6-10ii. The profiles for the metal release of Cd_7MT (Fig. 6-10A) and Zn_7MT (Fig. 6-10B) are very similar. Throughout the reaction, M_4MT forms as a major species, particularly when compared to the less prominent M_3MT peak that follows.

In the reactions of partially metallated samples, Cd_3MT (Fig. 6-10C) and Zn_3MT (Fig. 6-10D), the metals only begin to be displaced after the free cysteines have become oxidized.

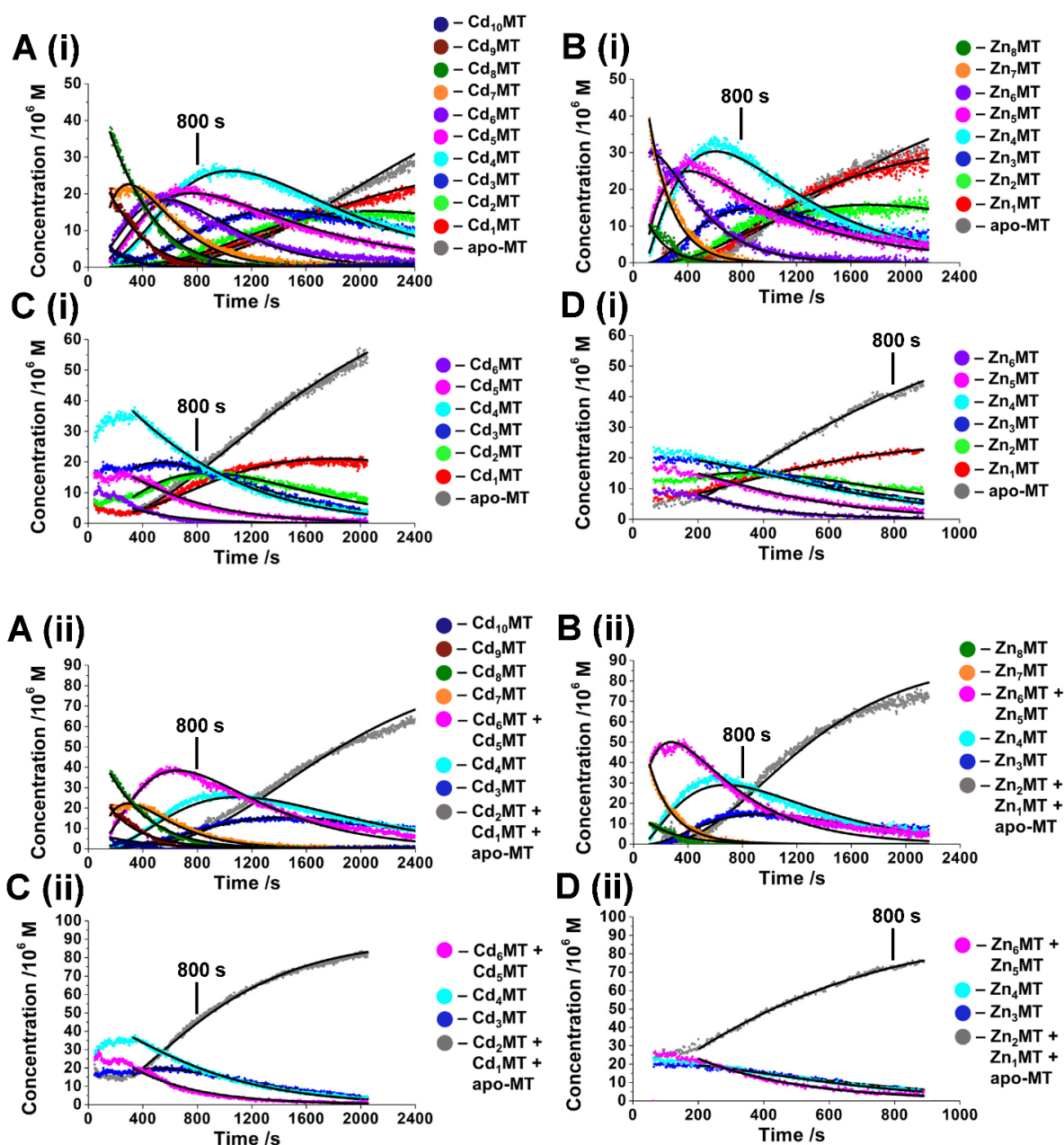


Figure 6-10. Fitted kinetic traces of MT oxidation monitored using ESI-MS. Fitted kinetic traces showing the metal loss over time due to a reaction of (A) $90 \mu\text{M}$ Cd_7MT , (B) $90 \mu\text{M}$ Zn_7MT , (C) $90 \mu\text{M}$ Cd_3MT , or (D) $90 \mu\text{M}$ Zn_3MT with 3 mM H_2O_2 (150 mol. eq.) at pH 7.4 monitored using ESI-MS. A time point at 800 s is indicated to clearly emphasise the timescale of each reaction. (i) The kinetic traces show the concentration of each individual metallated species over time. (ii) The kinetic traces show the concentration of the individual metallated species $M = 10, 9, 8, 7, 4, 3$ over time. The concentrations of $M = 6, 5$ and $M = 2, 1, 0$ have been added together into single traces to simplify the fitting process. Adapted from Korkola and Stillman, 2023 with permission from The American Chemical Society.

It takes about 400 s for Cd₃MT to begin releasing Cd(II), and about 200 s for Zn₃MT to begin releasing Zn(II). During this period, the Cd₄MT peak increases in magnitude. This property is not seen for partially metallated Zn₃MT, where all species remain present in the same ratio (Fig. 6-10D). The overall reactions of Cd₇MT, Zn₇MT, and Cd₃MT with H₂O₂ proceed at a very similar rate, while the Zn₃MT reaction is noticeably faster.

6.3.12 The rate constants quantify the demetallation steps of MT due to oxidation by H₂O₂

The rate constants derived from the fit of the kinetic traces allow for direct comparisons of the release pathways for all the conditions studied. These rate constants are plotted in Fig. 6-11 and listed in Table 6-3. Cd₁₀MT, Cd₉MT, Cd₈MT, and Cd₇MT each release a metal from fully metallated MT with sequentially higher rate constants. Similarly, the release of Zn(II) from Zn₇MT is higher than its release from Zn₈MT. Comparing the different metals, k_{8-7} for Cd(II)-bound MTs is slightly higher, and $k_{7-6/5}$ for Zn(II)-bound MTs is slightly higher.

The rate constant $k_{7-6/5}$ describes the process of releasing either one or two metals to form M₆MT or M₅MT. For both Cd₇MT and Zn₇MT, $k_{7-6/5}$ is the highest rate constant in the entire pathway. It is approximately three times higher than the following rate constant $k_{6-5/4}$, which is the combination of two pathways leading to M₄MT, a major species in the displacement. The equivalent rate constant when starting with partially metallated MTs is of a similar value.

The degradation of M₄MT to M₃MT is only 1.1 times faster than the preceding step for all starting conditions, with the exception of Zn₃MT, as determined by the rate constant k_{4-3} . For Zn₃MT, this value is approximately 1.4 times higher than $k_{6/5-4}$.

The multi-pathway release of M₃MT to a lower metal-loading status is overall kinetically favoured compared to the formation of M₃MT. This holds true for all starting conditions. The rate constant is 1.5 times higher for Cd₇MT and Cd₃MT, 1.8 times higher for Zn₇MT, and 1.3 times higher than for Zn₃MT.

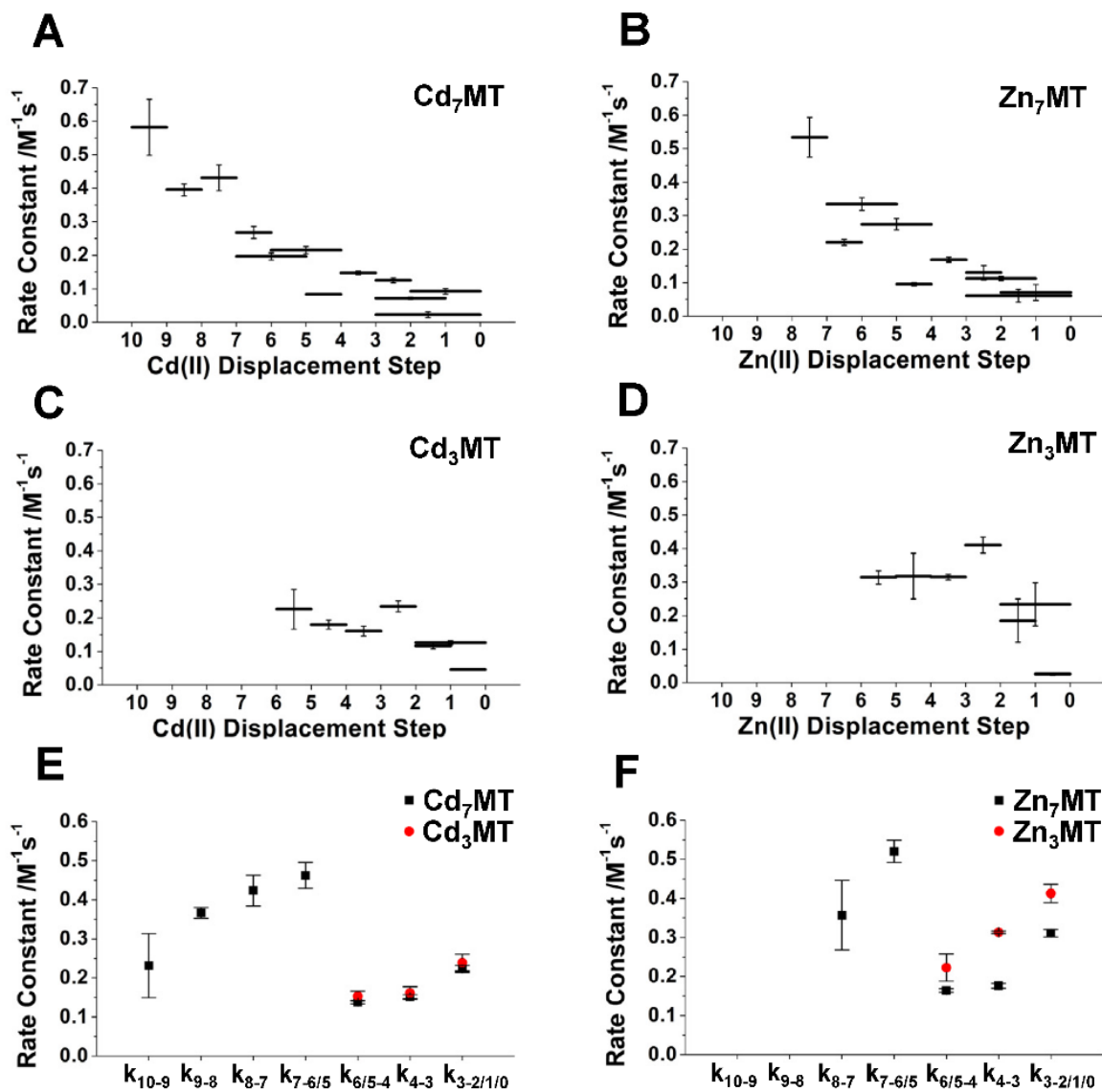


Figure 6-11. Rate constants resulting from MT oxidation-induced metal release. Plots of the rate constants for each demetallated step obtained from the fitted kinetic traces for a reaction of 90 μM (A) Cd_7MT , (B) Zn_7MT , (C) Cd_3MT , or (D) Zn_3MT with 13.5 mM H_2O_2 (150 mol. eq.) at pH 7.4 monitored using ESI-MS. (A–D) The rate constants for each individual metallated species are represented as horizontal lines drawn from the reactant M_nMT species to the product M_nMT species for each step. (E, F) The rate constants resulting from the fit of the kinetic traces where the concentrations of $\text{M} = 6, 5$ and $\text{M} = 2, 1, 0$ had been added together into single traces for a reaction between 90 μM Cd_7MT (black squares) or Cd_3MT (red circles) with 13.5 mM H_2O_2 (150 mol. eq.) and (B) 90 μM Zn_7MT (black squares) or Zn_3MT (red circles) with 13.5 mM H_2O_2 (150 mol. eq.) at pH 7.4 monitored using ESI-MS. Adapted from Korkola and Stillman, 2023 with permission from The American Chemical Society.

Comparing each step beginning from the release from M₇MT, both the partially and fully metallated Zn(II)-bound MTs release their metals faster than both the Cd(II)-bound MTs. Within a single metal identity, partially metallated MTs release their metals faster than fully metallated MTs.

Averaging all the rate constants from k_{7-6/5} to k_{3-2/1/0}, we calculated that Zn₇MT releases metals 1.2 times faster than Cd₇MT. Averaging only the rate constants from k_{6-5/4} to k_{3-2/1/0}

Table 6-3. Rate constants resulting from MT oxidation-induced metal release. The 2nd order rate constants for each fitted metal displacement step in a reaction of 90 μM Cd₇MT, Zn₇MT, Cd₃MT, or Zn₃MT with 3 mM H₂O₂ (150 mol. eq.) at pH 7.4 monitored using ESI-MS. The errors shown are a result of three experiments for each condition. (i) The rate constants (i) for each individual metallated species and (ii) from the fit of the kinetic traces where the concentrations of M = 6, 5 and M = 2, 1, 0 had been added together into single traces. Adapted from Korkola and Stillman, 2023 with permission from The American Chemical Society.

	Cd ₇ MT k (M ⁻¹ s ⁻¹)	Zn ₇ MT k (M ⁻¹ s ⁻¹)	Cd ₃ MT k (M ⁻¹ s ⁻¹)	Zn ₃ MT k (M ⁻¹ s ⁻¹)
(i)				
M ₁₀ + H ₂ O ₂ → M ₉	0.58 ± 0.08	-	-	-
M ₉ + H ₂ O ₂ → M ₈	0.40 ± 0.02	-	-	-
M ₈ + H ₂ O ₂ → M ₇	0.43 ± 0.04	0.53 ± 0.06	-	-
M ₇ + H ₂ O ₂ → M ₆	0.27 ± 0.02	0.220 ± 0.009	-	-
M ₇ + H ₂ O ₂ → M ₅ *	0.20 ± 0.01	0.33 ± 0.02	-	-
M ₆ + H ₂ O ₂ → M ₅	-	-	0.23 ± 0.06	0.31 ± 0.02
M ₆ + H ₂ O ₂ → M ₄ *	0.21 ± 0.01	0.27 ± 0.02	-	-
M ₅ + H ₂ O ₂ → M ₄	0.083 ± 0.002	0.095 ± 0.005	0.18 ± 0.01	0.32 ± 0.07
M ₄ + H ₂ O ₂ → M ₃	0.147 ± 0.006	0.168 ± 0.008	0.16 ± 0.01	0.315 ± 0.008
M ₃ + H ₂ O ₂ → M ₂	0.125 ± 0.007	0.13 ± 0.02	0.23 ± 0.02	0.41 ± 0.02
M ₃ + H ₂ O ₂ → M ₁ *	0.072 ± 0.004	0.113 ± 0.006	-	-
M ₃ + H ₂ O ₂ → M ₀ *	0.023 ± 0.008	0.06 ± 0.02	-	-
M ₂ + H ₂ O ₂ → M ₁	-	-	0.116 ± 0.008	0.18 ± 0.06
M ₂ + H ₂ O ₂ → M ₀ *	0.093 ± 0.008	0.07 ± 0.02	0.126 ± 0.006	0.23 ± 0.06
M ₁ + H ₂ O ₂ → M ₀	-	-	0.045 ± 0.002	0.026 ± 0.003
(ii)				
M ₁₀ + H ₂ O ₂ → M ₉	0.23 ± 0.08	-	-	-
M ₉ + H ₂ O ₂ → M ₈	0.37 ± 0.01	-	-	-
M ₈ + H ₂ O ₂ → M ₇	0.42 ± 0.04	0.36 ± 0.09	-	-
M ₇ + H ₂ O ₂ → M _{6/5}	0.46 ± 0.03	0.52 ± 0.03	-	-
M _{6/5} + H ₂ O ₂ → M ₄	0.138 ± 0.004	0.165 ± 0.005	0.15 ± 0.01	0.22 ± 0.03
M ₄ + H ₂ O ₂ → M ₃	0.151 ± 0.006	0.176 ± 0.006	0.16 ± 0.02	0.313 ± 0.003
M ₃ + H ₂ O ₂ → M _{2/1/0}	0.223 ± 0.009	0.311 ± 0.009	0.24 ± 0.02	0.41 ± 0.02

*Multiple metals are released in this step

to compare to the partially metallated MTs, we find that Cd₃MT releases metals 1.1 times faster than Cd₇MT. Also averaging the rate constants from $k_{6-5/4}$ to $k_{3-2/1/0}$, Zn₃MT releases metals 1.5 times faster than Zn₇MT and 1.7 times faster than Cd₃MT.

The pattern of rate constants for Cd₃MT is remarkably similar to that of Cd₇MT (Fig. 6-11A, C, E). However, the pattern differs slightly for Zn₃MT, with k_{4-3} noticeably higher than its Zn₇MT counterpart compared to the other rate constants (Fig. 6-11B, D, F).

6.3.13 The rate of demetallation of individual metals depends on the metal-thiolate cluster structures

The multiple bridging cysteines present in the two-domain cluster structure of Cd₇MT and Zn₇MT likely complicates the metal-release pathways. Oxidation of a bridging cysteine may destabilize two metals, resulting in both of their release in rapid succession. Oxidation of a terminal cysteine will only affect the single metal to which it binds. The fact that multiple different pathways such as M₇MT forming either M₆MT or M₄MT can occur suggests that the metals do not release in a specific order. On the other hand, partially metallated MTs have not yet formed the intricate thiolate network of the two-domain cluster structure. In this case, formation one disulfide bridge is less likely to disrupt multiple metals at once.

Cd₁₀MT, Cd₉MT, and Zn₈MT only form in significant quantities once MT has been exposed to H₂O₂. As each of these extra metals are displaced the rate constants become sequentially higher, possibly due to the extent of the oxidative damage. Likewise, the release of Zn(II) from Zn₈MT is unusually slower than for the release of Cd(II) from Cd₈MT likely because Zn₈MT represents the first species in the pathway. Cd₈MT has an average of one more oxidized cysteine residue than Zn₈MT which may make it more readily release a metal.

For fully metallated MTs, the rate constant $k_{7-6/5}$ represents the first metals released from the 2-domain M₇MT structure. If the metal release follows the M₇MT to M₆MT to M₄MT pathway, k_{6-4} has a comparable value to k_{7-6} and k_{7-5} for both Cd₇MT and Zn₇MT. The high rate constants show that the first two to three metals in the 2-domain structure are easily released due to oxidation compared to the remaining four to five.

The formation of M₄MT appears relatively slow despite its prominence in the spectra. However, this can be explained by the two pathways feeding into it. The M₆MT to M₄MT pathway is comparable in rate with previous steps, while the M₅MT to M₄MT pathway is quite slow. This suggests that the stable M₄MT structure has formed with one extra metal which is now resistant to displacement in a similar way to how M₁MT remains resistant to displacement even after all 20 cysteine residues have become oxidized.

Two pathways lead to the formation of M₄MT but only one pathway exists that leads to a single metal displacement from M₄MT to M₃MT. The rate constant k_{4-3} is low compared with the preceding steps apart from k_{5-4} , which implies that M₄MT is a particularly stable structure. Additionally, the higher value of $k_{3-2/1/0}$ supports this statement as M₃MT being unstable after the collapse of the M₄MT structure.

The kinetic data support the hypothesis that the Cd(II) in partially metallated Cd₃MT is shifting to form a protective cluster in the α domain. The rate constants for Cd₃MT displacement are only 1.1 times higher than those for Cd₇MT suggesting the Cd(II)-thiolate structures are the same between both conditions. Conversely, Zn₃MT does not shift to form a protective Zn₄MT cluster upon exposure to H₂O₂, as suggested by the higher k_{4-3} rate constant. The CD spectra did not show the presence of the Zn₄MT cluster structure.

6.3.14 Density function theory calculations suggest different reactivity of terminally bound and bridging cysteines

Molecular models of a [Cd₃(CH₃S)₉]³⁻ (Fig. 6-12Ai), [Zn₃(CH₃S)₉]³⁻ (Fig. 6-12Aii), and CH₃SH (Fig.6-12Aiii) were assembled as simple models of the β -domain cluster in fully metallated Cd₇MT and Zn₇MT and as a single Cys side chain. The six terminal and three bridging cysteines are labeled in the cluster structures. Electron density surfaces of selected molecular orbitals (MOs) generated from the [Cd₃(CH₃S)₉]³⁻, [Zn₃(CH₃S)₉]³⁻, and CH₃SH models were calculated. The highest occupied molecular orbital (HOMO) is shown in Fig. 6-12Bi for [Cd₃(CH₃S)₉]³⁻, Fig. 6-12Bii for [Zn₃(CH₃S)₉]³⁻, and Fig. 6-12Biii for CH₃SH. Fig. 6-12Ci depicts orbital 125 for [Cd₃(CH₃S)₉]³⁻ and Fig. 6-12Cii depicts orbital 126 for [Zn₃(CH₃S)₉]³⁻. The arrows indicate the non-bonding orbitals of sulfurs with high electron density. The energies for the calculated orbitals are shown in Fig. 6-12D.

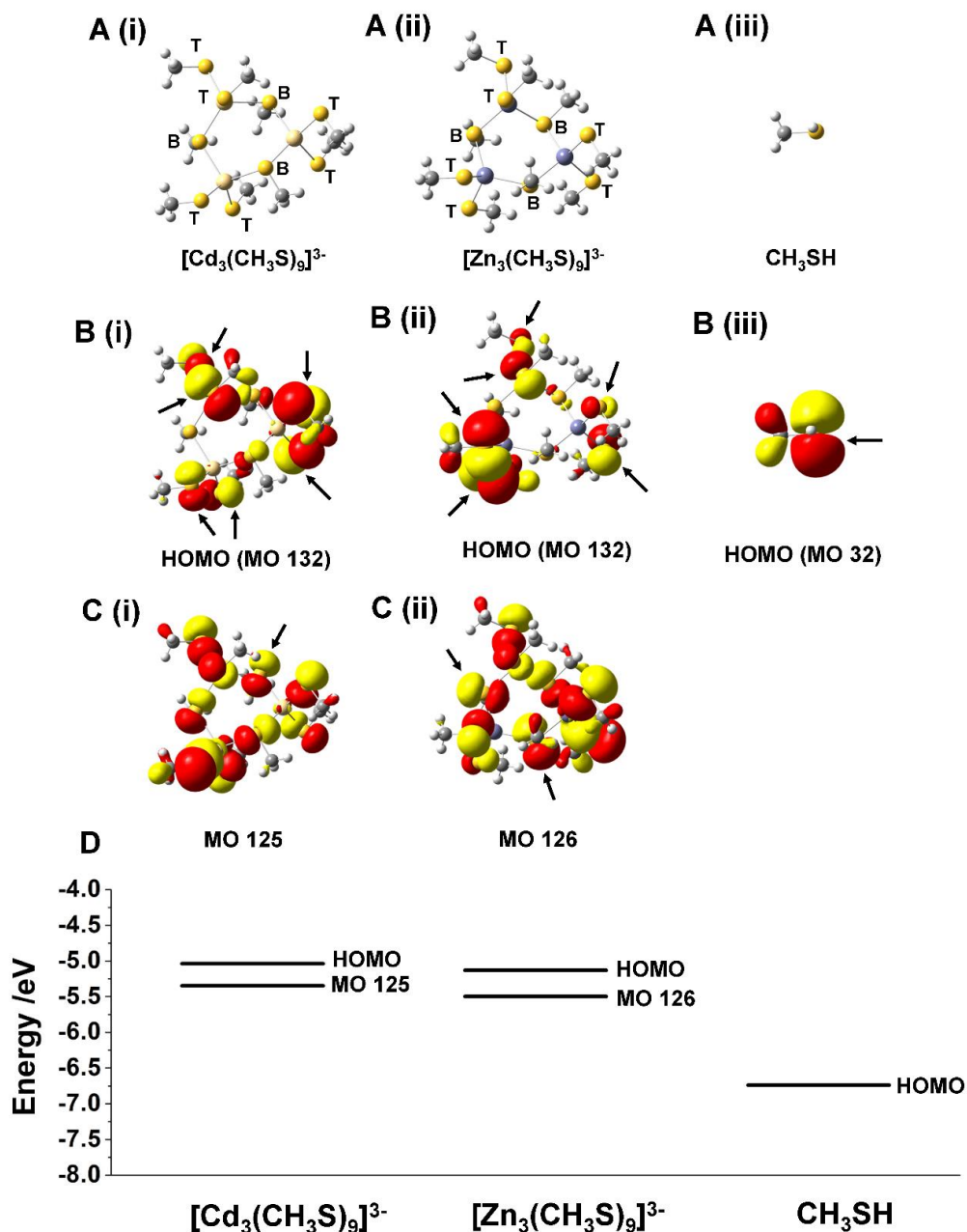


Figure 6-12. Molecular models and electron density surfaces of CH_3SH structures. (A) Optimized molecular models of (i) $[\text{Cd}_3(\text{CH}_3\text{S})_9]^{3-}$, (ii) $[\text{Zn}_3(\text{CH}_3\text{S})_9]^{3-}$, and (iii) CH_3SH . The terminally bound and bridging sulfurs are labeled with “T” and “B”, respectively. (B) Electron density surfaces of the highest occupied molecular orbitals (HOMO) for (i) $[\text{Cd}_3(\text{CH}_3\text{S})_9]^{3-}$, (ii) $[\text{Zn}_3(\text{CH}_3\text{S})_9]^{3-}$, and (iii) CH_3SH . (C) Electron density surfaces of (i) molecular orbital 125 for $[\text{Cd}_3(\text{CH}_3\text{S})_9]^{3-}$ and (ii) molecular orbital 126 for $[\text{Zn}_3(\text{CH}_3\text{S})_9]^{3-}$. The energies of the orbitals are shown in D and are (Bi) -5.04 eV, (Bii) -5.35 eV, (Biii) -6.74 eV, (Ci) -5.13 eV, and (Cii) -5.50 eV. The arrows indicate areas of high electron density on the non-bonding orbitals of the terminal and bridging sulfurs. Adapted from Korkola and Stillman, 2023 with permission from The American Chemical Society.

From the electron density surfaces, it can be seen that within the HOMOs for both structures, more electron density is present in the non-bonding pairs of the terminally bound cysteines. Conversely, only at lower energy levels do we begin to see electron density in the non-bonding pairs of the bridging cysteines.

As part of the mechanism of cysteine oxidation by H_2O_2 , the sulfur of a cysteine residue will perform a nucleophilic attack on the oxygen of H_2O_2 . Therefore, the fact that there is more electron density in the HOMO on the terminally bound sulfurs suggests that the terminally bound sulfur are more reactive towards oxidation. This is consistent with previous computational studies showing that the transition state of the reaction of H_2O_2 with a terminally bound sulfur was lower than that of the bridging sulfur, suggesting higher reactivity.²²⁶ More electron density is present on the CH_3SH sulfur HOMO compared to the metallated structures, which is in line with the free cysteines of apo-MT being more reactive towards oxidation than metallated MTs.

6.3.15 Metal displacement from MT depends on the extent of cluster formation

Particularly recently, the discussion of MT's role in Zn(II) distribution has been expanded to include the existence of more complicated $\text{M}_{0-7}(\text{SH})_{0-20}\text{MT}$ species. This mixture is dynamic and depends on both metal availability and redox state of the cell and has been illustrated in a cycle.¹¹⁰

Our data clearly show the effect of MT oxidation by H_2O_2 is dependent on the various possible metallated structures. The metal displacement speciation and kinetics from the two-domain Cd_7MT and Zn_7MT structures are remarkably similar. CD spectroscopy confirms the presence of the Cd_4S_{11} and Zn_4S_{11} cluster structures after partial oxidation, showing that the three metals in the β -domain are more labile than the four metals in the α -domain. This suggests that fully metallated MTs *in vivo* would release these metals from the β -domain more readily and only release from the α -domain under more extreme oxidizing conditions.

While the fully metallated Cd_7MT and Zn_7MT species undergo demetallation due to oxidation in a similar manner, the same cannot be said for partially metallated Cd_3MT and

Zn₃MT. Upon exposure to H₂O₂, much of the distributed Cd(II) will coalesce into a Cd₄MT species with a similar CD signal to that of the Cd₄S₁₁ structure. This species is stable and will undergo demetallation at a similar rate and with a similar profile of rate constants as the four Cd(II) from the α -domain of Cd₇MT. The distribution of Zn(II) in Zn₃MT does not shift to favour any particular species after exposure to H₂O₂. Also, the rate constant for the release of Zn₄MT to Zn₃MT is fast, suggesting Zn₄MT in this case is not a particularly stable structure.

Recent reports have shown that despite the two-domain Cd₇MT being used successfully as a model for Zn₇MT, the partially metallated structures are different. Cd₄MT at physiological pH binds primarily in the α -domain, while Zn₄MT appears to occupy both the β -domain and the α -domain.¹⁷⁶ Therefore, it is not surprising that the reactivity towards ROS is different between partially metallated Cd(II)-bound and Zn(II)-bound MTs.

6.4 Conclusions

MT's possible role in the protection against oxidative stress has been studied since the 1980s. Since then, numerous studies have linked the oxidation of MT with disulfide formation and subsequent metal release along with the suggestion that MT's function of Zn(II) homeostasis is linked to the redox environment. The majority of the techniques employed in the past have been limited to measuring averages of species in solutions. Thus, information about intermediate M_x(SH)_yMT species has been limited. As well, only recently has the relevance of partially metallated structures *in vivo* been acknowledged. No studies on the effect of oxidation on these forms of MT have been previously conducted.

The results in this Chapter combine data from UV-visible absorption spectroscopy, ESI-MS, CD spectroscopy, and DFT calculations to identify the intermediate species formed upon oxidation of Cd₇MT, Zn₇MT, Cd₃MT, and Zn₃MT with H₂O₂ and report on the impact of metal-loading status on oxidation.

The ESI-MS technique allows for the visualization of the complex M_x(SH)_yMT species formed as metals are displaced due to disulfide bond formation. The metallated structures

within MTs are resilient, only requiring an average of 2 reduced cysteines remaining per bound metal to maintain metallation.

Analysis of the species distributions in the ESI mass spectra, the resulting kinetic traces and rate constants, and the CD spectra show that the two-domain cluster structure plays an important role in the pathway of metal release and that the metals in the β -domain are more labile than those in the α -domain. Within each domain, the metals do not release in a defined, sequential order. Additionally, the release from the β -domain is less cooperative than for that of the α -domain, suggesting that the network of bridging cysteines is more critical for the structural integrity of the α -domain.

In partially metallated MTs, the distribution of Cd(II) bound will shift to favour the formation of the Cd₄MT cluster species in the α -domain upon exposure to H₂O₂. This differs from partially metallated Zn(II)-bound MTs, where the Zn(II) remains distributed in a non-cooperative manner after exposure to H₂O₂. These structures mean that partially metallated Zn(II)-bound MTs will release metals due to oxidation much faster than other MTs that bind metals in cluster structures.

Overall, these data show how the presence of metals not only provides great resilience against oxidation of MT, but that the structure of the metal-thiolate clusters provides an important role in this protection. Additionally, the metal-loading status plays a role in the consequences of oxidation on metal release. Cd(II) tends to stay in a cluster and resists oxidation, while Zn(II) is more easily displaced. This has implications for biological function, as released Zn(II) will induce more MT production, while toxic Cd(II) will stay sequestered.

Chapter 7

7 Conclusions

7.1 The Bias in Metallothionein Research: Challenges of Studying Intrinsically Disordered Proteins

The protein structural information obtained through X-ray crystallography in the mid-20th century, beginning with John Kendrew solving the structure of myoglobin, was groundbreaking.³⁷⁴ However, these results created a bias towards the idea that all proteins required a well-defined structure to function, as these were the only types of proteins which could be characterized with the technique.³⁷⁵ Within the past few decades, this dogma has been challenged as many proteins were discovered that lacked a well-ordered structure under native conditions and were difficult to characterize using traditional methods.²¹

This bias also persisted for the early research into metallothioneins (MTs), which were discovered in the same year as the first protein crystal structure was solved.⁶³ As X-ray crystallography and NMR spectroscopy were only possible for well-defined fully metallated structures, initially only the two-domain M₇MT structure was characterized.¹⁴³⁻¹⁴⁹ Spectroscopic techniques, that identified the presence of metal thiolate bonds, were also common.¹⁴⁰

A description of mammalian MTs is nearly always found in the introductions of publications, such as in these cited reviews spanning the past few decades showing that even today, the two-domain structure is highlighted as a key feature.^{110, 339, 341, 376-378}

Although the detailed knowledge of the Zn₇MT and Cd₇MT structure is valuable, it does not tell the complete story. Once the existence of metal-unsaturated MTs *in vivo* were confirmed, interest grew around understanding these states.¹⁵³⁻¹⁵⁵ With its first use for MTs in the 1990s,³⁷⁹ ESI-MS proved an important technique in the visualization of this small, dynamic protein due to its ability to resolve individual species.^{165-168, 171} In more recent years, tandem MS and ion mobility MS have also been used successfully to study metal-unsaturated MTs.^{162-163, 170, 176, 272, 307-308}

The research described in this thesis primarily utilized ESI-MS as a method to study different fluxional forms of MT. Multiple strategies were used to gain the desired structural information. In Chapter 3, the change in cysteine modification profiles in apo-MT under a range of denaturing conditions was monitored using ESI-MS as a measure of cysteine exposure. In Chapter 4, partial metallation with Zn(II) or Cd(II) in combination with cysteine modification was used to probe the exact M_xS_y stoichiometries formed under different conditions. In Chapter 5, the stepwise binding of Bi(III) to MT was investigated using the EDTA ligand as a competitor to determine relative binding constants from the speciation curves. In Chapter 6, the coupled cysteine oxidation and metal displacement reactions were monitored, and the individual rate constants were determined using ESI-MS. The ability to resolve individual species allowed for comparisons between the fully metallated and metal unsaturated MTs response to oxidation in terms of the structures formed. MD simulations, stopped-flow, CD spectroscopy, and absorption spectroscopy complemented the ESI-MS results. In the following sections, the findings based on each chapter are discussed as a whole.

7.1.1 Characterization of the apo-MT structure

Initially, the apo-MT was only acknowledged as a “random coil” based on spectroscopic signals,¹⁵⁶⁻¹⁵⁷ with the assumption that *de novo* synthesized MT cooperatively formed Zn_7MT *in vivo* to avoid degradation.^{144, 150-152}

A functional role for apo-MT began to be considered once apo-MTs and partially metallated MTs were isolated from *in vivo* conditions.¹⁵³⁻¹⁵⁵ Rigby and Stillman were among the first to investigate a possible structure-function relationship specifically for apo-MTs. They proposed that the structure of apo-MT was optimized for metal binding.¹⁶⁴

The first goal in this thesis was to characterize the structure of apo-MT. The results were presented in Chapter 3. Apo-MT indeed possesses many structural features expected of an intrinsically disordered protein such as fluxionality, lack of traditional secondary structural elements, resistance to extreme pH and temperature conditions, and a low stability towards chemical denaturation. However, apo-MT exhibits different structures under native and denaturing conditions with a cooperative transition between the states. Apo-MT's

calculated dimensions based on MD simulations are smaller than expected for a random coil.²⁶³ Also, it has a lower net charge and hydrophobicity than expected for an IDP.²⁵³ These findings led to the conclusion that apo-MT should be considered a molten globule IDP rather than a random coil.

The GdmCl-induced unfolding transition for apo-MT was monitored using ESI-MS and CD spectroscopy. In the ESI-MS experiments, the cysteine exposure as a function of GdmCl concentration was measured and in the CD spectroscopy experiments, the protein conformation as a function of GdmCl concentration was measured. Fig. 7-1 shows the resulting unfolding curves from both techniques. The concentrations of GdmCl required to induce complete cysteine exposure in the individual β -domain and α -domain fragments of apo-MT1a as determined by Irvine et al. using ESI-MS are also visualized in Fig. 7-1.²⁷³ The different GdmCl concentrations required to unfold the apo-MT reported by the two

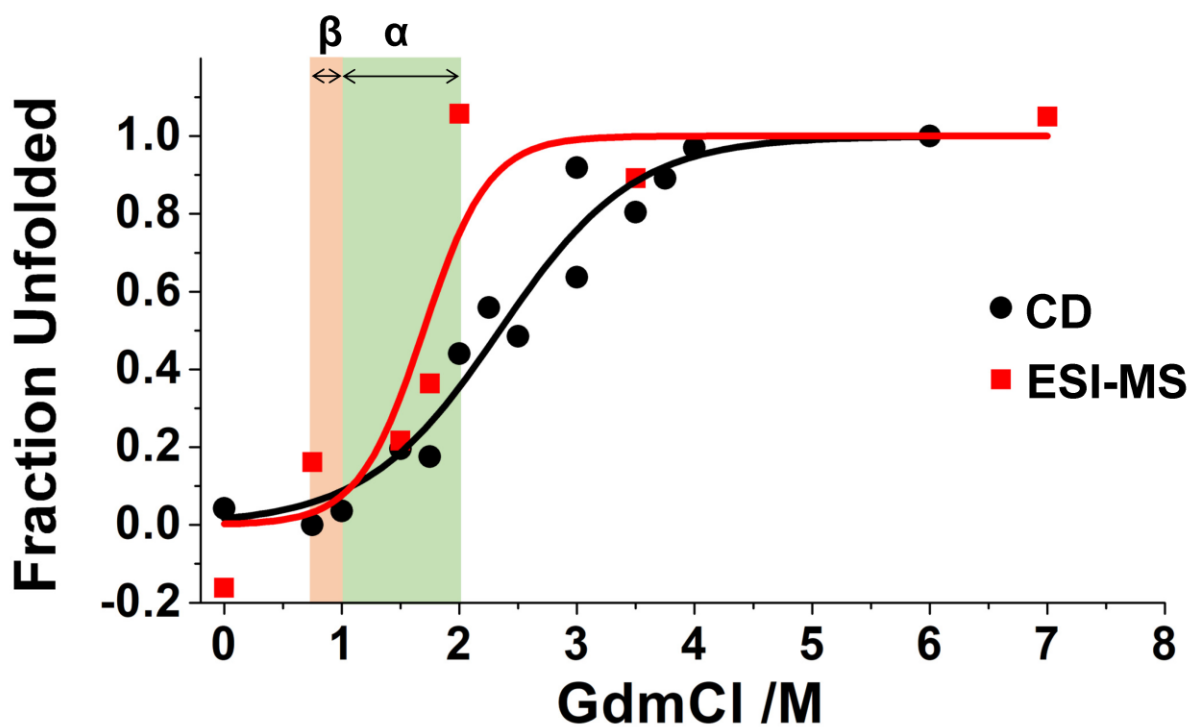


Figure 7-1. Comparison between the GdmCl-dependent unfolding curves monitored using CD spectroscopy and ESI-MS. The fraction of unfolded apo-MT1a as a function of GdmCl concentration monitored using CD spectroscopy (black circles) and ESI-MS (red squares). The ranges of unfolding monitored using ESI-MS for the individual β -domain and α -domain fragments determined by Irvine et al. 2018 are indicated with the shaded peach (β -domain) and green (α -domain) areas.

methods potentially indicate that the folding of apo-MT involves multiple steps with the partially buried arrangement of the cysteine residues forming as one of the final steps.

The cysteines become equally exposed in the $\beta\alpha$ MT during a similar range compared with the isolated α -domain (1-2 M GdmCl). Although the β -domain unfolds between 0.75 and 1 M GdmCl, there does not appear to be a significant structural change in the $\beta\alpha$ MT in this range. This is evidence that the domains formed with metals are not significant structural features in the apo- $\beta\alpha$ MT.

7.2 Metallothionein as a Zn(II)-Binding Intrinsically Disordered Protein

In a review discussing the evolution of MTs, Capdevila and Atrian state that the metallated MT structures themselves do not dictate function, but rather the function of metal binding dictates the structures that MTs adopt.³¹³ In other words, apo-MTs are not inactive. MTs are dynamic proteins, with the capability to bind or release metals based on environmental conditions, with all of these states being the “active” form. This contrasts a traditionally ordered metalloprotein such as a zinc finger, where the role of the zinc is to stabilize the native structure which is in turn essential for its function.^{18, 380} Without the zinc, there is no activity.

However, MTs do not necessarily defy the traditional structure-function paradigm. Some IDPs in the absence of binding partners, such as the nuclear coactivator binding domain (NCB) of CREB binding protein, adopt a compact molten globule structure which resembles a precursor to the final complex with one of its partners.^{29, 299} The flexibility of IDPs often allows for coupled binding and folding to many partners, resulting in many different final conformations.²⁹⁹ The intrinsically disordered apo-MT also adopts a structure that can be described as a molten globule and the metals could be considered analogous to IDP binding partners. As first proposed by Rigby and Stillman,^{160, 164} the apo-MT structure appears to be tuned for metal binding, particularly Zn(II) binding, as investigated in Chapter 4.

In Figure 7-2, the structural dependence of apo-MT on GdmCl monitored using CD spectroscopy (Chapter 3) is compared to that monitored through the reduction in rate constants measured using stopped flow (Chapter 4). The reduction in metallation rate only occurs after complete unfolding of the protein (over concentrations of 4 M GdmCl). This shows the resilience of MT being able to bind metals under a variety of conditions, but also a structural dependence on metallation. This further emphasizes the importance of apo-MT structure on function.

7.3 Partially Metallated Structures Formed in the Native Apo-MT and Their Impact on Oxidation

As discussed in Chapter 4, specific bridging metal-thiolate structures are involved in Zn(II) and Cd(II) binding at physiological pH. Considering the most abundantly formed species at each step identified in the mass spectra, Zn(II) preferentially forms Zn_2S_8 , Zn_3S_{10} , and Zn_4S_{13} , while Cd(II) preferentially forms Cd_2S_6 , Cd_3S_9 , and Cd_4S_{13} . The Cd(II) structures

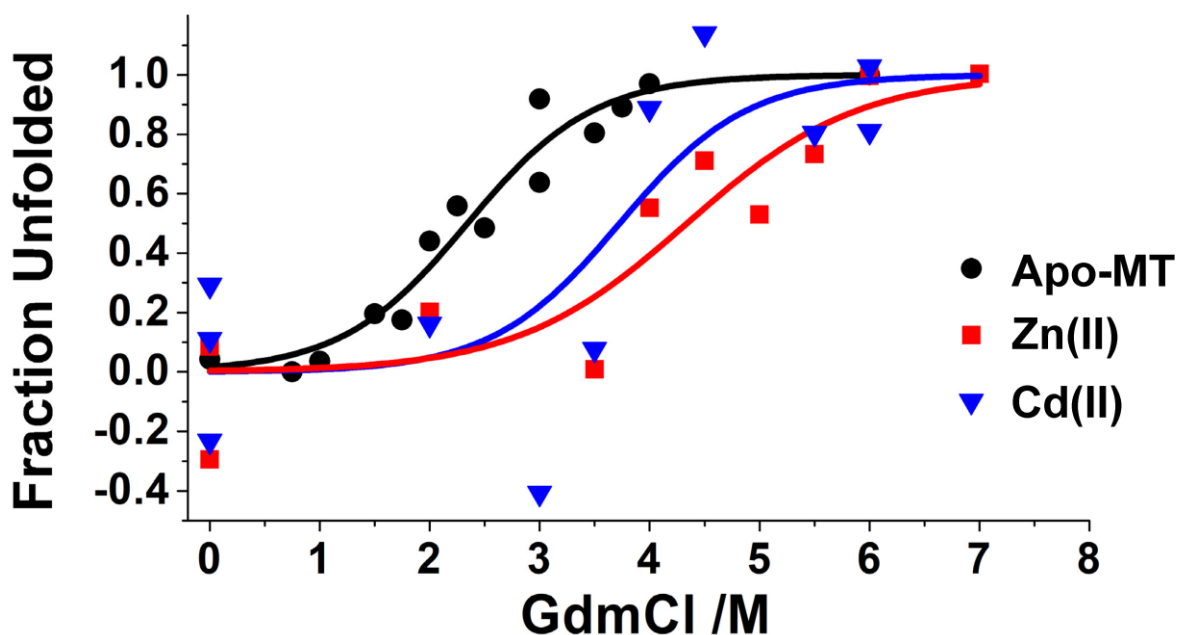


Figure 7-2. Comparison between the GdmCl-dependent unfolding curves monitored using CD spectroscopy, the Zn(II) metallation rate, and the Cd(II) metallation rate. The fraction of unfolded apo-MT1a as a function of GdmCl concentration monitored using CD spectroscopy (black circles), Zn(II) metallation rate (red squares), and Cd(II) metallation rate (blue triangles). The fraction unfolded values for each data set were obtained by Normalizing the data points between 0 and 1.

contain more bridging thiolates compared to those formed from Zn(II) binding. In addition to a metal binding function, MTs are also likely involved in redox process in the cell. The reactivity of these partially metallated MT structures, as well as fully metallated Zn₇MT and Cd₇MT, towards H₂O₂ was studied in Chapter 6.

Maret and Vallee initially put forth the idea that the function of MT is related to Zn(II) mobility as a function of the redox state of the cell, with acknowledgment to the metal-thiolate structures involved.¹¹⁶ They suggested that both the 3D arrangement of the cysteine residues in the clusters and the CC and CXXC motifs present in the mammalian MTs' primary structure allow for favourable disulfide formation.¹¹⁶ Additionally, research from the Freisinger group on the Zn₂γ domain of wheat MT Ec-1 has shown through mass spectrometry that specific disulfide bonds are formed upon oxidation with H₂O₂. The location of these disulfide bonds are consistent regardless of whether the starting MT was in the apo form or fully metallated with Zn(II).²²³ Other studies identified that the β-domain and α-domain clusters displayed a differential reactivity towards oxidizing agents, with the three metals in the β-domain being more reactive than the four metals in the α-domain.^{175,}

209-210, 224, 368-369

The findings in Chapter 6 agree with the model of a largely domain-specific metal release from both Cd₇MT and Zn₇MT following oxidation with H₂O₂. Zn₇MT and Cd₇MT also displayed very similar release pathways and rate constants to each other. This suggests that the structure of the metal-thiolate clusters has a greater influence on the release pathway than the metal identity.

This was the first time that the concurrent metal release and disulfide bond formation has been reported for mammalian MTs with ESI-MS providing a unique level of detail. Use of this method in combination with CD spectroscopy provided more details about the less well-studied partially metallated states. A much larger difference in the behavior between partially metallated Zn(II) and Cd(II) bound MTs was observed compared to the fully metallated MTs, with the Zn(II) MTs being much more susceptible to oxidation. Combining ESI-MS methods with CD spectroscopy revealed that the Cd(II) in partially

metallated MTs rearranges to form a structure resembling a Cd_4S_{11} cluster upon exposure to H_2O_2 , while Zn(II) does not rearrange in this manner.

Putting these results in context with those obtained in Chapter 4 suggests that the differential reactivity of the partially metallated Cd(II) and Zn(II) -bound MTs is due to the presence of more complex bridging thiolate structures in the Cd(II) -thiolate structures compared to the Zn(II) -thiolate structures. The bridging structures likely provide more protection towards the cysteines. *In vivo*, this mechanism could protect a cell experiencing both oxidative stress and heavy metal toxicity, where the Zn(II) would be released, while the toxic Cd(II) would remain sequestered.

Figure 7-3 summarizes potential major pathways of metallation and oxidation, combining the findings from Chapter 4 and Chapter 6. The partially metallated steps that display the most significant difference between Zn(II) and Cd(II) species under native conditions are shown. It is important to note that the partially metallated thiolate clusters shown are only examples of many possible structures based on the M_xS_y stoichiometry observed using ESI-MS.

Interestingly, formation of these specific bridging thiolate structures is disrupted if the apo-MT is denatured using GdmCl prior to metallation, as shown in Chapter 4. The result is the formation of more terminally bound structures that theoretically would be more susceptible to oxidation. This suggests that it is the apo-MT structure that has a direct impact on the metal-thiolate structures formed, which in turn confer protective effects on the MT. Disruption of the apo-MT structure may impact MTs functions at all levels.

7.4 pH-Dependence of Metallation

The results presented in this thesis also give insight into the highly pH-dependent MT metallation pathways. It was determined previously using a combination of ESI-MS and CD spectroscopy that metallation of apo-MT using Cd(II) and Zn(II) followed either a non-cooperative pathway nearer neutral pH, or a cooperative pathway at lower pHs with M_4S_{11} forming with no intermediate species.^{166-168, 171} It was hypothesized that this pH-dependent cluster formation was due to increased proton competition for the thiols only allowing for

the more stable cluster to form.^{161, 171} Preliminary stopped-flow studies of the Cd(II) metallation at varying pHs found that the cooperative pathway at lower pH levels was slower than the non-cooperative pathway at higher pH levels.¹⁶¹

Two conclusions came out of those studies that the research in this thesis has further addressed. First, it was hypothesized that the non-cooperative pathway proceeded via formation of multiple M_1S_4 structures using only terminally bound thiolates up to M_5S_{20} ,

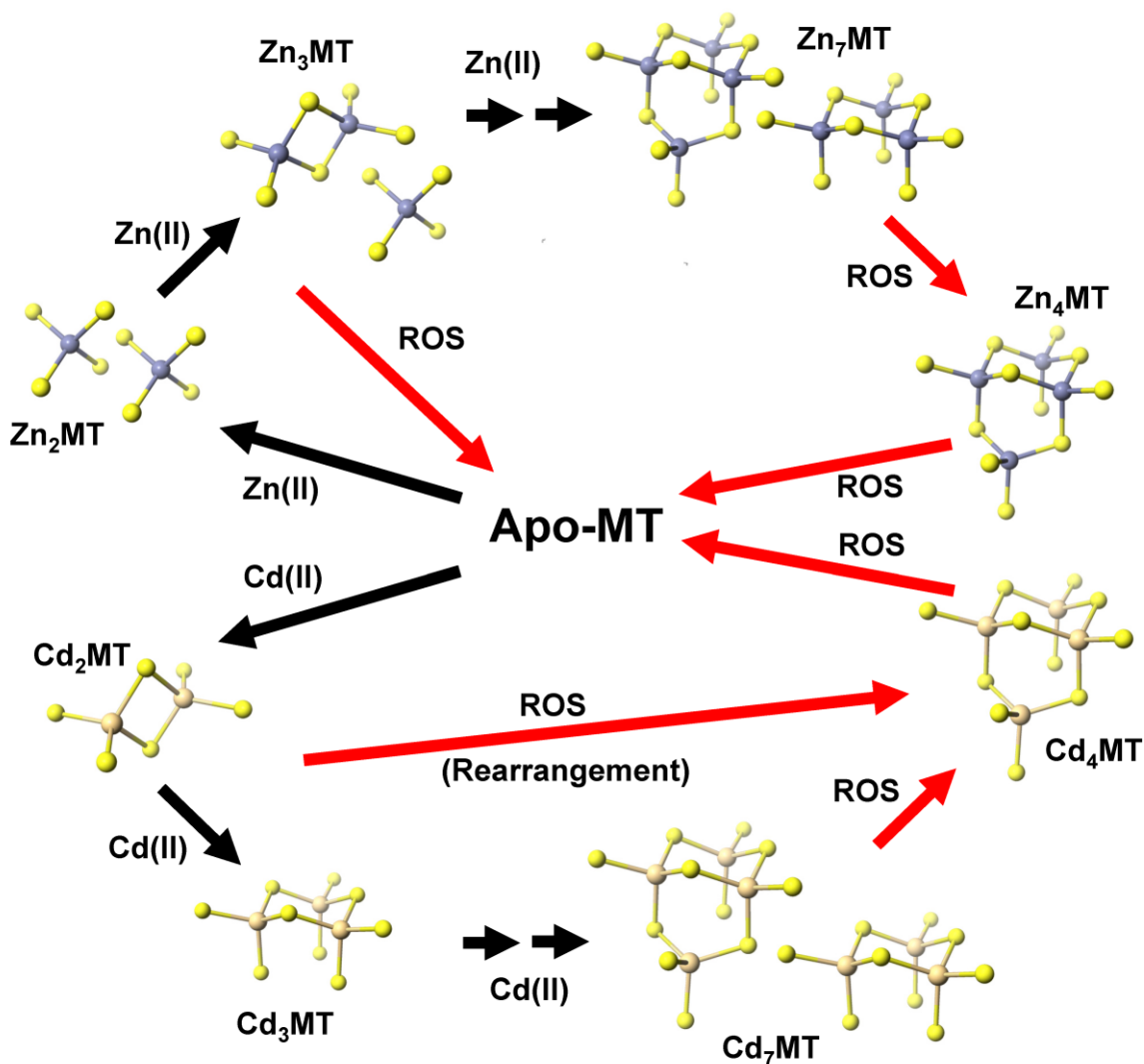


Figure 7-3. Major Zn(II) and Cd(II) structures formed during metallation and oxidation. A cycle showing possible structures that form upon Zn(II) or Cd(II) metallation of apo-MT and their response to oxidation. The M_2MT and M_3MT metallation intermediates are shown because they appear to display the greatest difference between Zn(II) and Cd(II). The structures are possibilities based on the M_xS_y stoichiometry observed using ESI-MS.

at which point no free thiolates would remain and clusters would need to form upon addition of the next metal.^{168, 171} As the results from Chapter 4 highlight, Zn(II) and Cd(II) binding pathways at pH 7.4 do not consist of only terminally bound intermediates, but rather a structure-dependent distribution of specific bridging thiolate structures distinct from the final α -domain M_4S_{11} cluster.

Second, the slower rate of the cooperative pathway was attributed to the four Cd(II) needing to bind in a concerted process to form a complex structure.¹⁶¹ However, in this study, only the rate of Cd(II) binding was characterized and the effect of thiol protonation on metal binding rate was not considered.

A comparison between the pH-dependence on the relative Cd(II) and Zn(II) binding rate constants, based on the data presented in Chapter 4, and the pH-dependence on the binding pathway¹⁷¹ are summarized in Fig. 7-4. A correlation can be seen between the switch from non-cooperative to cooperative Cd(II) binding and the reduction in rate constants (Fig. 7-4A). The Cd(II) results support the previous hypothesis that the change in binding pathway dictates the rate.¹⁶¹

Conversely, the pH-dependent Zn(II) binding rates in comparison to the binding pathways do not support this hypothesis. Rather, the Zn(II) binding slows drastically at a similar point to where the Cd(II) pathway begins to change, but still within the range of entirely non-cooperative binding for Zn(II) (Fig. 7-4B). The reduction in rate at the same point suggests a metal-independent mechanism is driving this phenomenon. Most likely, the necessary deprotonation of the thiols in the metal-free protein under lower pH conditions prior to metal binding is a rate determining step.

Amending the previous conclusion,¹⁶¹ rather than stating that the cooperative binding is slow, it can be hypothesized that the ability of the Cd(II) to form thermodynamically stable clusters under low pH conditions prevents more drastic reduction in rate compared the Zn(II). The implication is that MTs will display a much stronger preference for Cd(II) than for Zn(II) under low pH conditions *in vivo*, which may assist in keeping the toxic metal sequestered.

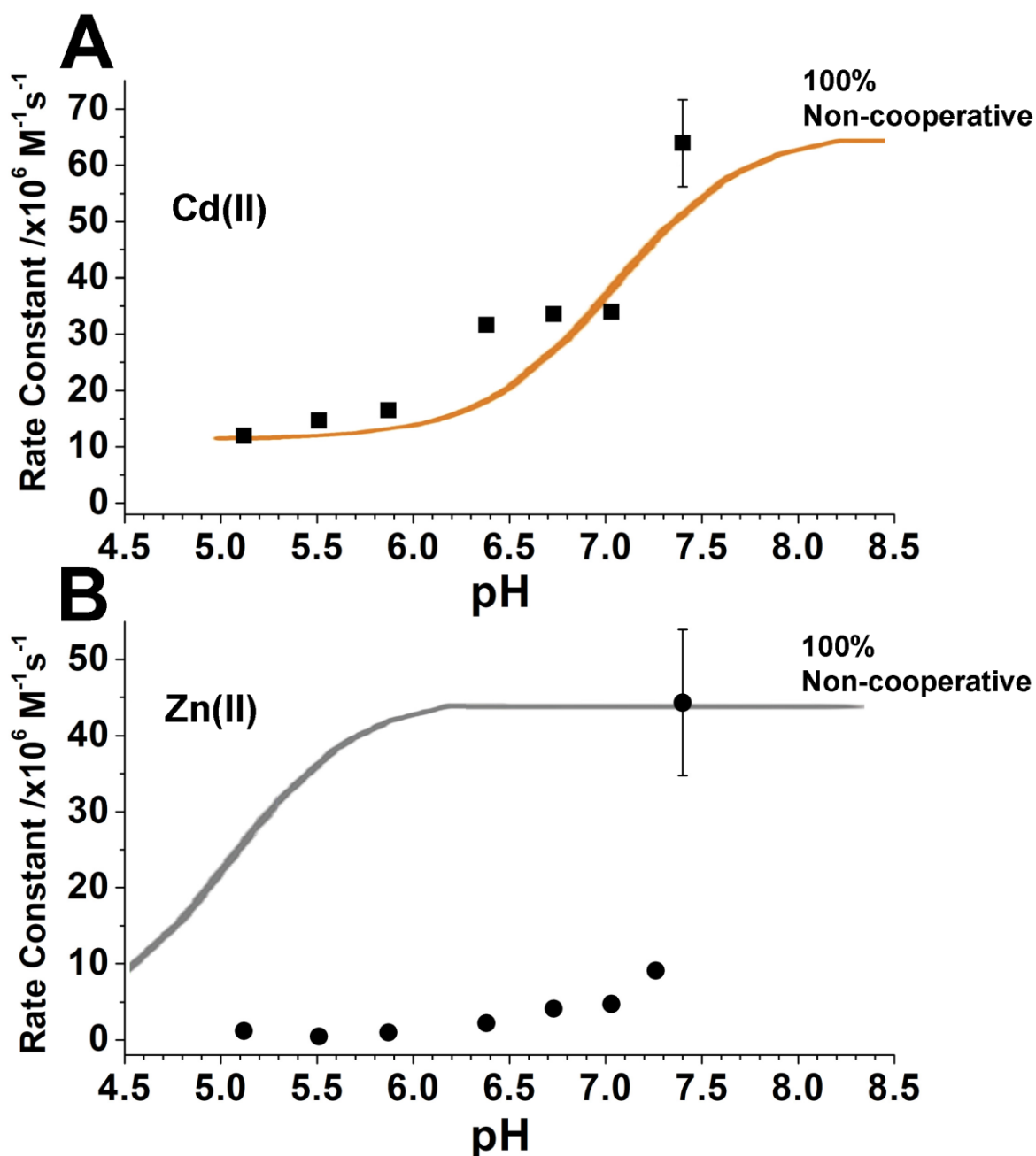


Figure 7-4. Comparison between the pH dependence of the rate constants of Zn(II) and Cd(II) binding to apo-MT, and the degree of cooperativity in the Zn(II) and Cd(II) binding pathways. A plot of relative rate constants resulting from a reaction of 5 μM apo-MT with either (A) 35 μM Cd(II) or (B) 35 μM Zn(II) as a function of pH. Overlaid are representations of the change in Cd(II) (orange) and Zn(II) (gray) binding pathways as a function of pH adapted from Irvine et al. 2016. Note that the orange and gray curves are not fits to the data points but rather serve as a comparison between the rate of metal binding and the metal binding pathway. The curves are scaled between their respective minimum and maximum rate constants. The curve maxima indicate a 100% non-cooperative binding pathway, and the curve minima indicate a 100% cooperative pathway.

7.5 Structural Control of Non-Traditional Metallation

The apo-MT structure also impacts the metallation of metals that bind in non-traditional pathways. In theory, the isolated β -domain of MT can bind up to three Bi(III). However, a stable $\text{Bi}_2\beta\text{MT}$ structure forms at physiological pH which tangles the protein, inhibiting further metallation. Unfolding the βMT using GdmCl increases the fraction of $\text{Bi}_3\beta\text{MT}$ that can form, suggesting that the bundled native structure plays a role in which cysteines bind the Bi(III). Bi(III) also does not display the domain specificity of other metals such as Zn(II), Cd(II), and Cu(I). Only 11 cysteines are free to bind modifier in $\text{Bi}_2\beta\alpha\text{MT}$, meaning that at least three are buried and inaccessible. In $\text{Bi}_2\beta\text{MT}$, three cysteines are free meaning none are inaccessible to modifier assuming a Bi_1S_3 stoichiometry. The different cysteine accessibility between the β -domain and the full $\beta\alpha\text{MT}$ implies different protein structures binding the two Bi(III).

In $\beta\alpha\text{MT}$, trypsin digestion experiments show that $\text{Bi}_2\beta\alpha\text{MT}$ likely forms between Cys 5 and Cys 41 due to the presence of an undigested Bi_2MT structure within this fragment (Fig. 7-5). The individual fragments containing Cys 24, Cys 26, and Cys 29, indicated in Fig. 7-5 are the least susceptible to trypsin digestion when comparing the digestion profiles of apo-MT and Bi_2MT . However, in apo-MT, these cysteines are found in more solvent exposed fragments both experimentally and in simulated data. Likewise, the fragment containing Cys 44, Cys 48, and Cys 50 does not appear to participate in Bi_2MT binding and is also considered a more buried fragment in the apo-MT. This is supporting evidence that it may be cysteine accessibility in the apo-MT driving the location that $\text{Bi}_2\beta\alpha\text{MT}$ forms in, rather than any domain specificity. However, Cys 57, Cys 59, and Cys 60 are likely exposed in the apo-MT and also do not seem to bind Bi_2MT , so there may be another explanation.

The Bi(III) binding pathway is remarkably different depending on whether it is titrated into apo-MT or Zn_7MT (Fig. 7-6). Bi(III) binding to apo-MT shows a cooperativity towards Bi_2MT and Bi_4MT and resists formation of Bi_6MT . Bi(III) binding to Zn_7MT readily forms Bi_6MT and Bi_7MT . No structures appear to form cooperatively, although as the ionization efficiencies for Bi(III) bound MTs and Zn(II) bound MTs are not the same, the information that can be extracted from the relative speciation is limited.

The favourable formation of Bi₆MT and the subsequent formation of Bi₇MT from Zn₇MT suggests that the Bi₆MT structure formed is different than the Bi₆MT structure formed in apo-MT. It is interesting that apo-MT at physiological pH is not conducive to full metallation using Bi(III), but displacement of a natively formed metallate structure can result in a stoichiometry the same as the replaced metal.

This is the first time that such a difference in structure formation based on MT's initial metal-loading status has been discussed. This should prompt further investigation into other heavy metals for which currently there is limited reported ESI-MS data, such as Ag(I) or Hg(II). Reports in structural differences in binding pathways between titration into apo-MT and Zn₇MT for these metals are currently limited to spectroscopic techniques.^{181-182,}

196, 364

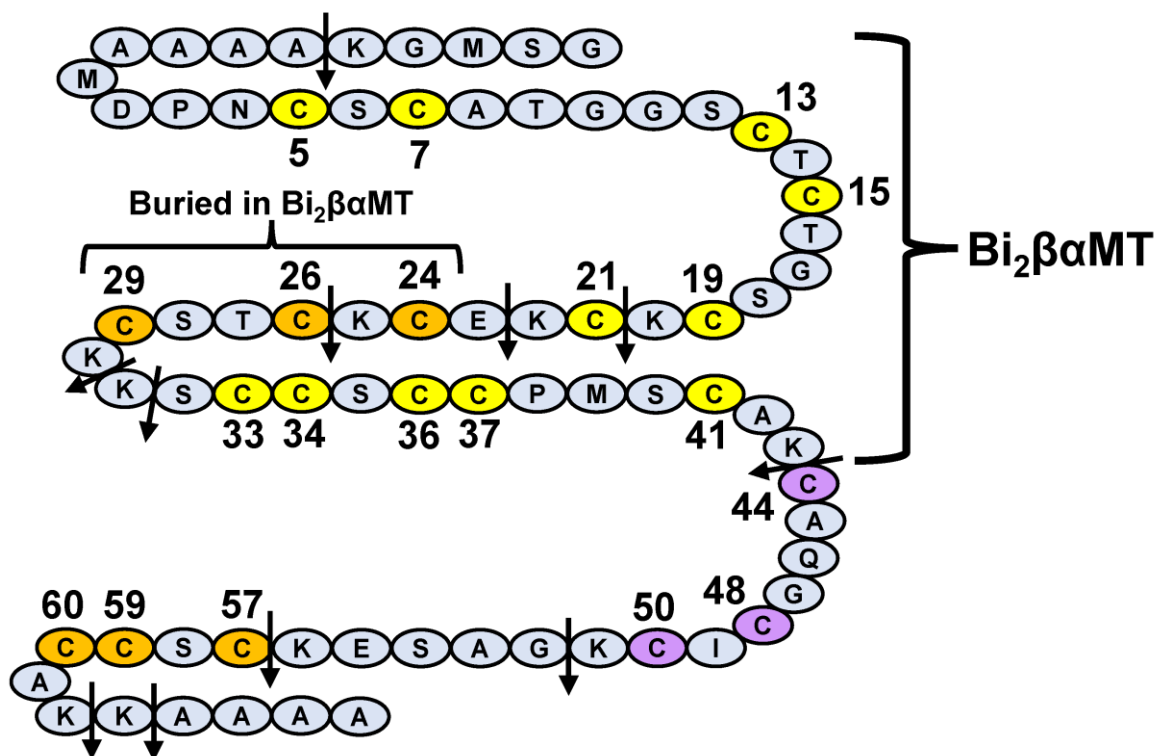


Figure 7-5. comparison between exposed cysteines in apo-MT and cysteines involved in Bi₂MT binding. The sequence of rhMT1a showing fragments with the most exposed (orange) and buried (purple) cysteine residues based on trypsin digestion and MD simulations. The arrows indicate the trypsin cut sites. The fragment which contains the intact Bi₂MT structure after digestion, as well as the individual fragments most inaccessible to trypsin digestion in Bi₂MT are indicated.

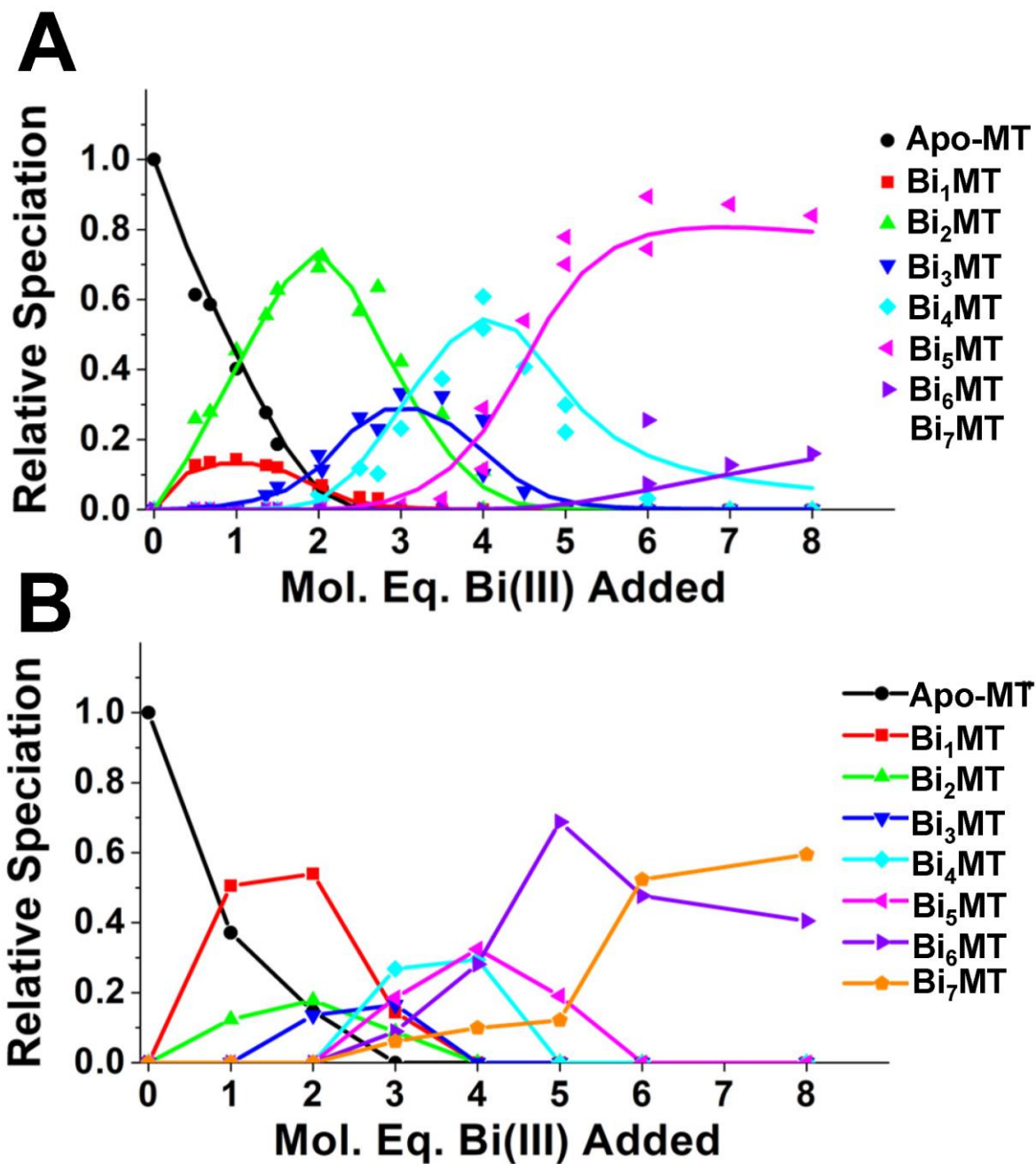


Figure 7-6. Speciation curves for the titration of Bi(III) into apo-β_αMT and Zn₇β_αMT. An experimental (points) and simulated (lines) speciation distribution showing the titration of [Bi(EDTA)]⁻ into apo-β_αMT and an experimental speciation distribution with the points connected showing only the Bi(III) content in each species.

The cysteine-rich nature of MTs confer promiscuity to the protein, allowing for a diverse set of metal binding partners. However, it appears that evolution has fine-tuned the metal binding properties for essential metals such as Zn(II) and Cu(I), which form elegant clusters.³¹³ This may not be the case for xenobiotic metals such as Bi(III) which have only relatively recently had therapeutic uses.³¹⁴ Therefore, it is important to understand these metals interactions with sulfur containing proteins and how they may differ to the behavior of essential metals. This is particularly important for cancer therapy, as MTs have been shown to interact with different proposed and widely utilized metallodrugs, possibly causing resistance.^{187-188, 189-190, 193}

7.6 The Many Structures of Metallothionein

Overall, the work presented in this thesis provides insight into MT species that were previously difficult to study. ESI-MS instrumentation was used to report on novel structural aspects of apo-MTs, partially metallated MTs, and oxidized MTs.

The various structures that exist in MT likely work together to form the structure-function relationship. Apo-MTs exist in a conformation optimal for metal binding, allowing for specific but diverse bridging thiolate structures to form which can then allow MTs to maintain homeostasis of essential metals and sequester heavy metals. The metals in these cluster structures can be displaced as a result of other metals binding or following oxidative stress. These processes may become disrupted by the presence of a xenobiotic metal that tangles the protein into a different conformation.

MT is a resilient protein that can withstand many different environments and stressors. It retains its functions through stressors such as extreme pHs, high temperatures, metal toxicity, or oxidative stress. As a result, this unique protein can only be understood by utilizing methods that embrace its fluxionality and diversity of structure at any given state.

References

1. Petsko, G. A.; Ringe, D., *Protein structure and function*. New Science Press: London, 2004.
2. Anfinsen, C. B.; Haber, E.; Sela, M.; White, F. H., Jr., The kinetics of formation of native ribonuclease during oxidation of the reduced polypeptide chain. *Proc. Natl. Acad. Sci. U. S. A.* **1961**, *47* (9), 1309-14.
3. Anfinsen, C. B., Principles that Govern the Folding of Protein Chains. *Science* **1973**, *181* (4096), 223-230.
4. Vocadlo, D. J.; Davies, G. J.; Laine, R.; Withers, S. G., Catalysis by hen egg-white lysozyme proceeds via a covalent intermediate. *Nature* **2001**, *412* (6849), 835-838.
5. Jomova, K.; Makova, M.; Alomar, S. Y.; Alwasel, S. H.; Nepovimova, E.; Kuca, K.; Rhodes, C. J.; Valko, M., Essential metals in health and disease. *Chem.-Biol. Interact.* **2022**, *367*, 110173.
6. Bowman, S. E. J.; Bridwell-Rabb, J.; Drennan, C. L., Metalloprotein Crystallography: More than a Structure. *Acc. Chem. Res.* **2016**, *49* (4), 695-702.
7. Pearson, R. G., Hard and Soft Acids and Bases. *J. Am. Chem. Soc.* **1963**, *85* (22), 3533-3539.
8. Cai, L.; Li, X. K.; Song, Y.; Cherian, M. G., Essentiality, toxicology and chelation therapy of zinc and copper. *Curr. Med. Chem.* **2005**, *12* (23), 2753-63.
9. Banci, L.; Bertini, I.; Ciofi-Baffoni, S.; Kozyreva, T.; Zovo, K.; Palumaa, P., Affinity gradients drive copper to cellular destinations. *Nature* **2010**, *465* (7298), 645-648.
10. Palumaa, P., Copper chaperones. The concept of conformational control in the metabolism of copper. *FEBS Lett.* **2013**, *587* (13), 1902-1910.
11. Weiss, A.; Murdoch, C. C.; Edmonds, K. A.; Jordan, M. R.; Monteith, A. J.; Perera, Y. R.; Rodríguez Nassif, A. M.; Petoletti, A. M.; Beavers, W. N.; Munneke, M. J.; Drury, S. L.; Krystofiak, E. S.; Thalluri, K.; Wu, H.; Kruse, A. R. S.; DiMarchi, R. D.; Caprioli, R. M.; Spraggins, J. M.; Chazin, W. J.; Giedroc, D. P.; Skaar, E. P., Zn-regulated GTPase metalloprotein activator 1 modulates vertebrate zinc homeostasis. *Cell* **2022**, *185* (12), 2148-2163.e27.
12. Marengo-Rowe, A. J., Structure-Function Relations of Human Hemoglobins. *Bayl. Univ. Med. Cent. Proc.* **2006**, *19* (3), 239-245.
13. Andreini, C.; Banci, L.; Bertini, I.; Rosato, A., Counting the Zinc-Proteins Encoded in the Human Genome. *J. Proteome Res.* **2006**, *5* (1), 196-201.

14. Krebs, J. F.; Ippolito, J.; Christianson, D.; Fierke, C., Structural and functional importance of a conserved hydrogen bond network in human carbonic anhydrase II. *J. Biol. Chem.* **1993**, *268* (36), 27458-27466.
15. Xue, Y.; Liljas, A.; Jonsson, B. H.; Lindskog, S., Structural analysis of the zinc hydroxide–Thr-199–Glu-106 hydrogen-bond network in human carbonic anhydrase II. *Proteins: Struct., Funct., Bioinf.* **1993**, *17* (1), 93-106.
16. Liljas, A., Carbonic anhydrase under pressure. *IUCrJ* **2018**, *5* (Pt 1), 4.
17. Kim, J. K.; Lee, C.; Lim, S. W.; Adhikari, A.; Andring, J. T.; McKenna, R.; Ghim, C.-M.; Kim, C. U., Elucidating the role of metal ions in carbonic anhydrase catalysis. *Nat. Commun.* **2020**, *11* (1), 4557.
18. Laity, J. H.; Lee, B. M.; Wright, P. E., Zinc finger proteins: new insights into structural and functional diversity. *Curr. Opin. Struct. Biol.* **2001**, *11* (1), 39-46.
19. Plaxco, K. W.; Gross, M., The importance of being unfolded. *Nature* **1997**, *386* (6626), 657-659.
20. Wright, P. E.; Dyson, H. J., Intrinsically unstructured proteins: re-assessing the protein structure-function paradigm. *J. Mol. Biol.* **1999**, *293* (2), 321-331.
21. Dunker, A. K.; Lawson, J. D.; Brown, C. J.; Williams, R. M.; Romero, P.; Oh, J. S.; Oldfield, C. J.; Campen, A. M.; Ratliff, C. M.; Higgs, K. W.; Ausio, J.; Nissen, M. S.; Reeves, R.; Kang, C.; Kissinger, C. R.; Bailey, R. W.; Griswold, M. D.; Chiu, W.; Garner, E. C.; Obradovic, Z., Intrinsically disordered protein. *J. Mol. Graphics Model.* **2001**, *19* (1), 26-59.
22. van der Lee, R.; Buljan, M.; Lang, B.; Weatheritt, R. J.; Daughdrill, G. W.; Dunker, A. K.; Fuxreiter, M.; Gough, J.; Gsponer, J.; Jones, D. T.; Kim, P. M.; Kriwacki, R. W.; Oldfield, C. J.; Pappu, R. V.; Tompa, P.; Uversky, V. N.; Wright, P. E.; Babu, M. M., Classification of Intrinsically Disordered Regions and Proteins. *Chem. Rev.* **2014**, *114* (13), 6589-6631.
23. Sato, M., Biological Significance of Intrinsically Disordered Protein Structure. *Chem-Bio Inform. J.* **2022**, *22*, 26-37.
24. Ward, J. J.; Sodhi, J. S.; McGuffin, L. J.; Buxton, B. F.; Jones, D. T., Prediction and Functional Analysis of Native Disorder in Proteins from the Three Kingdoms of Life. *J. Mol. Biol.* **2004**, *337* (3), 635-645.
25. Bondos, S. E.; Dunker, A. K.; Uversky, V. N., Intrinsically disordered proteins play diverse roles in cell signaling. *Cell Commun. Signal* **2022**, *20* (1), 20.
26. Salaun, C.; Greaves, J.; Tomkinson, N. C. O.; Chamberlain, L. H., The linker domain of the SNARE protein SNAP25 acts as a flexible molecular spacer that ensures efficient S-acylation. *J. Biol. Chem.* **2020**, *295* (21), 7501-7515.

27. Bhattacharyya, J.; Das, K. P., Molecular chaperone-like properties of an unfolded protein, *as*-casein. *J. Biol. Chem.* **1999**, *274* (22), 15505-15509.
28. Tskhovrebova, L.; Trinick, J., Titin: properties and family relationships. *Nat. Rev. Mol. Cell Biol.* **2003**, *4* (9), 679-689.
29. Radhakrishnan, I.; Pérez-Alvarado, G. C.; Parker, D.; Dyson, H. J.; Montminy, M. R.; Wright, P. E., Solution Structure of the KIX Domain of CBP Bound to the Transactivation Domain of CREB: A Model for Activator:Coactivator Interactions. *Cell* **1997**, *91* (6), 741-752.
30. Trivedi, R.; Nagarajaram, H. A., Intrinsically Disordered Proteins: An Overview. *Int. J. Mol. Sci.* **2022**, *23* (22), 14050.
31. Tompa, P.; Fuxreiter, M., Fuzzy complexes: polymorphism and structural disorder in protein-protein interactions. *Trends Biochem. Sci* **2008**, *33* (1), 2-8.
32. Ghosh, R. P.; Nikitina, T.; Horowitz-Scherer, R. A.; Gierasch, L. M.; Uversky, V. N.; Hite, K.; Hansen, J. C.; Woodcock, C. L., Unique Physical Properties and Interactions of the Domains of Methylated DNA Binding Protein 2. *Biochemistry* **2010**, *49* (20), 4395-4410.
33. Sharma, R.; Raduly, Z.; Miskei, M.; Fuxreiter, M., Fuzzy complexes: Specific binding without complete folding. *FEBS Lett.* **2015**, *589* (19, Part A), 2533-2542.
34. Cohen, F. E.; Kelly, J. W., Therapeutic approaches to protein-misfolding diseases. *Nature* **2003**, *426* (6968), 905-909.
35. Chaudhuri, T. K.; Paul, S., Protein-misfolding diseases and chaperone-based therapeutic approaches. *FEBS J.* **2006**, *273* (7), 1331-1349.
36. Atrián-Blasco, E.; Gonzalez, P.; Santoro, A.; Alies, B.; Faller, P.; Hureau, C., Cu and Zn coordination to amyloid peptides: From fascinating chemistry to debated pathological relevance. *Coord. Chem. Rev.* **2018**, *371*, 38-55.
37. Tamás, M. J.; Sharma, S. K.; Ibstedt, S.; Jacobson, T.; Christen, P., Heavy metals and metalloids as a cause for protein misfolding and aggregation. *Biomolecules* **2014**, *4* (1), 252-67.
38. Ingram, V. M., Gene mutations in human haemoglobin: the chemical difference between normal and sickle cell haemoglobin. *Nature* **1957**, *180*, 326-328.
39. Fraser-Pitt, D.; O'Neil, D., Cystic fibrosis – a multiorgan protein misfolding disease. *Future Sci. OA* **2015**, *1* (2).
40. Krumova, K.; Cosa, G., Chapter 1 Overview of Reactive Oxygen Species. In *Singlet Oxygen: Applications in Biosciences and Nanosciences, Volume 1*, The Royal Society of Chemistry: 2016; Vol. 1, pp 1-21.

41. Herb, M.; Schramm, M., Functions of ROS in Macrophages and Antimicrobial Immunity. *Antioxidants* **2021**, *10* (2), 313.
42. Hancock, J. T.; Desikan, R.; Neill, S. J., Role of reactive oxygen species in cell signalling pathways. *Biochem. Soc. Trans.* **2001**, *29* (2), 345-349.
43. Höhn, A.; König, J.; Grune, T., Protein oxidation in aging and the removal of oxidized proteins. *J. Proteomics* **2013**, *92*, 132-159.
44. Krisko, A.; Radman, M., Protein damage, ageing and age-related diseases. *Open Biol.* **2019**, *9* (3), 180249.
45. Shringarpure, R.; Davies, K. J., Protein turnover by the proteasome in aging and disease. *Free Radical Biol. Med.* **2002**, *32* (11), 1084-9.
46. Liguori, I.; Russo, G.; Curcio, F.; Bulli, G.; Aran, L.; Della-Morte, D.; Gargiulo, G.; Testa, G.; Cacciatore, F.; Bonaduce, D.; Abete, P., Oxidative stress, aging, and diseases. *Clin. Interv. Aging* **2018**, *13*, 757-772.
47. Aksenov, M. Y.; Aksenova, M. V.; Butterfield, D. A.; Geddes, J. W.; Markesbery, W. R., Protein oxidation in the brain in Alzheimer's disease. *Neuroscience* **2001**, *103* (2), 373-83.
48. Butterfield, D. A.; Kanski, J., Brain protein oxidation in age-related neurodegenerative disorders that are associated with aggregated proteins. *Mech. Ageing Dev.* **2001**, *122* (9), 945-962.
49. Zhong, S.; Li, L.; Shen, X.; Li, Q.; Xu, W.; Wang, X.; Tao, Y.; Yin, H., An update on lipid oxidation and inflammation in cardiovascular diseases. *Free Radical Biol. Med.* **2019**, *144*, 266-278.
50. Karran, P.; Brem, R., Protein oxidation, UVA and human DNA repair. *DNA Repair (Amst.)* **2016**, *44*, 178-185.
51. Hecker, M.; Wagner, A. H., Role of protein carbonylation in diabetes. *J. Inherit. Metab. Dis.* **2018**, *41* (1), 29-38.
52. Berlett, B. S.; Stadtman, E. R., Protein oxidation in aging, disease, and oxidative stress. *J. Biol. Chem.* **1997**, *272* (33), 20313-6.
53. Boronat, S.; García-Santamarina, S.; Hidalgo, E., Gel-free proteomic methodologies to study reversible cysteine oxidation and irreversible protein carbonyl formation. *Free Radical Res.* **2015**, *49* (5), 494-510.
54. Dalle-Donne, I.; Rossi, R.; Giustarini, D.; Milzani, A.; Colombo, R., Protein carbonyl groups as biomarkers of oxidative stress. *Clin. Chim. Acta* **2003**, *329* (1), 23-38.

55. Martinez-Vicente, M.; Sovak, G.; Cuervo, A. M., Protein degradation and aging. *Exp. Gerontol.* **2005**, *40* (8), 622-633.
56. Murray, C. I.; Van Eyk, J. E., Chasing cysteine oxidative modifications: proteomic tools for characterizing cysteine redox status. *Circ. Cardiovasc. Genet.* **2012**, *5* (5), 591.
57. Turell, L.; Zeida, A.; Trujillo, M., Mechanisms and consequences of protein cysteine oxidation: the role of the initial short-lived intermediates. *Essays Biochem.* **2020**, *64* (1), 55-66.
58. Iskusnykh, I. Y.; Zakharova, A. A.; Pathak, D., Glutathione in Brain Disorders and Aging. *Molecules* **2022**, *27* (1), 324.
59. Mudgal, V.; Madaan, N.; Mudgal, A.; Singh, R.; Mishra, S., Effect of toxic metals on human health. *Open Nutraceuticals J.* **2010**, *3* (1).
60. Tang, L.; Qiu, R.; Tang, Y.; Wang, S., Cadmium–zinc exchange and their binary relationship in the structure of Zn-related proteins: a mini review. *Metallomics* **2014**, *6* (8), 1313-1323.
61. Mason, R. P.; Reinfelder, J. R.; Morel, F. M. M., Uptake, Toxicity, and Trophic Transfer of Mercury in a Coastal Diatom. *Environ. Sci. Technol.* **1996**, *30* (6), 1835-1845.
62. Paithankar, J. G.; Saini, S.; Dwivedi, S.; Sharma, A.; Chowdhuri, D. K., Heavy metal associated health hazards: An interplay of oxidative stress and signal transduction. *Chemosphere* **2021**, *262*, 128350.
63. Margoshes, M.; Vallee, B. L., A cadmium protein from equine kidney cortex. *J. Am. Chem. Soc.* **1957**, *79* (17), 4813-4814.
64. Kägi, J. H.; Vallee, B. L., Metallothionein: a cadmium- and zinc-containing protein from equine renal cortex. *J. Biol. Chem.* **1960**, *235*, 3460-5.
65. Pulido, P.; Kägi, J. H. R.; Vallee, B. L., Isolation and Some Properties of Human Metallothionein. *Biochemistry* **1966**, *5* (5), 1768-1777.
66. Kägi, J.; Nordberg, M.; Chemists, A. S. o. B., *Metallothionein: Proceedings of the First International Meeting on Metallothionein and Other Low Molecular Weight Metal-binding Proteins*« Zürich, July 17–22, 1978. Birkhäuser Basel: 1979.
67. Kägi, J. H. R.; Kojima, Y.; Biochemistry, I. U. o., *Metallothionein II: Proceedings of the Second International Meeting on Metallothionein and Other Low Molecular Weight Metal-binding Proteins* : Zürich, August 21-24, 1985. Birkhäuser Verlag: 1987.
68. Kägi, J. H.; Vasák, M.; Lerch, K.; Gilg, D. E.; Hunziker, P.; Bernhard, W. R.; Good, M., Structure of mammalian metallothionein. *Environ. Health Perspect.* **1984**, *54*, 93-103.

69. Vasák, M.; Armitage, I., Nomenclature and possible evolutionary pathways of metallothionein and related proteins. *Environ. Health Perspect.* **1986**, *65*, 215-216.
70. Winge, D. R.; Nielson, K. B.; Gray, W. R.; Hamer, D. H., Yeast metallothionein. Sequence and metal-binding properties. *J. Biol. Chem.* **1985**, *260* (27), 14464-14470.
71. Nemer, M.; Wilkinson, D. G.; Travaglini, E. C.; Sternberg, E. J.; Butt, T. R., Sea urchin metallothionein sequence: key to an evolutionary diversity. *Proc. Natl. Acad. Sci. U. S. A.* **1985**, *82* (15), 4992-4.
72. Rauser, W. E., Phytochelatins and Related Peptides (Structure, Biosynthesis, and Function). *Plant Physiol.* **1995**, *109* (4), 1141-1149.
73. Binz, P.-A.; Kägi, J. H. R., Metallothionein: Molecular evolution and classification. In *Metallothionein IV*, Klaassen, C. D., Ed. Birkhäuser Basel: Basel, 1999; pp 7-13.
74. Cobbett, C.; Goldsbrough, P., PHYTOCHELATINS AND METALLOTHIONEINS: Roles in Heavy Metal Detoxification and Homeostasis. *Annu. Rev. Plant Biol.* **2002**, *53* (1), 159-182.
75. Robinson, N. J.; Tommey, A. M.; Kuske, C.; Jackson, P. J., Plant metallothioneins. *Biochem. J.* **1993**, *295* (1), 1-10.
76. Palacios, Ò.; Atrian, S.; Capdevila, M., Zn- and Cu-thioneins: a functional classification for metallothioneins? *J. Biol. Inorg. Chem.* **2011**, *16* (7), 991-1009.
77. Moleirinho, A.; Carneiro, J.; Matthiesen, R.; Silva, R. M.; Amorim, A.; Azevedo, L., Gains, losses and changes of function after gene duplication: study of the metallothionein family. *PLoS One* **2011**, *6* (4), e18487.
78. Kägi, J. H.; Kojima, Y., Chemistry and biochemistry of metallothionein. *Exp. Suppl.* **1987**, *52*, 25-61.
79. West, A. K.; Stallings, R.; Hildebrand, C. E.; Chiu, R.; Karin, M.; Richards, R. I., Human metallothionein genes: Structure of the functional locus at 16q13. *Genomics* **1990**, *8* (3), 513-518.
80. Suzuki, K. T.; Imura, N.; Kimura, M., *Metallothionein III : biological roles and medical implications*. Birkhäuser Verlag: Basel ;, 1993.
81. Li, Y.; Maret, W., Human metallothionein metallomics. *J. Anal. At. Spectrom.* **2008**, *23* (8), 1055-1062.
82. Uchida, Y.; Takio, K.; Titani, K.; Ihara, Y.; Tomonaga, M., The growth inhibitory factor that is deficient in the Alzheimer's disease brain is a 68 amino acid metallothionein-like protein. *Neuron* **1991**, *7* (2), 337-347.

83. Haq, F.; Mahoney, M.; Koropatnick, J., Signaling events for metallothionein induction. *Mutat. Res., Fundam. Mol. Mech. Mutagen.* **2003**, *533* (1), 211-226.
84. Masters, B.; Quaife, C.; Erickson, J.; Kelly, E.; Froelick, G.; Zambrowicz, B.; Brinster, R.; Palmiter, R., Metallothionein III is expressed in neurons that sequester zinc in synaptic vesicles. *J. Neurosci.* **1994**, *14* (10), 5844-5857.
85. Quaife, C. J.; Findley, S. D.; Erickson, J. C.; Froelick, G. J.; Kelly, E. J.; Zambrowicz, B. P.; Palmiter, R. D., Induction of a New Metallothionein Isoform (MT-IV) Occurs during Differentiation of Stratified Squamous Epithelia. *Biochemistry* **1994**, *33* (23), 7250-7259.
86. Bühler, R. H. O.; Kägi, J. H. R., Human hepatic metallothioneins. *FEBS Lett.* **1974**, *39* (2), 229-234.
87. Ryden, L.; Deutsch, H. F., Preparation and properties of the major copper-binding component in human fetal liver. Its identification as metallothionein. *J. Biol. Chem.* **1978**, *253* (2), 519-524.
88. Hartmann, H.-J.; Weser, U., Copper-thionein from fetal bovine liver. *Biochim. Biophys. Acta, Protein Struct.* **1977**, *491* (1), 211-222.
89. Calvo, J.; Jung, H.; Meloni, G., Copper metallothioneins. *IUBMB Life* **2017**, *69* (4), 236-245.
90. Palmiter, R. D.; Findley, S. D.; Whitmore, T. E.; Durnam, D. M., MT-III, a brain-specific member of the metallothionein gene family. *Proc. Natl. Acad. Sci. U. S. A.* **1992**, *89* (14), 6333-7.
91. Winge, D. R.; Premakumar, R.; Wiley, R. D.; Rajagopalan, K. V., Copper-chelatin: Purification and properties of a copper-binding protein from rat liver. *Arch. Biochem. Biophys.* **1975**, *170*, 253-266.
92. Stillman, M. J.; Gasyna, Z.; Zelazowski, A. J., A luminescence probe for metallothionein in liver tissue: emission intensity measured directly from copper metallothionein induced in rat liver. *FEBS Lett.* **1989**, *257* (2), 283-286.
93. Durnam, D. M.; Palmiter, R. D., Transcriptional regulation of the mouse metallothionein-I gene by heavy metals. *J. Biol. Chem.* **1981**, *256* (11), 5712-5716.
94. Rodilla, V.; Miles, A. T.; Jenner, W.; Hawksworth, G. M., Exposure of cultured human proximal tubular cells to cadmium, mercury, zinc and bismuth: toxicity and metallothionein induction. *Chem.-Biol. Interact.* **1998**, *115* (1), 71-83.
95. Waalkes, M. P.; Klaassen, C. D., Concentration of metallothionein in major organs of rats after administration of various metals. *Fundam. Appl. Toxicol.* **1985**, *5* (3), 473-7.

96. Albores, A.; Koropatnick, J.; Cherian, M. G.; Zelazowski, A. J., Arsenic induces and enhances rat hepatic metallothionein production in vivo. *Chem.-Biol. Interact.* **1992**, *85* (2-3), 127-40.
97. Garrett, S. H.; Belcastro, M.; Sens, M. A.; Somji, S.; Sens, D. A., Acute exposure to arsenite induces metallothionein isoform-specific gene expression in human proximal tubule cells. *J. Toxicol. Environ. Health, Part A* **2001**, *64* (4), 343-55.
98. Hogstrand, C.; Galvez, F.; Wood, C. M., Toxicity, silver accumulation and metallothionein induction in freshwater rainbow trout during exposure to different silver salts. *Environ. Toxicol. Chem.* **1996**, *15* (7), 1102-1108.
99. Butt, T.; Sternberg, E. J.; Mirabelli, C. K.; Crooke, S. T., Regulation of metallothionein gene expression in mammalian cells by gold compounds. *Mol. Pharmacol.* **1986**, *29* (2), 204-210.
100. Agrawal, S.; Flora, G.; Bhatnagar, P.; Flora, S. J., Comparative oxidative stress, metallothionein induction and organ toxicity following chronic exposure to arsenic, lead and mercury in rats. *Cell. Mol. Biol.* **2014**, *60* (2), 13-21.
101. Hart, B. A.; Eneman, J. D.; Gong, Q.; Durieux-Lu, C. C., Increased oxidant resistance of alveolar epithelial type II cells. Isolated from rats following repeated exposure to cadmium aerosols. *Toxicol. Lett.* **1995**, *81* (2-3), 131-9.
102. Reus, I. S.; Bando, I.; Andrés, D.; Cascales, M., Relationship between expression of HSP70 and metallothionein and oxidative stress during mercury chloride induced acute liver injury in rats. *J. Biochem. Mol. Toxicol.* **2003**, *17* (3), 161-8.
103. Ghorbel, I.; Chaabane, M.; Elwej, A.; Boudawara, O.; Abdelhedi, S.; Jamoussi, K.; Boudawara, T.; Zeghal, N., Expression of metallothioneins I and II related to oxidative stress in the liver of aluminium-treated rats. *Arch. Physiol. Biochem.* **2016**, *122* (4), 214-222.
104. Sato, M.; Bremner, I., Oxygen free radicals and metallothionein. *Free Radical Biol. Med.* **1993**, *14* (3), 325-337.
105. Soudani, N.; Chaâbane, M.; Ghorbel, I.; Elwej, A.; Boudawara, T.; Zeghal, N., Glyphosate disrupts redox status and up-regulates metallothionein I and II genes expression in the liver of adult rats. Alleviation by quercetin. *Gen. Physiol. Biophys.* **2019**, *38* (2), 123-134.
106. Koropatnick, J.; Leibbrandt, M.; Cherian, M. G., Organ-Specific Metallothionein Induction in Mice by X Irradiation. *Radiat. Res.* **1989**, *119* (2), 356-365.
107. Tomita, M.; Okuyama, T.; Katsuyama, H.; Ishikawa, T., Paraquat-induced gene expression in rat kidney. *Arch. Toxicol.* **2006**, *80* (10), 687-693.

108. Zhang, B.; Georgiev, O.; Hagmann, M.; Günes, C.; Cramer, M.; Faller, P.; Vasák, M.; Schaffner, W., Activity of metal-responsive transcription factor 1 by toxic heavy metals and H₂O₂ in vitro is modulated by metallothionein. *Mol. Cell. Biol.* **2003**, *23* (23), 8471-85.
109. Günther, V.; Lindert, U.; Schaffner, W., The taste of heavy metals: Gene regulation by MTF-1. *Biochim. Biophys. Acta, Mol. Cell Res.* **2012**, *1823* (9), 1416-1425.
110. Krężel, A.; Maret, W., The Bioinorganic Chemistry of Mammalian Metallothioneins. *Chem. Rev.* **2021**, *121* (23), 14594-14648.
111. Kelly, E. J.; Quaife, C. J.; Froelick, G. J.; Palmiter, R. D., Metallothionein I and II protect against zinc deficiency and zinc toxicity in mice. *J. Nutr.* **1996**, *126* (7), 1782-90.
112. Park, J. D.; Liu, Y.; Klaassen, C. D., Protective effect of metallothionein against the toxicity of cadmium and other metals. *Toxicology* **2001**, *163* (2), 93-100.
113. Liu, J.; Liu, Y.; Habeebu, S. S.; Klaassen, C. D., Susceptibility of MT-Null Mice to Chronic CdCl₂-Induced Nephrotoxicity Indicates That Renal Injury Is Not Mediated by the CdMT Complex. *Toxicol. Sci.* **1998**, *46* (1), 197-203.
114. Liu, J.; Liu, Y.; Goyer, R. A.; Achanzar, W.; Waalkes, M. P., Metallothionein-I/II Null Mice Are More Sensitive than Wild-Type Mice to the Hepatotoxic and Nephrotoxic Effects of Chronic Oral or Injected Inorganic Arsenicals. *Toxicol. Sci.* **2000**, *55* (2), 460-467.
115. Waalkes, M. P.; Liu, J.; Goyer, R. A.; Diwan, B. A., Metallothionein-I/II Double Knockout Mice Are Hypersensitive to Lead-Induced Kidney Carcinogenesis: Role of Inclusion Body Formation. *Cancer Res.* **2004**, *64* (21), 7766-7772.
116. Maret, W.; Vallee, B. L., Thiolate ligands in metallothionein confer redox activity on zinc clusters. *Proc. Natl. Acad. Sci. U. S. A.* **1998**, *95* (7), 3478-82.
117. Thornalley, P. J.; Vasák, M., Possible role for metallothionein in protection against radiation-induced oxidative stress. Kinetics and mechanism of its reaction with superoxide and hydroxyl radicals. *Biochim. Biophys. Acta* **1985**, *827* (1), 36-44.
118. Chubatsu, L. S.; Meneghini, R., Metallothionein protects DNA from oxidative damage. *Biochem. J.* **1993**, *291* (Pt 1) (Pt 1), 193-8.
119. Schwarz, M. A.; Lazo, J. S.; Yalowich, J. C.; Allen, W. P.; Whitmore, M.; Bergonia, H. A.; Tzeng, E.; Billiar, T. R.; Robbins, P. D.; Lancaster, J. R., Jr.; et al., Metallothionein protects against the cytotoxic and DNA-damaging effects of nitric oxide. *Proc. Natl. Acad. Sci. U. S. A.* **1995**, *92* (10), 4452-6.
120. Satoh, M.; Naganuma, A.; Imura, N., Effect of preinduction of metallothionein on paraquat toxicity in mice. *Arch. Toxicol.* **1992**, *66* (2), 145-8.

121. Quesada, A. R.; Byrnes, R. W.; Krezoski, S. O.; Petering, D. H., Direct reaction of H₂O₂ with sulfhydryl groups in HL-60 cells: zinc-metallothionein and other sites. *Arch. Biochem. Biophys.* **1996**, *334* (2), 241-50.
122. Krężel, A.; Maret, W., Zinc-buffering capacity of a eukaryotic cell at physiological pZn. *J. Biol. Inorg. Chem.* **2006**, *11* (8), 1049-1062.
123. Eide, D. J., Zinc transporters and the cellular trafficking of zinc. *Biochim. Biophys. Acta, Mol. Cell Res.* **2006**, *1763* (7), 711-722.
124. Petering, D. H.; Mahim, A., Proteomic high affinity Zn²⁺ trafficking: where does metallothionein fit in? *Int. J. Mol. Sci.* **2017**, *18* (6), 1289.
125. Colvin, R. A.; Holmes, W. R.; Fontaine, C. P.; Maret, W., Cytosolic zinc buffering and muffling: their role in intracellular zinc homeostasis. *Metallomics* **2010**, *2* (5), 306-17.
126. Simons, T. J., Intracellular free zinc and zinc buffering in human red blood cells. *J. Membr. Biol.* **1991**, *123* (1), 63-71.
127. Krezoski, S. K.; Villalobos, J.; Shaw, C. F., 3rd; Petering, D. H., Kinetic lability of zinc bound to metallothionein in Ehrlich cells. *Biochem. J.* **1988**, *255* (2), 483-91.
128. Maret, W., Oxidative metal release from metallothionein via zinc-thiol/disulfide interchange. *Proc. Natl. Acad. Sci. U. S. A.* **1994**, *91* (1), 237-41.
129. Chen, R. W.; Vasey, E. J.; Whanger, P. D., Accumulation and Depletion of Zinc in Rat Liver and Kidney Metallothioneins. *J. Nutr.* **1977**, *107* (5), 805-813.
130. Andrews, G. K.; Geiser, J., Expression of the Mouse Metallothionein-I and -II Genes Provides a Reproductive Advantage during Maternal Dietary Zinc Deficiency. *J. Nutr.* **1999**, *129* (9), 1643-1648.
131. Fong, L.; Tan, K.; Tran, C.; Cool, J.; Scherer, M. A.; Elovaris, R.; Coyle, P.; Foster, B. K.; Rofe, A. M.; Xian, C. J., Interaction of dietary zinc and intracellular binding protein metallothionein in postnatal bone growth. *Bone* **2009**, *44* (6), 1151-1162.
132. Michalska, A. E.; Choo, K. H., Targeting and germ-line transmission of a null mutation at the metallothionein I and II loci in mouse. *Proc. Natl. Acad. Sci. U. S. A.* **1993**, *90* (17), 8088-92.
133. Maret, W.; Larsen, K. S.; Vallee, B. L., Coordination dynamics of biological zinc "clusters" in metallothioneins and in the DNA-binding domain of the transcription factor Gal4. *Proc. Natl. Acad. Sci. U. S. A.* **1997**, *94* (6), 2233-2237.
134. Mason, A. Z.; Perico, N.; Moeller, R.; Thrippleton, K.; Potter, T.; Lloyd, D., Metal donation and apo-metalloenzyme activation by stable isotopically labeled metallothionein. *Mar. Environ. Res.* **2004**, *58* (2), 371-375.

135. Pinter, T. B. J.; Stillman, M. J., The Zinc Balance: Competitive Zinc Metalation of Carbonic Anhydrase and Metallothionein 1A. *Biochemistry* **2014**, *53* (39), 6276-6285.
136. Jacob, C.; Maret, W.; Vallee, B. L., Control of zinc transfer between thionein, metallothionein, and zinc proteins. *Proc. Natl. Acad. Sci. U. S. A.* **1998**, *95* (7), 3489-94.
137. Zeng, J.; Heuchel, R.; Schaffner, W.; Kägi, J. H. R., Thionein (apometallothionein) can modulate DNA binding and transcription activation by zinc finger containing factor Spl. *FEBS Lett.* **1991**, *279* (2), 310-312.
138. Feng, W.; Cai, J.; Pierce, W. M.; Franklin, R. B.; Maret, W.; Benz, F. W.; Kang, Y. J., Metallothionein transfers zinc to mitochondrial aconitase through a direct interaction in mouse hearts. *Biochem. Biophys. Res. Commun.* **2005**, *332* (3), 853-858.
139. Costello, L. C.; Guan, Z.; Franklin, R. B.; Feng, P., Metallothionein can function as a chaperone for zinc uptake transport into prostate and liver mitochondria. *J. Inorg. Biochem.* **2004**, *98* (4), 664-666.
140. Stillman, M. J., Metallothioneins. *Coord. Chem. Rev.* **1995**, *144*, 461-511.
141. Eva Freisinger, M. V., Cadmium in Metallothioneins. In *Cadmium: From Toxicity to Essentiality*, Astrid Sigel, H. S., Roland KO Sigel, Ed. Springer Science+Business Media: Dordrecht, 2013; Vol. 11, pp 339-371.
142. Furey, W. F.; Robbins, A. H.; Clancy, L. L.; Winge, D. R.; Wang, B. C.; Stout, C. D., Crystal Structure of Cd,Zn Metallothionein. *Science* **1986**, *231* (4739), 704-710.
143. Robbins, A. H.; McRee, D. E.; Williamson, M.; Collett, S. A.; Xuong, N. H.; Furey, W. F.; Wang, B. C.; Stout, C. D., Refined crystal structure of Cd, Zn metallothionein at 2.0 Å resolution. *J. Mol. Biol.* **1991**, *221* (4), 1269-93.
144. Stillman, M. J.; Shaw, C. F.; Suzuki, K. T., *Metallothioneins: Synthesis, Structure, and Properties of Metallothioneins, Phytochelatins, and Metal-thiolate Complexes*. VCH Publishers: 1992.
145. Arseniev, A.; Schultze, P.; Wörgötter, E.; Braun, W.; Wagner, G.; Vasák, M.; Kägi, J. H.; Wüthrich, K., Three-dimensional structure of rabbit liver [Cd₇]metallothionein-2a in aqueous solution determined by nuclear magnetic resonance. *J. Mol. Biol.* **1988**, *201* (3), 637-57.
146. Messerle, B. A.; Schäffer, A.; Vašák, M.; Kägi, J. H. R.; Wüthrich, K., Three-dimensional structure of human [113Cd₇]metallothionein-2 in solution determined by nuclear magnetic resonance spectroscopy. *J. Mol. Biol.* **1990**, *214* (3), 765-779.
147. Zangger, K.; Oz, G.; Otvos, J. D.; Armitage, I. M., Three-dimensional solution structure of mouse [Cd₇]-metallothionein-1 by homonuclear and heteronuclear NMR spectroscopy. *Protein Sci.* **1999**, *8* (12), 2630-2638.

148. Sutherland, D. E. K.; Willans, M. J.; Stillman, M. J., Single Domain Metallothioneins: Supermetalation of Human MT 1a. *J. Am. Chem. Soc.* **2012**, *134* (6), 3290-3299.
149. Calderone, V.; Dolderer, B.; Hartmann, H.-J.; Echner, H.; Luchinat, C.; Del Bianco, C.; Mangani, S.; Weser, U., The crystal structure of yeast copper thionein: the solution of a long-lasting enigma. *Proc. Natl. Acad. Sci. U. S. A.* **2005**, *102* (1), 51-56.
150. Feldman, S. L.; Failla, M. L.; Cousins, R. J., Degradation of rat liver metallothioneins in vitro. *Biochim. Biophys. Acta* **1978**, *544* (3), 638-46.
151. Davis, S. R.; Cousins, R. J., Metallothionein expression in animals: a physiological perspective on function. *J. Nutr.* **2000**, *130* (5), 1085-8.
152. Nielson, K. B.; Winge, D., Order of metal binding in metallothionein. *J. Biol. Chem.* **1983**, *258* (21), 13063-13069.
153. Yang, Y.; Maret, W.; Vallee, B. L., Differential fluorescence labeling of cysteinyl clusters uncovers high tissue levels of thionein. *Proc. Natl. Acad. Sci. U. S. A.* **2001**, *98* (10), 5556-5559.
154. Pattanaik, A.; Shaw, C. F.; Petering, D. H.; Garvey, J.; Kraker, A. J., Basal metallothionein in tumors: Widespread presence of apoprotein. *J. Inorg. Biochem.* **1994**, *54* (2), 91-105.
155. Petering, D. H.; Zhu, J.; Krezoski, S.; Meeusen, J.; Kiekenbush, C.; Krull, S.; Specher, T.; Dughish, M., Apo-Metallothionein Emerging as a Major Player in the Cellular Activities of Metallothionein. *Exp. Biol. Med.* **2006**, *231* (9), 1528-1534.
156. Pande, J.; Pande, C.; Gilg, D.; Vasak, M.; Callender, R.; Kägi, J., Raman, infrared, and circular dichroism spectroscopic studies on metallothionein: a predominantly "turn"-containing protein. *Biochemistry* **1986**, *25* (19), 5526-5532.
157. Vasák, M.; Galdes, A.; Hill, H. A.; Kägi, J. H.; Bremner, I.; Young, B. W., Investigation of the structure of metallothioneins by proton nuclear magnetic resonance spectroscopy. *Biochemistry* **1980**, *19* (3), 416-25.
158. Summers, K. L.; Mahrok, A. K.; Dryden, M. D. M.; Stillman, M. J., Structural properties of metal-free apometallothioneins. *Biochem. Biophys. Res. Commun.* **2012**, *425* (2), 485-492.
159. Hong, S.-H.; Hao, Q.; Maret, W., Domain-specific fluorescence resonance energy transfer (FRET) sensors of metallothionein/thionein. *Protein Eng., Des. Sel.* **2005**, *18* (6), 255-263.
160. Irvine, G. W.; Duncan, K. E. R.; Gullons, M.; Stillman, M. J., Metalation kinetics of the human α -metallothionein 1a fragment is dependent on the fluxional structure of the apo-protein. *Chem. Eur. J.* **2015**, *21* (3), 1269-1279.

161. Wong, D. L.; Korkola, N. C.; Stillman, M. J., Kinetics of competitive Cd²⁺ binding pathways: the realistic structure of intrinsically disordered, partially metallated metallothioneins. *Metallomics* **2019**, *11* (5), 894-905.
162. Chen, S.-H.; Chen, L.; Russell, D. H., Metal-Induced Conformational Changes of Human Metallothionein-2A: A Combined Theoretical and Experimental Study of Metal-Free and Partially Metalated Intermediates. *J. Am. Chem. Soc.* **2014**, *136* (26), 9499-9508.
163. Chen, S.-H.; Russell, D. H., How Closely Related Are Conformations of Protein Ions Sampled by IM-MS to Native Solution Structures? *J. Am. Soc. Mass. Spectrom.* **2015**, *26* (9), 1433-1443.
164. Rigby, K. E.; Stillman, M. J., Structural studies of metal-free metallothionein. *Biochem. Biophys. Res. Commun.* **2004**, *325* (4), 1271-1278.
165. Irvine, G. W.; Santolini, M.; Stillman, M. J., Selective cysteine modification of metal-free human metallothionein 1a and its isolated domain fragments: Solution structural properties revealed via ESI-MS. *Protein Sci.* **2017**, *26* (5), 960-971.
166. Rigby Duncan, K. E.; Stillman, M. J., Evidence for noncooperative metal binding to the α domain of human metallothionein. *FEBS J.* **2007**, *274* (9), 2253-2261.
167. Sutherland, D. E.; Stillman, M. J., Noncooperative cadmium (II) binding to human metallothionein 1a. *Biochem. Biophys. Res. Commun.* **2008**, *372* (4), 840-844.
168. Sutherland, D. E.; Summers, K. L.; Stillman, M. J., Noncooperative metalation of metallothionein 1a and its isolated domains with zinc. *Biochemistry* **2012**, *51* (33), 6690-6700.
169. Gehrig, P. M.; You, C.; Dallinger, R.; Gruber, C.; Brouwer, M.; Kägi, J. H.; Hunziker, P. E., Electrospray ionization mass spectrometry of zinc, cadmium, and copper metallothioneins: Evidence for metal-binding cooperativity. *Protein Sci.* **2000**, *9* (2), 395-402.
170. Chen, S.-H.; Russell, W. K.; Russell, D. H., Combining Chemical Labeling, Bottom-Up and Top-Down Ion-Mobility Mass Spectrometry To Identify Metal-Binding Sites of Partially Metalated Metallothionein. *Anal. Chem.* **2013**, *85* (6), 3229-3237.
171. Irvine, G. W.; Pinter, T. B.; Stillman, M. J., Defining the metal binding pathways of human metallothionein 1a: balancing zinc availability and cadmium seclusion. *Metallomics* **2016**, *8* (1), 71-81.
172. Yuan, A. T.; Korkola, N. C.; Wong, D. L.; Stillman, M. J., Metallothionein Cd₄S₁₁ cluster formation dominates in the protection of carbonic anhydrase. *Metallomics* **2020**, *12* (5), 767-783.
173. Carpenter, M. C.; Shami Shah, A.; DeSilva, S.; Gleaton, A.; Su, A.; Goundie, B.; Croteau, M. L.; Stevenson, M. J.; Wilcox, D. E.; Austin, R. N., Thermodynamics of Pb(ii)

and Zn(ii) binding to MT-3, a neurologically important metallothionein†. *Metallomics* **2015**, 8 (6), 605-617.

174. Krężel, A.; Maret, W., Dual Nanomolar and Picomolar Zn(II) Binding Properties of Metallothionein. *J. Am. Chem. Soc.* **2007**, 129 (35), 10911-10921.

175. Chen, S.-H.; Russell, D. H., Reaction of Human Cd7metallothionein and N-Ethylmaleimide: Kinetic and Structural Insights from Electrospray Ionization Mass Spectrometry. *Biochemistry* **2015**, 54 (39), 6021-6028.

176. Peris-Díaz, M. D.; Guran, R.; Domene, C.; de los Rios, V.; Zitka, O.; Adam, V.; Krężel, A., An Integrated Mass Spectrometry and Molecular Dynamics Simulations Approach Reveals the Spatial Organization Impact of Metal-Binding Sites on the Stability of Metal-Depleted Metallothionein-2 Species. *J. Am. Chem. Soc.* **2021**, 143 (40), 16486-16501.

177. Ngu, T. T.; Stillman, M. J., Arsenic Binding to Human Metallothionein. *J. Am. Chem. Soc.* **2006**, 128 (38), 12473-12483.

178. Ngu, T. T.; Krecisz, S.; Stillman, M. J., Bismuth binding studies to the human metallothionein using electrospray mass spectrometry. *Biochem. Biophys. Res. Commun.* **2010**, 396 (2), 206-212.

179. Melenbacher, A.; Korkola, N. C.; Stillman, M. J., The pathways and domain specificity of Cu(I) binding to human metallothionein 1A. *Metallomics* **2020**, 12 (12), 1951-1964.

180. Scheller, J. S.; Irvine, G. W.; Wong, D. L.; Hartwig, A.; Stillman, M. J., Stepwise copper(i) binding to metallothionein: a mixed cooperative and non-cooperative mechanism for all 20 copper ions. *Metallomics* **2017**, 9 (5), 447-462.

181. Zelazowski, A. J.; Gasyna, Z.; Stillman, M. J., Silver binding to rabbit liver metallothionein. Circular dichroism and emission study of silver-thiolate cluster formation with apometallothionein and the alpha and beta fragments. *J. Biol. Chem.* **1989**, 264 (29), 17091-9.

182. Dong, S. Y.; Shirzadeh, M.; Fan, L. Q.; Laganowsky, A.; Russell, D. H., Ag+ Ion Binding to Human Metallothionein-2A Is Cooperative and Domain Specific. *Anal. Chem.* **2020**, 92 (13), 8923-8932.

183. Nielson, K. B.; Atkin, C. L.; Winge, D. R., Distinct metal-binding configurations in metallothionein. *J. Biol. Chem.* **1985**, 260 (9), 5342-5350.

184. Lu, W.; Kasrai, M.; Bancroft, G. M.; Stillman, M. J.; Tan, K., Sulfur L-edge XANES study of zinc-, cadmium-, and mercury-containing metallothionein and model compounds. *Inorg. Chem.* **1990**, 29 (14), 2561-2563.

185. Cai, W.; Stillman, M. J., (Mercury) 18-metallothionein. *J. Am. Chem. Soc.* **1988**, *110* (23), 7872-7873.
186. Jiang, D.; Heald, S. M.; Sham, T.; Stillman, M. J., Structures of the cadmium, mercury, and zinc thiolate clusters in metallothionein: XAFS study of Zn7-MT, Cd7-MT, Hg7-MT, and Hg18-MT formed from rabbit liver metallothionein 2. *J. Am. Chem. Soc.* **1994**, *116* (24), 11004-11013.
187. Wong, D. L.; Stillman, M. J., Capturing platinum in cisplatin: kinetic reactions with recombinant human apo-metallothionein 1a. *Metallomics* **2018**, *10* (5), 713-721.
188. Pattanaik, A.; Bachowski, G.; Laib, J.; Lemkuil, D.; Shaw, C. F.; Petering, D. H.; Hitchcock, A.; Saryan, L., Properties of the reaction of cis-dichlorodiammineplatinum(II) with metallothionein. *J. Biol. Chem.* **1992**, *267* (23), 16121-16128.
189. Zhang, B.; Tang, W.; Gao, S.; Zhou, Y., Platinum binding to metallothionein. Analysis of circular dichroism spectra of complexes formed between metallothionein and platinum from cis- and trans-diamminedichloroplatinum. *J. Inorg. Biochem.* **1995**, *58* (1), 9-19.
190. Bulathge, A. W.; Villones, R. L. E.; Herbert, F. C.; Gassensmith, J. J.; Meloni, G., Comparative cisplatin reactivity towards human Zn7-metallothionein-2 and MTF-1 zinc fingers: potential implications in anticancer drug resistance. *Metallomics* **2022**, *14* (9).
191. Wong, D. L.; Stillman, M. J., Destructive interactions of dirhodium(ii) tetraacetate with β metallothionein rh1a. *Chem. Commun.* **2016**, *52* (33), 5698-5701.
192. Wong, D. L.; Stillman, M. J., Metallothionein: An Aggressive Scavenger—The Metabolism of Rhodium(II) Tetraacetate (Rh₂(CH₃CO₂)₄). *ACS Omega* **2018**, *3* (11), 16314-16327.
193. Casini, A.; Karotki, A.; Gabbiani, C.; Rugi, F.; Vašák, M.; Messori, L.; Dyson, P. J., Reactivity of an antimetastatic organometallic ruthenium compound with metallothionein-2: relevance to the mechanism of action†. *Metallomics* **2009**, *1* (5), 434-441.
194. Scheller, J. S.; Irvine, G. W.; Stillman, M. J., Unravelling the mechanistic details of metal binding to mammalian metallothioneins from stoichiometric, kinetic, and binding affinity data. *Dalton Trans.* **2018**, *47* (11), 3613-3637.
195. Bernhard, W.; Good, M.; Vašák, M.; Kägi, J. H., Spectroscopic studies and characterization of metallothioneins containing mercury, lead and bismuth. *Inorg. Chim. Acta* **1983**, *79*, 154-155.
196. Lu, W.; Stillman, M. J., Mercury-thiolate clusters in metallothionein. Analysis of circular dichroism spectra of complexes formed between. alpha.-metallothionein, apometallothionein, zinc metallothionein, and cadmium metallothionein and mercury (2+). *J. Am. Chem. Soc.* **1993**, *115* (8), 3291-3299.

197. Jiang, D. T.; Gui, Z. Q.; Heald, S. M.; Sham, T. K.; Stillman, M. J., XAFS of silver(I) metallothionein. *Phys. B* **1995**, 208-209, 729-730.
198. Gui, Z.; Green, A. R.; Kasrai, M.; Bancroft, G. M.; Stillman, M. J., Sulfur K-Edge EXAFS Studies of Cadmium-, Zinc-, Copper-, and Silver-Rabbit Liver Metallothioneins. *Inorg. Chem.* **1996**, 35 (22), 6520-6529.
199. Laib, J.; Shaw III, C. F.; Petering, D. H.; Eidsness, M. K.; Elder, R.; Garvey, J. S., Formation and characterization of aurothioneins: Au, Zn, Cd-thionein, Au, Cd-thionein, and (thiomalato-Au) x-thionein. *Biochemistry* **1985**, 24 (8), 1977-1986.
200. Stillman, M. J.; Presta, A.; Gui, Z.; Jiang, D. T., Spectroscopic studies of copper, silver and gold-metallothioneins. *Met.-Based Drugs* **1994**, 1 (5-6), 375-94.
201. Shaw III, C. F.; Laib, J. E.; Savas, M. M.; Petering, D. H., Biphasic kinetics of aurothionein formation from gold sodium thiomalate: a novel metallochromic technique to probe zinc (2+) and cadmium (2+) displacement from metallothionein. *Inorg. Chem.* **1990**, 29 (3), 403-408.
202. Sun, H.; Li, H.; Harvey, I.; Sadler, P. J., Interactions of Bismuth Complexes with Metallothionein(II). *J. Biol. Chem.* **1999**, 274 (41), 29094-29101.
203. Bongers, J.; Richardson, D. E.; Bell, J. U., Platinum(II) binding to metallothioneins. *J. Inorg. Biochem.* **1988**, 34 (1), 55-62.
204. Vasak, M.; Kaegi, J. H.; Holmquist, B.; Vallee, B. L., Spectral studies of cobalt (II)- and nickel (II)-metallothionein. *Biochemistry* **1981**, 20 (23), 6659-6664.
205. Bertini, I.; Luchinat, C.; Messori, L.; Vasak, M., Proton NMR studies of the cobalt (II)-metallothionein system. *J. Am. Chem. Soc.* **1989**, 111 (19), 7296-7300.
206. Palacios, Ò.; Leiva-Presa, À.; Atrian, S.; Lobinski, R., A study of the Pb(II) binding to recombinant mouse Zn7-metallothionein 1 and its domains by ESI TOF MS. *Talanta* **2007**, 72 (2), 480-488.
207. Good, M.; Vasak, M., Iron(II)-substituted metallothionein: evidence for the existence of iron-thiolate clusters. *Biochemistry* **1986**, 25 (26), 8353-8356.
208. Morelock, M.; Cormier, T.; Tolman, G., Technetium metallothioneins. *Inorg. Chem.* **1988**, 27 (18), 3137-3140.
209. Li, T. Y.; Minkel, D. T.; Shaw, C. F., 3rd; Petering, D. H., On the reactivity of metallothioneins with 5,5'-dithiobis-(2-nitrobenzoic acid). *Biochem. J.* **1981**, 193 (2), 441-6.
210. Savas, M. M.; Petering, D. H.; Shaw, C. F., On the rapid, monophasic reaction of the rabbit liver metallothionein .alpha.-domain with 5,5'-dithiobis (2-nitrobenzoic acid) (DTNB). *Inorg. Chem.* **1991**, 30 (3), 581-583.

211. Savas, M. M.; Shaw, C. F., 3rd; Petering, D. H., The oxidation of rabbit liver metallothionein-II by 5,5'-dithiobis(2-nitrobenzoic acid) and glutathione disulfide. *J. Biol. Inorg. Chem.* **1993**, *52* (4), 235-49.
212. Bordin, G.; Raposo, F. C.; Rodriguez, A. R., Chromatographic characterization of a hexapeptide containing three thiol groups, intrinsic to the metallothionein structure. *Chromatographia* **1994**, *39* (3), 146-154.
213. Haase, H.; Maret, W., Partial oxidation and oxidative polymerization of metallothionein. *Electrophoresis* **2008**, *29* (20), 4169-76.
214. Krizkova, S.; Adam, V.; Kizek, R., Study of metallothionein oxidation by using of chip CE. *Electrophoresis* **2009**, *30* (23), 4029-33.
215. Fliss, H.; Ménard, M., Hypochlorous acid-induced mobilization of zinc from metalloproteins. *Arch. Biochem. Biophys.* **1991**, *287* (1), 175-9.
216. Fliss, H.; Ménard, M., Oxidant-induced mobilization of zinc from metallothionein. *Arch. Biochem. Biophys.* **1992**, *293* (1), 195-9.
217. Zhu, J.; Meeusen, J.; Krezoski, S.; Petering, D. H., Reactivity of Zn-, Cd-, and Apo-Metallothionein with Nitric Oxide Compounds: In Vitro and Cellular Comparison. *Chem. Res. Toxicol.* **2010**, *23* (2), 422-431.
218. Jiménez, I.; Gotteland, M.; Zarzuelo, A.; Uauy, R.; Speisky, H., Loss of the metal binding properties of metallothionein induced by hydrogen peroxide and free radicals. *Toxicology* **1997**, *120* (1), 37-46.
219. Hu, H. Y.; Cheng, H. Q.; Li, Q.; Zou, Y. S.; Xu, G. J., Study of the redox properties of metallothionein in vitro by reacting with DsbA protein. *J. Protein Chem.* **1999**, *18* (6), 665-70.
220. St Croix, C. M.; Wasserloos, K. J.; Dineley, K. E.; Reynolds, I. J.; Levitan, E. S.; Pitt, B. R., Nitric oxide-induced changes in intracellular zinc homeostasis are mediated by metallothionein/thionein. *Am. J. Physiol.-Lung C.* **2002**, *282* (2), L185-92.
221. Malaiyandi, L. M.; Dineley, K. E.; Reynolds, I. J., Divergent consequences arise from metallothionein overexpression in astrocytes: zinc buffering and oxidant-induced zinc release. *Glia* **2004**, *45* (4), 346-53.
222. Vaher, M.; Romero-Isart, N.; Vašák, M.; Palumaa, P., Reactivity of Cd7-metallothionein with Cu(II) ions: evidence for a cooperative formation of Cd₃Cu(I)S₅-metallothionein. *J. Inorg. Biochem.* **2001**, *83* (1), 1-6.
223. Tarasava, K.; Chesnov, S.; Freisinger, E., Oxidation of the N-terminal domain of the wheat metallothionein Ec -1 leads to the formation of three distinct disulfide bridges. *Biopolymers* **2016**, *106* (3), 295-308.

224. Zangger, K.; Oz, G.; Haslinger, E.; Kunert, O.; Armitage, I. M., Nitric oxide selectively releases metals from the amino-terminal domain of metallothioneins: potential role at inflammatory sites. *FASEB J.* **2001**, *15* (7), 1303-5.
225. Feng, W.; Benz, F. W.; Cai, J.; Pierce, W. M.; Kang, Y. J., Metallothionein disulfides are present in metallothionein-overexpressing transgenic mouse heart and increase under conditions of oxidative stress. *J. Biol. Chem.* **2006**, *281* (2), 681-7.
226. Kassim, R.; Ramseyer, C.; Enescu, M., Oxidation reactivity of zinc-cysteine clusters in metallothionein. *J. Biol. Inorg. Chem.* **2013**, *18* (3), 333-42.
227. Van Holde, K. E.; Johnson, W. C.; Ho, P. S., *Principles of Physical Biochemistry*. Pearson/Prentice Hall: 2006.
228. Uversky, V. N., Natively unfolded proteins: A point where biology waits for physics. *Protein Sci.* **2002**, *11* (4), 739-756.
229. Stillman, M. J.; Zelazowski, A. J., Domain specificity in metal binding to metallothionein. A circular dichroism and magnetic circular dichroism study of cadmium and zinc binding at temperature extremes. *J. Biol. Chem.* **1988**, *263* (13), 6128-6133.
230. Uversky, V. N., What does it mean to be natively unfolded? *Eur. J. Biochem.* **2002**, *269* (1), 2-12.
231. Yamashita, M.; Fenn, J. B., Electrospray ion source. Another variation on the free-jet theme. *J. Phys. Chem.* **1984**, *88* (20), 4451-4459.
232. Alexandrov, M. L.; Gall, L. N.; Krasnov, N. V.; Nikolaev, V. I.; Pavlenko, V. A.; Shkurov, V. A., Extraction of ions from solutions under atmospheric pressure as a method for mass spectrometric analysis of bioorganic compounds. *Rapid Commun. Mass Spectrom.* **2008**, *22* (3), 267-270.
233. Fenn, J. B.; Mann, M.; Meng, C. K.; Wong, S. F.; Whitehouse, C. M., Electrospray Ionization for Mass Spectrometry of Large Biomolecules. *Science* **1989**, *246* (4926), 64-71.
234. Van Berkel, G. J.; Kertesz, V., Using the Electrochemistry of the Electrospray Ion Source. *Anal. Chem.* **2007**, *79* (15), 5510-5520.
235. Ho, C. S.; Lam, C. W.; Chan, M. H.; Cheung, R. C.; Law, L. K.; Lit, L. C.; Ng, K. F.; Suen, M. W.; Tai, H. L., Electrospray ionisation mass spectrometry: principles and clinical applications. *Clin. Biochem. Rev.* **2003**, *24* (1), 3-12.
236. Rayleigh, L., On the equilibrium of liquid conducting masses charged with electricity. *The London, Edinburgh, and Dublin Philosophical Magazine and Journal of Science* **1882**, *14* (87), 184-186.

237. Konermann, L.; Ahadi, E.; Rodriguez, A. D.; Vahidi, S., Unraveling the Mechanism of Electrospray Ionization. *Anal. Chem.* **2013**, *85* (1), 2-9.
238. Metwally, H.; Duez, Q.; Konermann, L., Chain Ejection Model for Electrospray Ionization of Unfolded Proteins: Evidence from Atomistic Simulations and Ion Mobility Spectrometry. *Anal. Chem.* **2018**, *90* (16), 10069-10077.
239. Guilhaus, M.; Selby, D.; Mlynski, V., Orthogonal acceleration time-of-flight mass spectrometry. *Mass Spectrom. Rev.* **2000**, *19* (2), 65-107.
240. Wiza, J. L., Microchannel plate detectors. *Nucl. Instrum. Methods* **1979**, *162* (1-3), 587-601.
241. Reinhold, B. B.; Reinhold, V. N., Electrospray ionization mass spectrometry: Deconvolution by an entropy-based algorithm. *J. Am. Soc. Mass. Spectrom.* **1992**, *3* (3), 207-215.
242. Alderighi, L.; Gans, P.; Ienco, A.; Peters, D.; Sabatini, A.; Vacca, A., Hyperquad simulation and speciation (HySS): a utility program for the investigation of equilibria involving soluble and partially soluble species. *Coord. Chem. Rev.* **1999**, *184* (1), 311-318.
243. Leach, A. R., *Molecular Modelling: Principles and Applications*. Prentice Hall: 2001.
244. Allinger, N. L.; Yuh, Y. H.; Lii, J. H., Molecular mechanics. The MM3 force field for hydrocarbons. 1. *J. Am. Chem. Soc.* **1989**, *111* (23), 8551-8566.
245. Lii, J. H.; Allinger, N. L., Molecular mechanics. The MM3 force field for hydrocarbons. 2. Vibrational frequencies and thermodynamics. *J. Am. Chem. Soc.* **1989**, *111* (23), 8566-8575.
246. Lii, J. H.; Allinger, N. L., Molecular mechanics. The MM3 force field for hydrocarbons. 3. The van der Waals' potentials and crystal data for aliphatic and aromatic hydrocarbons. *J. Am. Chem. Soc.* **1989**, *111* (23), 8576-8582.
247. Becke, A. D., Density-functional thermochemistry. III. The role of exact exchange. *The Journal of Chemical Physics* **1993**, *98* (7), 5648-5652.
248. Lee, C.; Yang, W.; Parr, R. G., Development of the Colle-Salvetti correlation-energy formula into a functional of the electron density. *Phys. Rev. B: Condens. Matter Mater. Phys.* **1988**, *37* (2), 785-789.
249. M. J. Frisch, G. W. T., H. B. Schlegel, G. E.; Scuseria, M. A. R., J. R. Cheeseman, G. Scalmani, V. Barone, B. Mennucci, G. A. Petersson, H. N., M. Caricato, X. Li, H. P. Hratchian, A. F.; Izmaylov, J. B., G. Zheng, J. L. Sonnenberg, M. Hada, M. Ehara, K. Toyota, R. Fukuda, J. H., M. Ishida, T. Nakajima, Y. Honda, O. Kitao, H. Nakai, T. Vreven, J. A. M., Jr., J. E. Peralta, F. Ogliaro, M. Bearpark, J. J.; Heyd, E. B., K. N. Kudin, V. N. Staroverov, T. Keith, R. Kobayashi, J.; Normand, K. R., A. Rendell, J. C. Burant, S. S. Iyengar, J. Tomasi, M.; Cossi, N. R., J. M. Millam, M. Klene, J. E. Knox, J. B. Cross,

V. Bakken, C.; Adamo, J. J., R. Gomperts, R. E. Stratmann, O. Yazyev, A. J. Austin, R.; Cammi, C. P., J. W. Ochterski, R. L. Martin, K. Morokuma, V. G.; Zakrzewski, G. A. V., P. Salvador, J. J. Dannenberg, S. Dapprich, A. D.; Daniels, O. F., J. B. Foresman, J. V. Ortiz, J. Cioslowski, D. J. Fox *Gaussian 09, Revision E.01*, Gaussian, Inc.: Wallingford CT, 2013., 2013.

250. Summers, S. P.; Abboud, K. A.; Farrah, S. R.; Palenik, G. J., Syntheses and structures of bismuth(III) complexes with nitrilotriacetic acid, ethylenediaminetetraacetic acid, and diethylenetriaminepentaacetic acid. *Inorg. Chem.* **1994**, *33* (1), 88-92.

251. Sutherland, D. E. K. Structural Motifs of Novel Metallothionein Proteins. The University of Western Ontario, London, Ontario, 2012.

252. Yuan, A. T.; Korkola, N. C.; Stillman, M. J., Apo-metalllothionein-3 cooperatively forms tightly compact structures under physiological conditions. *J. Biol. Chem.* **2023**, *299* (3), 102899.

253. Uversky, V. N.; Gillespie, J. R.; Fink, A. L., Why are “natively unfolded” proteins unstructured under physiologic conditions? *Proteins: Struct., Funct., Bioinf.* **2000**, *41* (3), 415-427.

254. Begun, A.; Molochkov, A.; Niemi, A. J., Protein tertiary structure and the myoglobin phase diagram. *Sci. Rep.* **2019**, *9* (1), 10819.

255. Uversky, V. N.; Ptitsyn, O. B., Further Evidence on the Equilibrium “Pre-molten Globule State”: Four-state Guanidinium Chloride-induced Unfolding of Carbonic Anhydrase B at Low Temperature. *J. Mol. Biol.* **1996**, *255* (1), 215-228.

256. Rösner, H. I.; Redfield, C., The Human α -Lactalbumin Molten Globule: Comparison of Structural Preferences at pH 2 and pH 7. *J. Mol. Biol.* **2009**, *394* (2), 351-362.

257. Roder, H.; Elöve, G. A.; Englander, S. W., Structural characterization of folding intermediates in cytochrome c by H-exchange labelling and proton NMR. *Nature* **1988**, *335* (6192), 700-704.

258. Radford, S. E.; Dobson, C. M.; Evans, P. A., The folding of hen lysozyme involves partially structured intermediates and multiple pathways. *Nature* **1992**, *358* (6384), 302-307.

259. Uversky, V. N.; Ptitsyn, O. B., "Partly Folded" State, a New Equilibrium State of Protein Molecules: Four-State Guanidinium Chloride-Induced Unfolding of. beta.-Lactamase at Low Temperature. *Biochemistry* **1994**, *33* (10), 2782-2791.

260. Ptitsyn, O. B.; Uversky, V. N., The molten globule is a third thermodynamical state of protein molecules. *FEBS Lett.* **1994**, *341* (1), 15-18.

261. Uversky, V. N.; Ptitsyn, O. B., All-or-none solvent-induced transitions between native, molten globule and unfolded states in globular proteins. *Fold Des.* **1996**, *1* (2), 117-122.
262. Smith, L. J.; Fiebig, K. M.; Schwalbe, H.; Dobson, C. M., The concept of a random coil: Residual structure in peptides and denatured proteins. *Fold Des.* **1996**, *1* (5), R95-R106.
263. Kohn, J. E.; Millett, I. S.; Jacob, J.; Zagrovic, B.; Dillon, T. M.; Cingel, N.; Dothager, R. S.; Seifert, S.; Thiyagarajan, P.; Sosnick, T. R.; Hasan, M. Z.; Pande, V. S.; Ruczinski, I.; Doniach, S.; Plaxco, K. W., Random-coil behavior and the dimensions of chemically unfolded proteins. *Proc. Natl. Acad. Sci. U. S. A.* **2004**, *101* (34), 12491-12496.
264. Uversky, V. N., Intrinsically Disordered Proteins and Their Environment: Effects of Strong Denaturants, Temperature, pH, Counter Ions, Membranes, Binding Partners, Osmolytes, and Macromolecular Crowding. *Protein J.* **2009**, *28* (7), 305-325.
265. Braun, W.; Vasák, M.; Robbins, A. H.; Stout, C. D.; Wagner, G.; Kägi, J. H.; Wüthrich, K., Comparison of the NMR solution structure and the x-ray crystal structure of rat metallothionein-2. *Proc. Natl. Acad. Sci. U. S. A.* **1992**, *89* (21), 10124-8.
266. Sewell, A. K.; Jensen, L. T.; Erickson, J. C.; Palmiter, R. D.; Winge, D. R., Bioactivity of Metallothionein-3 Correlates with Its Novel Beta Domain Sequence Rather Than Metal Binding Properties. *Biochemistry* **1995**, *34* (14), 4740-4747.
267. Öz, G.; Zangger, K.; Armitage, I. M., Three-dimensional structure and dynamics of a brain specific growth inhibitory factor: metallothionein-3. *Biochemistry* **2001**, *40* (38), 11433-11441.
268. Hasler, D. W.; Faller, P.; Vašák, M., Metal-Thiolate Clusters in the C-Terminal Domain of Human Neuronal Growth Inhibitory Factor (GIF). *Biochemistry* **1998**, *37* (42), 14966-14973.
269. Artells, E.; Palacios, Ò.; Capdevila, M.; Atrian, S., In vivo-folded metal-metallothionein 3 complexes reveal the Cu-thionein rather than Zn-thionein character of this brain-specific mammalian metallothionein. *FEBS J.* **2014**, *281* (6), 1659-1678.
270. Melenbacher, A.; Stillman, M. J., Metallothionein-3: ⁶³Cu(I) binds to human ⁶⁸Zn7-β_α MT3 with no preference for Cu4-β cluster formation. *The FEBS Journal* **2023**, *n/a* (n/a).
271. Klaassen, C. D., *Metallothionein IV*. Birkhäuser Basel: 1999; p XLVI, 650.
272. Drozd, A.; Wojewska, D.; Peris-Diaz, M. D.; Jakimowicz, P.; Krezel, A., Crosstalk of the structural and zinc buffering properties of mammalian metallothionein-2. *Metallomics* **2018**, *10* (4), 595-613.

273. Irvine, Gordon W.; Korkola, N.; Stillman, Martin J., Isolated domains of recombinant human apo-metallothionein 1A are folded at neutral pH: a denaturant and heat-induced unfolding study using ESI-MS. *Biosci. Rep.* **2018**, *38* (4).
274. Gasteiger, E.; Gattiker, A.; Hoogland, C.; Ivanyi, I.; Appel, R. D.; Bairoch, A., ExPASy: The proteomics server for in-depth protein knowledge and analysis. *Nucleic Acids Res.* **2003**, *31* (13), 3784-8.
275. Kyte, J.; Doolittle, R. F., A simple method for displaying the hydropathic character of a protein. *J. Mol. Biol.* **1982**, *157* (1), 105-132.
276. Otvos, J. D.; Armitage, I. M., Structure of the metal clusters in rabbit liver metallothionein. *Proc. Natl. Acad. Sci. U. S. A.* **1980**, *77*, 7094-7098.
277. Vijay-Kumar, S.; Bugg, C. E.; Cook, W. J., Structure of ubiquitin refined at 1.8Å resolution. *J. Mol. Biol.* **1987**, *194* (3), 531-544.
278. Tanford, C., Isothermal Unfolding of Globular Proteins in Aqueous Urea Solutions. *J. Am. Chem. Soc.* **1964**, *86* (10), 2050-2059.
279. Greene, R. F.; Pace, C. N., Urea and guanidine hydrochloride denaturation of ribonuclease, lysozyme, α -chymotrypsin, and b-lactoglobulin. *J. Biol. Chem.* **1974**, *249* (17), 5388-5393.
280. Becktel, W. J.; Schellman, J. A., Protein stability curves. *Biopolymers* **1987**, *26* (11), 1859-1877.
281. Palaniappan, V.; Bocian, D. F., Acid-induced transformations of myoglobin. Characterization of a new equilibrium heme-pocket intermediate. *Biochemistry* **1994**, *33* (47), 14264-14274.
282. Chen, R.; Jäättelä, M., Lysosome as a Central Hub for Rewiring PH Homeostasis in Tumors. *Cancers* **2020**, *12* (9).
283. Gatenby, R. A.; Gillies, R. J., Why do cancers have high aerobic glycolysis? *Nat. Rev. Cancer* **2004**, *4* (11), 891-9.
284. Si, M.; Lang, J., The roles of metallothioneins in carcinogenesis. *Journal of Hematology & Oncology* **2018**, *11* (1), 107.
285. El Ghazi, I.; Martin, B. L.; Armitage, I. M., New proteins found interacting with brain metallothionein-3 are linked to secretion. *Int. J. Alzheimers Dis.* **2010**, *2011*, 208634.
286. Ghazi, I. E.; Martin, B. L.; Armitage, I. M., Metallothionein-3 Is a Component of a Multiprotein Complex in the Mouse Brain. *Exp. Biol. Med.* **2006**, *231* (9), 1500-1506.

287. Myers, J. K.; Pace, C. N.; Scholtz, J. M., Denaturant m values and heat capacity changes: relation to changes in accessible surface areas of protein unfolding. *Protein Sci.* **1995**, *4* (10), 2138-48.
288. Taverna, D. M.; Goldstein, R. A., Why are proteins marginally stable? *Proteins* **2002**, *46* (1), 105-9.
289. Trevino, S. R.; Schaefer, S.; Scholtz, J. M.; Pace, C. N., Increasing protein conformational stability by optimizing beta-turn sequence. *J. Mol. Biol.* **2007**, *373* (1), 211-8.
290. Gast, K.; Damaschun, H.; Eckert, K.; Schulze-Forster, K.; Maurer, H. R.; Mueller-Frohne, M.; Zirwer, D.; Czarnecki, J.; Damaschun, G., Prothymosin alpha: A biologically active protein with random coil conformation. *Biochemistry* **1995**, *34* (40), 13211-13218.
291. Uversky, V. N.; Gillespie, J. R.; Millett, I. S.; Khodyakova, A. V.; Vasiliev, A. M.; Chernovskaya, T. V.; Vasilenko, R. N.; Kozlovskaya, G. D.; Dolgikh, D. A.; Fink, A. L.; Doniach, S.; Abramov, V. M., Natively Unfolded Human Prothymosin α Adopts Partially Folded Collapsed Conformation at Acidic pH. *Biochemistry* **1999**, *38* (45), 15009-15016.
292. Paz, A.; Zeev-Ben-Mordehai, T.; Lundqvist, M.; Sherman, E.; Mylonas, E.; Weiner, L.; Haran, G.; Svergun, D. I.; Mulder, F. A.; Sussman, J. L., Biophysical characterization of the unstructured cytoplasmic domain of the human neuronal adhesion protein neuroligin 3. *Biophys. J.* **2008**, *95* (4), 1928-1944.
293. Mukhopadhyay, S.; Krishnan, R.; Lemke, E. A.; Lindquist, S.; Deniz, A. A., A natively unfolded yeast prion monomer adopts an ensemble of collapsed and rapidly fluctuating structures. *Proc. Natl. Acad. Sci. U. S. A.* **2007**, *104* (8), 2649-2654.
294. Zurdo, J.; Sanz, J. M.; González, C.; Rico, M.; Ballesta, J. P. G., The Exchangeable Yeast Ribosomal Acidic Protein YP2 β Shows Characteristics of a Partly Folded State under Physiological Conditions. *Biochemistry* **1997**, *36* (31), 9625-9635.
295. Kazakov, A. S.; Markov, D. I.; Gusev, N. B.; Levitsky, D. I., Thermally induced structural changes of intrinsically disordered small heat shock protein Hsp22. *Biophys. Chem.* **2009**, *145* (2-3), 79-85.
296. Neyroz, P.; Zambelli, B.; Ciurli, S., Intrinsically disordered structure of *Bacillus pasteurii* UreG as revealed by steady-state and time-resolved fluorescence spectroscopy. *Biochemistry* **2006**, *45* (29), 8918-8930.
297. Rantalainen, K. I.; Uversky, V. N.; Permi, P.; Kalkkinen, N.; Dunker, A. K.; Mäkinen, K., Potato virus A genome-linked protein VPg is an intrinsically disordered molten globule-like protein with a hydrophobic core. *Virology* **2008**, *377* (2), 280-288.
298. Kurzbach, D.; Platzer, G.; Schwarz, T. C.; Henen, M. A.; Konrat, R.; Hinderberger, D., Cooperative unfolding of compact conformations of the intrinsically disordered protein osteopontin. *Biochemistry* **2013**, *52* (31), 5167-5175.

299. Kjaergaard, M.; Teilum, K.; Poulsen, F. M., Conformational selection in the molten globule state of the nuclear coactivator binding domain of CBP. *Proc. Natl. Acad. Sci. U. S. A.* **2010**, *107* (28), 12535-40.
300. Demarest, S. J.; Martinez-Yamout, M.; Chung, J.; Chen, H.; Xu, W.; Dyson, H. J.; Evans, R. M.; Wright, P. E., Mutual synergistic folding in recruitment of CBP/p300 by p160 nuclear receptor coactivators. *Nature* **2002**, *415* (6871), 549-553.
301. Wilson, C. J.; Apiyo, D.; Wittung-Stafshede, P., Role of cofactors in metalloprotein folding. *Q. Rev. Biophys.* **2004**, *37* (3-4), 285-314.
302. Mei, G.; Rosato, N.; Silva, N., Jr.; Rusch, R.; Gratton, E.; Savini, I.; Finazzi-Agro, A., Denaturation of human copper-zinc superoxide dismutase by guanidine hydrochloride: a dynamic fluorescence study. *Biochemistry* **1992**, *31* (32), 7224-7230.
303. Bushmarina, N. A.; Blanchet, C. E.; Vernier, G.; Forge, V., Cofactor effects on the protein folding reaction: Acceleration of α -lactalbumin refolding by metal ions. *Protein Sci.* **2006**, *15* (4), 659-671.
304. Miura, T.; Satoh, T.; Takeuchi, H., Role of metal–ligand coordination in the folding pathway of zinc finger peptides. *Biochim. Biophys. Acta, Protein Struct. Mol. Enzym.* **1998**, *1384* (1), 171-179.
305. Pagani, S.; Vecchio, G.; Iametti, S.; Bianchi, R.; Bonomi, F., On the role of the 2Fe-2S cluster in the formation of the structure of spinach ferredoxin. *Biochim. Biophys. Acta, Protein Struct. Mol. Enzym.* **1986**, *870* (3), 538-544.
306. Ejniak, J.; Robinson, J.; Zhu, J.; Försterling, H.; Shaw, C. F.; Petering, D. H., Folding pathway of apo-metallothionein induced by Zn^{2+} , Cd^{2+} and Co^{2+} . *J. Biol. Inorg. Chem.* **2002**, *88* (2), 144-52.
307. Peris-Díaz, M. D.; Guran, R.; Zitka, O.; Adam, V.; Krężel, A., Metal- and Affinity-Specific Dual Labeling of Cysteine-Rich Proteins for Identification of Metal-Binding Sites. *Anal. Chem.* **2020**, *92* (19), 12950-12958.
308. Dong, S.; Wagner, N. D.; Russell, D. H., Collision-Induced Unfolding of Partially Metalated Metallothionein-2A: Tracking Unfolding Reactions of Gas-Phase Ions. *Anal. Chem.* **2018**, *90* (20), 11856-11862.
309. Wolff, N. A.; Lee, W.-K.; Thévenod, F., Role of Arf1 in endosomal trafficking of protein–metal complexes and cadmium–metallothionein-1 toxicity in kidney proximal tubule cells. *Toxicol. Lett.* **2011**, *203* (3), 210-218.
310. Subramanian Vignesh, K.; Deepe Jr., G. S., Metallothioneins: Emerging Modulators in Immunity and Infection. *Int. J. Mol. Sci.* **2017**, *18* (10), 2197.
311. Curthoys, N. P.; Moe, O. W., Proximal tubule function and response to acidosis. *Clin. J. Am. Soc. Nephrol.* **2014**, *9* (9), 1627-38.

312. Rigby Duncan, K. E.; Stillman, M. J., Metal-dependent protein folding: Metallation of metallothionein. *J. Inorg. Biochem.* **2006**, *100* (12), 2101-2107.
313. Capdevila, M.; Atrian, S., Metallothionein protein evolution: a miniassay. *JBIC Journal of Biological Inorganic Chemistry* **2011**, *16* (7), 977-989.
314. Sun, H. Z.; Li, H. Y.; Sadler, P. J., The biological and medicinal chemistry of bismuth. *Chem. Ber. Recl.* **1997**, *130* (6), 669-681.
315. Korkola, N. C.; Scarrow, P. M.; Stillman, M. J., pH dependence of the non-cooperative binding of Bi³⁺ to human apo-metallothionein 1A: kinetics, speciation, and stoichiometry. *Metallomics* **2020**, *12* (3), 435-448.
316. Korkola, N. C.; Hudson, E.; Stillman, M. J., Structurally restricted Bi(III) metallation of apo- β MT1a: metal-induced tangling. *Metallomics* **2021**, *13* (5).
317. Yang, N.; Sun, H., Biocoordination chemistry of bismuth: Recent advances. *Coord. Chem. Rev.* **2007**, *251* (17-20), 2354-2366.
318. Gorbach, S. L., Bismuth Therapy in Gastrointestinal-Diseases. *Gastroenterology* **1990**, *99* (3), 863-875.
319. Mjos, K. D.; Orvig, C., Metallo drugs in medicinal inorganic chemistry. *Chem. Rev.* **2014**, *114* (8), 4540-63.
320. Salvador, J. A. R.; Figueiredo, S. A. C.; Pinto, R. M. A.; Silvestre, S. M., Bismuth compounds in medicinal chemistry. *Future Med. Chem.* **2012**, *4* (11), 1495-1523.
321. Badrigilan, S.; Choupani, J.; Khanbabaei, H.; Hoseini-Ghahfarokhi, M.; Webster, T. J.; Tayebi, L., Bismuth-Based Nanomaterials: Recent Advances in Tumor Targeting and Synergistic Cancer Therapy Techniques. *Adv. Healthcare Mater.* **2020**, *9* (7).
322. Cheng, Y.; Zhang, H. Y., Novel Bismuth-Based Nanomaterials Used for Cancer Diagnosis and Therapy. *Chem. Eur. J.* **2018**, *24* (66), 17405-17418.
323. Torrisi, L.; Silipigni, L.; Restuccia, N.; Cuzzocrea, S.; Cutroneo, M.; Barreca, F.; Fazio, B.; Di Marco, G.; Guglielmino, S., Laser-generated bismuth nanoparticles for applications in imaging and radiotherapy. *J. Phys. Chem. Solids* **2018**, *119*, 62-70.
324. Szostak, K.; Ostaszewski, P.; Pulit-Prociak, J.; Banach, M., Bismuth Oxide Nanoparticles in Drug Delivery Systems. *Pharm. Chem. J.* **2019**, *53* (1), 48-51.
325. Fowler, B. A.; Sexton, M. J., CHAPTER 22 - Bismuth. In *Handbook on the Toxicology of Metals (Third Edition)*, Nordberg, G. F.; Fowler, B. A.; Nordberg, M.; Friberg, L. T., Eds. Academic Press: Burlington, 2007; pp 433-443.
326. Yuan, S. F.; Wang, R. M.; Chan, J. F. W.; Zhang, A. J. X.; Cheng, T. F.; Chik, K. K. H.; Ye, Z. W.; Wang, S. Y.; Lee, A. C. Y.; Jin, L. J.; Li, H. Y.; Jin, D. Y.; Yuen, K. Y.;

- Sun, H. Z., Metallodrug ranitidine bismuth citrate suppresses SARS-CoV-2 replication and relieves virus-associated pneumonia in Syrian hamsters. *Nat. Microbiol.* **2020**, *5* (11), 1439-+.
327. Sadler, P. J.; Li, H. Y.; Sun, H. Z., Coordination chemistry of metals in medicine: target sites for bismuth. *Coord. Chem. Rev.* **1999**, *185-6*, 689-709.
328. Alkim, H.; Koksall, A. R.; Boga, S.; Sen, I.; Alkim, C., Role of Bismuth in the Eradication of *Helicobacter pylori*. *Am. J. Ther.* **2017**, *24* (6), e751-e757.
329. Ge, R. G.; Chen, Z.; Zhou, Q. L., The actions of bismuth in the treatment of *Helicobacter pylori* infections: an update. *Metallomics* **2012**, *4* (3), 239-243.
330. Zhang, L.; Mulrooney, S. B.; Leung, A. F. K.; Zeng, Y. B.; Ko, B. B. C.; Hausinger, R. P.; Sun, H. Z., Inhibition of urease by bismuth(III): Implications for the mechanism of action of bismuth drugs. *Biometals* **2006**, *19* (5), 503-511.
331. Jin, L.; Szeto, K. Y.; Zhang, L.; Du, W. H.; Sun, H. Z., Inhibition of alcohol dehydrogenase by bismuth. *J. Inorg. Biochem.* **2004**, *98* (8), 1331-1337.
332. Kondo, Y.; Satoh, M.; Imura, N.; Akimoto, M., Tissue-Specific Induction of Metallothionein by Bismuth as a Promising Protocol for Chemotherapy with Repeated Administration of Cis-Diamminedichloroplatinum (II) against Bladder-Tumor. *Anticancer Res.* **1992**, *12* (6B), 2303-2308.
333. Chan, S.; Wang, R. M.; Man, K.; Nicholls, J.; Li, H. Y.; Sun, H. Z.; Chan, G. C. F., A Novel Synthetic Compound, Bismuth Zinc Citrate, Could Potentially Reduce Cisplatin-Induced Toxicity Without Compromising the Anticancer Effect Through Enhanced Expression of Antioxidant Protein. *Transl. Oncol.* **2019**, *12* (5), 788-799.
334. Boogaard, P. J.; Slikkerveer, A.; Nagelkerke, J. F.; Mulder, G. J., The Role of Metallothionein in the Reduction of Cisplatin-Induced Nephrotoxicity by Bi³⁺-Pretreatment in the Rat In Vivo and In Vitro - Are Antioxidant Properties of Metallothionein More Relevant Than Platinum Binding. *Biochem. Pharmacol.* **1991**, *41* (3), 369-375.
335. Naganuma, A.; Satoh, M.; Imura, N., Specific reduction of toxic side effects of adriamycin by induction of metallothionein in mice. *Jpn. J. Cancer Res.* **1988**, *79* (3), 406-11.
336. Jing, L.; Yang, M.; Li, Y.; Yu, Y.; Liang, B. L.; Cao, L. G.; Zhou, X. Q.; Peng, S. Q.; Sun, Z. W., Metallothionein prevents doxorubicin cardiac toxicity by indirectly regulating the uncoupling proteins 2. *Food Chem. Toxicol.* **2017**, *110*, 204-213.
337. Satoh, M.; Naganuma, A.; Imura, N., Metallothionein Induction Prevents Toxic Side-Effects of Cisplatin and Adriamycin Used in Combination. *Cancer Chemother. Pharmacol.* **1988**, *21* (2), 176-178.

338. Naganuma, A.; Satoh, M.; Imura, N., Prevention of Lethal and Renal Toxicity of Cis-Diamminedichloroplatinum(II) by Induction of Metallothionein Synthesis without Compromising Its Antitumor-Activity in Mice. *Cancer Res.* **1987**, *47* (4), 983-987.
339. Sutherland, D. E.; Stillman, M. J., The "magic numbers" of metallothionein. *Metallomics* **2011**, *3* (5), 444-63.
340. Thirumoorthy, N.; Sunder, A. S.; Kumar, K. T. M.; Kumar, M. S.; Ganesh, G. N. K.; Chatterjee, M., A Review of Metallothionein Isoforms and their Role in Pathophysiology. *World J. Surg. Oncol.* **2011**, *9*.
341. Vasak, M., Advances in metallothionein structure and functions. *J. Trace Elem. Med Biol.* **2005**, *19* (1), 13-7.
342. Blindauer, C. A., Advances in the molecular understanding of biological zinc transport. *Chem. Commun.* **2015**, *51* (22), 4544-4563.
343. Suzuki, C. A.; Ohta, H.; Albores, A.; Koropatnick, J.; Cherian, M. G., Induction of metallothionein synthesis by zinc in cadmium pretreated rats. *Toxicology* **1990**, *63* (3), 273-84.
344. Roesijadi, G., Metallothionein and its role in toxic metal regulation. *Comp. Biochem. Physiol. C Toxicol. Pharmacol.* **1996**, *113* (2), 117-123.
345. Haq, F.; Mahoney, M.; Koropatnick, J., Signaling events for metallothionein induction. *Mutat. Res-Fund. Mol. M.* **2003**, *533* (1-2), 211-226.
346. Wang, Y. C.; Tsang, C. N.; Xu, F.; Kong, P. W.; Hu, L. G.; Wang, J. W.; Chu, I. K.; Li, H. Y.; Sun, H. Z., Bio-coordination of bismuth in *Helicobacter pylori* revealed by immobilized metal affinity chromatography. *Chem. Commun.* **2015**, *51* (92), 16479-16482.
347. Messerle, B. A.; Schaffer, A.; Vasak, M.; Kagi, J. H. R.; Wuthrich, K., Comparison of the solution conformations of human [Zn₇]-metallothionein-2 and [Cd₇]-metallothionein-2 using nuclear magnetic resonance spectroscopy. *J. Mol. Biol.* **1992**, *225*, 433-443.
348. Otvos, J. D.; Armitage, I. M., ¹¹³Cd NMR of metallothionein: direct evidence for the existence of polynuclear metal binding sites. *J. Am. Chem. Soc.* **1979**, *101*, 7734-7736.
349. Zangger, K.; Oz, G.; Otvos, J. D.; Armitage, I. M., Three-dimensional solution structure of mouse [Cd₇]-metallothionein-1 by homonuclear and heteronuclear NMR spectroscopy. *Protein Sci.* **1999**, *8*, 2630-2638.
350. Babula, P.; Masarik, M.; Adam, V.; Eckschlager, T.; Stiborova, M.; Trnkova, L.; Skutkova, H.; Provaznik, I.; Hubalek, J.; Kizek, R., Mammalian metallothioneins: properties and functions. *Metallomics* **2012**, *4* (8), 739-50.

351. Vasak, M.; Meloni, G., Chemistry and biology of mammalian metallothioneins. *J. Biol. Inorg. Chem.* **2011**, *16* (7), 1067-78.
352. Rodilla, V.; Miles, A. T.; Jenner, W.; Hawksworth, G. M., Exposure of cultured human proximal tubular cells to cadmium, mercury, zinc and bismuth: toxicity and metallothionein induction. *Chem. Biol. Interact.* **1998**, *115* (1), 71-83.
353. Satoh, M.; Miura, N.; Naganuma, A.; Matsuzaki, N.; Kawamura, E.; Imura, N., Prevention of adverse effects of gamma-ray irradiation after metallothionein induction by bismuth subnitrate in mice. *Eur. J. Cancer Clin. Oncol.* **1989**, *25* (12), 1727-31.
354. Kondo, Y.; Himeno, S.; Satoh, M.; Naganuma, A.; Nishimura, T.; Imura, N., Citrate enhances the protective effect of orally administered bismuth subnitrate against the nephrotoxicity of cis-diamminedichloroplatinum. *Cancer Chemother. Pharmacol.* **2004**, *53* (1), 33-38.
355. Ngu, T. T.; Easton, A.; Stillman, M. J., Kinetic Analysis of Arsenic–Metalation of Human Metallothionein: Significance of the Two-Domain Structure. *J. Am. Chem. Soc.* **2008**, *130* (50), 17016-17028.
356. Pinter, T. B.; Irvine, G. W.; Stillman, M. J., Domain Selection in Metallothionein 1A: Affinity-Controlled Mechanisms of Zinc Binding and Cadmium Exchange. *Biochemistry* **2015**, *54* (32), 5006-16.
357. Alderighi, L.; Gans, P.; Ienco, A.; Peters, D.; Sabatini, A.; Vacca, A., Hyperquad simulation and speciation (HySS): a utility program for the investigation of equilibria involving soluble and partially soluble species. *Coord. Chem. Rev.* **1999**, *184*, 311-318.
358. Skoog, D. A.; Skoog, D. A., *Fundamentals of analytical chemistry*. 8th ed.; Thomson-Brooks/Cole: Belmont, CA, 2004.
359. Sadler, P. J.; Sun, H. Z.; Li, H. Y., Bismuth(III) complexes of the tripeptide glutathione (γ -L-Glu-L-Cys-Gly). *Chem-Eur. J.* **1996**, *2* (6), 701-708.
360. Broekaert, J. A. C., Daniel C. Harris: Quantitative chemical analysis, 9th ed. *Anal. Bioanal. Chem.* **2015**, *407* (30), 8943-8944.
361. Melenbacher, A.; Heinlein, L.; Hartwig, A.; Stillman, M. J., 63Cu(I) binding to human kidney $68\text{Zn}7\text{-}\beta\alpha$ MT1A: determination of Cu(I)-thiolate cluster domain specificity from ESI-MS and room temperature phosphorescence spectroscopy. *Metallomics* **2022**, *15* (1).
362. Irvine, G. W.; Korkola, N.; Stillman, M. J., Isolated domains of recombinant human apo-metallothionein 1A are folded at neutral pH: a denaturant and heat-induced unfolding study using ESI-MS. *Biosci. Rep.* **2018**, *38* (4).
363. Yuan, A. T.; Korkola, N. C.; Wong, D. L.; Stillman, M. J., Metallothionein Cd4S11 cluster formation dominates in the protection of carbonic anhydrase. *Metallomics* **2020**.

364. Zelazowski, A. J.; Stillman, M. J., Silver binding to rabbit liver zinc metallothionein and zinc. alpha. and. beta. fragments. Formation of silver metallothionein with silver (I): protein ratios of 6, 12, and 18 observed using circular dichroism spectroscopy. *Inorg. Chem.* **1992**, *31* (16), 3363-3370.
365. Sato, M.; Sasaki, M.; Hojo, H., Antioxidative roles of metallothionein and manganese superoxide dismutase induced by tumor necrosis factor-alpha and interleukin-6. *Arch. Biochem. Biophys.* **1995**, *316* (2), 738-44.
366. Cai, L.; Klein, J. B.; Kang, Y. J., Metallothionein inhibits peroxyxynitrite-induced DNA and lipoprotein damage. *J. Biol. Chem.* **2000**, *275* (50), 38957-60.
367. Ruttkay-Nedecky, B.; Nejdil, L.; Gumulec, J.; Zitka, O.; Masarik, M.; Eckschlager, T.; Stiborova, M.; Adam, V.; Kizek, R., The role of metallothionein in oxidative stress. *Int. J. Mol. Sci.* **2013**, *14* (3), 6044-66.
368. Gan, T.; Munoz, A.; Shaw, C. F., 3rd; Petering, D. H., Reaction of ^{111}Cd -metallothionein with EDTA. A reappraisal. *J. Biol. Chem.* **1995**, *270* (10), 5339-45.
369. Shaw Iii, C. F.; He, L.; Muñoz, A.; Savas, M. M.; Chi, S.; Fink, C. L.; Gan, T.; Petering, D. H., Kinetics of reversible N-ethylmaleimide alkylation of metallothionein and the subsequent metal release. *J. Biol. Inorg. Chem.* **1997**, *2* (1), 65-73.
370. Krezel, A.; Maret, W., Different redox states of metallothionein/thionein in biological tissue. *Biochem. J.* **2007**, *402* (3), 551-8.
371. Kocyla, A.; Pomorski, A.; Kręzel, A., Molar absorption coefficients and stability constants of Zincon metal complexes for determination of metal ions and bioinorganic applications. *J. Inorg. Biochem.* **2017**, *176*, 53-65.
372. Hoops, S.; Sahle, S.; Gauges, R.; Lee, C.; Pahle, J.; Simus, N.; Singhal, M.; Xu, L.; Mendes, P.; Kummer, U., COPASI--a COMplex PATHway SIMulator. *Bioinformatics* **2006**, *22* (24), 3067-74.
373. Artemenko, K.; Mi, J.; Bergquist, J., Mass-spectrometry-based characterization of oxidations in proteins. *Free Radical Res.* **2015**, *49* (5), 477-93.
374. Kendrew, J. C.; Parrish, R. G.; Bragg, W. L., The crystal structure of myoglobin III. Sperm-whale myoglobin. *Proc. R. Soc. London, Ser. A* **1957**, *238* (1214), 305-324.
375. Uversky, V. N.; Dunker, A. K., Understanding protein non-folding. *Biochim. Biophys. Acta* **2010**, *1804* (6), 1231-64.
376. Hamer, D. H., Metallothionein. *Annu. Rev. Biochem.* **1986**, *55* (1), 913-951.
377. Vallee, B. L., The function of metallothionein. *Neurochem. Int.* **1995**, *27* (1), 23-33.

378. Coyle, P.; Philcox, J. C.; Carey, L. C.; Rofe, A. M., Metallothionein: the multipurpose protein. *Cell. Mol. Life Sci.* **2002**, *59* (4), 627-647.

379. Yu, X.; Wu, Z.; Fenselau, C., Covalent Sequestration of Melphalan by Metallothionein and Selective Alkylation of Cysteines. *Biochemistry* **1995**, *34* (10), 3377-3385.

380. Wilson, J. H., Pointing fingers at the limiting step in gene targeting. *Nat. Biotechnol.* **2003**, *21* (7), 759-760.

Appendix A: ESI-MS Mass Values

Table A-1. Theoretical average masses expected in the deconvoluted ESI mass spectra for a titration of NEM into rh β α MT1a, NEM into rh β α MT3, Bi(III) into rh β MT1a, and Bi(III) into rh α MT1a.

# Bound	rh β α MT1a NEM	rh β α MT3 NEM	rh β α MT1a Bi(III)	rh β MT1a Bi(III)	rh α MT1a Bi(III)
0	7405.8	8212.5	7405.8	3753.4	4082.9
1	7531.0	8337.6	7611.8	3959.4	4288.9
2	7656.1	8462.8	7817.7	4165.3	4494.8
3	7781.2	8587.9	8023.7	4371.3	4700.8
4	7906.3	8713.0	8229.6		
5	8031.5	8838.2	8435.6		
6	8156.6	8963.3	8641.6		
7	8281.7	9088.4	8847.5		
8	8406.9	9213.5			
9	8532.0	9338.7			
10	8657.1	9463.8			
11	8782.3	9588.9			
12	8907.4	9714.1			
13	9032.5	9839.2			
14	9157.6	9964.3			
15	9282.8	10089.5			
16	9407.9	10214.6			
17	9533.0	10339.7			
18	9658.2	10464.8			
19	9783.3	10590.0			
20	9908.4	10715.1			

Table A-2. Theoretical average masses expected in the deconvoluted ESI mass spectra for mixed Zn(II) and NEM species bound to rh β α MT1a. Only mixed species experimentally observed in the mass spectra are listed.

# NEM	Zn(II) 0	Zn(II) 1	Zn(II) 2	Zn(II) 3	Zn(II) 4	Zn(II) 5	Zn(II) 6	Zn(II) 7
0	7405.8	7469.2	7532.5	7595.9	7659.3	7722.6	7786.0	7849.4
5						8348.3		
6					8410.1			
7					8535.2			
8				8597.0				
9				8722.1				
10				8847.2				
11				8972.3				
12			9034.1					
13			9159.2					
14			9284.4					

Table A-3. Theoretical average masses expected in the deconvoluted ESI mass spectra for mixed Cd(II) and NEM species bound to rh β MT1a. Only mixed species experimentally observed in the mass spectra are listed.

# NEM	Cd(II) 0	Cd(II) 1	Cd(II) 2	Cd(II) 3	Cd(II) 4	Cd(II) 5	Cd(II) 6	Cd(II) 7	Cd(II) 8
0	7405.8	7516.2	7626.6	7737.0	7847.4	7957.8	8068.2	8178.6	8289.0
5						8583.4			
6									
7					8723.3				
8					8848.4				
9				8863.2					
10				8988.3					
11				9113.4					
12			9128.2						
13			9253.3						
14			9378.4						
15									
16		9518.3							

Table A-4. Theoretical average masses expected in the deconvoluted ESI mass spectra for a titration of Bi(III) into Zn₇rh β MT1a. Only species experimentally observed in the mass spectra are listed.

# Bi(III)	Zn(II) 0	Zn(II) 1	Zn(II) 2	Zn(II) 3	Zn(II) 4	Zn(II) 5	Zn(II) 6	Zn(II) 7
0								7849.4
1							7992.0	
2						8134.6		
3					8277.1			
4			8356.4	8419.7				
5		8499.0						
6	8641.6							
7	8847.5							

Appendix B: Additional MD Simulation Data

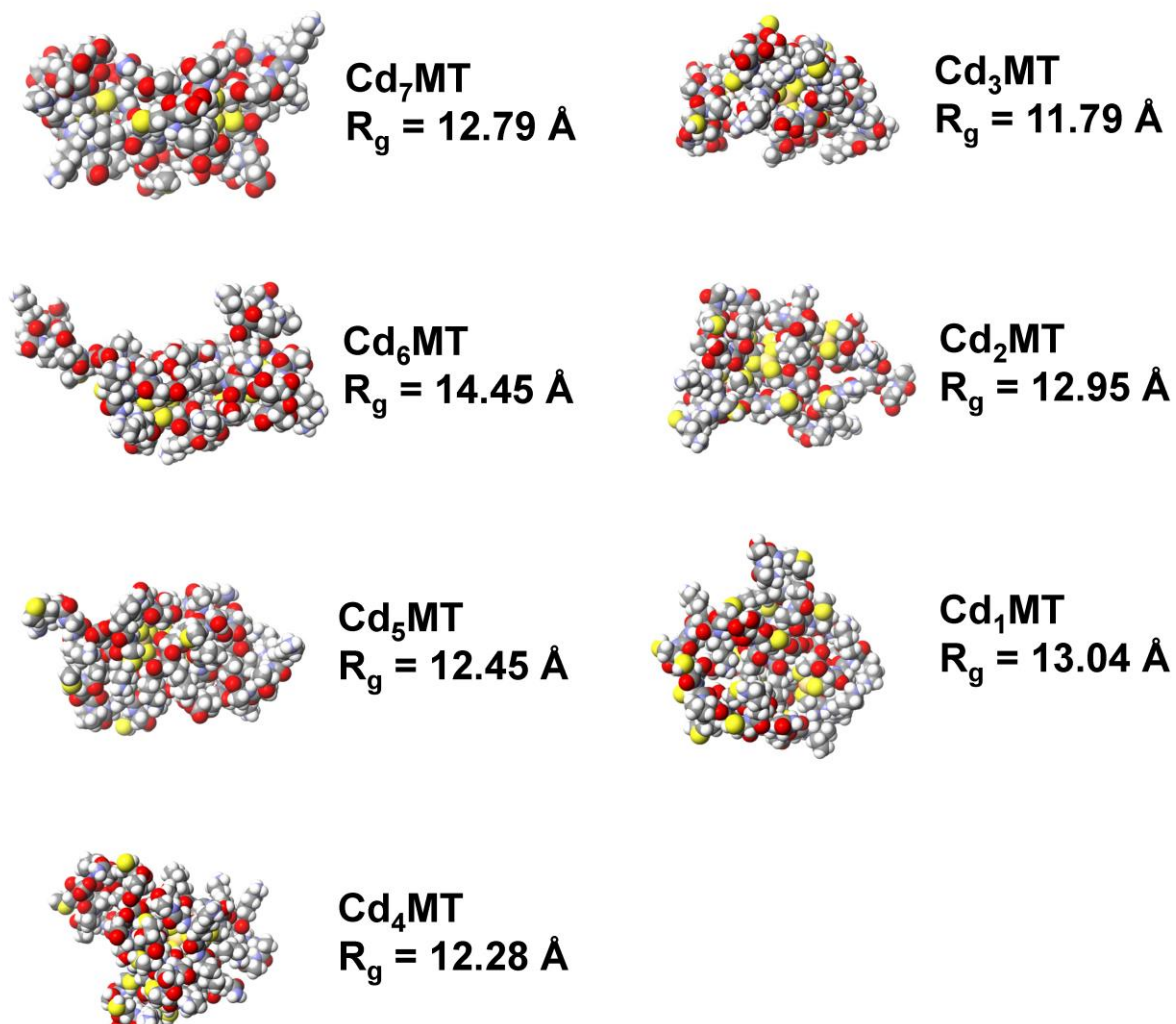


Figure B-1. MD simulations of a sequential demetallation of Cd₇MT represented by space-filling models. The models show each structure after 250 ps simulation at 300 K. The radius of gyration is shown beside its respective structure.

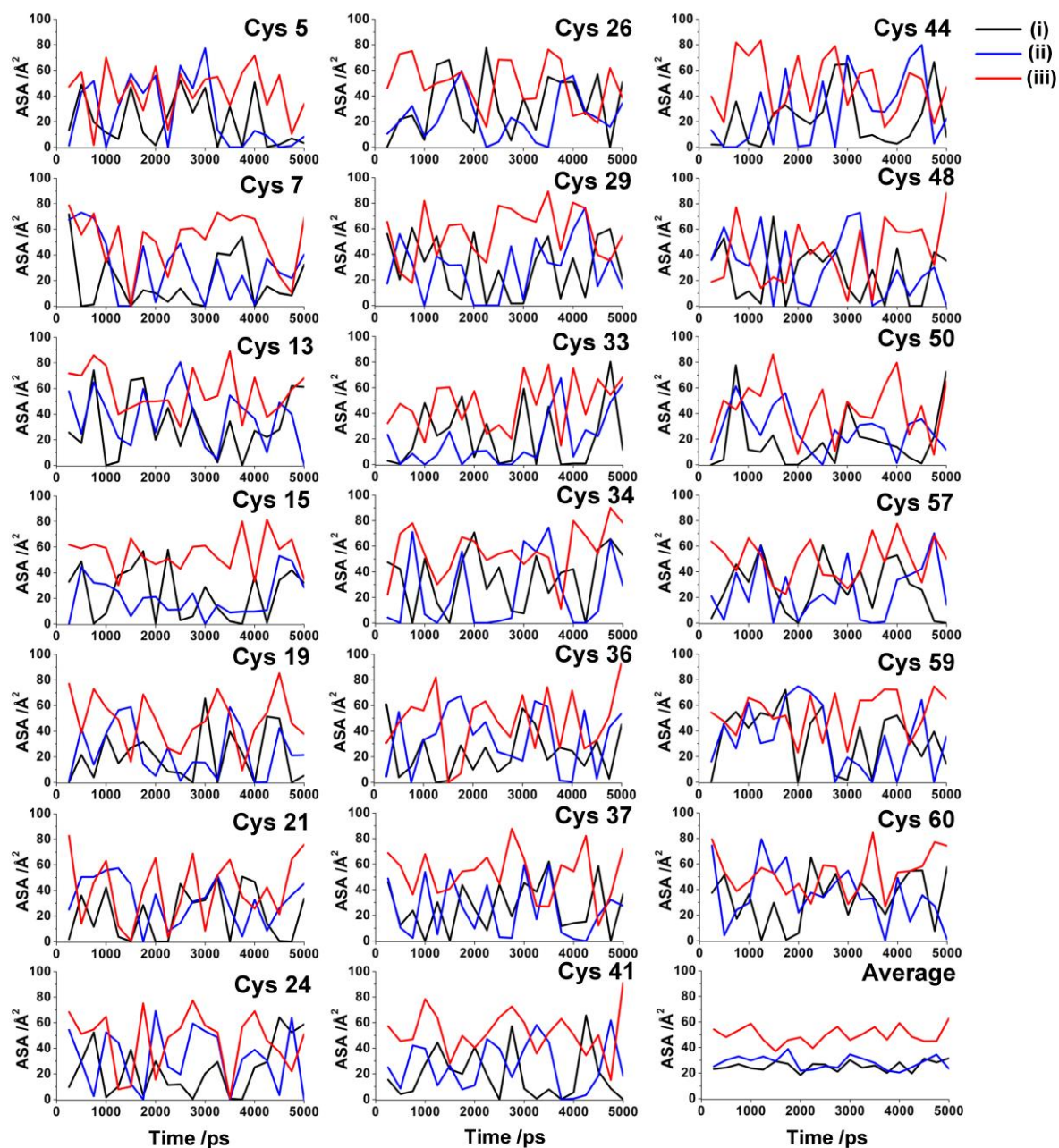


Figure B-2. ASA over time for individual cysteinyl sulfurs calculated from MD simulations of apo-MT1a at (i) 300 K after sequential demetallation, (ii) 300 K beginning from a linear sequence, and (iii) 1000 K beginning from a linear sequence.

Appendix C: Additional CD Spectroscopy Data

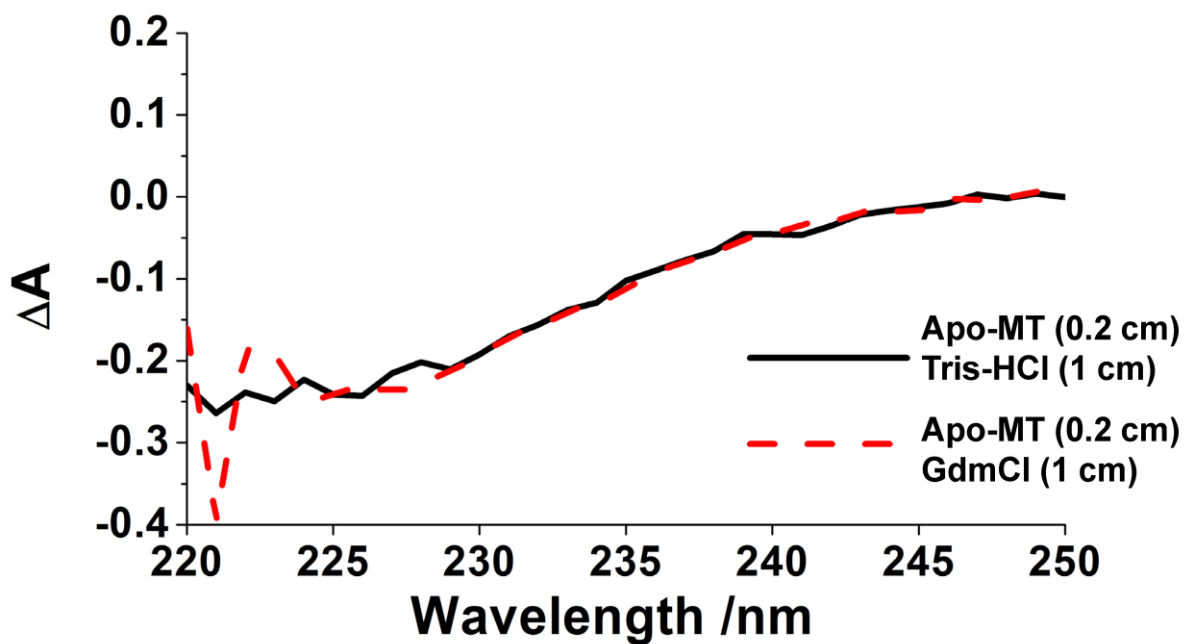


Figure C-1. A CD spectrum of 15 μM apo-MT1a in a 0.2 cm cuvette and 5 mM Tris-HCl in a separate 1 cm cuvette behind (black solid line). A CD spectrum of 15 μM apo-MT1a in a 0.2 cm cuvette and 1.4 M GdmCl in a separate 1 cm cuvette behind (red dashed line).

Appendix D: ESI-MS Validation Experiments

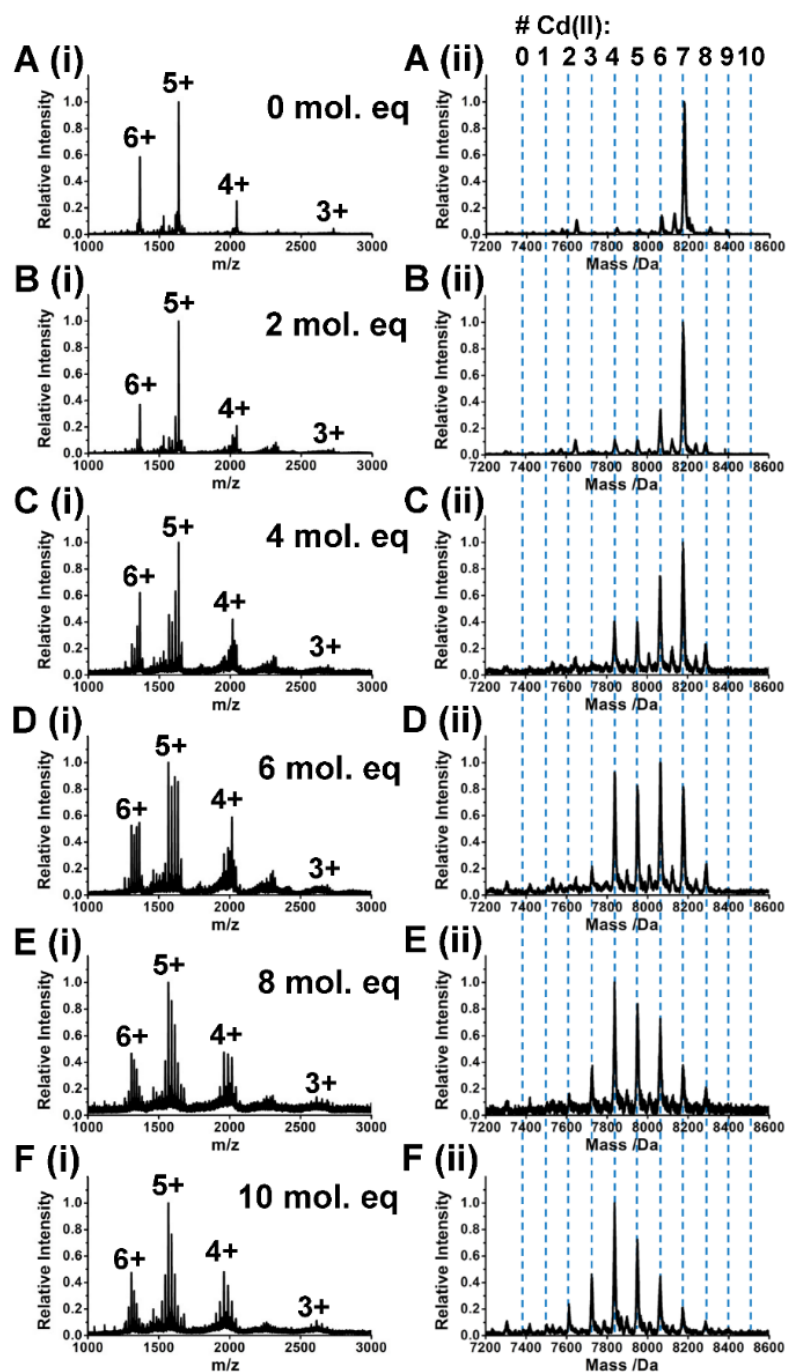


Figure D-1. A stepwise titration of H₂O₂ into 30 μM Cd₇MT at pH 7.4 monitored using ESI-MS. Selected (i) Charge state and (ii) deconvoluted ESI mass spectra show additions of (A) 0 mol. eq., (B) 2 mol. eq., (C) 4 mol. eq., (D) 6 mol. eq., (E) 8 mol. eq., and (F) 10 mol. eq. H₂O₂ to 30 μM Cd₇MT. ESI mass spectra were measured 24 h after mixing the reagents.

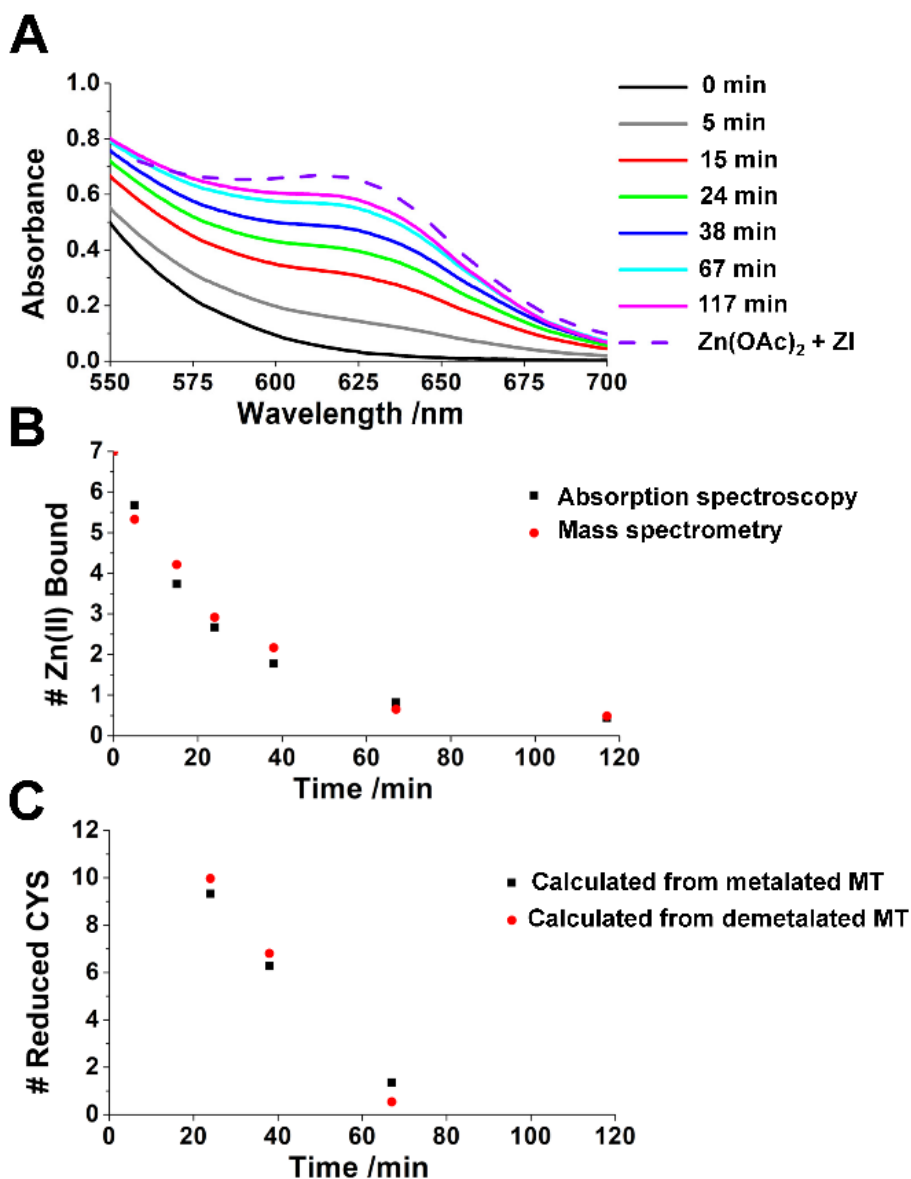


Figure D-2. A reaction of 17 μM Zn₇MT with 3.4 mM (200 mol. eq.) H₂O₂ in the presence of 0.5 mM TCEP and 1.2 mM ZI at pH 7.4 monitored over time. (A) Absorption spectra showing the reaction at various time points with the absorption band at 618 nm monitoring the binding of released Zn(II) to ZI. The dashed line shows the absorption spectrum of 119 μM Zn(II) with 1.2 mM ZI. (B) A plot of Zn(II) bound to MT over time. The black squares represent the amount of Zn(II) bound calculated by measuring the concentration of free Zn(II) over time with the ZI sensor ($\epsilon = 24\,200\ \text{M}^{-1}\text{cm}^{-1}$). The red circles represent the same reaction monitored by ESI-MS (in the absence of ZI) where the Zn(II) bound was calculated based on the weighted average intensity of the Zn₁₋₇MT peaks. (C) A plot of the total number of reduced cysteines over time measured by ESI-MS (in the absence of ZI). The black squares represent the number of reduced cysteines calculated based on the weighted average reduced cysteines for each metalated species in the spectrum. The red circles represent the number of reduced cysteines calculated from the average mass of apo-MT in demetalated solutions at particular time points.

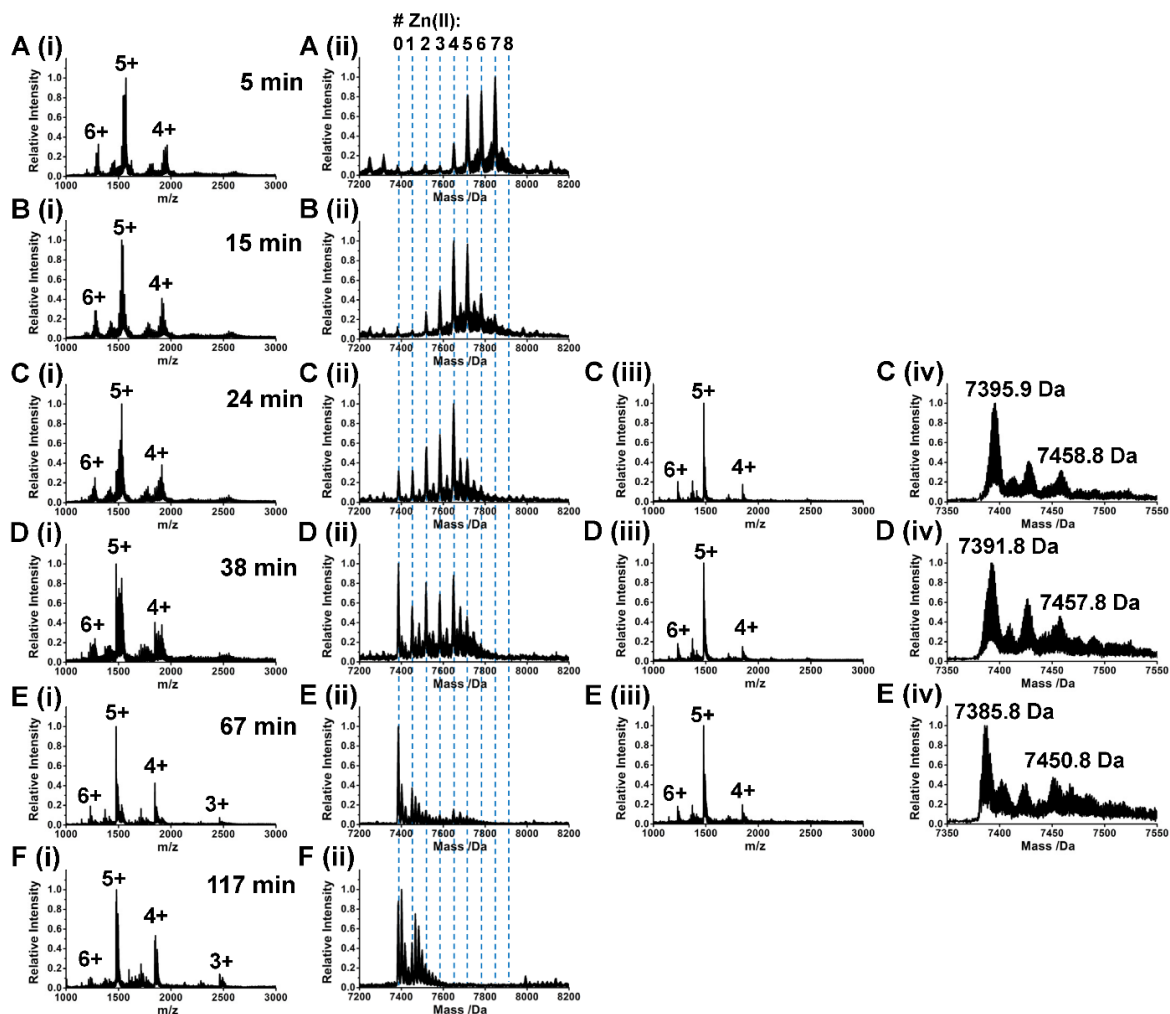


Figure D-3. A reaction of $17 \mu\text{M}$ Zn_7MT with 3.4 mM (200 mol. eq.) H_2O_2 in the presence of 0.5 mM TCEP at pH 7.4 monitored over time by ESI-MS. (i) Charge state and (ii) deconvoluted ESI mass spectra show the reaction at (A) 5 min, (B) 15 min, (C) 24 min, (D) 38 min, (E) 67 min, and (F) 117 min. (iii) Charge state and (iv) deconvoluted ESI mass spectra show the reacting MT demetallated by acidification at the time points (C) 24 min, (D) 38 min, and (E) 67 min.

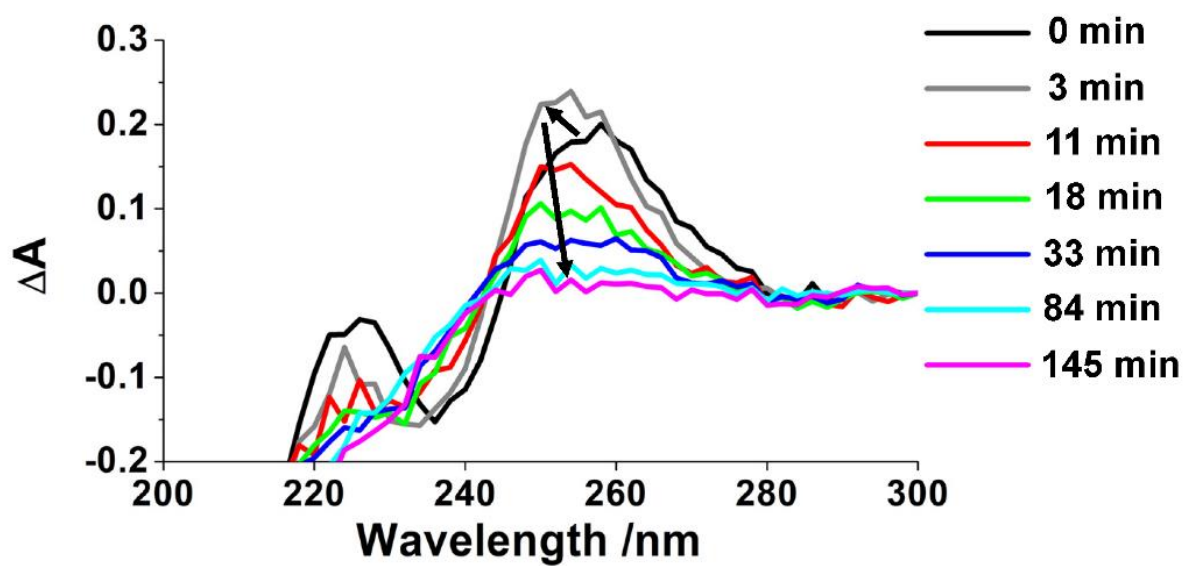


Figure D-4. A reaction of 25 μM Cd₇MT with 3.75 mM (150 mol. eq.) H₂O₂ in the presence of 0.5 mM TCEP at pH 7.4 monitored over time by CD spectroscopy.

Curriculum Vitae

Name: Natalie Korkola

Post-secondary Education and Degrees: University of Western Ontario
London, Ontario, Canada
2018-2023 Ph.D.

The University of Western Ontario
London, Ontario, Canada
2013-2018 B.A.

Honours and Awards: UWO CSC Travel Award
2023

Society of Biological Inorganic Chemistry Travel Grant
2022

NSERC Postgraduate Scholarship – Doctoral
2020-2023

Queen Elizabeth II Graduate Scholarship in Science and Technology
2019-2020

Related Work Experience Interim Mass Spectrometry Manager
The University of Western Ontario
2021-2022

Teaching Assistant
The University of Western Ontario
2018-2022

CanBIC Local Organizing Committee
Georgian Bay Conference on Bioinorganic Chemistry
2019, 2023

Analytical Student Intern
Parmalat
2016-2017

Publications:

9. Korkola, N. C., Stillman, M. J. 2023. Structural Role of Cadmium and Zinc in Metallothionein Oxidation by Hydrogen Peroxide: The Resilience of Metal–Thiolate Clusters. *J. Am. Chem. Soc.* 145 (11), 6383-6397. DOI: 10.1021/jacs.2c13578
8. Yuan, A. T., Korkola, N. C., Stillman, M. J. 2023. Apo-metallothionein-3 cooperatively forms tightly compact structures under physiological conditions. *J. Biol. Chem.* 299 (3), 102899. DOI: 0.1016/j.jbc.2023.102899
7. Korkola, N.C., Hudson, E., Stillman, M.J. 2021. Structurally restricted Bi(III) metallation of apo- β MT1a: metal-induced tangling. *Metallomics*. 13(5):mfab020. DOI: 10.1093/mtomcs/mfab023
6. Melenbacher, A., Korkola, N.C., Stillman, M.J. 2020. The pathways and domain specificity of Cu(I) binding to human metallothionein 1A, *Metallomics*, 2020, 12, 1951-1964. DOI: 10.1039/d0mt00215a
5. Wong, D.L., Yuan, A.T., Korkola, N.C., Stillman, M.J. 2020. Interplay between Carbonic Anhydrases and Metallothioneins: Structural Control of Metalation. *Int J Mol Sci.* 21(16):5697. doi: 10.3390/ijms21165697. PMID: 32784815; PMCID: PMC7460868.
4. Yuan, A.T.; Korkola, N.C.; Wong, D.L.; Stillman, M.J. 2020. Metallothionein Cd4S11 cluster formation dominates in the protection of carbonic anhydrase. *Metallomics*. 12, 767-783. DOI: 10.1039/d0mt00023j
3. Korkola, N.C.; Scarrow, P.M.; Stillman, M.J. 2020. pH dependence of the non-cooperative binding of Bi³⁺ to human apo-metallothionein 1a: kinetics, speciation, and stoichiometry. *Metallomics*. 12, 435-448. DOI: 10.1039/C9MT00285E
2. Wong, D.L.#; Korkola, N.C.#; Stillman, M.J. 2019. Kinetics of competitive Cd²⁺ binding pathways: the realistic structure of intrinsically disordered, partially metallated metallothioneins, *Metallomics*, 11, 894-905.*
Equal Contribution
*This paper was highlighted on the front cover of *Metallomics*.
1. Irvine, G.W.; Korkola, N.; Stillman, M.J. 2018. Isolated domains of recombinant human apo-metallothionein 1A are folded at neutral pH: a denaturant and heat-induced unfolding study using ESI-MS. *Biosci. Rep.*, 38(4), BSR20180592.

Conference Presentations:

9. Korkola, N.C., Stillman, M.J. “Structural Role of Cadmium and Zinc in Metallothionein Oxidation by Hydrogen Peroxide: The Resilience of Metal–Thiolate Clusters.” 20th International Conference on Biological Inorganic Chemistry. Adelaide, Australia, July 16th – 21st, 2023. Adelaide, Australia. (Oral Presentation)
8. Korkola, N.C., Stillman, M.J. “Oxidation-induced release of Cd(II) and Zn(II) thiolate structures from human metallothionein 1a.” 8th Georgian Bay International Conference on Bioinorganic Chemistry. Parry Sound, Canada. May 23rd – 27th, 2023. (Oral Presentation)
7. Korkola, N.C., Stillman, M.J. “Kinetics of oxidation induced cadmium and zinc release from human metallothionein 1a.” 16th European Biological Inorganic Chemistry Conference. Grenoble, France. July 17th – 21st, 2022. (Poster Presentation)
6. Korkola, N.C., Scarrow, P.; Hudson, E., Stillman, M.J. “Structurally restricted Bi(III) metallation of apo- β MT1a: metal-induced tangling.” The 2021 International Chemical Congress of Pacific Basin Societies. Virtual. December 16th – 21st, 2021. (Oral Presentation)
5. Korkola, N.C., Wong, D.L., Stillman, M.J. “The Rate of Cadmium Metallation of Metallothionein is Dependent on Structure and Binding Pathways.” 15th International Symposium on Applied Bioinorganic Chemistry. Nara, Japan. June 2nd – 5th, 2019. (Poster Presentation and Oral Flash Presentation)
4. Korkola, N.C., Wong, D.L., Stillman, M.J. “The Rate of Cadmium Metallation of Metallothionein is Dependent on Structure and Binding Pathways.” 7th Georgian Bay International Conference on Bioinorganic Chemistry. Parry Sound, Canada. May 21st – 25th, 2019. (Oral Presentation)
3. Korkola, N.C., Wong, D.L., Stillman, M.J. “Millisecond Metallation Reactions of Metallothionein.” The Ritsumeikan University – UWO International Showcase of Advances in Chemical and Bioinorganic Science. London, Canada. February 26th – 27th, 2019. (Oral Presentation)
2. Korkola, N.C., Wong, D.L., Stillman, M.J. “Metallation kinetics of metallothionein in the msec timescale using Stopped-Flow Methods.” 51st Inorganic Discussion Weekend. Waterloo, Canada. November 9th – 11th, 2018. (Oral Presentation)
1. Korkola, N.C., Stillman, M.J. “Studying the Folding of an Intrinsically Disordered Human Protein Using Electrospray Ionization Mass Spectrometry.” 46th Southern Ontario Undergraduate Student Chemistry Conference, Waterloo, Canada. March 24th, 2018. (Oral Presentation).